Investigating the impact of growth arrest mechanisms on tumour growth and responses to radiotherapy and hyperthermia



Chloé Colson
St Catherine's College
University of Oxford

A thesis submitted for the degree of
Doctor of Philosophy

Trinity 2023

Statement of Originality

This thesis is submitted to the University of Oxford in fulfilment of the requirements of the Doctor of Philosophy. This thesis contains no material which has been previously submitted for a degree or diploma at this University or any other. The modelling, analysis and numerical results in Chapters 2, 3, 4 and 5 of this thesis are the work of C. Colson under the supervision of H. M. Byrne and P. K. Maini. The work in Chapter 6 was carried out by C. Colson in collaboration with F. Sanchez-Garduño and T. Lorenzi, who contributed to the supervision of this work, alongside H. M. Byrne and P. K. Maini. The work in Chapters 2, 3 and 6 has been published in [45], [46] and [44], respectively.

Acknowledgements

First of all, I would like to gratefully acknowledge the Engineering and Physical Sciences Research Council (EPSRC) for funding this DPhil project. The work I have achieved over the last four years would not have been possible without the guidance and support of my wonderful supervisors Professors Helen Byrne and Philip Maini, who were an endless source of knowledge and inspiration for me and continuously pushed me to achieve my full potential. I would also like to thank my collaborators outside of the Mathematical Institute: Professors Faustino Sanchez-Garduño and Tommaso Lorenzi, for their knowledge, time and patience even during the most gruelling of moments.

In addition, I would like to acknowledge all of the friends who supported me from Oxford and further afield. Thank you to the members of the Wolfson Centre of Mathematical Biology and, in particular: Rahil – for dragging me out of the house for impromptu indoor cricket matches and "short" runs during the pandemic; Meredith – for indulging my slight cake addiction, from which I am slowly recovering; Becky – for distracting me on the best and worst of days with afternoons spent chatting away; Vedang – for the countless therapy sessions held in my office and the most flattering three words ever used to describe me; and Sofia – for always making me laugh (sometimes for reasons unknown). I would also like to thank my St Catz family: Giedre, Fede, Valentina and Julian, for outdoor workouts, dinners and trips to Wales that were invaluable during and post-pandemic. Moreover, I am eternally grateful for the unwavering support from Théophile and Diane, who, for more than a decade now, have never stopped being the best sounding board all the way from London/San Francisco/Paris. Last, but not least, thank you, Annabelle, for many foodie trips and (wholesome) gossip sessions, which never failed to take my mind off the struggles of my DPhil, at least temporarily.

Finally, and most importantly, I would like to thank my family. Christoph, thank you for your infallible support throughout the ups and downs of my DPhil, recognising that my love language is acts of service and, therefore, making my life a million times easier by embracing the role of the perfect house husband (while working a full-time job, mind you). Mum, dad, thank you for always encouraging me to believe in myself and dream big, and striving to provide me with all of the tools and opportunities to achieve these dreams. Lastly, I am grateful for my baby brother, Luca, who never stopped offering to write my thesis for me (thankfully, I didn't need to take him up on that).

Abstract

Developing targeted and effective treatment strategies for patients is at the forefront of cancer research today. Combination therapies that exploit different ways to treat cancer cells, while minimising adverse side-effects, have gained increased traction in recent years. In particular, hyperthermia (HT) has emerged as a promising candidate for enhancing tumour responses to radiotherapy (RT), a well-established cancer treatment used to treat more than 50% of cancer patients. However, an incomplete understanding of the interactions between RT and HT is hindering their combined use in the clinic. Inter- and intra-tumoural heterogeneity also impacts cancer progression and sensitivity to treatment. In this thesis, we develop a mathematical framework to characterise how two different mechanisms of growth control, namely growth arrest due to nutrient insufficiency and due to competition for space, may influence tumour dynamics during disease progression and under HT and/or RT.

We first develop a simple ordinary differential equation model of tumour growth which distinguishes between nutrient and space limited growth control. We find that there are three distinct growth regimes: nutrient limited, space limited and bistable, where both mechanisms of growth arrest coexist. We then extend our model to study the responses of tumours in each regime to RT and HT individually and in combination. In each regime, we determine the biological processes that may underpin positive and negative treatment outcomes and assess which treatment (RT, HT or RT + HT) and dosing regimen maximise the reduction in tumour burden. This work enables us to generate a set of hypotheses that may explain some of the widely varying tumour behaviours observed experimentally and clinically.

With a view to extending the preceding work to investigate how nutrient and space limited mechanisms of growth arrest influence tumour invasion, we study a simple model of tumour cell invasion into healthy tissue. This process has frequently been modelled by systems of coupled partial differential equations involving degenerate, cross-dependent diffusion. We propose a minimal model that captures these features, while remaining analytically tractable. We carry out a travelling wave analysis and prove the existence and uniqueness of two types of invasive fronts of tumour cells into the extracellular matrix (ECM), which differ according to whether the density of the ECM ahead of the wave front is at carrying capacity or not. We also establish relationships between the speed of invasion and key model parameters.

Contents

1 Introduction **1**

1.1 Overview 1

1.2 Cancer biology: tumour growth and invasion 2

1.3 Radiation and hyperthermic oncology 4

1.3.1 Radiation oncology 4

1.3.2 Hyperthermic oncology 5

1.3.3 Combining radiotherapy and hyperthermia 7

1.3.3.1 Biological rationale of combining radiation and hyperthermia 7

1.3.3.2 Typical treatment schedules for combination treatments . . 8

1.4 Mathematical models of tumour growth 8

1.5 Mathematical models of tumour invasion 10

1.5.1 Reaction-diffusion equation models of cancer invasion 11

1.5.2 Nonlinear, degenerate diffusion: from one-dimensional to multi-dimensional analysis 13

1.6 Mathematical models of tumour response to radiotherapy and hyperthermia 14

1.6.1 Modelling radiotherapy response 14

1.6.2 Modelling hyperthermia response 15

1.6.3 Modelling combined treatment response 16

1.7 Thesis structure 18

2 A simple ODE model of tumour growth that distinguishes between different mechanisms of growth arrest **20**

2.1 Introduction 20

2.2 Model development 21

2.2.1 The mathematical model 21

2.2.2 Non-dimensionalisation 23

2.3 Numerical simulations: tumour growth curves 24

2.3.1 Numerical setup 24

2.3.2 Simulating tumour growth 25

2.4 Steady state analysis . . . 27
2.4.1 Steady state solutions: existence and multiplicity . . . 27
2.4.1.1 Space limited steady states . . . 27
2.4.1.2 Nutrient limited steady states . . . 28
2.4.2 Stability analysis . . . 29
2.4.2.1 Space limited steady states . . . 29
2.4.2.2 Nutrient limited steady states . . . 30
2.5 The existence of three tumour growth regimes . . . 31
2.6 Discussion . . . 33

3 Investigating the influence of growth arrest mechanisms on tumour responses to radiotherapy 35
3.1 Introduction . . . 35
3.2 Model development . . . 37
3.2.1 The mathematical model . . . 37
3.2.2 Non-dimensionalisation . . . 39
3.2.3 Defining the dimensionless model parameters . . . 40
3.3 Numerical study: methods and set up . . . 41
3.4 Characterising tumour response to fractionated RT . . . 43
3.4.1 Tumours in monostable regimes: the NL and SL virtual tumour populations . . . 43
3.4.1.1 Typical responses to a conventional fractionation schedule . 43
3.4.1.2 The influence of the oxygen consumption rates, q_1 and q_3, on treatment outcome following a conventional fractionation schedule . . . 45
3.4.1.3 The effect of the dosing schedule on typical tumour response 50
3.4.2 Tumours in the bistable regime . . . 51
3.4.2.1 Typical response to a conventional fractionation schedule . 51
3.4.2.2 The influence of q_1, q_3 and V_0 on treatment outcome following a conventional fractionation schedule . . . 51
3.4.2.3 The effect of the dosing schedule on typical tumour response 55
3.5 Post-treatment tumour growth dynamics . . . 56
3.5.1 Steady state analysis . . . 56
3.5.2 Elucidating conditions for RT to drive steady state switching of tumours in bistable regimes . . . 57
3.6 Discussion . . . 60

4 Investigating the influence of growth arrest mechanisms on tumour responses to hyperthermia 63
4.1 Introduction . . . 63
4.2 Model development . . . 64
4.2.1 The mathematical model . . . 64
4.2.2 Non-dimensionlisation . . . 68
4.2.3 Defining the dimensionless parameters . . . 69
4.3 Numerical methods and set up . . . 70
4.4 Investigating tumour responses to mild HT . . . 71
4.5 Investigating tumour responses to high HT . . . 73
4.5.1 Short-term tumour responses . . . 73
4.5.2 Post-HT tumour dynamics . . . 80
4.5.3 Sensitivity of tumour responses to the thermal dose . . . 84
4.5.4 Sensitivity of tumour responses to the rate of angiogenesis . . . 85
4.6 Discussion . . . 88

5 Investigating the influence of growth arrest mechanisms on tumour responses to combinations of radiotherapy and hyperthermia 91
5.1 Introduction . . . 91
5.2 Methods . . . 92
5.2.1 The treatment schedules under consideration . . . 92
5.2.2 Numerical methods . . . 94
5.2.3 Comparing equivalent RT, HT and RT+HT treatments . . . 94
5.2.4 Determining the 'best' treatment and dosing regimen pair . . . 95
5.3 Investigating tumour responses to combined mild HT and RT . . . 97
5.4 Investigating tumour responses to combined high HT and RT . . . 99
5.4.1 Nutrient limited regimes . . . 99
5.4.1.1 Characterising interactions between conventional HT and RT 99
5.4.1.2 The influence of dosing regimen on interactions between HT and RT . . . 101
5.4.1.3 Determining the treatment and dosing regimen which maximise tumour response . . . 103
5.4.2 Space limited regimes . . . 106
5.4.2.1 Characterising interactions between conventional HT and RT 106
5.4.2.2 The influence of dosing regimen on interactions between HT and RT . . . 108

5.4.2.3 Determining the treatment and dosing regimen which maximise tumour response . . . 110
5.4.3 Bistable regimes . . . 111
5.5 Discussion . . . 112

6 Travelling wave analysis of a model of tumour invasion with degenerate, cross-dependent diffusion 116
6.1 Introduction . . . 116
6.2 The mathematical model . . . 117
6.3 Travelling wave analysis . . . 119
6.3.1 The travelling wave problem . . . 119
6.3.1.1 Preliminaries . . . 119
6.3.1.2 Desingularisation of the ODE system . . . 122
6.3.2 The existence and uniqueness of travelling wave solutions . . . 123
6.3.2.1 Local analysis of the equilibrium point $(1, 0, 0)$: defining the shooting parameter . . . 124
6.3.2.2 Monotonicity of solutions with respect to the shooting parameter . . . 126
6.3.2.3 The behaviour of solutions at infinity . . . 131
6.3.2.4 Solutions converging to the equilibrium point $(0, 0, 1)$ . . . 132
6.3.2.5 Solutions converging to the equilibrium point $(0, 0, \bar{m})$ with $\bar{m} \in [0, 1)$ . . . 138
6.4 Numerical simulations: demonstration of analytical results . . . 147
6.4.1 Numerical methods and set-up . . . 147
6.4.2 Travelling wave solutions . . . 148
6.4.3 Elucidating the wave speed that emerges in the PDE model . . . 148
6.5 Discussion . . . 150

7 Conclusions and Future Work 153
7.1 Summary of work . . . 154
7.2 Future work . . . 157
7.2.1 Validation against experimental data . . . 157
7.2.2 Spatial modelling . . . 157
7.2.3 A more realistic depiction of angiogenesis in the presence and absence of treatment . . . 159
7.2.4 Accounting for healthy tissue response to treatment . . . 160
7.3 Final remarks . . . 160

A Defining the parameters for our model of tumour growth and response to hyperthermia and radiotherapy **162**
A.1 Defining the tumour growth parameters 162
A.2 Defining the radiotherapy parameters 166
A.3 Defining the hyperthermia parameters 166

B Tumour response to mild HT is not significantly affected by the values of $\widetilde{\alpha}_{\mathbf{V}}$ and $\widetilde{\alpha}_{\mathbf{RO2}}$ **168**

C Tumour response to RT+HT: additional numerical results **170**
C.1 Comparing tumour responses to equivalent RT, HT and RT+HT protocols 170
C.1.1 Appendix for Section 5.4.1.1 170
C.1.2 Appendix for Section 5.4.1.2 171
C.1.3 Appendix for Section 5.4.2.1 172
C.1.4 Appendix for Section 5.4.2.2 173
C.2 The importance of how RT and HT are coordinated 173
C.3 The influence of the rate of damage-induced angiogenesis, κ_0 174
C.4 The influence of how we define the 'best' treatment 176

References **178**

Chapter 1

Introduction

1.1 Overview

Second only to cardiovascular diseases, cancer is one of the leading causes of mortality worldwide, with 10 million recorded deaths in 2020 [235]. This has prompted extensive research aiming to understand the biological mechanisms underpinning cancer and develop effective therapeutic protocols to improve patient prognosis.

Existing well-established treatment modalities, such as radiotherapy (RT), chemotherapy (CT) and immunotherapy (IT), are applied via highly-regulated dosing protocols to maximise treatment efficacy. However, their efficacy is often limited by early termination of treatment due to adverse side-effects. This has resulted in an increased focus on the development of combination therapies, which exploit different anti-cancer effects, while limiting treatment toxicity. Hyperthermia (HT), which involves heating tumour cells above physiological temperatures, has emerged as a promising candidate for enhancing the efficacy of RT, in particular. Many experimental and clinical studies combining HT and RT have been conducted, but with mixed success [117]. The lack of conclusive results can be attributed to incomplete understanding of their interactions.

Another key factor impacting treatment efficacy is heterogeneity in treatment response. Recent technological advances, such as the development of single-cell sequencing, have demonstrated that tumours of the same type can exhibit high inter- and intra-tumour heterogeneity at the genetic and phenotypic levels [155]. Such heterogeneity can significantly influence tumour responses to treatment with the emergence of resistant phenotypes enabling tumour progression and recurrence [12, 156]. For example, breast cancer is typically classified into four sub-types based on tumour expression of oestrogen, progesterone and human epidermal growth factor receptors, and each sub-type is associated with a different standard of care and prognosis [266]. Understanding how tumour heterogeneity impacts sensitivity to treatment is, therefore, an essential step towards patient-specific treatment design.

In this thesis, we develop a mathematical framework to characterise how two different mechanisms of growth control, namely growth arrest due to nutrient insufficiency and due to competition for space, may influence tumour dynamics during disease progression and when HT and/or RT are applied. One key goal of this work is to use mathematical modelling to generate hypotheses that may explain some of the widely varying tumour behaviours observed experimentally and clinically, in the context of tumour invasion and responses to HT and RT. By producing such experimentally testable predictions relating to how HT and RT should be combined, we also aim to guide treatment protocol design.

In this chapter, we review the relevant biological and mathematical literature. In Section 1.2, we discuss key aspects of cancer biology that underpin solid tumour growth and invasion. Section 1.3 focusses on defining RT and HT in the context of cancer therapy; we discuss how RT and HT are applied and outline their individual mechanisms of action. We also emphasise the biological rationale for combining HT and RT and summarise combined dosing regimens that have been tested in the clinic.

Mathematical modelling has been used to study many aspects of cancer biology. Section 1.4 provides an overview of the mathematical approaches that have been proposed to study tumour growth. We demonstrate that, regardless of their complexity, most models of tumour growth consider a single mechanism of growth arrest. In Section 1.5, we review efforts to model tumour invasion, before focussing on describing existing reaction-diffusion equation models. We also highlight key numerical and analytical results on the behaviour of such models.

In order to guide treatment planning using mathematical modelling, a number of treatment response models have been developed, more so for RT than HT. We review these models in Section 1.6.

This introductory chapter concludes in Section 1.7 with an overview of the structure of the remainder of the thesis and a summary of each chapter.

Sections 1.2 and 1.4, Sections 1.3.1 and 1.6.1, and Section 1.5.2 are largely based on parts of the introductions of publications by C. Colson et al.: [45], [46] and [44], respectively.

1.2 Cancer biology: tumour growth and invasion

Solid tumour growth and invasion are complex processes involving interactions between multiple different cell types, e.g., healthy, tumour and immune cells, as well as other tissue components such as the vasculature and the extracellular matrix (ECM), a scaffold of proteins that holds cells in place and initiates cellular signalling pathways associated with migration, differentiation and proliferation [18, 260]. Each of these, and their interactions,

can be affected in different ways by anti-cancer therapies, which has prompted extensive experimental research to understand tumour growth dynamics and how they may be affected by treatment.

Solid tumour growth is typically separated into two stages: the avascular and the vascular stages [38]. Avascular growth has largely been studied experimentally using *in vitro* three-dimensional (3D) multicellular tumour spheroids as they replicate a number of biological and microenvironmental properties of tumours *in vivo*. Thus, they are considered representative of the growth kinetics of small avascular tumours [106].

For tumour spheroids grown in free suspension, all cells in the 3D cell aggregate initially proliferate by consuming nutrients (e.g., oxygen and glucose) that diffuse from the boundary of the spheroid, resulting in initial exponential growth. As the cell numbers and spheroid volume increase, the outermost cells form a proliferative rim while those in the central regions become quiescent (i.e., alive, but non-proliferative) as their access to crucial nutrients decreases. This results in linear growth of the tumour spheroid. Quiescent cells eventually die due to prolonged nutrient deprivation, forming a necrotic core of dead cellular material that degrades over time. Thus, a tumour spheroid may gradually approach an equilibrium size at which the rate of cell proliferation in the well-oxygenated outer rim balances the rate of cell degradation in the nutrient-starved necrotic region [103, 131, 173]. It has also been shown that tumour spheroids grown in agarose gels of varying stiffness evolve to contact-inhibited equilibria as mechanical stress can lead to cell cycle arrest and apoptosis [137], reducing the rate of cell proliferation, potentially to zero, and/or increasing the rate of cell death [103].

The above descriptions illustrate how *in vitro* tumour spheroids may attain nutrient or space limited equilibria depending on whether nutrient insufficiency or mechanical stress is dominant. We, therefore, expect that similar nutrient and space limited mechanisms of growth arrest may be active during the growth of *in vivo* tumours.

Now, for a tumour growing *in vivo* to progress beyond its avascular equilibrium, it must develop its own vasculature via angiogenesis [38]. Angiogenesis begins when tumour cells secrete various diffusible chemical species (e.g., vascular endothelial growth factor) into the surrounding tissue, triggering the growth of new blood vessels towards the tumour. Once vascularised, a tumour can access the nutrients necessary for further, rapid growth and discard metabolic waste.

At the same time, some tumour cells may acquire an invasive phenotype, i.e., low cell-cell adhesion, high cell-ECM adhesion, high motility and increased resistance to apoptosis [98]. They then start locally proliferating and migrating into the surrounding healthy tissue. To do so, they remodel, or degrade, the ECM by producing matrix-degrading enzymes, such as matrix metalloproteinases [39, 230]. They may also acidify the tissue microenvironment

by favouring glycolytic metabolism even in aerobic conditions (i.e., the 'Warburg effect'), resulting in healthy cell death [87, 258]. Finally, tumour cells which migrate to pre-existing blood vessels may enter these vessels and then travel to other tissues, where they establish secondary tumours or metastases.

1.3 Radiation and hyperthermic oncology

1.3.1 Radiation oncology

Radiotherapy is used to treat more than 50% of cancer patients [148]. It involves the delivery of energy rays to a tissue region containing both cancerous and healthy tissue. Balancing treatment efficacy and undesirable side-effects in normal tissues is, therefore, integral to the design of radiation protocols. Radiation protocols usually involve small doses, called fractions, delivered at regular intervals for fixed time periods. While a typical fractionation schedule consists of 2 Gy doses delivered Monday to Friday for up to 7 weeks [1], the dose, frequency and treatment duration can be varied to deliver a fixed total dose. The latter is often termed the Maximum Tolerated Dose (MTD), i.e., the highest dose which does not cause adverse side-effects [81].

Radiation induces both direct and indirect cytotoxic effects by causing DNA damage to cancer cells that can prove fatal, via various cell death pathways, if left unrepaired. Mitotic catastrophe (MC) is considered the most common cause of cell death post-irradiation. Irradiated cells typically die from MC during mitosis or the interphase that follows, within one or two cell-cycles post-irradiation. Direct effects arise from interactions between ionising particles and DNA, while indirect effects arise from interactions between ionising particles and water, which create reactive oxygen species that subsequently react with DNA. Indirect effects are more common, which is why hypoxic, i.e., poorly oxygenated, tumours are often radio-resistant [89]. Intratumoural oxygen levels are a key factor influencing tumour radio-sensitivity. Another key factor is the tumour cell proliferation rate, with cells in the G2 or mitosis phases of the cell cycle being most sensitive to RT.

We distinguish between three main types of DNA damage: single-strand breaks (SSBs), double-strand breaks (DSBs) and base damages. SSBs and base damages are more common than DSBs [161, 242]. However, only around 30% of cellular death is due to SSBs and base damages, as their main repair pathway, the base excision repair (BER) mechanism, is robust against mutations and very effective [148]. On the other hand, the non-homologous end joining (NHEJ) and homologous recombination (HR) repair mechanisms for DSBs are error-prone and the latter can only be activated during certain phases of the cell cycle (S and G2, specifically). Therefore, cell death is primarily due to DSBs.

RT can also affect the tumour vasculature in a dose-dependent way. Low dose radiation ($< 2\,\mathrm{Gy}$) can promote angiogenesis [152, 153] and vascular normalisation [196], thus increasing tumour perfusion and reducing hypoxia. By contrast, high dose radiation ($> 10\,\mathrm{Gy}$) can cause vascular damage and necrosis [232, 250], which reduces tumour perfusion and increases hypoxia. The effects of RT on the vasculature are typically weaker at moderate doses: RT does not promote angiogenesis, nor does it cause vascular damage, but it may transiently enhance vessel normalisation.

1.3.2 Hyperthermic oncology

While records of heat being used to treat cancer date back to around 2000 BC [21], modern scientific interest in hyperthermia as a cancer treatment only began in the mid-1970s, i.e., nearly a century after ionising radiation was first discovered. Since then, much experimental and clinical research has been devoted to investigating the biological mechanisms of action of HT. Unfortunately, they are still not fully understood due to inconclusive or contradictory findings [109, 249]. In what follows, we discuss the physiological effects of HT that have the strongest supporting evidence and are most relevant to radiation oncology (see the Schematic in Figure 1.1). Note that the interactions of HT and the immune system are beyond the scope of this thesis and we refer the interested reader to the following reviews [14, 224] for further details.

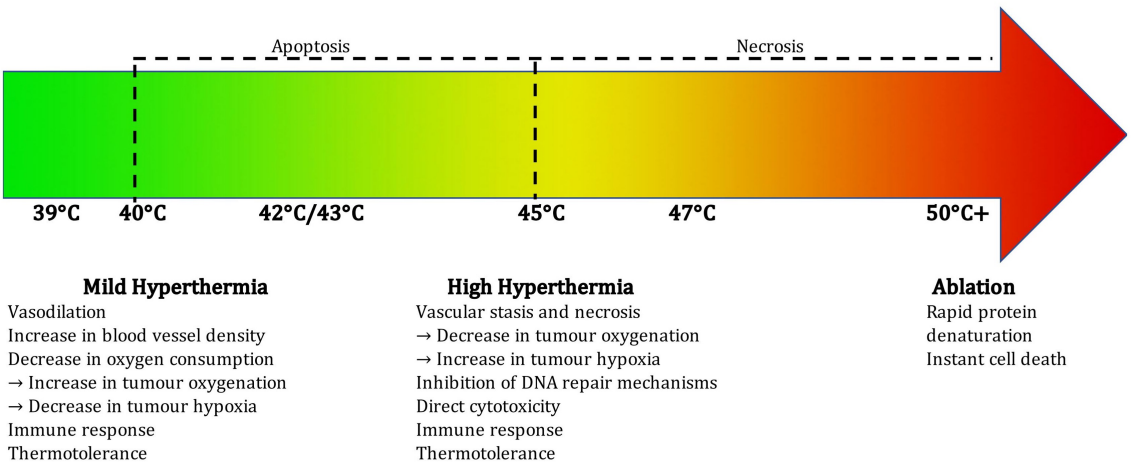


Figure 1.1: Schematic listing the effects of hyperthermia and the temperatures at which they occur.

HT entails heating tumour cells internally or externally at temperatures in the range $39-50°\mathrm{C}$. Different methods (e.g., microwave heating [210], ultrasound [268], hyperthermic perfusion [93] and nano-particle based HT [13]) are used depending on the type, location and

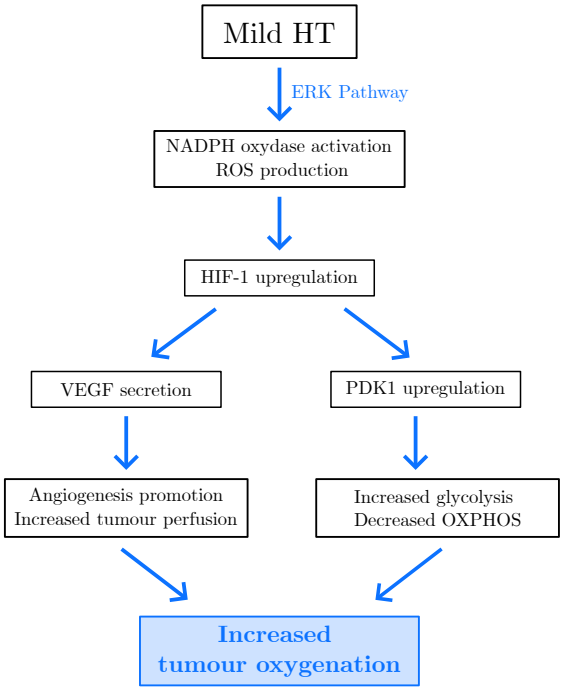


Figure 1.2: Schematic showing how mild HT increases tumour oxygenation.

progression of a patient's tumour: HT is usually administered locally or regionally for non-metastatic disease, while whole body HT is reserved for metastatic disease. In contrast to RT, there is no standard HT treatment schedule. This is because HT is typically used only as an adjuvant treatment [15, 265] and, as such, the protocol depends on the primary treatment it is complementing. (We return to this when discussing combined RT and HT treatment schedules in Section 1.3.3.) That being said, one key factor that must be accounted for when planning HT treatments is thermotolerance, which increases with temperatures in the range $39 - 45°C$ [85, 94, 121]. Thermotolerance is a process by which the upregulation of certain heat shock proteins (HSP70s and HSP90s) enables tumour cells to acquire a transient resistance to heat cytotoxicity [141]. Since experimental evidence suggests that thermotolerance lasts an average of $24 - 48$h after its induction [265], HT fractions should be applied at least two days apart.

The treatment dose, termed thermal dose, is quantified by the tissue temperature achieved and heating duration [134], and allows us to distinguish between two main types of HT: mild and high.

Mild hyperthermia. Mild HT typically refers to heating at temperatures no higher than $42°C$ for $30 - 60$ min. This form of HT is primarily used to sensitise cancer cells to other treatment modalities, as its main effect is to increase tumour oxygenation via increased tumour perfusion [170] and/or a reduction in oxygen consumption rates [168, 255].

The increase in micro-circulation can be largely attributed to heat-induced vasodilation, which fades within 1 h after heating according to both experiments [108, 124, 234, 248] and mathematical modelling [19]. Further, at least two processes may reduce oxygen consumption rates [118] for up to $24 - 48$ h [113, 221, 228, 255]. First, heat may preferentially target respiratory enzymes (over glycolytic enzymes) by inactivating and denaturing them [136, 125], resulting in a (transient) switch from anaerobic to glycolytic metabolism. Second, as shown in Figure 1.2, mild HT can activate hypoxia-inducible-factor 1 (HIF-1) through a cascade of non-hypoxia-driven biological events [168]. This inhibits oxidative phosphorylation (OXPHOS) and promotes glycolysis following upregulation of pyruvate dehydrogenase kinase 1 (PDK1). It also promotes tumour angiogenesis for $24 - 48$ h following the upregulation of vascular endothelial growth factor (VEGF) [168]. The latter contributes to the increase in tumour perfusion.

High hyperthermia. High hyperthermia corresponds to heating at temperatures higher than 42°C for $30 - 60$ min. High HT is considered to have three key effects: (1) it can cause direct cytotoxic effects on tumour cells, with protein denaturation hypothesised to be the main mode of hyperthermic cell kill [119], (2) it can induce vascular stasis, damage and necrosis [11, 65, 226], and (3) it can inhibit DNA repair pathways, e.g., the BER, NHEJ and HR pathways [179].

Treatments above 50°C are referred to as thermal ablation. Small, inoperable tumours are heated to very high temperatures (typically $50 - 80$°C) for very short durations in order to cause irreparable cellular damage, inevitably leading to apoptotic and necrotic cell death [42]. While this form of thermal treatment is now commonplace, it is beyond the scope of this thesis, so we refer the interested reader to some excellent reviews [42, 92].

1.3.3 Combining radiotherapy and hyperthermia

1.3.3.1 Biological rationale of combining radiation and hyperthermia

Despite a lack of comprehensive understanding of the mechanisms underpinning HT and how it interacts with RT, there is a wealth of *in vitro*, preclinical and clinical evidence [43, 64, 109, 165, 183, 184] providing a strong biological basis for combining HT with RT. By referring to the biology described in Sections 1.3.1 and 1.3.2, we make the following hypotheses that may explain the synergistic interactions between HT and RT:

1. Mild HT increases the efficacy of radiation treatments by improving tumour perfusion, which reduces tumour hypoxia (Section 1.3.2), a defining characteristic of aggressive tumours that can contribute to tumour cell survival and tumour development [175], and promote cancer cell resistance to radiotherapy [25, 26] (Section 1.3.1).

2. High HT increases RT-induced cytotoxicity by inhibiting the DNA repair mechanisms (Section 1.3.2), such as BER, NEHJ and HR, that are responsible for repairing radiation-induced damage (Section 1.3.1).

3. High HT contributes to the overall efficacy of combined treatment by causing tumour and endothelial cell death.

There is no clear consensus among experimentalists and clinicians about whether mild or high HT is the more potent radiosensitiser [15]. One of our key aims is, thus, to test the preceding hypotheses and shed light on which of mild or high HT is more effective when combined with RT.

1.3.3.2 Typical treatment schedules for combination treatments

We now summarise the range of combination treatment schedules that have been applied in the clinic [43, 57, 165]. We note that, in many cases, information about the study design and treatment protocol is incomplete.

Most RT schedules are designed in a standard way: a MTD in the range $24 - 100\,\text{Gy}$ is fixed and radiation is delivered $1 - 5$ times per week via fractions with doses in the range $1 - 5\,\text{Gy}$. There is greater variability in HT protocols. As for RT, HT is fractionated and heating is applied $1 - 3$ times per week, at minimum temperatures in the range $42 - 45°\text{C}$ for $30 - 120\,\text{min}$. The total number of HT fractions is either determined by the length of the RT schedule (e.g., 5 weeks of RT is combined with 5 weeks of HT) or fixed such that HT is applied for a certain number of weeks at the start of treatment.

Information about how RT and HT are coordinated (i.e., in terms of the order of, and delay between, the two treatments) is limited. That said, in most clinical trials, HT is typically applied within $30 - 240\,\text{min}$ after RT.

1.4 Mathematical models of tumour growth

Many mathematical approaches have been proposed to model the avascular and vascular stages of tumour growth. These include continuum, differential equation models (phenomenological or mechanistic) [6, 30, 172, 209], discrete, individual based models (IBMs) [164, 257] and hybrid models combining differential equations and IBMs [37, 204]. Despite their differences, most models share a common characteristic: they focus on a single mechanism of growth control or a group of mechanisms of growth control, whose effects are indistinguishable. We show this using the following concise and non-exhaustive summary.

Phenomenological ordinary differential equation (ODE) models are the simplest; they aim to describe tumour growth dynamics without explicitly incorporating the underlying

biological processes. Two popular ODE models that can represent a tumour's initial exponential growth, followed by linear growth and finally growth saturation are the logistic and Gompertz models [172]:

$$\frac{\mathrm{d}T}{\mathrm{d}t} = rT\left(1 - \frac{T}{K}\right) \quad \text{(logistic)}, \tag{1.1}$$

$$\frac{\mathrm{d}T}{\mathrm{d}t} = -rT\ln\left(\frac{T}{K}\right) \quad \text{(Gompertz)}. \tag{1.2}$$

In Equations (1.1) and (1.2), $r > 0$ is the tumour growth rate and $K > 0$ is the carrying capacity. The carrying capacity has been defined in several different ways; including the free space available for the tumour to occupy [144] and the volume that can be reached given nutrient availability [267]. However, irrespective of how the carrying capacity, K, is defined, a unique growth-limiting process is explicitly incorporated in these models: the tumour reaches an equilibrium at which the proliferation rate of the tumour cells tends to zero (with no cell death). This assumption also applies to ODE models which include a time-dependent carrying capacity, e.g., the following model of vascular tumour growth developed by Hahnfeldt et al. [95]:

$$\begin{cases} \dfrac{\mathrm{d}T}{\mathrm{d}t} = -rT\ln\left(\dfrac{T}{K}\right), \\ \dfrac{\mathrm{d}K}{\mathrm{d}t} = -\lambda K + bT - dKT^{(2/3)}, \end{cases} \tag{1.3}$$

where $\lambda > 0$ is the rate of vascular decay, $b > 0$ is the rate of vascular growth due to short-range stimulation (e.g., by angiogenic factors such as VEGF) and $d > 0$ is the rate of vascular loss due to long-range inhibition. Here, the tumour volume exhibits Gompertzian growth, with a carrying capacity $K(t)$ that varies in time to account for dynamic changes in the vascular support to the tumour.

The above ODE models do not provide significant mechanistic insight into the biological processes underpinning tumour growth, unlike more complex, spatially-resolved partial differential equation (PDE) models. The seminal model developed by Greenspan [91] considers a 3D, radially-symmetric, avascular tumour whose proliferation and death rates depend on the concentration of oxygen, which diffuses into the tumour and is consumed by tumour cells. This mechanistic model reduces to a reaction-diffusion equation for the oxygen concentration and an integro-differential equation for the evolution of the outer tumour radius. It predicts that the tumour will reach an equilibrium size at which the rate of cell death in nutrient-poor regions balances the rate of cell proliferation in nutrient-rich regions. This is the same growth arrest mechanism described both by two-phase models of avascular tumour growth considering tumour cells and extracellular fluid [24, 31] and the three phase model comprising tumour cells, dead material and extracellular fluid developed by Lewin et al. [140]. Alternatively, Panovska et al. [186] proposed a coupled system of nonlinear PDEs to

describe vascular tumour growth, via the invasion of the surrounding healthy tissue, and angiogenesis. While this model predicts that the tumour will reach a steady state at which the rates of cell death and cell birth balance, it incorporates both mechanical constraints (which limit cell proliferation) and nutrient constraints (which induce cell death) to tumour growth. In other words, several growth-limiting mechanisms are considered, but their effects are combined from a mathematical perspective.

In contrast to the preceding spatially-resolved, continuum models, Enderling et al. [66] extended the hybrid model of vascular tumour growth and invasion into healthy tissue developed by Anderson [4] to represent a tumour which reaches a steady state as proliferating tumour cells run out of space. In particular, growth control is a result of the tumour cell proliferation rate converging to zero, in the absence of cell death. Finally, Drasdo and Höhme [61] developed a discrete model of tumour growth that describes the *in vitro* growth of two-dimensional (2D) monolayers and 3D multicellular spheroids. The mechanism responsible for growth control differs for 2D monolayers, which are contact-inhibited, and 3D spheroids, which are nutrient-inhibited. Regardless, in both experimental set-ups, a tumour reaches an equilibrium size as cell proliferation and cell death rates balance.

Each of the aforementioned models considers one of two distinct growth-limiting mechanisms: (1) growth arrest via a cessation of cell proliferation, with no cell death, and (2) growth arrest via the rates of cell death and cell proliferation balancing. This observation motivates the development of a simple ODE model of tumour growth that distinguishes between these two mechanisms of growth arrest in Chapter 2.

1.5 Mathematical models of tumour invasion

As a hallmark of cancer [98], tumour invasion has been studied using a range of mathematical models. Initial approaches comprised coupled systems of PDEs where tumour cell migration is governed by diffusion, and chemotactic and/or haptotactic cues, e.g., see [5, 27, 39, 44, 74, 83, 107, 151, 154, 158, 169, 177, 191, 192, 225, 233]. Such reaction-diffusion-taxis models describe the emergence of an invasive front of cancer cells, i.e., a travelling wave, and provide insight into the speed and depth of invasion. Discrete and hybrid approaches based on similar biological assumptions have also been developed. They allow individual cells to be tracked and can more easily incorporate intracellular dynamics and cell-cell interactions explicitly [4, 5, 79, 115, 203, 220, 243].

Another important class of cancer invasion models are non-local models that account for the cell-cell and cell-matrix adhesion processes that facilitate cell movement in addition to the previously considered chemotactic and haptotactic cues [8, 40, 58, 70, 84, 105, 223]. Finally, we highlight multiphase models of tumour invasion which decompose the tissue into distinct phases (e.g., tumour cells, healthy cells, vasculature and ECM) and apply principles

of mass and momentum balance to these phases [48, 80, 112, 240] to determine the governing equations. These models typically include both local and non-local interactions between the constituent phases.

While we have given a brief overview of mathematical models of tumour invasion, our focus in this thesis is on a reaction-diffusion (R-D) PDE model of tumour invasion. We, therefore, review models of this type below.

1.5.1 Reaction-diffusion equation models of cancer invasion

The seminal model of acid-mediated tumour invasion by Gatenby and Gawlinski [83] describes the spatio-temporal interactions of healthy cells, tumour cells and the acid produced by tumour cells. Denoting the healthy cell density, tumour cell density and acid concentration, at position x and time t, by $M(x,t)$, $N(x,t)$ and $L(x,t)$, respectively, the model takes the form

$$\begin{cases} \dfrac{\partial M}{\partial t} = M(1 - M - \alpha L), \\ \dfrac{\partial N}{\partial t} = \dfrac{\partial}{\partial x}\left[D_{\mathrm{N}}(1-M)\dfrac{\partial N}{\partial x}\right] + \beta N(1-N), \\ \dfrac{\partial L}{\partial t} = \dfrac{\partial^2 L}{\partial x^2} + \gamma(N - L), \end{cases} \tag{1.4}$$

where $0 \leq D_{\mathrm{N}} \ll 1$ and β, $\gamma > 0$ are $\mathcal{O}(1)$. The parameter $\alpha > 0$ measures the toxicity of acidic H+ ions on the normal tissue. For $\alpha \geq 1$, the R-D system describes the eradication of normal tissue following tumour cell invasion. By contrast, if $0 < \alpha < 1$, the model predicts that a residual healthy cell density, of size $1 - \alpha$, remains behind the spreading benign wave. A numerical investigation of travelling wave solutions of Equations (1.4) predicted the formation of an interstitial gap (i.e., a region practically devoid of cells) ahead of the invading tumour front for large values of α. Experiments confirmed the existence of the interstitial gap, and the model has generated novel and accurate predictions regarding tumour invasion. This is one of the reasons why this model and its variants have been extensively investigated [74, 107, 154, 158, 169, 233]. We now review some of these extensions of the Gatenby-Gawlinski model.

Holder et al. [107] modify (1.4) by adding a cellular competition term in the equation for M and replacing the acid production term in the equation for L by a logistic growth term. Their resulting model is

$$\begin{cases} \dfrac{\partial M}{\partial t} = M(1 - M - \alpha(N + L)), \\ \dfrac{\partial N}{\partial t} = \dfrac{\partial}{\partial x}\left[D_{\mathrm{N}}(1-M)\dfrac{\partial N}{\partial x}\right] + \beta N(1-N), \\ \dfrac{\partial L}{\partial t} = \dfrac{\partial^2 L}{\partial x^2} + \gamma_1 N(1-N) - \gamma_2 L. \end{cases} \tag{1.5}$$

This generalization was motivated by the fact that tumours tend to present with very heterogeneous acid profiles and there is some experimental evidence of higher acid concentrations near the region of the interstitial gap. Another generalization of the Gatenby-Gawlinski model was proposed by McGillen et al. [158]. They added competition terms in the equations for M and N and incorporated acid-mediated tumour decay in the equation for N. Their model takes the form

$$\begin{cases} \dfrac{\partial M}{\partial t} = M(1 - M - \alpha_1 N - \alpha_2 L), \\ \dfrac{\partial N}{\partial t} = \dfrac{\partial}{\partial x}\left[D_{\mathrm{N}}(1-M)\dfrac{\partial N}{\partial x}\right] + \beta N(1 - N - \delta_1 M - \delta_2 L), \\ \dfrac{\partial L}{\partial t} = \dfrac{\partial^2 L}{\partial x^2} + \gamma(N - L). \end{cases} \tag{1.6}$$

In a recent paper, Moschetta and Simeoni [169] proposed a numerical scheme to solve the Gatenby-Gawlinksi model and, subsequently, derived a simplified version of this model. In particular, by assuming that $L = N$ in system (1.4), they obtained the following system:

$$\begin{cases} \dfrac{\partial M}{\partial t} = M(1 - M - \alpha N), \\ \dfrac{\partial N}{\partial t} = \dfrac{\partial}{\partial x}\left[D_{\mathrm{N}}(1-M)\dfrac{\partial N}{\partial x}\right] + \beta N(1 - N). \end{cases} \tag{1.7}$$

Assuming that $L = N$ is reasonable when $\gamma \to \infty$ in the equation for L in (1.4) and is further justified by the similarities in the tumour cell and acid profiles described by the full system. The key qualitative features of the full model are successfully captured by the reduced model, which has prompted further numerical [157] and analytical [82] investigations of system (1.7). Finally, Browning et al. [27] derived an experimentally-motivated R-D model of invasion that describes the evolution of the density of healthy skin tissue, melanoma cells and a tissue-degrading chemical produced by the melanoma cells. As in [169], they reduce their model to a system describing the densities of the healthy and the tumour cell populations, M and N. Their reduced model takes the following form:

$$\begin{cases} \dfrac{\partial M}{\partial t} = -\alpha M N, \\ \dfrac{\partial N}{\partial t} = \dfrac{\partial}{\partial x}\left[D_{\mathrm{N}}(1-M)\dfrac{\partial N}{\partial x}\right] + \beta N(1 - N - M). \end{cases} \tag{1.8}$$

The models (1.4)–(1.8) vary in their complexity, but they are all characterised by a nonlinear, degenerate tumour cell diffusion term. In Chapter 6, we analyse a minimal model of tumour invasion, which contains a similar diffusion term [44].

1.5.2 Nonlinear, degenerate diffusion: from one-dimensional to multi-dimensional analysis

As mentioned above, a key component of the aforementioned models of tumour invasion is the nonlinear, degenerate diffusion term for the tumour cell density. Travelling wave solutions (TWS) governed by this type of diffusion have been extensively studied in the case of one-dimensional (dimensionless) R-D PDEs of the form

$$\frac{\partial N}{\partial t} = \frac{\partial}{\partial x}\left[D(N)\frac{\partial N}{\partial x}\right] + f(N). \tag{1.9}$$

Different forms of the diffusion coefficient D have been considered, with an emphasis on whether the function has one ([9, 32, 53, 54, 149, 214, 215]) or multiple ([60, 69, 149]) degeneracies. In general, if f is of Fisher–Kolmogoroff–Petrovsky–Piscounoff (Fisher–KPP) type, i.e., $f \in C[0,1]$ with $f(0) = f(1) = 0$ and $f(N) > 0 \,\forall\, n \in (0,1)$, then Equation (1.9) supports TWS of the form $N(x,t) = n(y) = n(x - ct)$ satisfying asymptotic conditions $\lim_{y\to-\infty} n(y) = 1$ and $\lim_{y\to+\infty} n(y) = 0$ if and only if $c \geq c^*$, where the minimum wave speed $c^* > 0$ is defined as the threshold speed below which no TWS exist. In addition, if $c = c^*$, then the TWS is of sharp type (i.e., there is a discontinuity in the spatial derivative at the front) and, for each $c > c^*$, there exists a smooth TWS.

It is non-trivial to extend these existence results to R-D systems because studying trajectories in higher-dimensional phase spaces brings additional complexity. It has nonetheless been done for specific R-D PDE models. Kawasaki et al. [123] developed an R-D PDE model with cross-dependent diffusivities to describe spatiotemporal pattern formation in colonies of bacteria. Numerical and analytical studies of this model [150, 216] have shown the existence of TWS for wave speeds $c \geq c^*$, where the minimum wave speed c^* was estimated numerically. Until recently, most analytical progress has been restricted to models in which motility is driven by haptotaxis or chemotaxis [151, 177, 193, 194]. In particular, the existence of TWS for the Gatenby-Gawlinski model (1.4) has been largely supported by numerical results and partial analytical results [51, 74, 107, 158, 169, 238]. The reduced model (1.8) by Browning et al. [27] has also mainly been studied numerically, with a few partial analytical results available [63]. However, Gallay and Mascia [82] recently proved the existence of weak TWS of system (1.7) for any positive wave speed $c > 0$.

After presenting our new model of tumour invasion in Chapter 6, we will conduct a travelling wave analysis and rigorously prove the existence of a continuum of TWS for this model.

1.6 Mathematical models of tumour response to radiotherapy and hyperthermia

1.6.1 Modelling radiotherapy response

Various facets of tumour response to RT have been investigated through mathematical modelling, including tumour responses to specific RT treatment schedules [68, 116, 138, 202, 207], designing patient-specific RT dosing schedules [3, 16], accounting for RT-induced healthy tissue damage [99, 231] and optimising RT schedules accordingly [100, 110, 132, 133, 212]), and assessing the influence of heterogeneity on tumour sensitivity to RT [2, 35, 67, 96, 197, 198].

Despite having different aims, the aforementioned models typically assume that radiation induces instantaneous tumour cell death via the accumulation of a sufficiently large number of unrepaired DSBs, or interactions between multiple non-lethal SSBs [36]. In particular, cell kill is modelled using the Linear-Quadratic (LQ) model [160], which predicts that the fraction, S_{LQ}, of tumour cells that survive exposure to a dose D (Gy) of radiation is given by

$$S_{\mathrm{LQ}}(D) = \exp\left(-\left(\alpha D + \beta D^2\right)\right), \tag{1.10}$$

where $\alpha > 0$ and $\beta > 0$ denote the tissue-specific radiosensitivity to 'single-hit' radiation events and 'multi-hit' radiation events, respectively. Different tumour types are classified according to the dose, $D = \alpha/\beta$, at which the linear and quadratic damage components are equal. Early-responding, fast-proliferating (e.g., head and neck, liver and bladder) tumours have higher values of α/β, while late-responding, slow-growing (e.g., prostate, bone and breast) tumours have lower values of α/β [246]. While the values of α and β can be estimated from patients undergoing RT treatment [246], they are usually derived from 2D monolayer or 3D multicellular spheroid assays. As such, they are representative of the long-term amount of cell kill and contain limited information about how the RT cell kill rate evolves during treatment, e.g., in response to combined treatment with an adjuvant modality such as HT or CT.

Alternative models describe RT cell kill as a time-dependent process [50, 88, 145, 163, 176, 219, 239, 259]. For instance, Neira et al. [176] assume that a tumour cell population growing logistically can be sub-lethally or lethally damaged at a rate proportional to the constant radiation dose rate, which is defined as the radiation dose divided by the duration of RT application. Lethally-damaged cells are doomed to die, while sub-lethally damaged cells are either repaired or become lethally-damaged as they accumulate sufficient damage. By assuming further that only undamaged cells proliferate, Neira et al. [176] obtained reasonable fits of their model to *in vitro* data from nine cell lines and *in vivo* mouse data from four cell lines. By accounting for different types of damage (sub-lethal vs. lethal),

damage repair and cell death in the case of insufficient repair or misrepair, such models keep track of both the rate of cell death and the tumour composition (i.e., undamaged, damaged and dead cells) during treatment. The latter is important as dead material has been shown to have a notable effect on tumour growth post-treatment [139].

In Chapter 3, we will introduce a time-dependent RT response model inspired by Neira et al. [176], with some modifications and extensions.

1.6.2 Modelling hyperthermia response

As for RT, a range of modelling approaches have been used to describe tumour response to HT. To quantify heat-induced cell death, probabilistic survival functions similar, or equivalent, to the LQ model, have been proposed (see [29] and [263]). The Arrhenius model was the first such model; it defines the fraction, S_{A}, of tumour cells that survive heating at a temperature of $T\,^{\circ}\mathrm{C}$ for $\tau\,\mathrm{min}$ as

$$S_{\mathrm{A}}(\tau, T) = \exp\left(A \exp\left(\frac{-E_{\mathrm{a}}}{R(273.15 + T)}\right)\tau\right), \tag{1.11}$$

where A is a constant, E_{a} is the activation energy, R is the universal gas constant and the factor of $273.15\,\mathrm{K}\,^{\circ}\mathrm{C}^{-1}$ converts the temperature from Celsius to Kelvin [263].

More recently, Brüningk et al. [29] derived a survival model that can be applied to RT, HT and their combination by assuming that HT radiosensitises cells by inhibiting DNA repair mechanisms. This model states that the fraction, $S_{\alpha_{\mathrm{R}}}$, of tumour cells that survive heating at a temperature of $T\,^{\circ}\mathrm{C}$ for a duration of $\tau\,\mathrm{min}$ is given by

$$S_{\alpha_{\mathrm{R}}}(\tau, T) = \begin{cases} \exp\left(-[(\alpha_0(T) - \alpha_{\mathrm{R}}(T))\tau + \beta(T)\tau^2]\right), & \text{if } \tau \leqslant \tau^*(T) = \frac{\alpha_{\mathrm{R}}(T)}{2\beta(T)}, \\ \exp\left(-\left[\alpha_0(T)\tau - \dfrac{\alpha_{\mathrm{R}}^2(T)}{4\beta(T)}\right]\right), & \text{if } \tau > \tau^*(T), \end{cases} \tag{1.12}$$

where the parameters α_0, α_{R} and β are treatment-dependent. The logarithm of Equation (1.12) is linear-quadratic below some threshold temperature, and linear otherwise. Equation (1.12) can, therefore, be viewed as an extension of the LQ model for RT alone.

The limitations of using such models to predict HT-induced cell death within more complex models of tumours undergoing HT treatment, such as the multiscale model developed by Brüningk et al. [28], are the same as for the LQ model for RT response. In light of this, some time-dependent cell death models have been proposed [181].

Further, significant work has focussed on providing accurate predictions of intratumoural temperatures which can be achieved by different HT administration methods. More specifically, several spatially-resolved heat transfer models have been proposed to predict how variable tumour perfusion affects the time-dependent, intratumoural temperature distribution during HT. Pennes [188] developed the first bioheat transfer model based on the

classical Fourier law, which assumes a linear relationship between the heat flux, $\vec{q}$, and the temperature gradient,$\vec{\nabla}T$:

$$\vec{q}(\vec{x},t) = -k\vec{\nabla}T(\vec{x},t). \tag{1.13}$$

Here, $\vec{x}$ is the position of a point in the material considered, t is time and k is the thermal conductivity [111]. Pennes's model has been widely used to study temperature distributions during HT [10, 208, 241]. More complex models include thermal wave models [34, 251], dual-phase lag models [130, 244] and fractional models [72, 147]. These typically neglect HT cell kill or assume first-order kinetics (e.g., the Arrhenius survival model) in order to minimise model complexity. An exception is the transport-based PDE model by Bosque et al. [20], which simultaneously describes the growth of a tumour within healthy tissue, between two blood vessels, the temperature distribution in the healthy and tumour tissues and the two blood vessels during HT, and time-dependent HT cell kill. Their model of HT-induced cell kill is based on the survival model (1.12) by Brüningk et al. [29].

Several models have also been developed to study the heat shock response (HSR) observed following changes in temperature [62, 189, 195, 205, 218, 236]. These models typically consist of ODEs that describe the dynamics of the synthesis of HSP70 (or HSP90) and its interactions with key intracellular components. Given the role of HSP70 and HSP90 in mediating thermotolerance following HT, Rybiński et al. [211] used a HSR model to quantify the intensity and duration of HT-induced thermotolerance and investigated the efficacy of HT combined with CT. The influence of heat shock proteins on tumour invasion into healthy tissue has also been studied [237].

Finally, there have been attempts to model the increase in tumour perfusion via vasodilation during mild HT [19].

The above review reveals that (to the best of our knowledge) there is no comprehensive mathematical model that describes the range of HT effects described in Section 1.3.2. Most models of HT response also neglect tumour growth and, thus, do not describe tumour evolution during and post-treatment. We seek to fill this gap in the literature with the time-dependent model of HT response presented in Chapter 4.

1.6.3 Modelling combined treatment response

Very few mathematical models describe tumour response to combinations of RT and HT. Existing approaches typically use the LQ model and modify the radiosensitivity parameters, α and β, to account for the increase in cell death due to HT [28, 52]. While these temperature-dependent survival functions implicitly capture the thermal enhancement of RT response, they do not distinguish between the different ways in which HT may lead

to radio-sensitisation. In particular, they provide limited mechanistic insight into the interactions between HT and RT, and the different ways in which HT may enhance tumour response to RT.

Scheidegger et al. [219] investigated the effect of HT-induced inhibition of DNA repair on tumour response to RT by coupling an ODE model of the time-dependent inactivation and activation of repair proteins by HT with a dynamic model of RT cell kill. In their 'Multi-Hit Repair' model of RT response, tumour cells sequentially acquire up to $k > 1$ RT-induced hits (i.e., lesions) at a rate proportional to the assumed constant radiation dose rate. Tumour cells are assumed to die from RT damage if they possess at least one lesion and each lesion can be repaired at a time- and HT-dependent rate, $r(t)$. This results in a discrete, structured population model with $k+1$ compartments that tracks the evolution of the number of cells with $i \in [\![0, k]\!]$ lesions.

Assuming only HT can damage repair proteins, they define the repair rate, $r(t)$, as follows. The proportions of active and inactive repair proteins are denoted by Υ and Λ, respectively, and their dynamics are described via the following system of ODEs:

$$\begin{cases} \dfrac{\mathrm{d}\Upsilon}{\mathrm{d}t} = \underbrace{-k_1\Upsilon}_{\substack{\text{rate of protein} \\ \text{inactivation}}} + \underbrace{k_2\Lambda}_{\substack{\text{rate of protein} \\ \text{activation}}}, & \text{(1.14a)} \\ \dfrac{\mathrm{d}\Lambda}{\mathrm{d}t} = k_1\Upsilon - k_2\Lambda, & \text{(1.14b)} \end{cases}$$

where $k_1 = k_1(t)$ is non-zero when HT is administered and zero otherwise, whereas $k_2 > 0$ is assumed to be constant.

Before HT has been applied, $\Upsilon = 1$ and $\Lambda = 0$ (i.e., all repair proteins are intact). If a single high HT treatment is applied at $t = t_{\mathrm{H}}$ (min) for a duration δ_{H} (min), one can solve (1.14a)–(1.14b) subject to the initial conditions $(\Upsilon(0), \Lambda(0)) = (1, 0)$ to obtain

$$\Lambda(t) = \begin{cases} 0, & \text{if } 0 \le t < t_{\mathrm{H}}, \\ \dfrac{k_1}{k_1+k_2}\left(1 - e^{-(k_1+k_2)(t-t_{\mathrm{H}})}\right), & \text{if } t_{\mathrm{H}} \le t < t_{\mathrm{H}} + \delta_{\mathrm{H}}, \\ \dfrac{k_1}{k_1+k_2}\left(1 - e^{-(k_1+k_2)\delta_{\mathrm{H}}}\right) e^{-k_2(t-(t_{\mathrm{H}}+\delta_{\mathrm{H}}))}, & \text{if } t \ge t_{\mathrm{H}} + \delta_{\mathrm{H}}, \end{cases} \tag{1.15}$$

and $\Upsilon(t) = 1 - \Lambda(t)$.

The repair rate $r(t)$ is defined in terms of $\Lambda(t)$ as follows

$$r(t) = r_0 \exp\left(-\mu_\Lambda \Lambda(t)\right), \tag{1.16}$$

where the constant $r_0 > 0$ is the repair rate in the absence of HT (i.e., when $\Lambda(t) \equiv 0$) and the constant $\mu_\Lambda > 0$ indicates the extent to which HT inhibits damage repair.

In view of developing a comprehensive model of tumour response to combinations of HT and RT, we will follow [219] to account for HT-induced DNA repair inhibition. In particular, we will define the repair rate of RT-damaged cells according to Equation (1.16) (see Chapter 4).

1.7 Thesis structure

The remainder of this thesis comprises five chapters in which we investigate how two distinct mechanisms of growth arrest influence tumour responses to radiotherapy and hyperthermia, alone and in combination.

First, in **Chapter 2**, we propose a simple ODE model of solid tumour growth to investigate how specific mechanisms of growth arrest may affect tumour responses to different combination cancer therapies. We consider the interactions of tumour cells with the physical space in which they proliferate and a nutrient supplied by the tumour vasculature, our aim being to capture two distinct growth arrest mechanisms. More specifically, we seek to describe growth arrest due to (1) nutrient insufficiency, when cell proliferation and death rates balance, and (2) competition for space, when proliferation ceases, with no cell death. We combine numerical simulations with a steady-state analysis to determine the possible tumour growth scenarios exhibited by the model. We find that there are three distinct growth regimes: a nutrient limited (NL) regime, a space limited (SL) regime and a bistable (BS) regime, in which both growth arrest mechanisms are simultaneously active. Thus, the new model exhibits the behaviours required to investigate and distinguish tumour responses to different cancer treatments.

In **Chapter 3**, we extend the model developed in **Chapter 2** to investigate how nutrient and space limited mechanisms of growth control affect tumour cell responses to fractionated RT. We construct three virtual populations of NL, SL and BS tumours and, for each population, we simulate tumour responses to a conventional fractionation schedule consisting of 5×2 Gy fractions per week for 8 weeks. We determine the average response and investigate how the values of key parameters (i.e., the tumour oxygen consumption rates and the vascular volume) lead to extremal behaviour. We also consider how the dose fraction and frequency impact the tumour response (for a fixed total dose). We find that tumours in the SL regime typically respond best to RT, while those in the BS regime respond worst. For tumours in each regime, we identify the biological processes that may explain the positive and negative treatment outcomes and the dosing regimen which maximises the reduction in tumour burden.

In **Chapter 4**, we adapt the model from **Chapter 3** to study tumour responses to fractionated HT. We distinguish between the effects of mild HT, which re-oxygenates the tumour via vasodilation and a reduction in the rate of oxygen consumption by tumour cells,

and high HT, which causes cell and vascular damage and an associated angiogenic response. Using the NL, SL and BS virtual cohorts introduced in **Chapter 3**, we study the response of tumours in each regime to 'conventional' mild and high HT treatment schedules and assess how the tumour oxygen consumption rates and the vascular volume impact tumour responses to these schedules. We also investigate how the thermal dose (for a fixed treatment duration and number of weekly fractions) impacts tumour response to HT. We find that mild HT has a negligible effect across the virtual cohorts, while high HT can be very effective at reducing tumour burden across the virtual cohorts, provided the HT-induced angiogenic response is sufficiently weak. In particular, tumours in the NL and BS regimes respond best to HT, while those in the SL cohort have a more limited response. We also find that the best HT responders are typically the worst RT responders, and conversely.

Building on the work in **Chapters 3** and **4**, **Chapter 5** focusses on investigating tumour responses to combinations of RT and HT using the methodology employed in **Chapters 3** and **4**. We characterise the interactions between RT and HT across the three virtual cohorts and a range of combined treatment schedules. This enables us to determine the best treatment (RT, HT and RT+HT) and dosing regimen for each tumour. We find that mild HT cannot significantly enhance the tumour responses to RT. By contrast, high HT can act as a potent radiosensitiser for all NL and BS tumours and most SL tumours, provided the HT-induced angiogenic response is sufficiently weak. That said, all BS tumours and most NL tumours respond better to HT alone than combined treatment, suggesting that HT should be considered even before RT. Finally, combined treatment schedules that maximise the total HT dose tend to produce the largest reduction in tumour burden.

With a view to extending the work in **Chapters 2–5** to investigate the impact of growth arrest mechanisms on tumour invasion, in **Chapter 6** we present a simple model of tumour invasion into extracellular matrix. The model is characterised by degenerate cross-dependent diffusion and we focus on obtaining an analytical understanding of the model's behaviour. We perform a travelling wave analysis of the model and prove the existence of a continuum of travelling wave solutions by extending the shooting argument developed by Gallay and Mascia [82]. Using a combination of analytical and numerical results, we characterise the minimum wave speed and hypothesise that it depends monotonically on the rate at which tumour cells degrade the ECM and the ECM density far ahead of the tumour front.

The thesis concludes in **Chapter 7**, where we summarise our main results and discuss potential avenues for future work.

Chapter 2

A simple ODE model of tumour growth that distinguishes between different mechanisms of growth arrest

2.1 Introduction

In vitro experiments investigating the influence of nutrient inhibition and mechanical constraints on the growth of three-dimensional tumour spheroids have shown that two distinct mechanisms can contribute to growth arrest. More specifically, tumour spheroids may reach (1) a diffusion-limited (i.e., nutrient limited) equilibrium, when cell proliferation rates in nutrient-rich regions balance cell death rates in nutrient-poor regions [103, 131, 173], or (2) a contact-inhibited (i.e., space limited) equilibrium in which mechanical stress reduces cell proliferation rates to zero, and there is no cell death [55, 56, 103, 166, 167]. Further, Helmlinger et al. [103] showed that tumour spheroids originating from the same cell line may reach a nutrient or space limited equilibrium depending on whether nutrient inhibition or mechanical stress is dominant. This indicates that both mechanisms of growth control can be simultaneously active.

In spite of this, we saw in Section 1.4 that most existing models of tumour growth focus on a single growth-limiting process. In particular, many spatially-averaged phenomenological ordinary differential equation (ODE) models typically predict that a tumour reaches a steady state as the proportion of proliferating cells converges to zero (with no explicit cell death) [95, 172], while spatially-resolved models (PDE, IBM or hybrid) predict that a tumour reaches steady state when cell birth and death rates balance [61, 91, 140, 186].

With a longer term goal of investigating how mechanisms of growth limitation affect tumour responses to treatment, in this chapter, we develop a novel model of vascular tumour growth that distinguishes between two alternative growth-limiting mechanisms:

1. growth arrest in response to nutrient insufficiency, which translates into the balancing of cell proliferation and death,

2. growth arrest in response to competition for space, which corresponds to a cessation of proliferation, with no cell death.

The resulting model retains the simplicity of phenomenological models, while providing mechanistic insight and capturing the behaviour of more complex models. We focus on vascular tumours as, in practice, most tumours are vascular when they are detected [38]. Further, different treatments affect the vasculature in different ways, and these may be significant when considering combination treatments.

We begin this chapter by deriving the ODE model of vascular tumour growth (Section 2.2). We then investigate its behaviour by presenting numerical results in Section 2.3 and by performing a steady state analysis in Section 2.4. Combining our numerical and analytical results, we identify the different tumour growth scenarios that the model exhibits (Section 2.5).

The work presented in Sections 2.2, 2.3 and 2.4 has been published in the following paper:
Colson, C., Byrne, H. M. and Maini, P. K. 2022. Combining mechanisms of growth arrest in solid tumours: a mathematical investigation. Bulletin of Mathematical Biology, 84(8), 80.

The work presented in Section 2.5 has been published in the following paper:
Colson, C., Maini, P. K. and Byrne, H. M. 2023. Investigating the influence of growth arrest mechanisms on tumour responses to radiotherapy. Bulletin of Mathematical Biology, 85(8), 74.

2.2 Model development

2.2.1 The mathematical model

In this section, we present a new model of vascular tumour growth, which considers the interactions of a tumour with the physical space in which it is growing and a nutrient supplied by its vasculature. Our first simplifying assumption is that the vascular volume remains constant during tumour growth. In particular, we neglect angiogenesis and vascular remodelling and view the vascular volume, V, as a model parameter (rather than a dynamic variable) which influences the availability of nutrient and space and, thus, the tumour's carrying capacity. We make this simplifying assumption in order to limit the complexity of the ODE model so that we may focus on our aim of describing two growth-limiting mechanisms using a model that exhibits rich solution structure.

Now, denoting the tumour cell volume by T and the nutrient concentration by c, we propose the following system of time-dependent ODEs:

$$\frac{\mathrm{d}T}{\mathrm{d}t} = \underbrace{q_2^* cT(S_{\max} - (T+V))}_{\text{tumour cell proliferation}} - \underbrace{[\delta_1^*(c_{\min}^* - c)]\, H(c_{\min}^* - c)T}_{\text{cell death due to nutrient starvation}}, \tag{2.1}$$

$$\frac{\mathrm{d}c}{\mathrm{d}t} = \underbrace{g^*(c_{\max}^* - c)V}_{\text{nutrient delivery}} - \underbrace{q_1^* cT}_{\substack{\text{baseline nutrient} \\ \text{consumption}}} - \underbrace{q_3^* cT(S_{\max} - (T+V))}_{\substack{\text{additional nutrient} \\ \text{consumption for proliferation}}}, \tag{2.2}$$

where

$$V \equiv V_0^* \coloneqq V(0) \quad \text{and} \quad H(x) = \begin{cases} 1, & \text{if } x \geq 0, \\ 0, & \text{if } x < 0, \end{cases} \tag{2.3}$$

is the Heaviside step function. We also impose the following initial conditions

$$T(0) = T_0 \in [0, S_{\max} - V_0^*], \quad c(0) = c_0 \in [0, c_{\max}^*]. \tag{2.4}$$

Our model is based on the following assumptions:

- There is a fixed amount of physical space, $S_{\max}$, which can be occupied by T and V; the available free space is $S = S_{\max} - (T+V)$.

- Tumour cells, T, need space and nutrient in order to proliferate. We assume that they proliferate at a rate proportional to the nutrient concentration, c, and the amount of free space available, S, with constant of proportionality $q_2^* > 0$.

- Below a fixed nutrient concentration, $c_{\min}^* > 0$, tumour cells die of nutrient starvation at a rate that is a monotonically decreasing function of c for $0 \leq c < c_{\min}^*$ such that (1) no tumour cells die at $c = c_{\min}^*$ and (2) when $c = 0$ the death rate of tumour cells attains its maximal value of $\delta_1^* c_{\min}^*$, where $\delta_1^* > 0$ is a constant of proportionality. We refer to $c_{\min}^*$ as the threshold for severe nutrient deficiency.

- A nutrient, c, chosen to be oxygen, is supplied by the tumour vasculature, V, at a rate that is a monotonically decreasing function of c for $0 \leq c \leq c_{\max}^*$ such that (1) no oxygen is supplied if the oxygen concentration in the tumour attains the value $c_{\max}^* > c_{\min}^* > 0$ and (2) the maximal supply rate of oxygen is attained when $c = 0$ and is equal to $g^* c_{\max}^*$, with $g^* > 0$. Here, $c_{\max}^*$ represents the oxygen concentration in the vasculature and g^* represents the rate of oxygen exchange per unit volume area of blood vessels.

- Tumour cells consume nutrient for maintenance at a rate proportional to c, with rate constant $q_1^* > 0$. They consume additional nutrient for proliferation at a rate proportional to the proliferation rate, with a conversion factor $k^* > 0$ defined such

that $q_3^* = \frac{q_2^*}{k^*} > 0$. We distinguish between these two types of oxygen uptake as we expect tumour cells to require oxygen for survival in the absence of proliferation and, in particular, when a space limited equilibrium is reached. We support this choice by noting that mitochondrial, cell surface and basal oxygen consumption rates have been quantified separately in a range of murine and human tumour cell lines [104], and the oxygen consumption rates of cells grown *in vitro* in two-dimensional monolayers have also been measured during different growth phases (i.e., exponential and plateau) [22, 120]. This experimental evidence suggests that it is possible to separately estimate different types of oxygen consumption rates.

- Given the above assumptions, physically realistic solutions for T and c, respectively, satisfy $0 \leq T(t) + V_0^* \leq S_{\max}$ and $0 \leq c(t) \leq c_{\max}^*$ for all $t \geq 0$; this justifies the initial conditions (2.4).

2.2.2 Non-dimensionalisation

In order to reduce the number of parameters in our model, we non-dimensionalise the system (2.1)–(2.3) by introducing the following scalings:

$$\widehat{T} = \frac{T}{S_{\max}}, \quad \widehat{S} = \frac{S}{S_{\max}}, \quad \widehat{V} = \frac{V}{S_{\max}}, \quad \widehat{c} = \frac{c}{c_{\max}^*}, \quad \widehat{t} = \frac{t}{\tau}.$$

Recalling that $V \equiv V_0^*$ and dropping hats for notational convenience, we obtain the following system:

$$\frac{\mathrm{d}T}{\mathrm{d}t} = q_2 cT(1 - (T + V_0)) - \delta_1(c_{\min} - c)H(c_{\min} - c)T, \tag{2.5}$$

$$\frac{\mathrm{d}c}{\mathrm{d}t} = g(1 - c)V_0 - q_1 cT - q_3 cT(1 - (T + V_0)), \tag{2.6}$$

subject to the following initial conditions

$$T(0) = T_0 \in [0, 1 - V_0], \quad c(0) = c_0 \in [0, 1], \tag{2.7}$$

where

$$\begin{aligned} V_0 &= \frac{V_0^*}{S_{\max}}, \quad q_1 = q_1^* S_{\max}\tau, \quad q_3 = q_3^* S_{\max}^2 \tau, \quad q_2 = q_2^* S_{\max} c_{\max}^* \tau, \\ c_{\min} &= \frac{c_{\min}^*}{c_{\max}^*}, \quad \delta_1 = \delta_1^* c_{\max}^* \tau, \quad g = g^* S_{\max}\tau. \end{aligned} \tag{2.8}$$

Given that $k^* = q_2^*/q_3^*$, we define $k > 0$ such that $q_3 = \frac{q_2}{k}$:

$$k = \frac{c_{\max}^*}{S_{\max}} k^*. \tag{2.9}$$

2.3 Numerical simulations: tumour growth curves

2.3.1 Numerical setup

We solve the ODE system (2.5)–(2.6) for $t \in (0, t^*]$, where $t^* > 0$, using ODE45, a single step MATLAB built-in solver for non-stiff ODEs that is based on an explicit Runge-Kutta (4,5) formula, the Dormand-Prince pair [59]. We impose the initial conditions $(T(0), c(0)) = (0.05, 1)$. We choose $T(0) = 0.05$ so that the tumour is initially much smaller than the available free space (i.e., $0 < T \ll 1$), but large enough to be vascular with $V_0 \in (0, 0.005]$. The choice of $c(0) = 1$ ensures that the tumours are, initially, well-oxygenated.

We seek to characterise the qualitative behaviour of the model and assess its suitability for benchmarking combination cancer treatments. As such, accurately estimating parameter values by fitting the model to experimental data is beyond the scope of this work. We instead combine parameter values from different sources and preliminary numerical simulations to fix the values of $c_{\min}$, g and k (see Appendix A.1). Further, we consider biologically realistic ranges of possible values for the remaining parameters, which are motivated by the arguments in Appendix A.1. Our dimensionless parameter choices are listed in Table 2.1.

Parameter	Definition	Value(s)
$c_{\min}$	Anoxic oxygen threshold	10^{-2}
g	Rate of oxygen exchange per unit vascular volume	5
k	Conversation factor	10^{-2}
q_1	O_2 consumption rate for maintenance	$[10^{-2}, 10]$
q_3	O_2 consumption rate for proliferation	$[10^{-2}, 10]$
q_2	Proliferation rate	q_3/k
δ_1	Rate of death by nutrient starvation	q_2
V_0	Initial vascular volume	$(0, 5 \times 10^{-3}]$

Table 2.1: List of dimensionless parameters and values assigned to them for the purpose of the model analysis and numerical simulations.

Remark 2.3.1. In what follows, we assume that the dimensionless rates of cell proliferation and cell death due to nutrient starvation are equal (i.e., $\delta_1 = q_2$). This simplifying assumption reduces the number of system parameters and is consistent with experimental evidence which suggests that cell proliferation and death rates are highly correlated for some tumours [135, 146, 247]. Our numerical and analytical studies reveal that the results in this chapter are not affected by this assumption (see Appendix A.1).

2.3.2 Simulating tumour growth

For fixed values of the oxygen consumption rates for maintenance and proliferation, q_1 and q_3, we observe how the tumour growth dynamics change as we vary the initial vascular volume, V_0. The results presented in Figure 3.1 show that the model exhibits initial exponential or linear growth followed by a reduced growth rate as the tumour reaches a limiting size. These dynamics are characteristic of both experimental data and existing phenomenological models [61, 129, 172].

We note also that the tumour specific parameters q_1, q_3 and V_0 appear to determine the tumour's limiting size, which can vary markedly between parameter sets (see Figures 2.1c and 2.1e). In particular, comparison of Figures 2.1d and 2.1f with Figures 2.1c and 2.1e, suggests that the large differences in the equilibrium tumour sizes depend on whether oxygen levels are above, or below, the oxygen threshold for severe hypoxia. This hints at the existence of different growth regimes, which could be characterised by different growth limiting mechanisms. We investigate this further in the following section where we perform a steady state analysis.

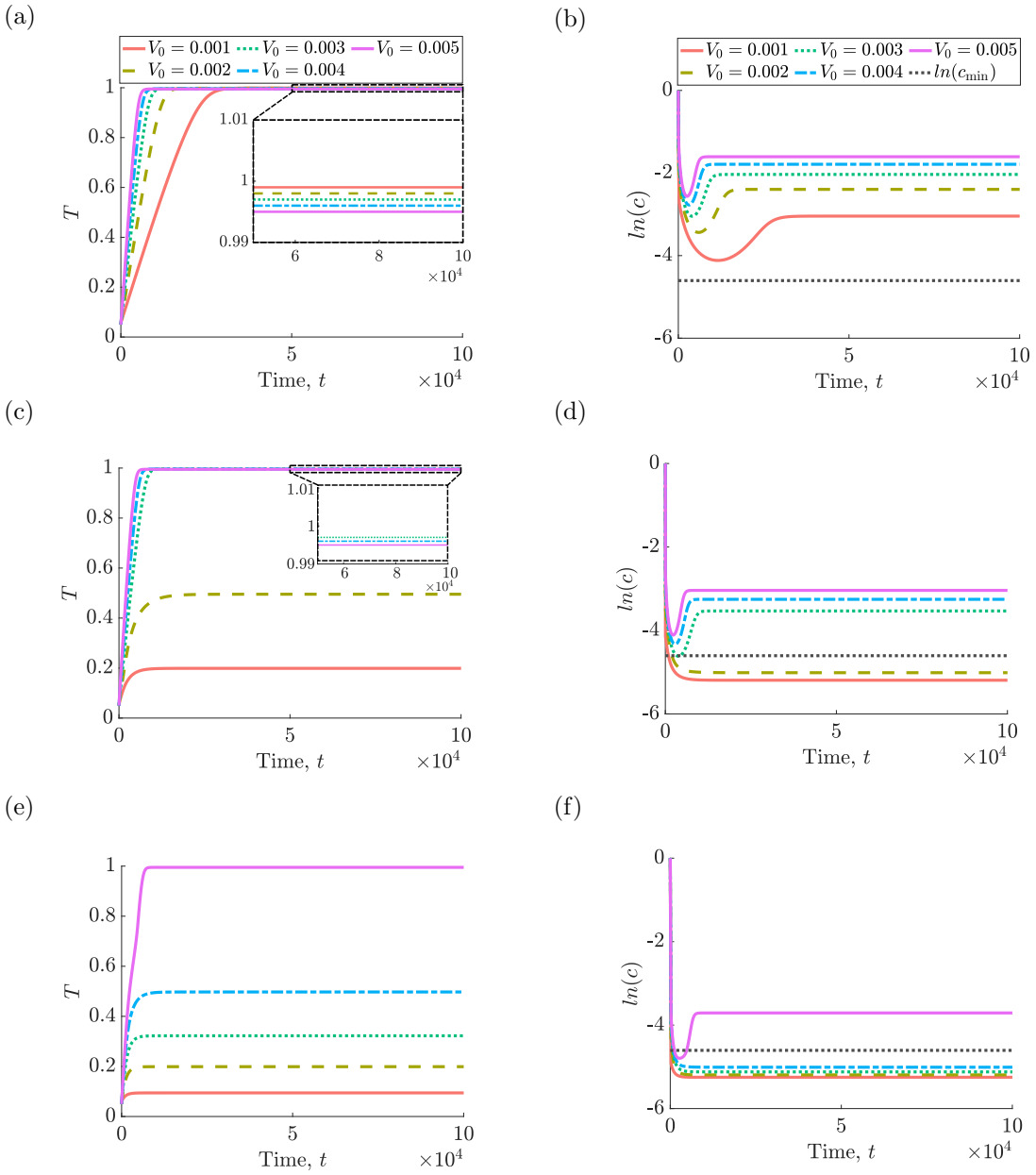


Figure 2.1: We solve Equations (2.5)–(2.6) for $t \in (0, 10^5]$ subject to initial conditions $(T(0), c(0)) = (0.05, 1)$. We fix (a)–(b) $(q_1, q_3) = (0.1, 1)$, (c)–(d) $(q_1, q_3) = (0.5, 5)$ and (e)–(f) $(q_1, q_3) = (1, 10)$ and vary $V_0 \in \{0.001, 0.002, 0.003, 0.004, 0.005\}$. In (a), (c) and (e), we plot the time evolution of the tumour volume, $T(t)$; in (b), (d) and (f), we depict the evolution of the logarithm of the oxygen concentration, $c(t)$. In (a) and (c), we also include a magnified view of the growth curves as they approach their respective steady states. All tumours grow to a limiting size, which decreases with q_1 and q_3. The equilibrium size also increases with V_0, when the steady state oxygen concentration is below $c_{\min}$, and decreases with V_0 otherwise. In contrast, the steady state oxygen concentration always increases with V_0.

2.4 Steady state analysis

We now perform a steady state analysis of Equations (2.5)–(2.6) in order to understand how varying q_1, q_3 and V_0, the oxygen consumption rates for proliferation and maintenance and the initial vascular volume, respectively, impacts the equilibrium tumour volume. The model dynamics depend on whether the tumour is in a nutrient-rich (i.e., $c_{\min} \leq c \leq 1$) or a nutrient-poor regime (i.e., $0 \leq c < c_{\min}$). We, therefore, investigate the existence and stability of steady state solutions in each of these regimes separately, referring to steady states for which $c_{\min} \leq c \leq 1$ as space limited (SL) and those for which $0 \leq c < c_{\min}$ as nutrient limited (NL).

2.4.1 Steady state solutions: existence and multiplicity

2.4.1.1 Space limited steady states

When nutrient is plentiful (i.e., $c_{\min} \leq c \leq 1$), the steady state solutions satisfy

$$\begin{cases} q_2 cT(1-(T+V_0)) = 0, & \text{(2.10a)} \\ g(1-c)V_0 - q_1 cT - q_3 cT(1-(T+V_0)) = 0. & \text{(2.10b)} \end{cases}$$

Since $0 < V_0 < 1$, it is straightforward to show that there are two steady states:

$$\text{SS}_1: \quad (T_1^*, c_1^*) = (0, 1), \tag{2.11}$$

$$\text{SS}_2: \quad (T_2^*, c_2^*) = \left(1 - V_0, \frac{V_0}{V_0 + (q_1/g)(1-V_0)}\right). \tag{2.12}$$

SS_1 represents a tumour-free state, while SS_2 represents tumours which occupy all of the available free space; their growth is limited by space availability and, at steady state, there is no cell proliferation or death.

Clearly, SS_1 is an admissible steady state for all combinations of parameters, and the condition on V_0 implies that $T_2^* = 1 - V_0 > 0$ for SS_2. For c_2^* to lie in the appropriate nutrient regime, we require $c_2^* \geq c_{\min}$ ($c_2^* < 1$ follows trivially). This condition is satisfied for all $q_3 > 0$ when the following relationship holds:

$$q_1 \leq g\left(\frac{1}{c_{\min}} - 1\right)\frac{V_0}{1-V_0} =: \bar{q_1}. \tag{2.13}$$

For g and $c_{\min}$ fixed, inequality (2.13) implies that steady state SS_2 exists if q_1 is bounded above by an increasing function of V_0. In other words, SS_2 exists if the tumour's maintenance needs at equilibrium can be supported by its vasculature.

2.4.1.2 Nutrient limited steady states

When nutrient is limited (i.e., $0 \leq c < c_{\min}$), the steady state solutions satisfy

$$\begin{cases} T\left(q_2 c(1-(T+V_0)) - \delta_1(c_{\min}-c)\right) = 0, & \text{(2.14a)} \\ g(1-c)V_0 - q_1 cT - q_3 cT(1-(T+V_0)) = 0. & \text{(2.14b)} \end{cases}$$

If $T \equiv 0$, then we have $c \equiv 1$ as $V_0 > 0$. However, this is not a valid steady state in the NL regime, since $1 = c > c_{\min}$. Therefore, we suppose $T > 0$ and seek solutions of (2.14a)–(2.14b) by determining the intersection points of the T- and c-nullclines. Using (2.14a), we find that the non-zero T-nullcline is given by:

$$T(c) = (1-V_0) - \frac{\delta_1}{q_2}\left(\frac{c_{\min}}{c} - 1\right), \tag{2.15}$$

which, given that we assume $\delta_1 = q_2$, reduces to

$$T(c) = (1-V_0) - \left(\frac{c_{\min}}{c} - 1\right). \tag{2.16}$$

To determine the c-nullcline, we solve the quadratic equation (2.14b) for T and find it has two solution branches:

$$T_{\pm}(c) = \frac{q_1 + q_3(1-V_0) \pm \sqrt{(q_1+q_3(1-V_0))^2 - 4q_3 g V_0(1-c)/c}}{2q_3}. \tag{2.17}$$

We can now determine the steady state values for c by equating (2.16) and each branch in (2.17) and solving for $c_{\pm}$ corresponding to $T_{\pm}$. We find:

$$\begin{cases} c_{\pm} = \dfrac{c_{\min}(X \mp \sqrt{X^2 + 4q_3 Y})}{2Y}, & \text{if } V_0 \neq \dfrac{2(q_3-q_1)}{g+q_3-q_1}, \quad \text{(2.18a)} \\ c_{-} = \dfrac{c_{\min}(q_3(g+q_3-q_1))}{2\frac{g}{c_{\min}}(q_1-q_3) - g(q_1-3q_3) + (q_1-q_3)^2}, & \text{if } V_0 = \dfrac{2(q_3-q_1)}{g+q_3-q_1}, \quad \text{(2.18b)} \end{cases}$$

where

$$\begin{cases} X = q_1 - 3q_3 + \left(\frac{g}{c_{\min}} + q_3\right) V_0, \\ Y = 2(q_1-q_3) + (g+q_3-q_1)V_0. \end{cases} \tag{2.19}$$

We note here that we obtain a unique steady state value for c (i.e., (2.18b)) when the curve $T(c)$ defined by (2.16) intersects only one of the branches $T_{\pm}(c)$ defined by (2.17). In particular, $T(c)$ intersects $T_{-}(c)$.

We conclude that there are at most two NL steady states:

$$\mathrm{SS}_3: \quad (T_3^*, c_3^*) = (T(c_-), c_-), \tag{2.20}$$

$$\mathrm{SS}_4: \quad (T_4^*, c_4^*) = (T(c_+), c_+), \quad \text{if } V_0 \neq \frac{2(q_3-q_1)}{g+q_3-q_1}, \tag{2.21}$$

where $T(c)$ is defined by (2.16) and $c_{\pm}$ are defined by (2.18a)–(2.18b). SS_3 and SS_4, which always satisfy $\mathrm{SS}_3 < \mathrm{SS}_4$, represent tumours that are not SL (i.e., $0 < T(c) < 1 - V_0$); their

growth is limited by nutrient availability and, at steady state, the rates of cell proliferation and death are non-zero and balance.

As for SL steady states, in order to exist and be physically realistic, SS_3 and SS_4 must satisfy $0 \leq T \leq 1 - V_0$ and $0 \leq c < c_{\min}$. Given the expression for $T(c)$ provided in (2.16) and assuming that $0 \leq c < c_{\min}$, we have $T(c) < 1 - V_0$ for any parameter combination. Due to the complexity of the expressions for the steady states SS_3 and SS_4, extensive algebraic manipulation is required to determine the regions in parameter space in which the remaining conditions hold. Using Mathematica, we find that, for fixed V_0, SS_3 is an admissible steady state under the following conditions:

- for all $q_3 > 0$ when $q_1 > \bar{q_1}$, where $\bar{q_1}$ was defined in (2.13);
- for all $q_3 > \bar{q_3}$ when $q_1 \leq \bar{q_1}$, where $\bar{q_1}$ was defined in (2.13) and $\bar{q_3}$ is given by

$$\begin{aligned}\bar{q_3} := & \frac{-q_1 + \left(\frac{3g}{c_{\min}} - 2 + q_1\right) V_0 - \frac{g}{c_{\min}} V_0^2}{(1 - V_0)^2} + \frac{2g^{1/2}}{(1 - V_0)^2} \times \\ & \left[-\left(\frac{2}{c_{\min}} - 1\right) q_1 V_0 + \left(g\left(\frac{2}{c_{\min}^2} - \frac{3}{c_{\min}} + 1\right) + q_1\left(\frac{3}{c_{\min}} - 1\right)\right) V_0^2 \right. \\ & \left. - \left(g\left(\frac{1}{c_{\min}^2} - \frac{1}{c_{\min}}\right) + \frac{q_1}{c_{\min}}\right) V_0^3 \right]^{1/2}.\end{aligned} \tag{2.22}$$

It is possible to show that, for fixed g and $c_{\min}$, $\bar{q_3}$ is an increasing function of V_0 (for q_1 fixed) and a decreasing function of q_1 (for V_0 fixed). As such, SS_3 exists when there is no non-trivial SL steady state (here, the vascular volume V_0 cannot sustain an SL tumour's oxygen requirements for maintenance). SS_3 also exists when there is a non-trivial SL steady state (here, V_0 can sustain an SL tumour's oxygen requirements for maintenance, but the oxygen requirements for proliferation (q_3) are too high, given the oxygen requirements for maintenance (q_1) and nutrient supply (V_0)). By contrast, SS_4 is an admissible steady state only in the second case (i.e., for all $q_3 > \bar{q_3}$ when $q_1 \leq \bar{q_1}$, given V_0 fixed).

2.4.2 Stability analysis

In the previous section, we identified the model's steady state solutions and their regions of existence in (V_0, q_1, q_3)-space for fixed g and $c_{\min}$. We now investigate their stability.

2.4.2.1 Space limited steady states

We first perform a linear stability analysis for steady states SS_1 and SS_2; we compute the Jacobian of the system (2.5)–(2.6) when $c_{\min} \leq c \leq 1$ at each steady state and find the corresponding eigenvalues. The Jacobians of the system evaluated at SS_1 and SS_2 are,

respectively,

$$J|_{\mathrm{SS}_1} = \begin{pmatrix} q_2(1-V_0) & 0 \\ -q_1 - q_3(1-V_0) & -gV_0 \end{pmatrix}, \tag{2.23}$$

$$J|_{\mathrm{SS}_2} = \begin{pmatrix} \frac{-q_2V_0(1-V_0)}{V_0+(q_1/g)(1-V_0)} & 0 \\ [q_3(1-V_0)-q_1]\frac{V_0}{V_0+(q_1/g)(1-V_0)} & -gV_0 - q_1(1-V_0) \end{pmatrix}. \tag{2.24}$$

It is straightforward to show that the eigenvalues (λ_1, λ_2) and (μ_1, μ_2) for the Jacobians evaluated at SS_1 and SS_2 can be written as follows:

$$\begin{cases} \lambda_1 = q_2(1-V_0) > 0, \\ \lambda_2 = -gV_0 < 0, \end{cases} \qquad \begin{cases} \mu_1 = \dfrac{-q_2(1-V_0)V_0}{V_0+(q_1/g)(1-V_0)} < 0, \\ \mu_2 = -gV_0 - q_1(1-V_0) < 0. \end{cases} \tag{2.25}$$

Since $q_1, q_2 > 0$ and $0 < V_0 < 1$, it is clear that SS_1 is unstable and SS_2 is locally stable. Thus, in the SL regime, tumour elimination is not possible and the tumour persists.

2.4.2.2 Nutrient limited steady states

We can perform a similar stability analysis for SS_3 and SS_4. When $0 \leq c < c_{\min}$, the Jacobian of the system (6.9)–(6.10) is

$$J|_{(T^*,c^*)} = \begin{pmatrix} q_2c^*(1-2T^*-V_0) - \delta_1(c_{\min}-c^*) & q_2T^*(1-T^*-V_0) + \delta_1T^* \\ -q_1 - q_3(1-2T^*-V_0) & -gV_0 - q_1T^* - q_3T^*(1-T^*-V_0) \end{pmatrix}. \tag{2.26}$$

Since equations (2.14a)–(2.14b) hold at both SS_3 and SS_4, it is straightforward to show that $J_{11} < 0$, $J_{22} < 0$ and $J_{12} > 0$ for $J|_{\mathrm{SS}_3}$ and $J|_{\mathrm{SS}_4}$ (for all possible parameter sets). Determining the sign of J_{21} for SS_3 and SS_4 is difficult due to the algebraic complexity of the expressions for T and c at these steady states. Therefore, we establish the sign of J_{21} for specific cases by performing phase plane analyses. Figure 2.2 contains two phase portraits for parameter sets that, respectively, correspond to a region of parameter space where SS_3 is the only NL steady state and another where the two NL steady states exist (see Figure 2.3). These phase portraits show that, for these parameter sets, $J_{21} < 0$ for SS_3 whereas $J_{21} > 0$ for SS_4. Phase portraits for other parameter sets (results not shown) suggest that the sign of J_{21} remains unchanged for both steady states, irrespective of the values of the parameters.

Given the signs of each component of the Jacobian evaluated, respectively, at SS_3 and SS_4, we now discuss the stability of these two steady states. Since $J_{11} < 0$ and $J_{22} < 0$ for SS_3 and SS_4, the trace of the Jacobian is negative for both steady states. For SS_3, the determinant of the Jacobian is positive, which implies that SS_3 is locally stable. In contrast, for SS_4, the determinant could be positive or negative depending on the parameter values (since $J_{11}J_{22} > 0$ and $J_{12}J_{21} > 0$). Therefore, we cannot confirm whether SS_4 is stable

or not, but the phase portrait in Figure 2.2b shows that SS_4 is unstable for that specific parameter set. Constructing phase portraits for other parameter sets (results not shown) suggests that SS_4 is unstable, irrespective of parameter values. We conclude that SS_3 is locally stable, and conjecture that SS_4 is unstable.

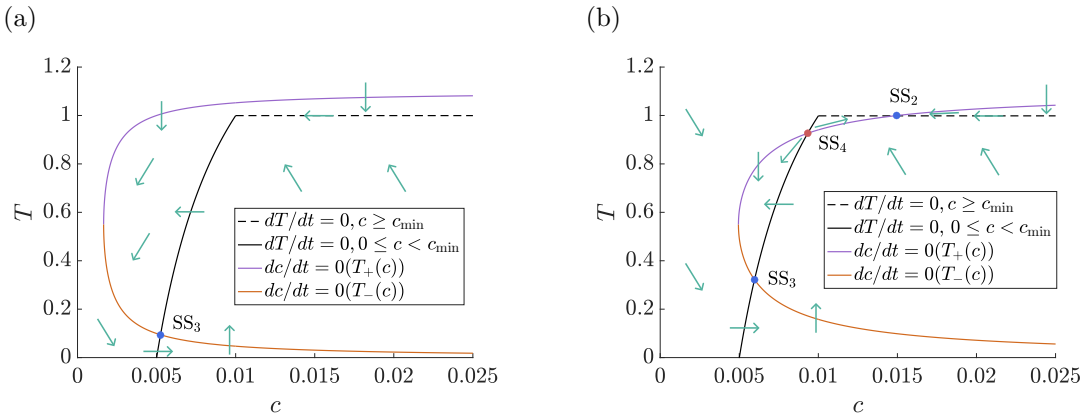


Figure 2.2: Phase portrait for equations (2.5)–(2.6), where (a) $(V_0, q_1, q_3) = (0.0005, 0.5, 5)$ and (b) $(V_0, q_3, q_1) = (0.0015, 0.5, 5)$. From (a) and (b), we can find the sign of the component J_{21} of the Jacobian (2.26) evaluated at SS_3 and SS_4: J_{21} is, respectively, negative and positive. Since, for SS_3, we also have J_{11}, $J_{22} < 0$ and $J_{12} > 0$, this implies that SS_3 is stable. In contrast, we cannot definitively determine the stability of SS_4 using the signs of the components of the Jacobian. However, we can see from the trajectories in (b) that SS_4 is unstable.

2.5 The existence of three tumour growth regimes

The results in Section 2.4 indicate that Equations (2.5)–(2.6) admit two non-trivial, stable steady states: (1) a nutrient limited steady state (SS_3), attained when cell proliferation balances cell death due to nutrient insufficiency; (2) a space limited steady state (SS_2), attained when cell proliferation ceases due to lack of space, with no cell death.

Further, we find that the admissible stable NL and SL steady state solutions lie in different regions of parameter space. For fixed $c_{\min}$ and g, these regions can be defined by the values of q_1, q_3 and V_0. Figure 2.3 depicts these regions in (q_3, V_0)-space for three values of q_1 and fixed values of $c_{\min} = 0.01$ and $g = 5$.

Given q_1, there exists a threshold value of V_0, which we denote by V_N, which is independent of q_3, such that only the NL steady state exists for $0 < V_0 \leq V_N$. Tumours in this region of parameter space (e.g., A_1 and A_2) are said to be in an NL growth regime. Further, for a fixed value of q_1, if q_3 is sufficiently large relative to q_1, then there exists another threshold value of V_0, which we denote by V_S, such that only the SL steady state exists for $V_0 \geq V_S > V_N$. Tumours in this region of parameter space (e.g., C_1, B_2 and C_2) are said to be in an SL growth regime. In this case, for $V_N < V_0 < V_S$, the NL and SL

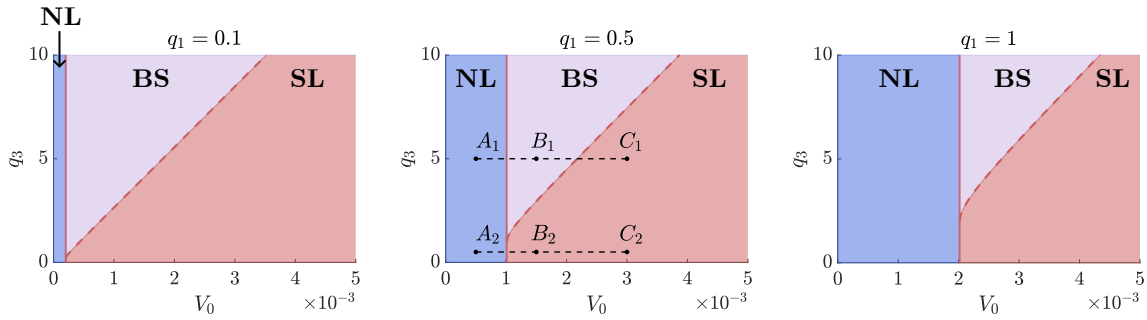


Figure 2.3: For $q_1 \in \{0.1, 0.5, 1\}$, we show the regions of (V_0, q_3)-space in which only the stable NL steady state exists (blue), only the stable SL steady state exists (red) and both the stable NL and SL steady states co-exist (BS, purple). The solid and dashed red lines represent the boundaries between the three regions. For $q_1 = 0.5$, the points A_1–C_1 correspond to $(V_0, q_3) \in \{(0.0005, 5), (0.0015, 5), (0.003, 5)\}$, respectively, and A_2–C_2 to $(V_0, q_3) \in \{(0.0005, 0.5), (0.0015, 0.5), (0.003, 0.5)\}$, respectively. Tumours defined by parameter sets A_1–C_1 have values of q_3 which are sufficiently larger than q_1 that there is bi-stability, while, for A_2–C_2, bistability does not occur.

steady states co-exist. In this region of parameter space, a tumour (e.g., B_1) may evolve to either steady state depending on its initial conditions. We consider such tumours to be in a bistable (BS) growth regime. Finally, for $q_3 \lesssim q_1$, if $V_0 > V_{\mathrm{N}}$, then a unique steady state exists and it is of SL type.

Figure 2.4 shows the time evolution of the tumour cell volume, T, and the intratumoural oxygen concentration, c, and the corresponding bifurcation diagrams for tumours A_1–C_1 and A_2–C_2. In all cases, the NL steady state values for T and c (T^* and c^*) are smaller than the SL ones. This is consistent with the assumption that, in the absence of angiogenesis, well-oxygenated tumours attain larger volumes than poorly-oxygenated tumours. Further, tumours in a BS regime evolve to their NL steady state for initial conditions satisfying $0 < T(0) \ll T^*$, which we use to simulate tumour growth. As the values of T^* and c^* for NL tumours increase with V_0, tumours in a BS regime will grow to larger volumes than tumours in an NL regime (and smaller volumes than tumours in an SL regime). We also note that, in BS regimes, there is a large jump in T^* and c^* at V_{S}, the threshold value of V_0 separating the BS and SL regimes. In contrast, in monostable regimes, T^* and c^* depend continuously on V_0.

Combining the preceding results, we conclude that, depending on (V_0, q_1, q_3), there are three possible scenarios for tumour growth:

1. Space limited growth: the tumour has access to sufficient nutrient to grow to an SL steady state at which cell proliferation ceases due to space constraints, with no cell death. This corresponds to density-dependent growth inhibition.

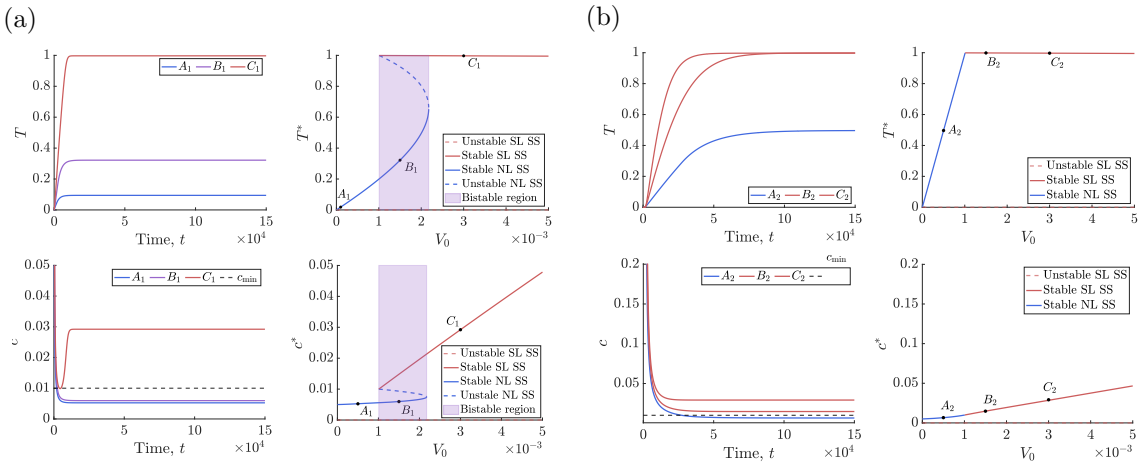


Figure 2.4: We solve Equations (2.5)–(2.6) for $t \in (0, 10^5]$ subject to initial conditions $(T(0), c(0)) = (0.05, 1)$. In (a), (q_1, q_3, V_0) correspond to points A_1–C_1 in Figure 2.3 and, in (b), they correspond to points A_2–C_2. The remaining model parameters are fixed at the default values in Table 2.1. We plot the evolution of the tumour volume and oxygen concentration in time and the corresponding bifurcation diagrams, which show how the steady state values for T and c (T^* and c^*) change as V_0 varies. In both cases, the NL steady state increases with V_0 and is smaller than the SL steady state, which decreases with V_0. The tumour in a BS regime (B_1) grows to its NL steady state.

2. Nutrient limited growth: the tumour grows to an NL steady state at which cell proliferation balances cell death due to nutrient insufficiency. This corresponds to nutrient-dependent growth inhibition.

3. Bistable growth: the system is bistable and the tumour grows to an NL steady state given physically realistic initial conditions ($0 < T(0) \ll T^*$).

2.6 Discussion

In this chapter, we developed a novel nonlinear ODE model of solid tumour growth which distinguishes between growth arrest due to nutrient inhibition, when the rates of cell proliferation and cell death balance, and growth arrest due to contact inhibition, when the rate of cell proliferation becomes zero, with no cell death.

Numerical simulations of the model showed that the desired qualitative growth trends are preserved: initial exponential and/or linear growth is followed by convergence to a parameter-dependent limiting size. Further, a steady state analysis revealed that, depending on the oxygen consumption rates, q_1 and q_3, and the vascular volume, V_0, there are three distinct tumour growth regimes: nutrient limited, space limited and bistable, where both mechanisms of growth arrest coexist.

Despite the simplicity of the model, it exhibits a rich solution structure and we expect that it can provide additional insight compared to models of tumour growth which typically

only represent a single growth-limiting mechanism [61, 91, 95, 140, 172, 186]. This is because distinct growth arrest mechanisms may influence tumour responses to treatment in different ways.

In the three chapters that follow, we conduct a detailed investigation into how nutrient and space limited mechanisms of growth arrest may influence tumour responses to radiotherapy (RT) and hyperthermia (HT), alone and in combination. More specifically, we extend the tumour growth model developed in this chapter to incorporate tumour responses to RT and HT and use the resulting dynamic model to conduct an in-depth study of treatment outcomes for tumours in the NL, SL and BS growth regimes. In doing so, we aim to determine the biological processes that may explain positive and negative treatment outcomes and assess which treatments (RT, HT or RT+HT) and dosing regimens maximise anti-cancer effects.

Chapter 3

Investigating the influence of growth arrest mechanisms on tumour responses to radiotherapy

3.1 Introduction

Developing effective therapeutic protocols to improve the prognosis of cancer patients requires an understanding of the biological mechanisms that influence tumour responses to treatment. For instance, while radiotherapy (RT) is a well-established cancer treatment, its efficacy is limited, not only by its intolerable side effects, but also by inter-tumour heterogeneity at the genetic and phenotypic levels, which can significantly influence tumour sensitivity to RT [90, 261]. In this chapter, we investigate how two mechanisms of growth control, namely growth arrest in response to nutrient insufficiency and to competition for space, may affect tumour responses to fractionated RT.

Radiation induces both direct and indirect DNA damage to tumour cells, which can lead to immediate or delayed cell death if the damage is not repaired. In particular, a number of cell death pathways, operating on different timescales, may be responsible for RT cell kill [71, 180], which implies that viable cells that are fated to die due to RT can remain in the tumour volume, alongside surviving viable cells and dead cells, for a certain duration post-radiation. The presence of dead and dying material may affect RT response dynamics by modulating both the efficacy of each individual RT fraction and the growth dynamics between fractions and post-treatment [139].

As discussed in Section 1.6.1, mathematical models of tumour response to RT typically use the Linear-Quadratic (LQ) model to quantify dose-dependent, radiation-induced, cell death. Since the LQ model's parameters are usually determined from experimental cell survival data, this model provides limited insight into the dynamics of the RT-induced cell death rate. Adopting instead a time-dependent description of RT response that captures sub-lethal and lethal damage, damage repair and cell death following insufficient repair

[50, 88, 176, 239] allows us to track RT cell death over time together with the evolution of the tumour composition during treatment. This can help elucidate the interplay between the effects of RT and tumour growth dynamics. A time-dependent description is also more appropriate when combining RT with other treatments, such as hyperthermia (HT), that may affect the RT cell kill rates and tumour growth dynamics.

The ordinary differential equation (ODE) model of tumour growth presented in Chapter 2 distinguishes between nutrient and space limited mechanisms of growth arrest and exhibits three distinct growth regimes: nutrient limited (NL), space limited (SL) and bistable (BS), where both mechanisms of growth arrest coexist. In this chapter, we extend this growth model to include the time-dependent effects of RT, as a prelude to studying combinations of RT and HT, and in order to investigate how the different mechanisms of growth control affect tumour sensitivity to RT. To systematically study tumour responses in each growth regime, we construct three virtual populations of NL, SL and BS tumours. For each population, we initially consider tumour responses to a conventional fractionation schedule consisting of 5×2 Gy fractions per week for 8 weeks. We determine average responses for each cohort and explore how values of key parameters (i.e., the tumour oxygen consumption rates and the vascular volume) generate extremal (i.e., strongly positive and negative) behaviour. We then study the impact of the fraction dose and dosing frequency on tumour response. In doing so, we seek to identify the biological processes that may explain positive and negative treatment outcomes and the dosing regimens which achieve the largest reductions in tumour burden during treatment.

This chapter is structured as follows. In Section 3.2, we extend the tumour growth model developed in Chapter 2 to account for the biological effects of RT. Section 3.3 outlines the numerical study we performed in order to investigate the response of tumours in the NL, SL and BS growth regimes to different fractionated RT protocols. We then characterise tumour responses during treatment using the output from numerical simulations in Section 3.4. We finally look at post-treatment growth dynamics using a steady state analysis and complementary numerical results in Section 3.5.

The work presented in this chapter has been published in the following paper:
Colson, C., Maini, P. K. and Byrne, H. M. 2023. Investigating the influence of growth arrest mechanisms on tumour responses to radiotherapy. Bulletin of Mathematical Biology, 85(8), 74.

3.2 Model development

3.2.1 The mathematical model

In this section, we incorporate tumour response to RT into the growth model developed in Chapter 2. We follow the structure of the radiation response model developed by Neira et al. [176] and, as such, adopt a time-dependent description of radiotherapy. In more detail, we introduce the dependent variables T_{S} and T_{R} to denote the volumes of tumour cells that have been, respectively, sub-lethally and lethally damaged by RT. We suppose that the tumour is exposed to a total dose $D\,(\mathrm{Gy})$ of RT at a constant rate $R\,(\mathrm{Gy/min})$ over the time period $t_{\mathrm{R}} \leq t \leq t_{\mathrm{R}} + \delta_{\mathrm{R}}\,(\mathrm{min})$ so that

$$R(t) = \begin{cases} D/\delta_{\mathrm{R}}, & \text{if } t_{\mathrm{R}} \leq t \leq t_{\mathrm{R}} + \delta_{\mathrm{R}}, \\ 0, & \text{otherwise.} \end{cases} \tag{3.1}$$

Let $\Sigma = T + T_{\mathrm{S}} + T_{\mathrm{R}} + V_0^*$ be the total tumour volume. We propose the following system of time-dependent ODEs to describe tumour growth and response to RT (see also the schematic in Figure 3.1):

$$\frac{\mathrm{d}T}{\mathrm{d}t} = q_2^* cT(S_{\max} - \Sigma) - \delta_1^*(c_{\min}^* - c)H(c_{\min}^* - c)T - \underbrace{\lambda^* cRT}_{\substack{\text{direct} \\ \text{lethal damage}}} - \underbrace{\nu^* cRT}_{\substack{\text{sub-lethal} \\ \text{damage}}} + \underbrace{\mu^* T_{\mathrm{S}}}_{\text{repair}}, \tag{3.2}$$

$$\frac{\mathrm{d}T_{\mathrm{S}}}{\mathrm{d}t} = q_{2,\mathrm{S}}^* cT_{\mathrm{S}}(S_{\max} - \Sigma) - \delta_{1,\mathrm{S}}^*(c_{\min}^* - c)H(c_{\min}^* - c)T_{\mathrm{S}} + \nu^* cRT - \mu^* T_{\mathrm{S}} - \underbrace{\xi^* T_{\mathrm{S}}}_{\substack{\text{post-RT death} \\ \text{due to MC}}} - \underbrace{\lambda_{\mathrm{S}}^* cRT_{\mathrm{S}}}_{\substack{\text{indirect} \\ \text{lethal damage}}}, \tag{3.3}$$

$$\frac{\mathrm{d}T_{\mathrm{R}}}{\mathrm{d}t} = \lambda^* cRT + (\xi^* + \lambda_{\mathrm{S}}^* cR)T_{\mathrm{S}} - \underbrace{\eta_{\mathrm{R}}^* T_{\mathrm{R}}}_{\text{clearance}}, \tag{3.4}$$

$$\frac{\mathrm{d}c}{\mathrm{d}t} = g^*(c_{\max} - c)V_0^* - q_1^* cT - q_3^* cT(S_{\max} - \Sigma) - q_{1,\mathrm{S}}^* cT_{\mathrm{S}} - q_{3,S}^* cT_{\mathrm{S}}(S_{\max} - \Sigma), \tag{3.5}$$

where

$$H(x) = \begin{cases} 1, & \text{if } x \geq 0, \\ 0, & \text{if } x < 0, \end{cases} \tag{3.6}$$

is the Heaviside step function and we impose the following initial conditions

$$T(0) = T_0 \in [0, S_{\max} - V_0^*], \quad T_{\mathrm{S}}(0) = 0, \quad T_{\mathrm{R}}(0) = 0, \quad c(0) = c_0 \in [0, c_{\max}^*]. \tag{3.7}$$

We assume that undamaged tumour cells, T, proliferate, die due to nutrient insufficiency and consume oxygen for proliferation and maintenance as in Equations (2.1)–(2.2). They

suffer sub-lethal and lethal damage during irradiation at rates proportional to the oxygen concentration, c, and the RT dose rate, R, with proportionality constants $\nu^* > 0$ and $\lambda^* > 0$, respectively. We further suppose that sub-lethal damage is either repaired at a constant rate $\mu^* > 0$, or leads to tumour cell death via two distinct pathways. Firstly, sub-lethal damage may become lethal as it accumulates at a rate proportional to the oxygen concentration, c, and the RT dose rate, R, with proportionality constant $\lambda_{\mathrm{S}}^* > 0$. Secondly, sub-lethally damaged cells, T_{S}, may undergo mitotic catastrophe (MC) if they attempt to divide with mis- or un-repaired DNA damage; we assume this occurs at a constant rate $\xi^* > 0$.

Sub-lethally damaged cells, T_{S}, also consume oxygen for maintenance and proliferation, proliferate and die due to nutrient insufficiency similarly to undamaged cells, T, although at different rates. More specifically, they proliferate at a rate proportional to the oxygen concentration, c, and the available space, with proportionality constant $q_{2,\mathrm{S}}^* = \theta_2 q_2^* > 0$, where $\theta_2 \in (0, 1)$. The latter ensures that damaged cells proliferate more slowly than undamaged cells as they expend more energy repairing RT damage than proliferating. Accordingly, sub-lethally damaged cells consume oxygen for maintenance at a rate proportional to c, with rate constant $q_{1,\mathrm{S}}^* = \theta_1 q_1^* > 0$, where $\theta_1 > 1$. They also consume oxygen for proliferation at a rate proportional to the proliferation rate, with conversion factor $k > 0$ such that $q_{3,\mathrm{S}}^* = \frac{q_{2,\mathrm{S}}^*}{k}$. For simplicity, we assume the same conversion factor for T and T_{S} cells. Since $q_{2,\mathrm{S}}^* = \theta_2 q_2^*$ and $q_3^* = \frac{q_2^*}{k}$, we also have $q_{3,\mathrm{S}}^* = \theta_2 q_3^*$, i.e., damaged cells consume less oxygen for proliferation than undamaged cells. Lastly, as for T cells, T_{S} cells die from nutrient insufficiency when $c < c_{\min}^*$, at a rate proportional to the difference between c and $c_{\min}^*$, with proportionality constant $\delta_{1,\mathrm{S}}^* > 0$.

Lethally-damaged cells, T_{R}, are considered to be dead: their damage cannot be repaired, they do not consume oxygen or proliferate, but they occupy space and are degraded at a constant rate $\eta_{\mathrm{R}}^* > 0$.

One final, important model assumption is that radiation only affects tumour cells, i.e., we neglect any effects RT may have on tumour angiogenesis, vascular remodelling and injury. This simplifying assumption enables us to focus on elucidating how mechanisms of growth arrest influence one particular type of tumour response to RT, i.e., the cellular response.

The initial condition for c in (3.7) is defined as that in the absence of treatment in (2.4), and the initial conditions for T_{S} and T_{R} in (3.7) follow from the absence of damaged material prior to the first RT fraction. Physically realistic solutions for T satisfy $0 \leq T(t) + T_{\mathrm{S}}(t) + T_{\mathrm{R}}(t) + V_0^* \leq S_{\max}$ for all $t \geq 0$; the initial condition for T in (3.7) follows.

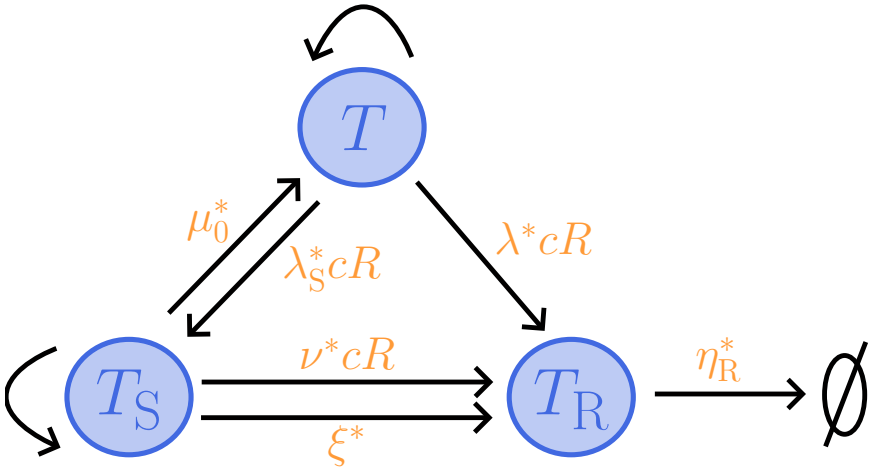


Figure 3.1: Schematic showing the interactions between undamaged (T), damaged (T_S) and dead (T_R) tumours cells in response to RT, and the proliferation of T and T_S cells as described in the model defined by Equations (3.1)–(3.5). R denotes the RT dose rate defined by (3.1) and c denotes the intratumoural oxygen concentration.

3.2.2 Non-dimensionalisation

We non-dimensionalise Equations (3.1)–(3.5) by introducing the following scalings:

$$\widehat{T} = \frac{T}{S_{\max}}, \quad \widehat{T}_S = \frac{T_S}{S_{\max}}, \quad \widehat{T}_R = \frac{T_R}{S_{\max}}, \quad \widehat{V_0} = \frac{V_0^*}{S_{\max}},$$
$$\widehat{c} = \frac{c}{c_{\max}^*}, \quad \widehat{R} = \frac{R}{R_{\max}}, \quad \widehat{t} = \frac{t}{\tau}.$$

In Chapter 5, we will seek to describe the interactions between the time-dependent effects of RT (i.e., tumour cell damage and repair) and HT (i.e., tumour re-oxygenation, tumour cell and vascular death, and inhibition of DNA repair mechanisms). These effects operate on timescales of minutes to days and, therefore, to capture each of these effects, we set the timescale of interest to be $\tau = 1\,\text{min}$. The maximum dose rate is also fixed to be $R_{\max} = 1\,\text{Gy/min}$ [128]. Then, given that $q_{1,S}^* = \theta_1 q_1^*$, $q_{2,S}^* = \theta_2 q_2^*$ and $q_{3,S}^* = \theta_2 q_3^*$ and dropping hats for notational convenience, we obtain the following dimensionless system:

$$\frac{\mathrm{d}T}{\mathrm{d}t} = q_2 cT(1 - \Sigma) - (\delta_1(c_{\min} - c)H(c_{\min} - c) + \lambda cR + \nu cR)T + \mu T_S, \quad (3.8)$$

$$\frac{\mathrm{d}T_S}{\mathrm{d}t} = \theta_2 q_2 cT_S(1 - \Sigma) - (\delta_{1,S}(c_{\min} - c)H(c_{\min} - c) + \lambda_S cR + \mu + \xi)T_S + \nu cRT, \quad (3.9)$$

$$\frac{\mathrm{d}T_R}{\mathrm{d}t} = \lambda cRT + (\xi + \lambda_S cR)T_S - \eta_R T_R, \quad (3.10)$$

$$\frac{\mathrm{d}c}{\mathrm{d}t} = g(1 - c)V_0 - q_1(T + \theta_1 T_S)c - q_3\left(T + \theta_2 T_S\right)c(1 - \Sigma), \quad (3.11)$$

subject to the following initial conditions:

$$T(0) = T_0 \in [0, 1 - V_0], \quad T_S(0) = 0, \quad T_R(0) = 0, \quad c(0) = c_0 \in [0, 1], \quad (3.12)$$

and where we have introduced the following dimensionless parameter groupings:

$$
\begin{aligned}
&q_1 = q_1^* S_{\max}\tau,\ q_3 = q_3^* S_{\max}^2\tau,\ q_2 = q_2^* S_{\max}^2 c_{\max}^*\tau,\ k = \frac{c_{\max}^*}{S_{\max}}k^*,\\
&c_{\min} = \frac{c_{\min}^*}{c_{\max}^*},\ \delta_1 = \delta_1^* c_{\max}^*\tau,\ \delta_{1,\mathrm{S}} = \delta_{1,\mathrm{S}}^* c_{\max}^*\tau,\ g = g^* S_{\max}\tau,\\
&\lambda = \lambda^* c_{\max}^* R_{\max}\tau,\ \lambda_{\mathrm{S}} = \lambda_{\mathrm{S}}^* c_{\max}^* R_{\max}\tau,\ \nu = \nu^* c_{\max}^* R_{\max}\tau,\\
&\mu = \mu^*\tau,\ \xi = \xi^*\tau,\ \eta_{\mathrm{R}} = \eta_{\mathrm{R}}^*\tau.
\end{aligned}
\tag{3.13}
$$

3.2.3 Defining the dimensionless model parameters

We seek to study the impact of two distinct growth arrest mechanisms on the qualitative tumour response to RT. We, therefore, fix parameters related to tumour cell responses to RT at the values stated in Table 3.1. The values of ν, λ, λ_{S}, μ and η_{R} are based on values found in the literature [176, 229] (see Appendix A.2) and we assume $\lambda = \lambda_{\mathrm{S}}$, for simplicity. Assuming that the average duration of the cell cycle in healthy cells [17] and in cancer cells is approximately the same, we set $\xi = 5 \times 10^{-4}$ so that cells that undergo mitotic catastrophe have a half-life of approximately 24h. The parameters that define the RT dosing schedules (e.g., the dose rate, R) are summarised in the Methods section.

We fix the tumour growth parameters as in Chapter 2 (see Table 2.1). In particular, we fix the values of $c_{\min}$, g and k and consider a biologically realistic range of values for q_1, q_3 and V_0 as these parameters have a strong influence on the qualitative behaviour of the model in the absence of treatment (see Chapter 2). We make the simplifying assumption that, as for undamaged cells, $\delta_{1,\mathrm{S}} = q_{2,\mathrm{S}}$. Finally, we set $\theta_1 = 10$ and $\theta_2 = 0.1$ to represent a 10-fold increase in oxygen consumption for maintenance and a 10-fold decrease in oxygen consumption for proliferation in damaged cells.

Parameters	Definition	Value
ν	RT sub-lethal damage rate	10
$\lambda, \lambda_{\mathrm{S}}$	RT lethal damage rate	1
μ	Repair rate constant	5×10^{-3}
ξ	Rate of death by mitotic catastrophe	5×10^{-4}
η_{R}	Clearance rate of cells killed by RT	5×10^{-5}
θ_1	Proportionality constant relating q_1 and $q_{1,\mathrm{S}}$	10
θ_2	Proportionality constant relating q_2 and $q_{2,\mathrm{S}}$ (q_3 and $q_{3,\mathrm{S}}$)	0.1

Table 3.1: List of dimensionless RT response parameters and values assigned to them for the purpose of the model analysis and numerical simulations.

3.3 Numerical study: methods and set up

Our aim is to understand the qualitative response of tumours in nutrient limited, space limited and bistable regimes to a range of fractionated radiotherapy treatments. As a first step, we create three virtual tumour populations. We fix all tumour growth model parameters, except the oxygen consumption rates for maintenance and proliferation and the vascular volume, q_1, q_3 and V_0, respectively, at the default values stated in Table 3.1. We fix $V_0 = 0.0005$, $V_0 = 0.005$ and $V_0 = 0.00275$ for tumours in the virtual NL, SL and BS cohorts, respectively. Allowing q_1 and q_3 to vary, we generate three virtual tumour populations of size $N = 250$ by randomly selecting N (q_1, q_3) pairs, corresponding to the NL, SL and BS regimes, respectively. Each pair is formed by sampling pairs of values of q_1 and q_3 from the uniform distributions defined in Table 3.2, which are relevant to a particular growth regime (NL, SL or BS).

Cohort	NL	SL	BS
Distribution used to sample q_1	$U(\bar{q_1}, 10)$	$U(0.01, \bar{q_1})$	$U(0.01, \bar{q_1})$
Distribution used to sample q_3	$U(0.01, 10)$	$U(0.01, \bar{q_3})$	$U(\bar{q_3}, 10)$

Table 3.2: Uniform distributions $U(a, b)$ used to sample the pairs of q_1 and q_3 values that correspond to the NL, SL and BS cohorts, respectively. Here, $\bar{q_1}$ and $\bar{q_3}$ are defined by Equations (2.13) and (2.22), respectively. Recall that, for V_0 fixed, $\bar{q_1}$ is the threshold value above which only NL steady states exist, while, for V_0 and $q_1 \leq \bar{q_1}$ fixed, $\bar{q_3}$ is the threshold value above which both NL and SL steady states co-exist and below which only SL steady states exist.

Figure 3.2 shows the steady state values in the absence of treatment of the tumour volume and the logarithm of the oxygen concentration, T^* and $\ln(c^*)$, for the sets of (q_1, q_3) pairs that, respectively, define the NL, SL and BS virtual cohorts. Tumours in the NL cohort have the smallest values of T^* and c^*, while tumours in the SL cohort have the largest values. Further, in the NL and BS cohorts, T^* decreases as q_1 and q_3 increase, whereas $T^* = 1 - V_0 = 0.995$ for all tumours in the SL cohort. By contrast, the variability in c^* is low in the NL and BS cohorts, while c^* decreases significantly as q_1 increases in the SL cohort.

We now define the RT protocols of interest. We vary the dose $D \in [\![0, 5]\!]$ (Gy) and the number of doses per week $N_{\text{frac}} = \{1, 3, 5\}$. We assume that each dose is administered in $\delta_{\text{R}} = 10\,\text{min}$ and vary the dimensionless dose rate, $R := \frac{D}{\delta_{\text{R}} R_{\max}} \in \{0.1, 0.2, 0.3, 0.4, 0.5\}$. We suppose that all fractions are applied at the same time of day and the first weekly fraction is applied on Mondays, with subsequent fractions applied at equally spaced time intervals during Monday to Friday (e.g., 3 doses per week corresponds to doses on Monday,

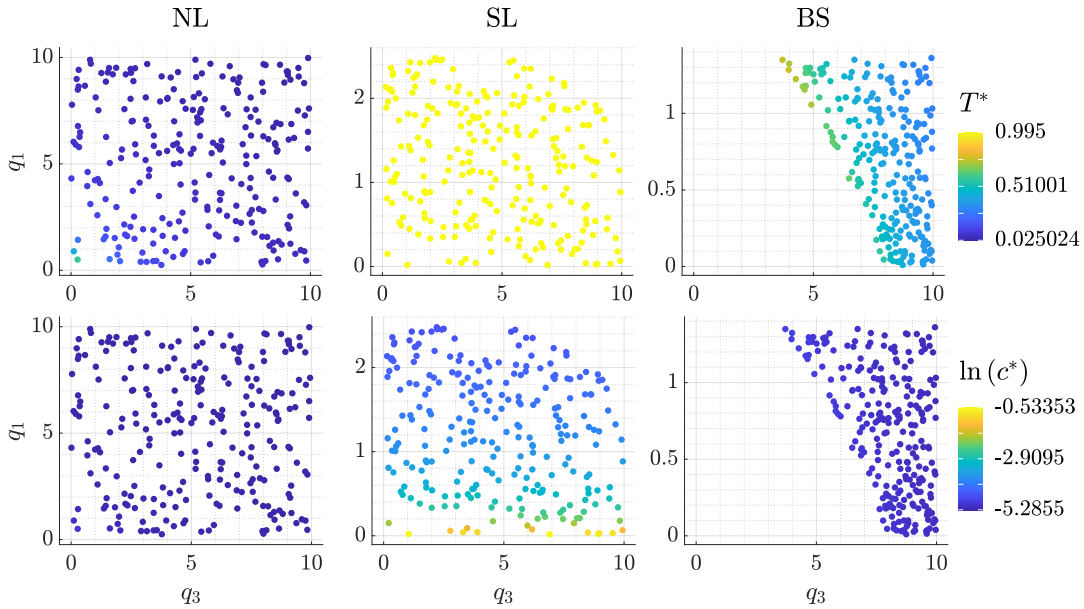


Figure 3.2: The scatter plots show the steady state values in the absence of treatment of the tumour volume and the logarithm of the oxygen concentration, T^* and $\ln(c^*)$, for each (q_1, q_3) pair used to, respectively, generate the set of virtual NL, SL and BS tumours. Note that tumours in the BS cohort attain their NL steady state.

Wednesday and Friday). The duration of each fractionation schedule is determined so that the total dose administered is 80 Gy (or the closest multiple of D to 80 Gy).

For each set of tumours and each RT protocol, we solve Equations (3.8)–(3.11) numerically for $t \in (0, t^*]$, $t^* > 0$, using ODE45, a single step MATLAB built-in solver for non-stiff ODEs that is based on an explicit Runge-Kutta (4,5) formula, the Dormand-Prince pair [59]. If t_{end} is the time at which the RT schedule ends, then we set $t^* := t_{\text{end}} + 10^6$ to ensure that the tumour has reached steady state by the end of the simulation. For simplicity, we impose the initial conditions

$$(T(0), T_{\text{S}}(0), T_{\text{R}}(0), c(0)) = (T^*, 0, 0, c^*), \tag{3.14}$$

where T^* and c^* are defined, for each cohort, in Figure 3.2. All RT parameters are fixed at the default values listed in Table 3.1.

For each simulation, we record $\bar{T}$, $\bar{T}_{\text{S}}$ and $\bar{T}_{\text{R}}$, the mean undamaged, damaged and dead cell volumes in the last week of treatment, respectively. We define the percent change in (mean) viable and total cell volumes between the start and the end of treatment as follows:

$$\Delta^{\text{R}}_{\text{viable}} := 100 \times \frac{(\bar{T} + \bar{T}_{\text{S}}) - T_0}{T_0} \quad \text{and} \quad \Delta^{\text{R}}_{\text{total}} := 100 \times \frac{\bar{\Sigma} - \Sigma_0}{\Sigma_0}, \tag{3.15}$$

where

$$\Sigma_0 = T_0 + V_0, \quad \Sigma = T + T_{\text{S}} + T_{\text{R}} + V_0.$$

We also quantify the end-of-treatment tumour composition (relative to the total tumour volume at the start of treatment) as follows:

$$\%T := 100 \times \frac{\bar{T}}{\Sigma_0}, \quad \%T_{\mathrm{S}} := 100 \times \frac{\bar{T_{\mathrm{S}}}}{\Sigma_0}, \quad \%T_{\mathrm{R}} := 100 \times \frac{\bar{T_{\mathrm{R}}}}{\Sigma_0} \quad \text{and} \quad \%V_0 := 100 \times \frac{V_0}{\Sigma_0}. \tag{3.16}$$

We note that the variables defined in (3.16) can be used to describe $\Delta^{\mathrm{R}}_{\mathrm{total}} = (\%T + \%T_{\mathrm{S}} + \%T_{\mathrm{R}} + \%V_0) - 100$. Henceforth, for brevity, we refer to the relative changes in tumour cell volumes, as defined in (3.15) and (3.16), as changes in tumour cell volumes. Finally, we record $\bar{c}$, the mean oxygen concentration in the last week of treatment, and the post-treatment steady state values of all dependent variables.

3.4 Characterising tumour response to fractionated RT

In this section, we investigate the response of tumours in the NL, SL and BS virtual populations to fractionated RT. For each regime, we initially study tumour response to a conventional fractionation schedule consisting of 5×2 Gy fractions per week for 8 weeks. We determine the average response and explore how certain values of the oxygen consumption rates for maintenance and proliferation and the vascular volume, q_1, q_3 and V_0, respectively, generate extremal behaviour. We also study the impact of the dose and dosing frequency on tumour response. We consider monostable regimes before looking at the bistable regime.

3.4.1 Tumours in monostable regimes: the NL and SL virtual tumour populations

3.4.1.1 Typical responses to a conventional fractionation schedule

Figure 3.3 shows the RT response of two NL and SL tumours, which both experience a decrease in viable tumour cell volume, $T + T_{\mathrm{S}}$, during treatment. Since, in both cases, the dependent variables evolve to time periodic solutions within 5 weeks of treatment, we deduce that there is a maximum reduction in the viable cell volume that can be achieved with this fractionation schedule. This value, which we denote by $\Delta^{\mathrm{R}}_{\mathrm{viable}}$, is significantly larger for the SL tumour (at approximately 37.6%) than for the NL tumour (at approximately 4.36%). RT is more effective for the SL tumour as it is better oxygenated than the NL tumour and, hence, experiences a higher rate of RT cell kill and greater accumulation of dead material, T_{R}, than the NL tumour.

Figure 3.3 also shows that, for both tumours, the oxygen concentration and the viable tumour cell volume decrease when RT is applied. This is because T and T_{S} cells consume oxygen at different rates: we recall that the oxygen consumption rates of sub-lethally damaged cells satisfy $q_{1,\mathrm{S}} = 10q_1$ and $q_{3,\mathrm{S}} = 0.1q_3$. Therefore, changes in tumour composition during treatment will alter the overall oxygen consumption rate of viable tumour cells,

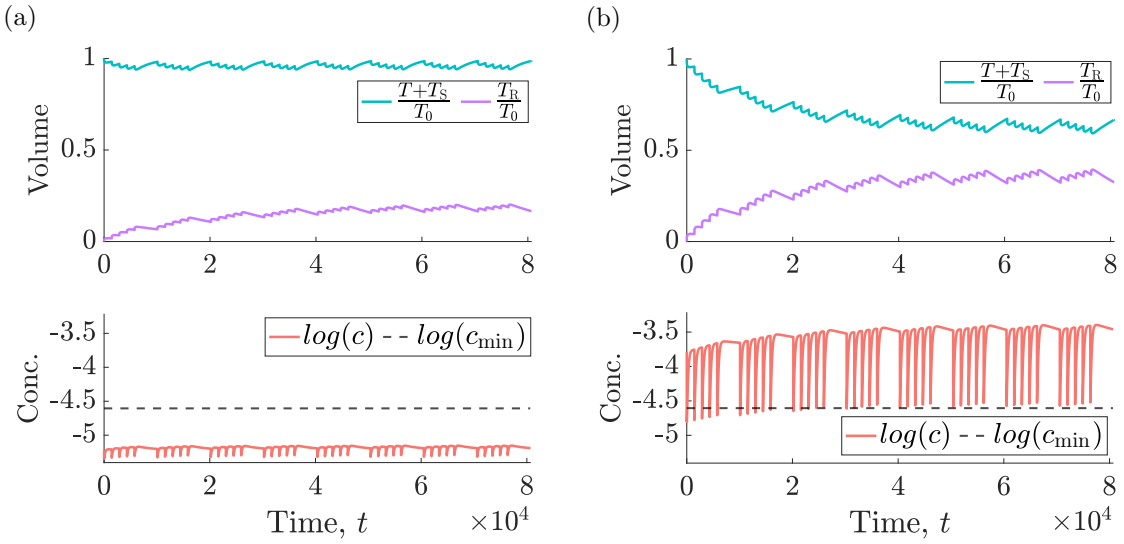


Figure 3.3: For a conventional fractionation schedule, we solve Equations (3.8)–(3.11) for $t \in (0, 8 \times 10^4]$ subject to initial conditions (3.14). In (a), we set $(q_1, q_3, V_0) = (0.832, 2.98, 0.0005)$, which corresponds to an NL tumour. In (b), we set $(q_1, q_3, V_0) = (1.08, 8.83, 0.005)$, which corresponds to an SL tumour. Although both tumours exhibit a decrease in viable cell volume, RT cell kill and accumulation of dead material is more significant for the SL than the NL tumour for this choice of parameter values.

leading to transient, or persistent, changes in the oxygen concentration, depending on the values of q_1 and q_3.

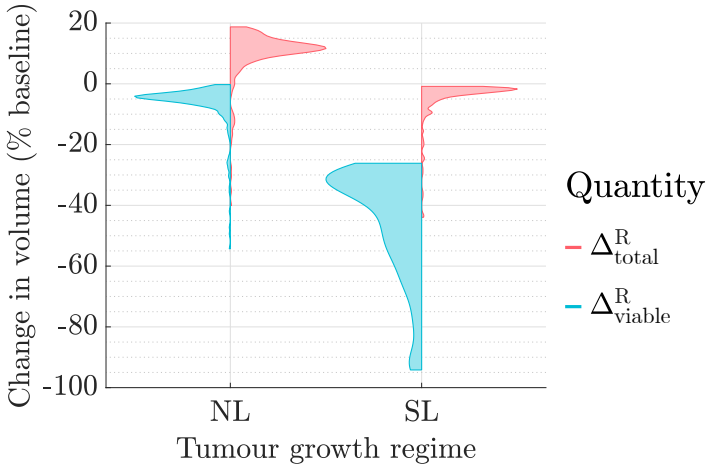


Figure 3.4: For virtual cohorts of NL and SL tumours, the violin plots show the distributions of Δ^R_{viable} and Δ^R_{total}. The viable cell volume of all NL and SL tumours decreases during RT, with SL tumours showing greater percentage changes. The total volume decreases for all SL tumours, while it increases for most NL tumours.We identify several outliers, which exhibit significantly larger reductions in their viable and total cell volumes.

Figure 3.4 shows the distributions of Δ^R_{viable} and Δ^R_{total}, following a conventional fractionation schedule, across the NL and SL virtual populations. We note that the behaviour

shown in Figure 3.3 for specific NL and SL tumours is representative of the average behaviour of each virtual population. In particular, tumours in the SL cohort typically respond well to treatment, with median and $(Q1, Q3)$ values of $\Delta^{\mathrm{R}}_{\mathrm{viable}}$ equal to -37.9 and $(-30.7, -54.1)$, respectively, and $\Delta^{\mathrm{R}}_{\mathrm{total}} < 0$ across the virtual population. Given the initial conditions (3.14), this follows from SL tumours fully occupying the available space at the start of treatment. Tumours in the NL cohort typically respond less well to treatment, with median and $(Q1, Q3)$ values of $\Delta^{\mathrm{R}}_{\mathrm{viable}}$ equal to -4.57 and $(-3.52, -6.53)$, respectively, and $\Delta^{\mathrm{R}}_{\mathrm{total}} > 0$, for at least 90% of tumours. When the net RT-induced cell death is minimal, NL tumours, which do not occupy all available free space at the start of treatment, can grow larger due to increases in the dead cell volume. We also note that the value of $\Delta^{\mathrm{R}}_{\mathrm{total}} - \Delta^{\mathrm{R}}_{\mathrm{viable}}$ is larger for SL tumours since they accumulate more dead material.

In both regimes, we observe outliers, which undergo much larger reductions in $T + T_{\mathrm{S}}$ and Σ than the average tumour. This suggests that certain parameter values within the NL and SL regimes correspond to tumours which are more sensitive to RT than the average NL and SL tumour.

3.4.1.2 The influence of the oxygen consumption rates, q_1 and q_3, on treatment outcome following a conventional fractionation schedule

We now investigate the role of q_1 and q_3 in tumour response to RT. The scatter plots in Figure 3.5 show the values of $\Delta^{\mathrm{R}}_{\mathrm{viable}}$ and $\Delta^{\mathrm{R}}_{\mathrm{total}}$ across the (q_1, q_3) pairs which define the NL virtual population. The response of NL tumours is most sensitive to the value of q_3, with smaller values leading to greater reductions in viable and total cell volumes. Higher values of q_1 are also associated with larger reductions in viable and total cell volumes. To understand these findings, we study the response to RT of four representative tumours corresponding to (q_1, q_3) sets, A_1, B_1, C_1 and D_1 (see Figure 3.5 and Table 3.3).

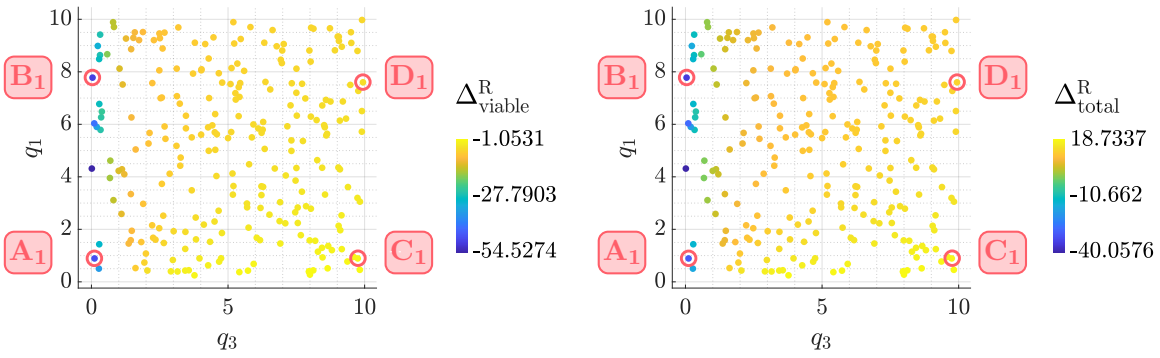
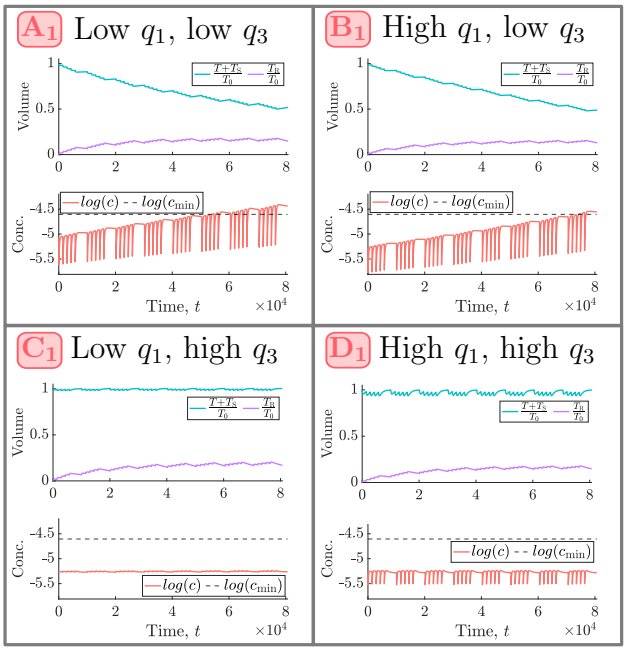


Figure 3.5: The scatter plots show the values of $\Delta^{\mathrm{R}}_{\mathrm{viable}}$ and $\Delta^{\mathrm{R}}_{\mathrm{total}}$, following a conventional fractionation schedule, for each (q_1, q_3) pair used to generate the set of virtual NL tumours. $\Delta^{\mathrm{R}}_{\mathrm{viable}}$ and $\Delta^{\mathrm{R}}_{\mathrm{total}}$ increase with q_3 and decrease with q_1.

Comparing the response of tumours A_1 and B_1 to tumours C_1 and D_1 in Figure 3.6a, we see that a smaller value of q_3 implies higher average oxygen levels and slower cell proliferation (since $q_2 = 0.01q_3$). We propose two mechanisms that could explain the increased efficacy of RT for low values of q_3: (1) higher rates of RT cell kill due to increased oxygenation or (2) limited regrowth between RT fractions due to decreased proliferation.

(a)



(b)

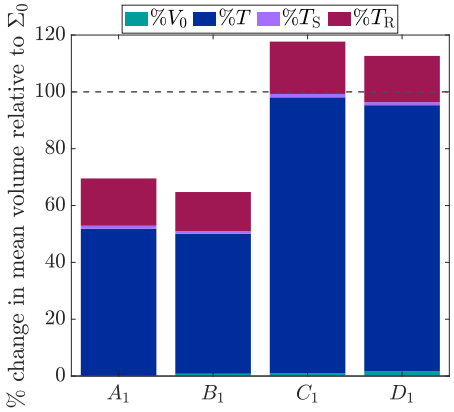


Figure 3.6: (a) For a conventional fractionation schedule, we solve Equations (3.8)–(3.11) for $t \in (0, 8 \times 10^4]$ subject to initial conditions (3.14). In A_1–D_1, we fix $V_0 = 0.0005$ and (q_1, q_3) as indicated by the points A_1, B_1, C_1 and D_1 in Figure 3.5, which correspond to NL tumours. (b) Bar graph showing the mean composition of tumours A_1–D_1 in the last week of a conventional fractionation schedule, where $\%T$, $\%T_S$, $\%T_R$ and $\%V_0$ are defined in Equation (3.16). Tumours with small values of q_3 (A_1, B_1) undergo sustained reductions in $T + T_S$ during treatment, leading to larger reductions in total volume. Tumours with large values of q_3 (C_1, D_1) experience transient reductions in $T + T_S$, as they regrow to their initial volume during the weekend break from RT, and their total volume increases as they accumulate dead material. A high value of q_1 (B_1, D_1) leads to a modest improvement in the tumour response, but does not yield a large reduction in tumour volume.

While oxygen levels are higher in tumours A_1 and B_1 than tumours C_1 and D_1, respectively, when RT is applied (see Figure 3.6a), their values of $\%T_R$ are slightly smaller (16.65% (A_1) vs. 18.42% (C_1) and 13.79% (B_1) vs. 16.29% (D_1); see Figure 3.6b). This suggests that the net increase in oxygen levels when values of q_3 are small does not significantly impact the rates of cell kill due to RT. By contrast, Figure 3.6a shows that the relative increases in the viable cell volumes of tumours A_1 and B_1 between fractions are marginal, whereas the relative increases in the viable cell volumes of tumours C_1 and D_1 between fractions are sufficiently large for them to return to their initial volumes over the

week-end break from RT. This indicates that the value of q_3 impacts the reduction in the tumour burden by modulating tumour regrowth between fractions (rather than by increasing RT-induced cell death).

Figure 3.6b also shows that a larger value of q_1 can slightly increase the magnitude of the reductions in $\Delta^{\mathrm{R}}_{\mathrm{viable}}$ and $\Delta^{\mathrm{R}}_{\mathrm{total}}$. Since high values of q_1 lead to lower average oxygen levels (Figure 3.6a), RT cell kill rates are smaller, while the rate of cell death due to hypoxia is larger than for low values of q_1. The balance between these two processes determines whether cell death increases or decreases as q_1 increases. For tumours C_1 and D_1, Figure 3.6a shows that the reduction in $T + T_{\mathrm{S}}$ following RT is greater, and the increase in T_{R} is smaller, for larger values of q_1. This confirms that a larger reduction in tumour burden can be achieved for large values of q_1 despite a reduction in RT-induced cell death: in such cases, increased cell death due to hypoxia drives the reduction in tumour volume.

Tumour	q_1	q_3
A_1	8.91×10^{-1}	1.14×10^{-1}
B_1	7.78	4.01×10^{-2}
C_1	8.91×10^{-1}	9.75
D_1	7.60	9.94

Table 3.3: Parameter sets A_1, B_1, C_1 and D_1 corresponding to the representative NL tumours.

Overall, we have shown that low values of q_3 and high values of q_1 characterise the best NL responders. Since Figures 3.6a and 3.6b suggest that the value of q_1 has a less significant influence on tumour reduction than q_3, we conclude that growth limitation between RT fractions, rather than high rates of cell death due to RT or oxygen insufficiency, has the greatest influence on the efficacy of RT for NL tumours.

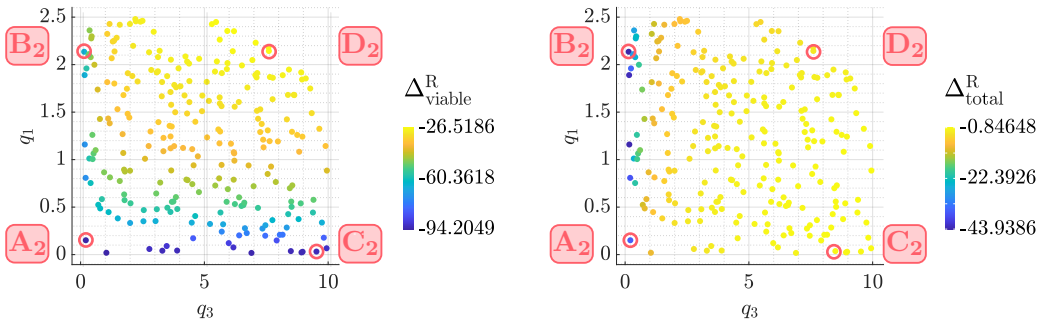


Figure 3.7: The scatter plots show the values of $\Delta^{\mathrm{R}}_{\mathrm{viable}}$ and $\Delta^{\mathrm{R}}_{\mathrm{total}}$, following a conventional fractionation schedule, for the (q_1, q_3) pairs used to generate the set of virtual SL tumours. Smaller values of $\Delta^{\mathrm{R}}_{\mathrm{viable}}$ are obtained for low values of q_1 and/or q_3, while smaller values of $\Delta^{\mathrm{R}}_{\mathrm{total}}$ are obtained for low values of q_3.

Figure 3.7 shows the values of $\Delta^{\mathrm{R}}_{\mathrm{viable}}$ and $\Delta^{\mathrm{R}}_{\mathrm{total}}$ across the (q_1, q_3) pairs which define the SL virtual population. The response of SL tumours is sensitive to the values of both q_1 and q_3: greater reductions in viable cell volume are obtained for smaller values of q_1 and/or

q_3, while greater reductions in total cell volume are obtained for smaller values of q_3. To understand these results, we study the response to RT of tumours corresponding to four representative (q_1, q_3) sets A_2, B_2, C_2 and D_2 (see Figure 3.7 and Table 3.4).

Figures 3.8a and 3.8b reveal that A_2 and C_2 accumulate a larger number of dead cells than tumours B_2 and D_2. This difference in tumour composition is amplified during treatment and the parameter which influences this distinction most is q_1. Figure 3.8a shows that for low values of q_1 (tumours A_2 and C_2), the intratumoural oxygen concentration, c, is at least 10-fold higher than for high values of q_1 (tumours B_2 and D_2). In particular, $c \gg c_{\min}$ throughout treatment when q_1 is small, which means that there is no cell death due to nutrient insufficiency and cell death is solely attributable to RT. Therefore, the decreases in viable cell volumes (and corresponding increases in dead cell volumes) in tumours A_2 and C_2 following each RT fraction are driven by cell kill due to RT, which is enhanced by low values of q_1.

For tumours B_2 and D_2, Figure 3.8a also shows that, even though the oxygen concentration transiently drops below $c_{\min}$ when each RT fraction is applied, there is a net increase in c throughout treatment and, in particular, the weekly average oxygen concentration remains above $c_{\min}$ (result not shown). Therefore, we expect RT cell kill to increase during the fractionation schedule and cell death due to hypoxia to decrease. Since RT cell kill remains limited by low oxygen levels for both tumours, neither of the two proposed cell death mechanisms is responsible for the increased RT efficacy for tumour B_2 compared to tumour D_2. However, Figure 3.8a reveals that the relative increase in $T + T_S$ between fractions is smaller for tumour B_2, which is characterised by low q_3. We conclude that the increased RT efficacy is driven by reduced tumour regrowth between fractions (as for NL tumours with low q_3).

Figure 3.8b shows further that low values of q_3 enable greater reductions in total tumour volume, Σ. Since, for tumours B_2 and D_2, the values of $\%T_R$ are comparable while the value of $\%T$ is smaller for tumour B_2, the larger reduction in Σ observed for tumour B_2 is due to increased net cell death (as described above). In contrast, for tumours A_2 and C_2, the values of $\%T$ are comparable while the value of $\%T_R$ is smaller for tumour A_2. The larger reduction in Σ observed for tumour A_2 is, therefore, due to a smaller accumulation of dead material, which occurs when lower viable cell volumes (caused by slower tumour regrowth between fractions) and/or lower oxygen levels reduce RT-induced cell death.

Tumour	q_1	q_3
A_2	1.51×10^{-1}	2.10×10^{-1}
B_2	2.14	1.43×10^{-1}
C_2	3.21×10^{-2}	9.53
D_2	2.14	7.61

Table 3.4: Parameter sets A_2, B_2, C_2 and D_2 corresponding to the representative SL tumours.

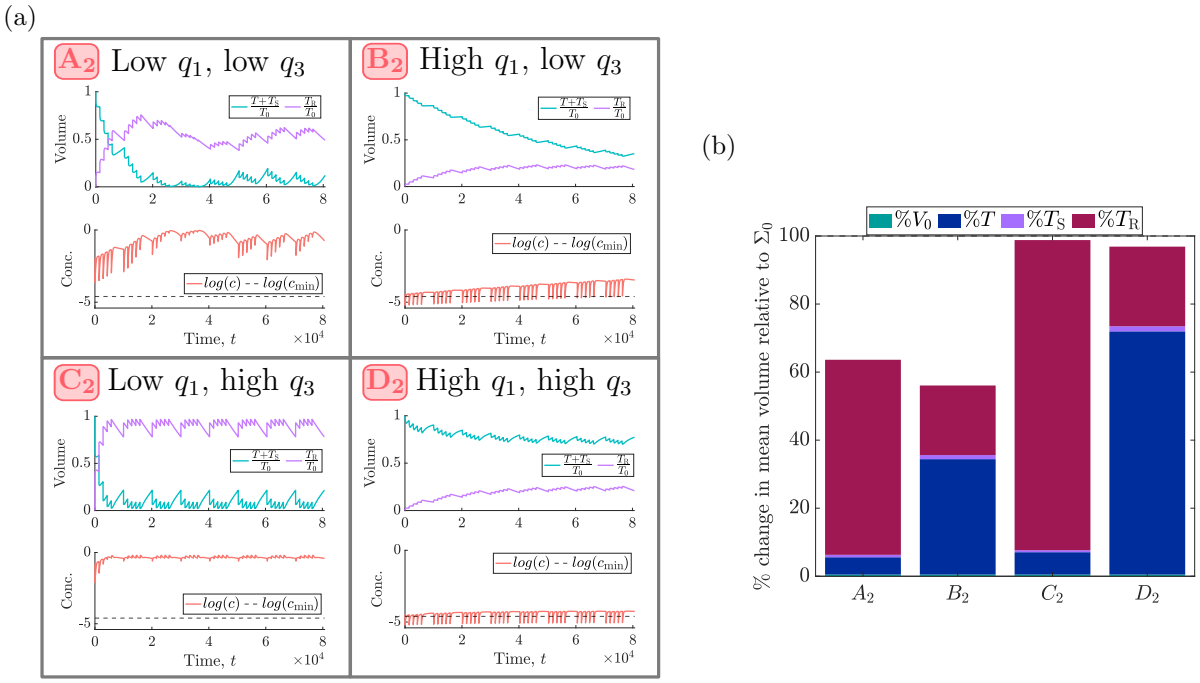


Figure 3.8: (a) For a conventional fractionation schedule, we solve Equations (3.8)–(3.11) for $t \in (0, 8 \times 10^4]$ subject to initial conditions (3.14). In A_2–D_2, we fix $V_0 = 0.005$ and (q_1, q_3) as indicated by the points A_2, B_2, C_2 and D_2 in Figure 3.7, which correspond to SL tumours. (b) Bar graph showing the mean composition of tumours A_2–D_2 in the last week of a conventional fractionation schedule, where $\%T$, $\%T_S$, $\%T_R$ and $\%V_0$ are defined in Equation (3.16). We observe three qualitative behaviours: (1) low q_1 (A_2, C_2) is associated with high oxygen levels, high rates of RT cell kill and a large accumulation of dead cell material; (2) high q_1 and low q_3 (B_2) implies a smaller reduction in viable volume due to smaller RT cell kill and a greater reduction in total volume due to limited inter-fraction tumour growth and smaller dead cell accumulation; (3) high q_1 and q_3 (D_2) leads to modest reductions in viable and total volumes due to low rates of RT cell kill and high rates of cell proliferation. Overall, the values of q_1 and q_3 influence the tumour composition and the total tumour volume, respectively.

Overall, we have shown that two mechanisms can contribute to the increased efficacy of RT for certain tumours in an SL regime. These mechanisms are cell death due to RT and limited tumour regrowth between RT doses. Their relative contributions depend on the values of q_1 and q_3. More specifically, when q_1 is small, RT cell kill is the dominant mechanism contributing to increased net cell death and, when q_3 is also small, limited regrowth between fractions ensures a larger reduction in total tumour volume. When q_1 is large and q_3 is small, limited regrowth between fractions determines the response to RT by ensuring larger reductions in viable and total cell volumes.

3.4.1.3 The effect of the dosing schedule on typical tumour response

We now consider how, for a fixed total dose, the dose rate, R, and the number of fractions per week, N_{frac}, affect tumour responses to RT. For the virtual cohorts of NL and SL tumours, Figures 3.9 and 3.10, respectively, show the distributions of $\Delta^{\text{R}}_{\text{viable}}$ and $\Delta^{\text{R}}_{\text{total}}$ for fractionation schedules with $R \in \{0.1, 0.3, 0.5\}$ and $N_{\text{frac}} \in \{1, 3, 5\}$. For NL tumours, the mean reduction in viable volume and the difference between the viable and total volumes increase with R and N_{frac}. However, the maximum reduction in viable and total volumes typically decreases with R (for fixed N_{frac}), and the mean and maximum increases in total volume also increase with R and N_{frac}. Therefore, a higher dosing frequency and/or dose may not lead to greater RT efficacy for tumours in the NL regime. By contrast, for SL tumours, on average, the reduction in the viable and total volumes and the difference between the viable and total volumes increase with R and N_{frac}. The response of SL tumours is, thus, consistent with the current, standard approach to RT protocol design, which aims to maximise RT cell kill by applying the highest tolerable total dose, in sufficiently frequent fractions, to the tumour. This result is also supported by other modelling approaches. For example, Lewin et al. [138] developed a spatially-resolved model of avascular tumour growth and RT cell death which predicted that there is a minimum RT dose, for a fixed dosing frequency, and a minimum dosing frequency, for a fixed RT dose, below which tumours grow during treatment.

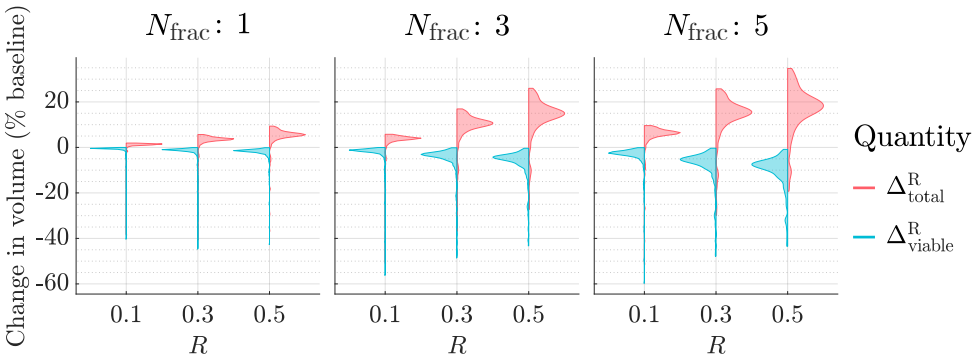


Figure 3.9: For the virtual NL population, we show how the distributions of $\Delta^{\text{R}}_{\text{viable}}$ and $\Delta^{\text{R}}_{\text{total}}$ change as the dose rate, $R \in \{0.1, 0.3, 0.5\}$, and the number of fractions per week, $N_{frac} \in \{1, 3, 5\}$, vary. The mean value of $\Delta^{\text{R}}_{\text{viable}}$ decreases, while the mean values of $\Delta^{\text{R}}_{\text{total}}$ and $\Delta^{\text{R}}_{\text{total}} - \Delta^{\text{R}}_{\text{viable}}$ increase as R and N_{frac} increase.

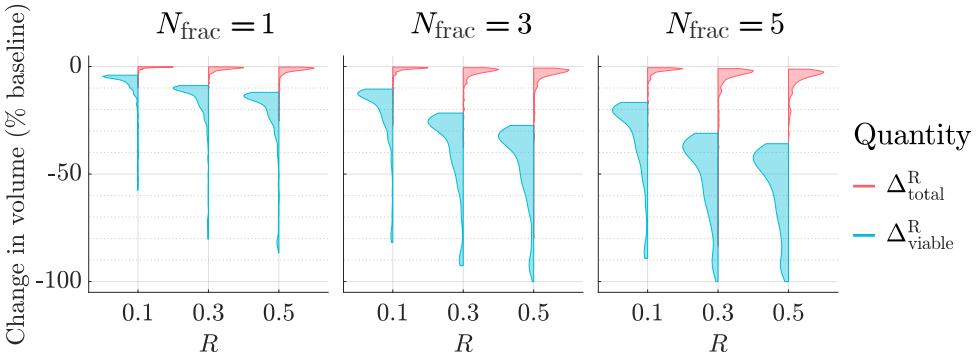


Figure 3.10: For the virtual SL population, we show how the distributions of $\Delta^{\text{R}}_{\text{viable}}$ and $\Delta^{\text{R}}_{\text{total}}$ change as the dose rate, $R \in \{0.1, 0.3, 0.5\}$, and the number of fractions per week, $N_{\text{frac}} \in \{1, 3, 5\}$, vary. The mean values of $\Delta^{\text{R}}_{\text{viable}}$ and $\Delta^{\text{R}}_{\text{total}}$ decrease, while the mean value of $\Delta^{\text{R}}_{\text{total}} - \Delta^{\text{R}}_{\text{viable}}$ increases as R and N_{frac} increase.

3.4.2 Tumours in the bistable regime

3.4.2.1 Typical response to a conventional fractionation schedule

Figure 3.11a shows the average response to a conventional RT schedule of a tumour in a BS regime, which has been treated at its NL steady state. RT has a detrimental effect as tumour regrowth between fractions and over the weekend outweighs RT-induced cell death. The dead cell volume also increases throughout treatment, implying an increase in total volume. Figure 3.11b further shows that, for the BS virtual cohort, $\Delta^{\text{R}}_{\text{viable}} > 0$ for at least 80% of tumours and $\Delta^{\text{R}}_{\text{total}} > 0$ for all tumours. This reveals that most tumours in the BS virtual cohort respond badly to RT, given initial conditions that correspond to their NL steady state.

The results in Figure 3.11b also indicate that a few virtual tumours are more or less sensitive to RT than the average tumour in the BS virtual population: while their total volume increases during RT, their viable volume undergoes a $20-80\%$ decrease or $40-80\%$ increase, respectively, by the end of treatment. We investigate the response to RT of these outliers in more detail in the following section.

3.4.2.2 The influence of q_1, q_3 and V_0 on treatment outcome following a conventional fractionation schedule

As for tumours in monostable regimes, we study the influence of the oxygen consumption rates for maintenance and proliferation, q_1 and q_3, on tumour response to RT, but we also study the role played by the vascular volume, V_0. More specifically, we introduce a function V_{d}, which quantifies how close a tumour in the BS regime lies to the NL and SL regimes (see the schematic in Figure 3.12):

$$V_{\text{d}}(V_0) = \frac{V_0 - V_{\text{N}}}{V_{\text{S}} - V_{\text{N}}}, \tag{3.17}$$

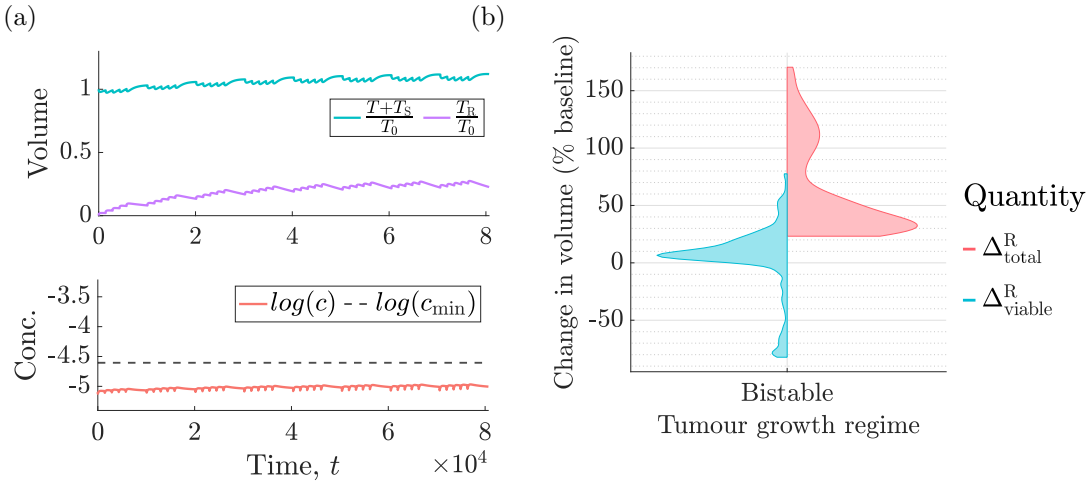


Figure 3.11: (a) For a conventional fractionation schedule, we solve Equations (3.8)–(3.11) for $t \in (0, 8 \times 10^4]$ subject to initial conditions (3.14). We set $(q_1, q_3, V_0) = (0.787, 8.38, 0.00275)$. This tumour represents the typical behaviour in a BS regime. (b) Violin plots representing the distributions of Δ^R_{viable} and Δ^R_{total}. While the effect of RT is deleterious for most tumours, with several outliers experiencing larger than average increases in viable and total volumes, there are tumours that exhibit larger than average decreases in viable volume.

where V_N and V_S are the threshold values of V_0 below and above which only NL and SL steady states exist. Further,

$$\begin{cases} V_d \to 0 \text{ as } V_0 \to V_N, \\ V_d \to 1 \text{ as } V_0 \to V_S. \end{cases} \tag{3.18}$$

In particular, $V_d \gtrapprox 0$ for tumours which are close to the NL regime, whereas $V_d \lessapprox 1$ for tumours which are close to the SL regime.

The scatter plots in Figure 3.13 show the values of Δ^R_{viable} and Δ^R_{total} across the (q_1, q_3) and (q_1, V_d) pairs corresponding to the BS virtual population. We note that the values of q_3 and V_d are correlated: for fixed q_1, the lowest values of V_d correspond to the highest values of q_3 and vice versa. It is, therefore, sufficient to describe the response of tumours in a BS regime with respect to the values of q_1 and V_d. The largest reductions in viable volume are obtained for lower values of q_1 and $V_d \lessapprox 1$, whereas the largest increases in viable volume are obtained for higher values of q_1 and intermediate values of V_d. Those tumours with the smallest and largest values of Δ^R_{viable} also undergo the largest increases in total volume: for intermediate to high values of V_d, Δ^R_{total} decreases as V_d and q_1 increase.

We now select four representative (q_1, q_3, V_d) sets A_3, B_3, C_3 and D_3 (see Figure 3.13 and Table 3.5) and study the corresponding tumours' response to RT. Figures 3.14a and 3.14b show that tumours A_3 and B_3 decrease in viable volume, with A_3 experiencing a larger than average reduction, while C_3 and D_3 increase in viable volume, with C_3 experiencing

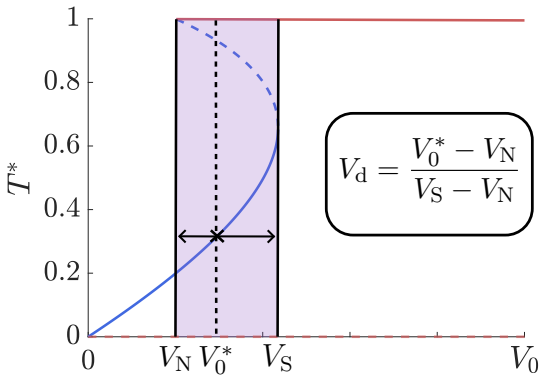


Figure 3.12: Schematic bifurcation diagram showing how, for fixed values of q_1 and q_3, the steady state value of the tumour cell volume, T^*, changes with V_0. The shaded purple region represents the bistable region, where V_N and V_S are the threshold values of V_0 below and above which only NL and SL steady states exist. For tumours with $V_N < V_0^* < V_S$, we define V_d by (3.17) to quantify the relative proximity of $T^*(V_0^*)$ to the monostable NL and SL regions.

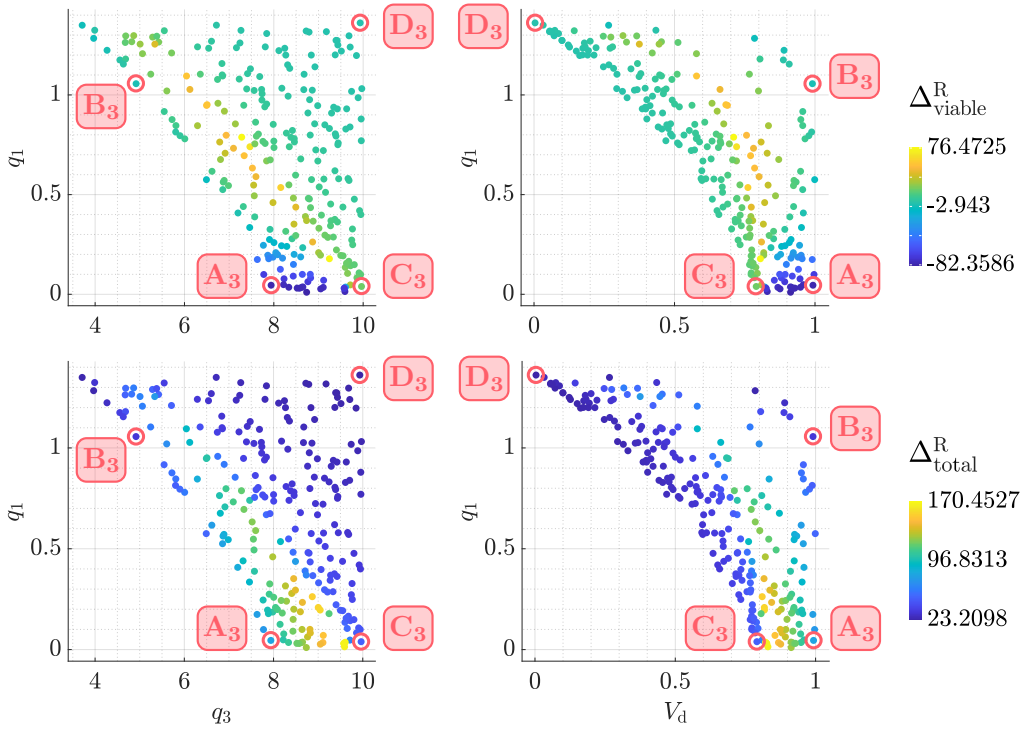
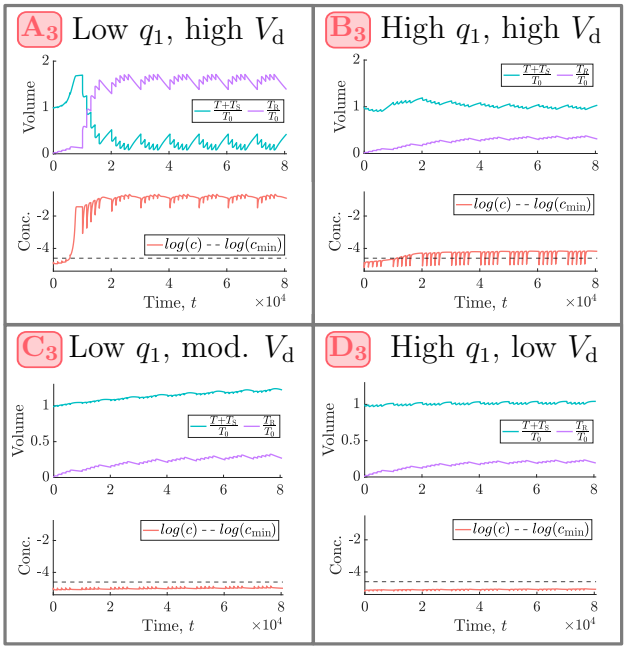


Figure 3.13: The scatter plots show the values of Δ^R_{viable} and Δ^R_{total}, following a conventional fractionation schedule, for the (q_1, q_3) and (q_1, V_d) pairs used to generate the set of virtual tumours in a BS regime. The smallest values of Δ^R_{viable} are associated with lower values of q_1 and q_3 and $V_d \lesssim 1$, while the largest values of Δ^R_{viable} are associated with higher values of q_1, lower values of q_3 and intermediate values of V_d. Δ^R_{total} is largest for the tumours with the smallest and largest values of Δ^R_{viable}.

a larger than average increase. While tumours A_3 and C_3 have low q_1, $V_\mathrm{d} \approx 1$ for A_3 and $V_\mathrm{d} \approx 0.8$ for C_3. Similarly, while tumours B_3 and D_3 have high q_1, $V_\mathrm{d} \approx 1$ for B_3 and $V_\mathrm{d} \approx 0$ for D_3. Given (3.18), this suggests that the behaviour of tumours in a BS regime that lie sufficiently close to the SL or NL regions will be, respectively, similar to that of SL or NL tumours with values of q_1 and q_3 of the same order of magnitude.

(a)



(b)

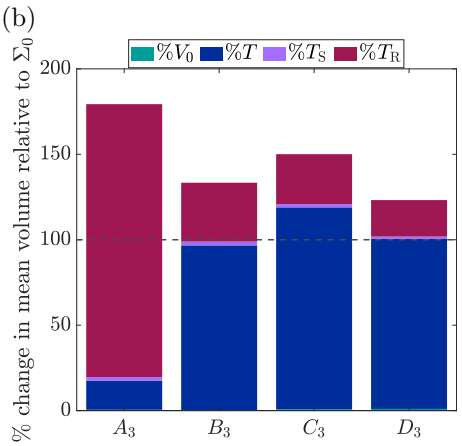


Figure 3.14: (a) For a conventional fractionation schedule, we solve Equations (3.8)–(3.11) for $t \in (0, 8 \times 10^4]$ subject to initial conditions (3.14). In A_3–D_3, we fix $V_0 = 0.00275$ and (q_1, q_3) as indicated by the points A_3, B_3, C_3 and D_3 in Figure 3.13. (b) Bar graph showing the mean composition of tumours A_3–D_3 in the last week of a conventional fractionation schedule, where $\%T$, $\%T_\mathrm{S}$, $\%T_\mathrm{R}$ and $\%V_0$ are defined in Equation (3.16). A_3 and B_3 decrease in viable volume and increase in total volume, while C_3 and D_3 increase in both viable and total volumes. Tumour A_3, which has low q_1 and $V_\mathrm{d} \approx 1$, experiences larger than average decreases and increases in viable and total volumes, respectively. By contrast, tumour C_3, which has an intermediate value of V_d, experiences larger than average increases in viable and total volumes.

More specifically, tumours A_3 and B_3 respond to RT similarly to SL tumours C_2 and D_2, respectively (recall Figures 3.8a and 3.8b), while tumour D_3 responds similarly to NL tumour D_1 (recall Figures 3.6a and 3.6b). For tumour A_3, this response involves an initial large increase in viable and total volumes as the tumour evolves towards

Tumour	q_1	q_3	V_d
A_3	4.55×10^{-2}	7.94	0.993
B_3	1.06	4.92	0.991
C_3	3.92×10^{-2}	9.96	0.791
D_3	1.36	9.93	0.00376

Table 3.5: Parameter sets A_3, B_3, C_3 and D_3 corresponding to the representative tumours in the BS cohort.

its SL steady state, followed by a substantial increase in RT cell kill, the average oxygen concentration and the dead cell volume. Despite the reduction in viable volume, the accumulation of dead material implies a significant increase in total volume. The same qualitative behaviour is observed for tumour B_3, with less RT-induced cell death and dead material accumulation as the oxygen concentration remains significantly lower than for A_3. As a result, the increase in total volume is also smaller. For tumour D_3, cell death due to RT and hypoxia is outweighed by the tumour regrowth between fractions, leading to small increases in viable and total volumes.

Further, while tumour C_3 lies closest to the SL region ($V_{\mathrm{d}} \approx 0.8$), it remains within the basin of attraction of its NL steady state, unlike tumours A_3 and B_3. In particular, the increase in the oxygen concentration for C_3 is not sufficiently rapid for the tumour to enter, during treatment, an SL regime where, on average, $c > c_{\mathrm{min}}$. Therefore, the increase in viable volume is constant, but gradual, with a smaller accumulation of dead material. This explains why C_3 undergoes a larger than average increase in viable volume, with a moderate increase in total volume.

In summary, we have identified two extremal regions of parameter space in which tumours in a BS regime undergo larger decreases and increases in viable volume (and larger increases in total volume) than typical tumours in this regime. Tumours which are sufficiently close to the boundary of the BS and SL regimes and consume little oxygen for maintenance experience larger than average decreases in viable cell volume as they transition from their NL to their SL steady state and RT cell death is enhanced by higher oxygen levels. By contrast, tumours which are close to the boundary between the BS and SL regimes, but not sufficiently close, undergo larger than average increases in viable volume, regardless of the value of q_1. This occurs as they attempt, and fail, to transition from their NL to their SL steady state and, thus, RT cell death remains limited by low oxygen levels and outweighed by tumour regrowth between fractions.

3.4.2.3 The effect of the dosing schedule on typical tumour response

For the virtual population of tumours in a BS regime, we show in Figure 3.15 how the dose rate, R, and the number of fractions per week, N_{frac}, affect tumour response to RT when the total dose is fixed. On average, a higher number of fractions per week (for fixed R) and a higher dose rate (for fixed N_{frac}) lead to greater increases in the viable and total cell populations. While these results contrast with those for tumours in SL regimes, we see that the maximum reduction in viable volume increases with R and N_{frac}, as for SL tumours. Overall, these results indicate that, in most cases, increasing the RT dose and frequency may be deleterious (as for NL tumours).

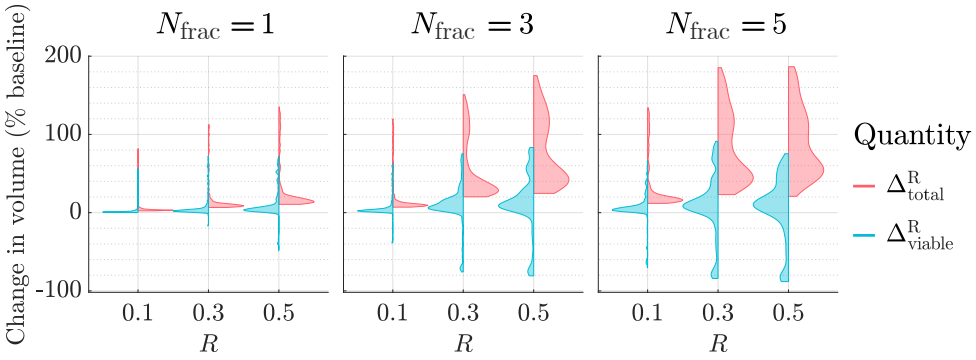


Figure 3.15: For the virtual BS population, we show how the distributions of $\Delta^{\text{R}}_{\text{viable}}$ and $\Delta^{\text{R}}_{\text{total}}$ change as the dose rate, $R \in \{0.1, 0.3, 0.5\}$ and the number of fractions per week, $N_{\text{frac}} \in \{1, 3, 5\}$, vary. The mean and maximum values of $\Delta^{\text{R}}_{\text{viable}}$ increase, while its minimum value decreases, as R and N_{frac} increase. The mean, minimum and maximum values of $\Delta^{\text{R}}_{\text{total}}$ increase as R and N_{frac} increase. There is an exception for $N_{\text{frac}} = 5$, where the maximum value of $\Delta^{\text{R}}_{\text{viable}}$ and minimum value of $\Delta^{\text{R}}_{\text{total}}$ decrease with $R \geq 3$.

3.5 Post-treatment tumour growth dynamics

In the previous section, we discussed the short-term response to RT of tumours in different growth regimes, distinguishing between tumours in monostable (NL and SL) and bistable regimes. We now investigate the long-term response to RT by studying post-treatment tumour growth dynamics and, in particular, the tumour steady states attained following treatment.

3.5.1 Steady state analysis

We first perform a steady state analysis of the system (3.8)–(3.11) to understand the potential long-term effects of RT. Upon completion of a radiation protocol, we have $R \equiv 0$ thereafter. We, therefore, seek steady state solutions by setting $R = 0$ and $\frac{\text{d}}{\text{d}t} = 0$ in Equations (3.8)–(3.11) and solving the following system

$$q_2 c T(1 - \Sigma) - \delta_1(c_{\min} - c)H(c_{\min} - c)T + \mu T_{\text{S}} = 0, \tag{3.19}$$

$$\theta_2 q_2 c T_{\text{S}}(1 - \Sigma) - (\delta_{1,\text{S}}(c_{\min} - c)H(c_{\min} - c) + \mu + \xi))T_{\text{S}} = 0, \tag{3.20}$$

$$\xi T_{\text{S}} - \eta_{\text{R}} T_{\text{R}} = 0, \tag{3.21}$$

$$g(1 - c)V_0 - q_1(T + \theta_1 T_{\text{S}})c - q_3\left(T + \theta_2 T_{\text{S}}\right)c(1 - \Sigma) = 0. \tag{3.22}$$

Denoting the steady state solutions by T^*, T^*_{S}, T^*_{R} and c^*, Equation (3.21) implies that $T^*_{\text{S}} = \frac{\eta_{\text{R}}}{\xi} T^*_{\text{R}}$. Therefore, we have either $T^*_{\text{S}} = T^*_{\text{R}} = 0$ or $T^*_{\text{S}}, T^*_{\text{R}} > 0$. Suppose that $T^*_{\text{S}}, T^*_{\text{R}} > 0$. We can show, by contradiction, that there are no physically realistic steady

state solutions satisfying this condition by, first, proving that there are no SL steady states with T_S^*, $T_R^* > 0$ and, then, proving that there are no NL steady states with T_S^*, $T_R^* > 0$.

If $c^* \geq c_{\min}$, then Equation (3.19) gives

$$T^* = \frac{-\mu T_S^*}{q_2 c^* (1 - \Sigma)} < 0, \tag{3.23}$$

since $T_S^* > 0$ and $\Sigma < 1$ by assumption and $\mu > 0$ and $q_2 > 0$ by definition. Since $T^* > 0$ is required for a physically realistic solution, there are no SL steady states with T_S^*, $T_R^* > 0$.

If $0 < c^* < c_{\min}$, then Equation (3.19) implies that

$$\frac{q_2}{\delta_1}(1 - \Sigma) - \frac{(c_{\min} - c^*)}{c^*} = -\frac{\mu T_S^*}{\delta_1 c^* T^*} < 0. \tag{3.24}$$

Since $q_2 = \delta_1$, we have

$$(1 - \Sigma) - \frac{(c_{\min} - c^*)}{c^*} = -\frac{\mu T_S^*}{\delta_1 c^* T^*} < 0. \tag{3.25}$$

Then, Equation (3.20) implies that

$$\frac{\theta_2 q_2}{\delta_{1,S}}(1 - \Sigma) - \frac{(c_{\min} - c^*)}{c^*} = \frac{(\mu + \xi)}{\delta_{1,S} c^*} > 0. \tag{3.26}$$

Since $\theta_2 q_2 = \delta_{1,S}$, we have

$$(1 - \Sigma) - \frac{(c_{\min} - c^*)}{c^*} = \frac{(\mu + \xi)}{\delta_{1,S} c^*} > 0. \tag{3.27}$$

Comparing Equations (3.25) and (3.27), we obtain a contradiction. This implies that there are no NL steady states with T_S^*, $T_R^* > 0$. We, therefore, conclude that NL and SL steady state solutions of the system (3.8)–(3.11) must have $T_S^* = T_R^* = 0$. It is then straightforward to show that the solutions of the system (3.19)–(3.22) with $T_S^* = T_R^* = 0$ are equal to the steady state solutions in the absence of treatment (see Chapter 2).

We have shown that RT preserves the steady states and growth regimes observed in the absence of treatment. We conclude that, given $T(0) = T^*$, tumours in monostable regimes at the start of treatment will return to their original tumour volume, $\Sigma_0 = T^* + V_0$, and composition ($T_S^* = T_R^* = 0$) after RT. In contrast, tumours in a BS regime either return to their original, NL steady state, or evolve to their SL steady state.

3.5.2 Elucidating conditions for RT to drive steady state switching of tumours in bistable regimes

The steady state analysis showed that tumours in BS regimes may attain either an NL or an SL steady state following treatment. In particular, such tumours may undergo large increases in tumour volume in response to RT as they switch from an NL steady state to a larger SL steady state. Recall the tumours A_3–D_3 that we defined in Section 3.4.2: Figure

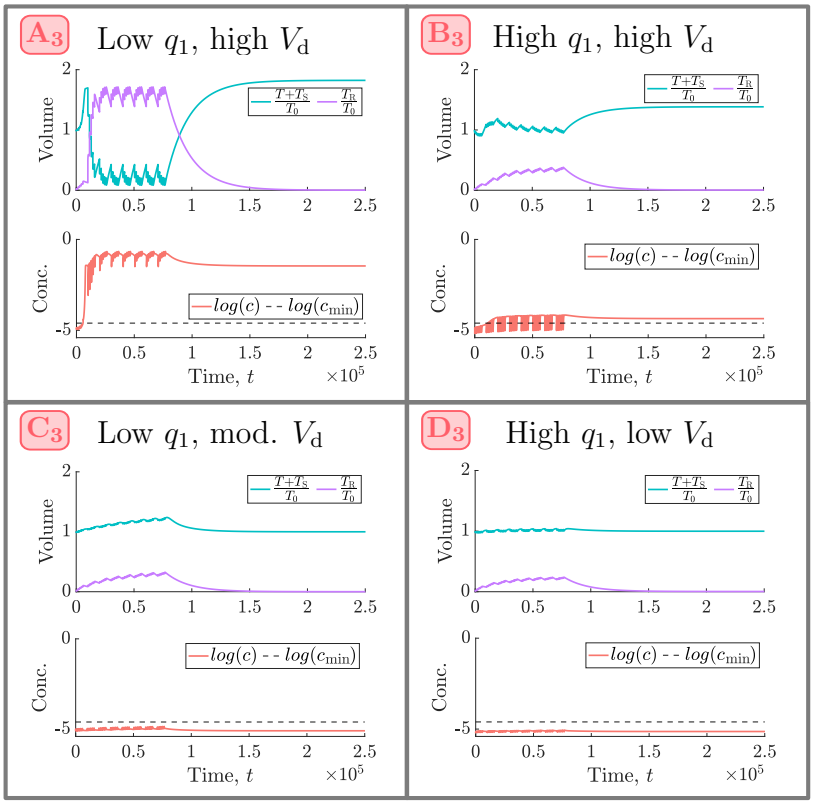


Figure 3.16: For a conventional fractionation schedule, we solve Equations (3.8)–(3.11) for $t \in (0, 2.5 \times 10^5]$ subject to initial conditions (3.14). In A_3–D_3, we fix $V_0 = 0.00275$ and (q_1, q_3) as indicated by the points A_3, B_3, C_3 and D_3 in Figure 3.13, which correspond to tumours in a BS regime. Tumours C_3 and D_3 evolve to their NL steady state following treatment, whereas tumours A_3 and B_3 switch to their SL steady state.

3.16 shows their response to RT both during, and following, a conventional fractionation schedule.

Tumours C_3 and D_3 underwent increases in viable volume during treatment and then returned to their NL steady state following treatment: the effect of RT was not strong enough to cause a switch in steady state. By contrast, tumours A_3 and B_3 experienced reductions in viable volume during treatment and then evolved to their SL steady state following treatment. The oxygen concentration in both of these tumours increased beyond the hypoxic threshold, c_{min}, during (A_3) or following (B_3) RT and remained above this threshold level thereafter. This enabled the viable cell population to grow unchecked until the SL equilibrium was reached.

In contrast to tumours C_3 and D_3, we recall that tumours A_3 and B_3 are characterised by $V_d \approx 1$, where V_d is defined in (3.17). They are also, respectively, characterised by high and low values of q_1, the oxygen consumption rate for maintenance. This suggests that tumours which are near to the boundary between the BS and SL regions in parameter space are most susceptible to undergoing a switch in steady state volume in response to

RT, irrespective of the value of q_1. Figure 3.17 shows that this observation holds across a range of RT protocols.

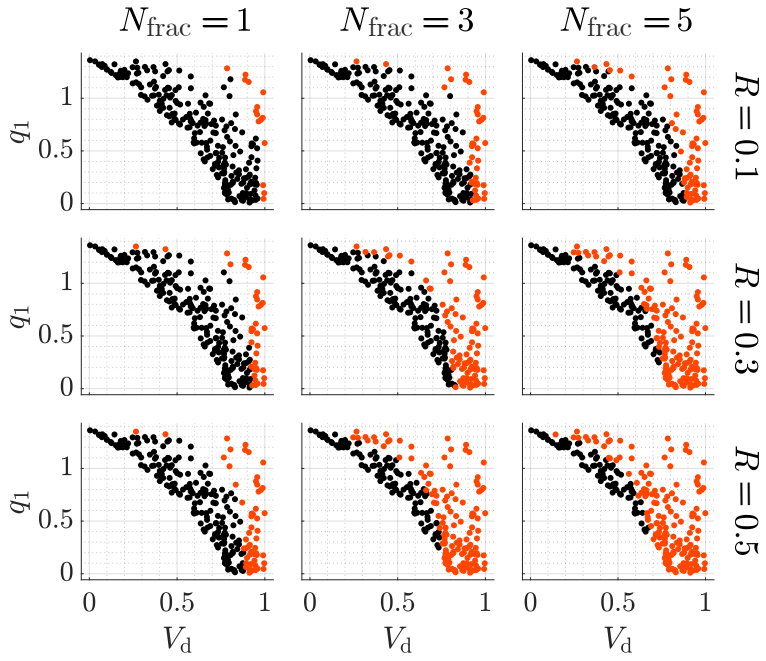


Figure 3.17: For the virtual BS tumour population and fractionation schedules with $R \in \{0.1, 0.3, 0.5\}$ and $N_{\text{frac}} \in \{1, 3, 5\}$, the scatter plots show the (q_1, V_{d}) pairs that correspond to tumours that switch (red) and do not switch (black) steady state. The former are typically characterised by larger values of V_{d}.

Figure 3.17 also indicates that the probability of a tumour switching steady state typically increases with fraction dose and dosing frequency. We illustrate this for a particular tumour in the BS regime in Figure 3.18, which shows the response of tumour C_3 to three different fractionation protocols: (1) 5×2 Gy for 8 weeks in Figure 3.18a, (2) 5×3 Gy for 5.2 weeks in Figure 3.18b and (3) 3×3 Gy for 8.67 weeks in Figure 3.18c. Comparing Figures 3.18a and 3.18b, we see that a switch in steady state is observed when the fraction dose is 3 Gy, showing how the likelihood of a tumour switching steady state increases with dose. Further, comparing Figures 3.18b and 3.18c highlights how a lower dosing frequency can prevent the transition from an NL to an SL steady state.

These results suggest that a lower RT dose and dosing frequency may prevent uncontrolled increases in tumour volume following RT for tumours in BS regimes. As with our observations for short-term treatment responses, this challenges the assumption that a higher dose, applied with a higher frequency, will lead to a greater reduction in tumour volume.

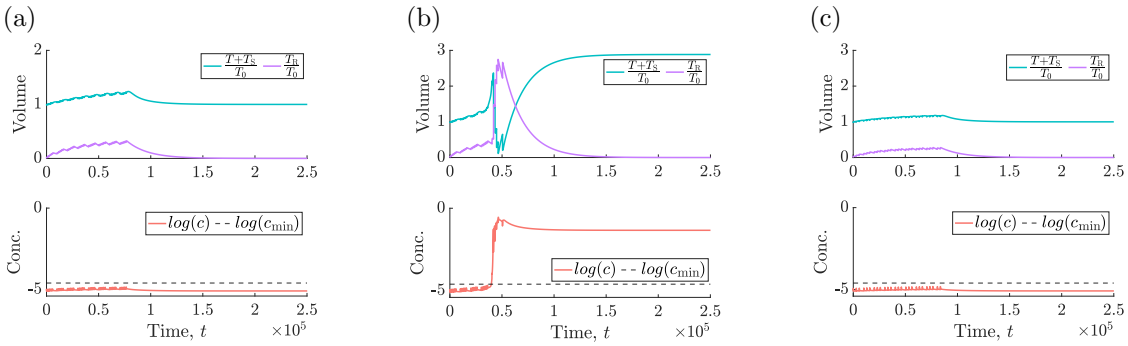


Figure 3.18: We solve Equations (3.8)–(3.11) for $t \in (0, 2.5\times10^5]$ subject to initial conditions (3.14). We fix dose rates (a) $R = 0.2$ and (b),(c) $R = 0.3$ and simulate (a) daily fractions, Monday to Friday, for 8 weeks, (b) daily fractions, Monday to Friday, for 5.2 weeks and (c) fractions on Monday, Wednesday and Friday for 8.67 weeks. We fix $V_0 = 0.00275$ and (q_1, q_3) as indicated by parameter set C_3 in Table 3.5. Comparing (a), (b) and (c) shows how lower RT doses and less frequent dosing both prevent the tumour C_3 from evolving to its SL steady state following treatment.

3.6 Discussion

Having derived a model of tumour growth which distinguishes between nutrient and space limited mechanisms of growth arrest in Chapter 2, this chapter focussed on investigating how these two mechanisms can influence tumour responses to fractionated radiotherapy. We extended the growth model to account for the time-dependent cell damage due to RT, damage repair and cell death, keeping track of the time evolution of the undamaged, damaged and dead tumour cell volumes. We then studied the RT response of tumours in the nutrient limited, space limited and bistable growth regimes described by the model in the absence of treatment. Interestingly, we found that the short- and long-term responses of tumours in monostable regimes (i.e., NL and SL) can be distinguished from those of tumours in BS regimes.

Tumours in the SL regime typically respond well to RT in the short-term, as they experience high rates of RT cell kill (due to high oxygen levels) and occupy the entire available space at the start of treatment ($\Sigma_0 = T_0 + V_0 = 1$), implying a decrease in both their viable and total volumes during fractionation. By contrast, tumours in the NL regime typically respond less well since low rates of RT cell kill (due to low oxygen levels) and the availability of free space for further growth ($\Sigma_0 < 1$) imply smaller reductions in their viable volume than for SL tumours and increases in their total volume as dead material accumulates and the tumour grows between fractions. That being said, certain NL and SL tumours respond much better than the average tumour in their respective regimes.

By identifying parameter regions which give rise to these outliers, we determined different mechanisms that may underpin successful RT. For NL tumours, RT efficacy is maximised

when regrowth between fractions is minimised, while, for SL tumours, increased RT efficacy may be due to limited regrowth (as for NL tumours) and/or RT cell kill. The additional SL-specific mechanism is a consequence of low rates of RT cell kill for NL tumours due to low oxygenation. This explains how the different growth arrest mechanisms that characterise the NL and SL regimes can affect short-term tumour response to RT.

In the long-term, tumours in NL and SL regimes always return to their pre-treatment steady state volume, irrespective of the effects of RT during treatment. Our model, therefore, predicts that any change in the tumour burden during radiation is transient for these tumours. This result follows from our simplifying assumption that the vascular volume remains constant during tumour growth and RT.

We also found that most tumours in the BS regime respond badly to RT in the short-term, as the combination of low rates of RT cell kill (due to low oxygen levels) and high rates of inter-fraction regrowth (due to high values of the oxygen consumption rate for proliferation, q_3) lead to increases in their viable and total cell volumes during RT. As for monostable regimes, outliers which lie, in parameter space, near the boundary between BS and SL regions, exhibit more extreme responses to RT. In these cases, the intratumoural oxygen concentration is close to, and smaller than, $c_{\min}$, the threshold concentration below which cells die due to nutrient insufficiency. If RT induces a net increase in oxygen levels such that $c > c_{\min}$, then cell death due to nutrient insufficiency ceases and RT drives the tumour to its SL steady state. This leads to a significant increase in RT-induced cell death and dead cell accumulation, resulting in large decreases and increases in viable and total volumes, respectively. By contrast, if RT induces a net increase in oxygen levels such that $c \leq c_{\min}$, then RT causes large increases in viable and total volumes as the tumour grows towards, and fails to reach, its SL steady state. Here, RT cell kill is outweighed by tumour growth between fractions throughout treatment. Irrespective of whether these outliers experience increases or decreases in viable volume, they evolve to their larger SL steady state following RT. Therefore, the model predicts that, in the BS regime, RT usually has a detrimental effect on tumour growth.

A final key result relates to RT dosing schedules. We found that, in SL regimes, applying larger doses at higher frequency typically increases RT efficacy, whereas, in NL and BS regimes, administering lower doses at lower frequency can increase RT efficacy for outliers and lessen, or prevent, large increases in tumour burden across the virtual cohorts. The latter result is counter-intuitive and challenges the assumption that giving the maximum tolerable dose is the best course of treatment. In practice, we are unlikely to know in which growth regime a patient's tumour lies in when treatment starts. Therefore, if we can determine a tumour's growth regime by monitoring its response to a given treatment protocol, then this would allow us to adapt the treatment protocol to target the best

outcome possible. In particular, for tumours in the SL regime, one could maximise the reduction in tumour burden by increasing the RT dose or dosing frequency, while, for tumours in the NL and BS regime, it might be preferable to halt treatment early in order to prevent large increases in tumour burden.

In this chapter, we characterised tumour responses to RT across the NL, SL and BS growth regimes and, in doing so, we determined the processes which may affect tumour sensitivity to RT in each regime. In the following chapter, we conduct a similar study to investigate the influence of nutrient and space limited mechanisms of growth arrest on tumour responses to hyperthermia. By assessing tumour sensitivity to HT in each regime, we will develop some insight into which tumours are most and least likely to experience an improved RT response when RT is combined with HT. These hypotheses will then be tested in Chapter 5, where we will study tumour responses to combinations of RT and HT.

Chapter 4

Investigating the influence of growth arrest mechanisms on tumour responses to hyperthermia

4.1 Introduction

In Chapter 3, we extended the model of tumour growth developed in Chapter 2 to include tumour response to radiotherapy (RT) and investigated how nutrient and space limited mechanisms of growth control impact RT sensitivity. This chapter focusses on characterising the impact of the two aforementioned growth arrest mechanisms on tumour responses to hyperthermia (HT).

We saw in Section 1.3.2 that the biological effects of HT depend on thermal dose, which is typically defined as a function of heating temperature and duration. Excluding ablation, which requires temperatures beyond 50 °C, two main types of HT are of clinical interest: mild HT, which re-oxygenates a tumour via vasodilation and a reduction in oxygen consumption rates, and high HT, which damages tumour and endothelial cells, induces a damage-associated angiogenic response, and inhibits DNA repair mechanisms. A key question in hyperthermic oncology remains which of these types of HT is more effective, especially when applied in combination with other treatments, such as RT. Here, we will consider tumour responses to mild and high HT and, in so doing, attempt to shed light on the answer to this question.

Most mathematical models that have been proposed to study tumour response to HT are either cell survival models (like the LQ model for RT) that quantify the proportion of cell death after a given thermal dose [263] or partial differential equation models of the intratumoural temperature distribution during HT [34, 72, 130, 147, 188, 244, 251]. While several models describe time-dependent HT cell kill [181], DNA repair inhibition during HT [262] or vasodilation and changes in blood flow under HT [19], there is no mathematical model in the literature, to the best of our knowledge, which captures all of the key effects of

mild and high HT. In this chapter, we propose a simple modelling framework that describes the time-dependent effects of mild and high HT and that can be used for a comprehensive study of tumour response to HT.

Given our ultimate aim of studying tumour responses to combinations of RT and HT in Chapter 5, we extend, in Section 4.2, the model of tumour growth and response to RT presented in Chapter 3 to incorporate tumour response to HT. In Section 4.3, we systematically investigate tumour response to fractionated mild and high HT in the nutrient limited (NL), space limited (SL) and bistable (BS) growth regimes using the three virtual tumour populations constructed in Chapter 3. In Section 4.4, we show that the effects of mild HT are negligible across all three regimes by considering the short- and long-term responses to a conventional mild HT fractionation schedule. Section 4.5 focusses on tumour response to high HT. For each virtual cohort, we initially consider short-term (Section 4.5.1) and long-term (Section 4.5.2) tumour responses to a conventional high HT fractionation schedule. As for RT, we determine the average response and explore how certain values of the oxygen consumption rates generate extremal behaviour. In Sections 4.5.3 and 4.5.4, we then also study the influence of the (high HT) thermal dose and the rate of angiogenesis on tumour response, respectively. This enables us to identify the factors that may enhance, and the dosing regimen that maximises, the reduction in tumour burden.

4.2 Model development

4.2.1 The mathematical model

In this section, we extend the model (3.8)–(3.11), which describes tumour dynamics under RT, to incorporate tumour response to HT. We distinguish between the effects of mild and high HT, assuming that the former re-oxygenates the tumour via vasodilation and a reduction in oxygen consumption rates, while the latter kills tumour and endothelial cells, induces a damage-associated angiogenic response and inhibits DNA repair mechanisms.

We introduce the dependent variable T_{H} to denote the HT-damaged tumour cell volume and let $\Sigma = T + T_{\mathrm{R}} + T_{\mathrm{S}} + T_{\mathrm{H}} + V$ denote the total tumour volume. Then, we propose the following system of time-dependent ordinary differential equations (ODEs) to describe tumour responses to combination treatments comprising RT and HT (see the schematic in Figure 4.1):

$$\frac{\mathrm{d}T}{\mathrm{d}t} = \underbrace{(1-\alpha_{\mathrm{RO2}}(t))q_2^* cT(S_{\max}-\Sigma)}_{\substack{\text{undamaged cell}\\ \text{proliferation, reduced by mild HT}}} - \big(\delta_1^*(c_{\min}^*-c)H(c_{\min}^*-c) + \lambda^* cR + \nu^* cR\big)T$$
$$+ \mu^* T_{\mathrm{S}} - \underbrace{\beta^*(t)T}_{\substack{\text{high HT}\\ \text{damage}}}, \quad (4.1)$$

$$\frac{\mathrm{d}T_{\mathrm{S}}}{\mathrm{d}t} = \underbrace{(1-\alpha_{\mathrm{RO2}}(t))\theta_2 q_2^* c T_{\mathrm{S}}(S_{\max}-\Sigma)}_{\substack{\text{sub-lethally damaged cell}\\ \text{proliferation, reduced by mild HT}}} - \big(\delta_{1,\mathrm{S}}^*(c_{\min}^*-c)H(c_{\min}^*-c) + \lambda_{\mathrm{S}}^* cR + \mu^* + \xi^*\big)T_{\mathrm{S}}$$

$$+ \nu^* cRT - \underbrace{\beta^*(t)T_{\mathrm{S}}}_{\substack{\text{high HT}\\ \text{damage}}}, \quad (4.2)$$

$$\frac{\mathrm{d}T_{\mathrm{R}}}{\mathrm{d}t} = \lambda^* cRT + (\xi^* + \lambda_{\mathrm{S}}^* cR)T_{\mathrm{S}} - \eta_{\mathrm{R}}^* T_{\mathrm{R}}, \quad (4.3)$$

$$\frac{\mathrm{d}T_{\mathrm{H}}}{\mathrm{d}t} = \beta^*(t)(T+T_{\mathrm{S}}) - \underbrace{\eta_{\mathrm{H}}^* T_{\mathrm{H}}}_{\text{clearance}}, \quad (4.4)$$

$$\frac{\mathrm{d}V}{\mathrm{d}t} = \underbrace{\kappa_0^* T_{\mathrm{H}}}_{\substack{\text{damage-induced}\\ \text{angiogenesis}}} - \underbrace{\beta^*(t)V}_{\substack{\text{high}\\ \text{HT damage}}}, \quad (4.5)$$

$$\frac{\mathrm{d}c}{\mathrm{d}t} = \underbrace{(1+\alpha_{\mathrm{V}}(t))g^*(c_{\max}^*-c)V}_{\substack{\text{nutrient delivery,}\\ \text{increased by mild HT}}} - \underbrace{(1-\alpha_{\mathrm{RO2}}(t))q_1^*(T+\theta_1 T_{\mathrm{S}})c}_{\substack{\text{baseline oxygen consumption,}\\ \text{reduced by mild HT}}} -$$

$$\underbrace{(1-\alpha_{\mathrm{RO2}}(t))q_3^*\,(T+\theta_2 T_{\mathrm{S}})\,c(S_{\max}-\Sigma)}_{\substack{\text{oxygen consumption for proliferation,}\\ \text{reduced by mild HT}}}, \quad (4.6)$$

subject to the following initial conditions:

$$\begin{aligned} &T(0)=T_0,\ V(0)=V_0, \text{ with } T_0+V_0\in[0,S_{\max}],\\ &T_{\mathrm{S}}(0)=0, \quad T_{\mathrm{R}}(0)=0, \quad T_{\mathrm{H}}(0)=0, \quad c(0)=c_0\in[0,c_{\max}^*]. \end{aligned} \quad (4.7)$$

The initial condition for c in (4.7) is defined as that in the absence of treatment in (2.4), and the initial conditions for T_{S}, T_{R} and T_{H} in (4.7) follow from the absence of damaged material prior to the first RT and HT fractions. Further, physically realistic solutions for T and V satisfy $0 \le T(t)+T_{\mathrm{S}}(t)+T_{\mathrm{R}}(t)+T_{\mathrm{H}}(t)+V(t) \le S_{\max}$ for all $t \ge 0$. Since we also assume that $V_0 > 0$ (recall Chapter 2), the initial conditions for T and V in (4.7) follow.

Accounting for high HT. We assume that exposure to high HT irreversibly damages viable tumour cells, T and T_{S}, at a constant rate $\widetilde{\beta} > 0$ over the heating period $t_{\mathrm{H}} \le t \le t_{\mathrm{H}} + \delta_{\mathrm{H}}$ (min) so that

$$\beta^*(t) = \begin{cases} \widetilde{\beta}, & \text{if } t_{\mathrm{H}} \le t \le t_{\mathrm{H}}+\delta_{\mathrm{H}},\\ 0, & \text{otherwise.} \end{cases} \quad (4.8)$$

Since we suppose that heat-damage is irreparable, we let damaged cells, T_{H}, degrade at a constant rate $\eta_{\mathrm{H}}^* > 0$ in Equation (4.4). Endothelial cells also experience irreversible heat damage at the time-dependent rate $\beta^*(t)$, given by (4.8), but, unlike damaged cells, dead vascular material is immediately cleared from the system. This assumption stems

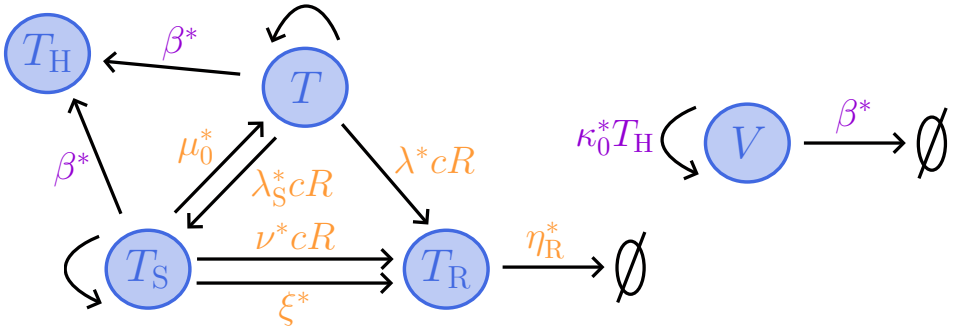


Figure 4.1: Schematic showing the interactions between T, T_S, T_R and T_H cells, the vasculature V and the oxygen concentration c in response to high HT and RT in the model (4.1)–(4.6). The rates in orange and purple represent the effects of RT and high HT, respectively.

from the fact that vascular stasis and necrosis in response to heating occur more rapidly than heat-induced cell death [227]. We further assume that heat-damaged cells, T_H, release angiogenic factors which promote vascular growth at a rate which is proportional to T_H, with proportionality constant $\kappa_0^* > 0$.

Lastly, we account for the inhibition of DNA repair under high HT by modifying the repair rate following exposure to RT alone so that it also depends on the exposure to high HT. Following [219] (see Section 1.6.3 for full details), we define the time evolution of the amount of inactive repair proteins relative to the total amount of repair proteins following exposure to a single dose of high HT as

$$\Lambda(t) = \begin{cases} 0, & \text{if } 0 \leq t < t_H, \\ \frac{k_1}{k_1+k_2}\left(1 - e^{-(k_1+k_2)(t-t_H)}\right), & \text{if } t_H \leq t < t_H + \delta_H, \\ \frac{k_1}{k_1+k_2}\left(1 - e^{-(k_1+k_2)\delta_H}\right) e^{-k_2(t-(t_H+\delta_H))}, & \text{if } t \geq t_H + \delta_H, \end{cases} \tag{4.9}$$

where $k_1 > 0$ and $k_2 > 0$ are the constant rates of inactivation and reactivation of repair proteins, respectively. Then, the time-dependent repair rate $\mu^*(t)$ can be defined as

$$\mu^*(t) = \mu_0 \exp\left(-\mu_\Lambda \Lambda(t)\right), \tag{4.10}$$

where $\mu_\Lambda > 0$ represents the extent of DNA repair inhibition by HT (see Figure 4.2a).

Accounting for mild HT. We assume that mild HT increases tumour oxygenation by increasing blood flow via vasodilation and by reducing oxygen consumption rates as tumour cells switch from an oxidative to glycolytic phenotype. We suppose that both processes begin when tumour heating starts, and continue until the target intratumoural temperature is reached. The increased vasodilation and reduced oxygen consumption rates are then considered, respectively, maximal and minimal (given this treatment), and assumed to remain at these levels until heating stops and the effects of mild HT reverse.

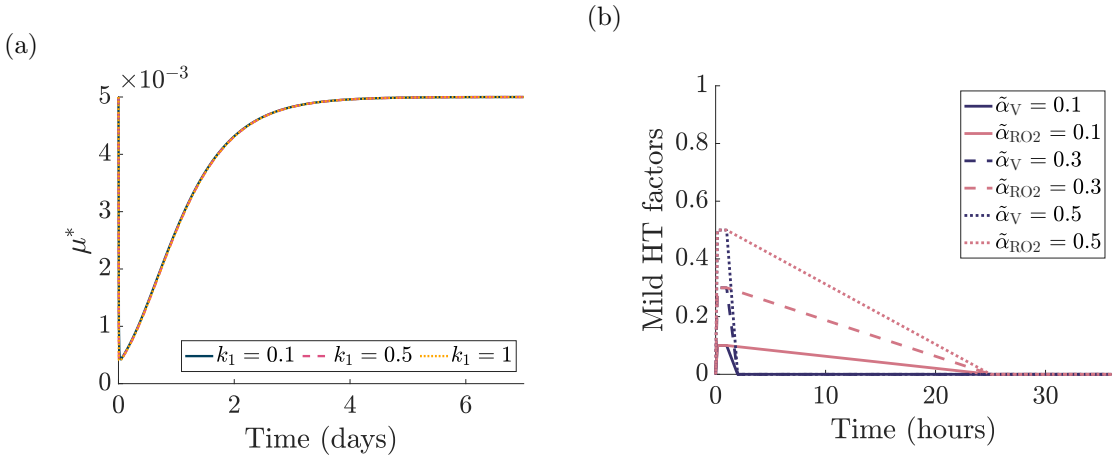


Figure 4.2: (a) Given a high HT treatment of duration $\delta_{\mathrm{H}} = 60\,\mathrm{min}$ starting at time $t_{\mathrm{H}} = 0$, we plot $\mu^*(t)$ for $t \in [0, 7]$ days. The parameters k_2 and μ_Λ are fixed to the values stated in Table 4.1 and we vary $k_1 = 100\widetilde{\beta}$ for $\widetilde{\beta} \in \{0.001, 0.005, 0.01\}$. For these parameter values, there is no significant difference in the time evolution of μ^* for increasing $\widetilde{\beta}$; inhibition of DNA repair is treatment-independent. (b) Given a mild HT treatment of duration $\delta_{\mathrm{H}} = 60\,\mathrm{min}$ starting at time $t_{\mathrm{H}} = 0$, we plot $\alpha_{\mathrm{V}}(t)$ and $\alpha_{\mathrm{RO2}}(t)$ for $t \in [0, 36]$ hours. The parameters t_1, $t_{2,\mathrm{V}}$ and $t_{2,\mathrm{RO2}}$ are fixed at the values in Table 4.1 and we vary $\widetilde{\alpha}_{\mathrm{V}} = \widetilde{\alpha}_{\mathrm{RO2}} \in \{0.1, 0.3, 0.5\}$.

Accordingly, we incorporate vasodilation by multiplying the oxygen source term in Equation (4.6) by $1 + \alpha_{\mathrm{V}}(t)$, where $0 \leq \alpha_{\mathrm{V}}(t) \leq 1$ is a time-dependent piece-wise linear function of the form

$$\alpha_{\mathrm{V}}(t) = \begin{cases} \widetilde{\alpha}_{\mathrm{V}} \frac{t - t_{\mathrm{H}}}{t_1}, & \text{for } t_{\mathrm{H}} \leq t < t_{\mathrm{H}} + t_1, \\ \widetilde{\alpha}_{\mathrm{V}}, & \text{for } t_{\mathrm{H}} + t_1 \leq t < t_{\mathrm{H}} + \delta_{\mathrm{H}}, \\ \widetilde{\alpha}_{\mathrm{V}} \left(1 - \frac{t - t_{\mathrm{H}} - \delta_{\mathrm{H}}}{t_{2,\mathrm{V}}}\right), & \text{for } t_{\mathrm{H}} + \delta_{\mathrm{H}} \leq t \leq t_{\mathrm{H}} + \delta_{\mathrm{H}} + t_{2,\mathrm{V}}, \\ 0, & \text{otherwise}, \end{cases} \tag{4.11}$$

where $0 \leq \widetilde{\alpha}_{\mathrm{V}} \leq 1$ is the maximal vasodilation factor, δ_{H} is the heating duration, and t_1 and $t_{2,\mathrm{V}}$ are the time needed to achieve maximum vasodilation and the duration of vasodilation, respectively (see Figure 4.2b).

The reduction in oxygen consumption rates is modelled similarly (see Figure 4.2b). We multiply q_1^* and q_3^* in Equation (4.6) (and hence $q_2^* = k^* q_3^*$ in Equations (4.1) and (4.2)) by $1 - \alpha_{\mathrm{RO2}}(t)$, where $0 \leq \alpha_{\mathrm{RO2}}(t) < 1$ is defined by (4.11), with $\widetilde{\alpha}_{\mathrm{V}}$ replaced by $0 \leq \widetilde{\alpha}_{\mathrm{RO2}} < 1$, the proportion by which oxygen consumption rates are reduced, and $t_{2,\mathrm{V}}$ is replaced by $t_{2,\mathrm{RO2}}$, the duration of this reduction. We note that this implies that mild HT also reduces tumour cell proliferation in our model.

4.2.2 Non-dimensionlisation

We non-dimensionalise Equations (4.1)–(4.6) and the initial conditions (4.7) by introducing the following scalings:

$$\widehat{T} = \frac{T}{S_{\max}}, \quad \widehat{T}_{\mathrm{S}} = \frac{T_{\mathrm{S}}}{S_{\max}}, \quad \widehat{T}_{\mathrm{H}} = \frac{T_{\mathrm{H}}}{S_{\max}}, \quad \widehat{T}_{\mathrm{R}} = \frac{T_{\mathrm{R}}}{S_{\max}},$$
$$\widehat{V} = \frac{V}{S_{\max}}, \quad \widehat{S} = \frac{S}{S_{\max}}, \quad \widehat{c} = \frac{c}{c^*_{\max}}, \quad \widehat{R} = \frac{R}{R_{\max}}, \quad \widehat{t} = \frac{t}{\tau}.$$

As in Chapter 3, the timescale of interest is fixed to be $\tau = 1\,\mathrm{min}$, which is the timescale for the duration of RT and HT, and the maximum dose rate $R_{\max} = 1\,\mathrm{Gy/min}$ [128]. Recall that $\Sigma = T + T_{\mathrm{S}} + T_{\mathrm{R}} + T_{\mathrm{H}} + V$ and $q_2 = kq_3$ for $k > 0$. Then, dropping hats for notational convenience, we obtain the following dimensionless system:

$$\frac{\mathrm{d}T}{\mathrm{d}t} = (1 - \alpha_{\mathrm{RO2}}(t))q_2 cT(1-\Sigma) - \big(\delta_1(c_{\min} - c)H(c_{\min} - c) + \beta(t) + \lambda cR + \nu cR\big)T + \mu(t)T_{\mathrm{S}}, \quad (4.12)$$

$$\frac{\mathrm{d}T_{\mathrm{S}}}{\mathrm{d}t} = (1 - \alpha_{\mathrm{RO2}}(t))\theta_2 q_2 cT_{\mathrm{S}}(1-\Sigma) - \big(\delta_{1,\mathrm{S}}(c_{\min} - c)H(c_{\min} - c) + \beta(t) + \lambda_{\mathrm{S}} cR + \mu(t) + \xi\big)T_{\mathrm{S}} + \nu RcT, \quad (4.13)$$

$$\frac{\mathrm{d}T_{\mathrm{H}}}{\mathrm{d}t} = \beta(t)(T + T_{\mathrm{S}}) - \eta_{\mathrm{H}} T_{\mathrm{H}}, \quad (4.14)$$

$$\frac{\mathrm{d}T_{\mathrm{R}}}{\mathrm{d}t} = \lambda cRT + (\xi + \lambda_{\mathrm{S}} cR)T_{\mathrm{S}} - \eta_{\mathrm{R}} T_{\mathrm{R}}, \quad (4.15)$$

$$\frac{\mathrm{d}V}{\mathrm{d}t} = \kappa_0 T_{\mathrm{H}} - \beta(t)V, \quad (4.16)$$

$$\frac{\mathrm{d}c}{\mathrm{d}t} = (1 + \alpha_{\mathrm{V}}(t))g(1-c)V - (1 - \alpha_{\mathrm{RO2}}(t))\left(q_1(T + \theta_1 T_{\mathrm{S}})c + q_3\left(T + \theta_2 T_{\mathrm{S}}\right)c(1-\Sigma)\right), \quad (4.17)$$

subject to initial conditions

$$\begin{aligned} &T(0) = T_0,\ V(0) = V_0,\ \text{with} T_0 + V_0 \in [0,1], \\ &T_{\mathrm{S}}(0) = 0, \quad T_{\mathrm{R}}(0) = 0, \quad T_{\mathrm{H}}(0) = 0, \quad c(0) = c_0 \in [0,1], \end{aligned} \quad (4.18)$$

where

$$\begin{aligned} &q_1 = q_1^* S_{\max}\tau,\ q_3 = q_3^* S_{\max}^2\tau,\ q_2 = q_2^* S_{\max}^2 c^*_{\max}\tau,\ k = \frac{S_{\max}}{c^*_{\max}}k^*, \\ &c_{\min} = \frac{c^*_{\min}}{c^*_{\max}},\ \delta_1 = \delta_1^* c^*_{\max}\tau,\ \delta_{1,\mathrm{S}} = \delta^*_{1,\mathrm{S}} c^*_{\max}\tau,\ g = g^* S_{\max}\tau, \\ &\lambda = \lambda^* c^*_{\max} R_{\max}\tau,\ \lambda_{\mathrm{S}} = \lambda^*_{\mathrm{S}} c^*_{\max} R_{\max}\tau,\ \nu = \nu^* c^*_{\max} R_{\max}\tau, \\ &\beta(t) = \beta^*(t)\tau,\ \kappa_0 = \kappa_0^*\tau,\ \mu(t) = \mu^*(t)\tau,\ \xi = \xi^*\tau,\ \eta_{\mathrm{H}} = \eta^*_{\mathrm{H}}\tau,\ \eta_{\mathrm{R}} = \eta^*_{\mathrm{R}}\tau. \end{aligned} \quad (4.19)$$

4.2.3 Defining the dimensionless parameters

In this chapter, we investigate how nutrient and space limited mechanisms of growth control impact qualitative tumour responses to mild and high HT. We set $R \equiv 0$ to indicate the absence of RT and fix parameters related to tumour growth at the values stated in Table 2.1 in Chapter 2. We fix parameters related to tumour responses to HT at the values and ranges stated in Table 4.1.

For high HT, the values of κ_0, η_{H}, μ_Λ, k_1 and k_2 are based on values found in the literature [114, 262], while we determine a physically realistic range for $\widetilde{\beta}$ from preliminary numerical simulations (see Appendix A.3). For mild HT, none of the parameter values are readily available in the literature. Therefore, as for $\widetilde{\beta}$, we determine ranges for $\widetilde{\alpha}_{\mathrm{V}}$ and $\widetilde{\alpha}_{\mathrm{RO2}}$ from additional preliminary numerical simulations (see Appendix A.3). The values of t_1, $t_{2,\mathrm{V}}$ and $t_{2,\mathrm{RO2}}$ may depend on tumour type, vascular integrity and the method of HT application. However, for simplicity, we set $t_1 = 10\,\mathrm{min}$, as this value was used in [19] for the time required to reach the target temperature in a human brain tumour (in their model, this time was assumed to be approximately the same as the time to maximal vasodilation). We also fix $t_{2,\mathrm{V}} = 60\,\mathrm{min}$ and $t_{2,\mathrm{RO2}} = 1440\,\mathrm{min}$ since experimental evidence suggests that re-oxygenation following mild HT can last $12 - 48\,\mathrm{h}$ [113, 221, 228], whereas vasodilation typically lasts less than an hour [19, 108]. We note that these values may overestimate $t_{2,\mathrm{V}}$ and $t_{2,\mathrm{RO2}}$ for tumours exposed to mild HT.

HT	Parameters	Definition	Value(s)
High	$\widetilde{\beta}$	Rate of HT-induced damage	$[10^{-3}, 10^{-2}]$
	κ_0	Rate of damage-induced angiogenesis	$[10^{-8}, 10^{-6}]$
	η_{H}	Clearance rate of cells killed by HT	5×10^{-5}
	μ_Λ	HT weighing factor	2.5
	k_1	Repair protein inactivation rate	$100\widetilde{\beta}$
	k_2	Repair protein reactivation rate	0.001
Mild	$\widetilde{\alpha}_{\mathrm{V}}$, $\widetilde{\alpha}_{\mathrm{RO2}}$	Mild HT factors	$[0.1, 0.5]$
	t_1	Time needed to reach maximal vasodilation	10
	$t_{2,\mathrm{V}}$	Duration of the vasodilation effect	60
	$t_{2,\mathrm{RO2}}$	Duration of the reduction in O_2 consumption	1440

Table 4.1: List of dimensionless HT response parameters and values assigned to them for the purpose of the model analysis and numerical simulations.

4.3 Numerical methods and set up

Following our study of tumour response to RT in Chapter 3, we aim here to investigate the response of tumours to mild and high HT in the NL, SL and BS regimes. For consistency with Chapter 3, we consider the HT response of the same three virtual tumour populations.

As discussed in Section 1.3.3.2, HT dosing regimens vary considerably across clinical trials [43, 101]. In general, HT is administered once or twice a week when it is combined with RT throughout the treatment schedule. The heating duration and temperature are typically in the range $30 - 90\,\text{min}$ and $39 - 50\,^{\circ}\text{C}$, respectively [187]. In light of these considerations, we define the HT treatments as follows. We set the duration of mild and high HT to be $\delta_{\text{H}} = 60\,\text{min}$ and assume a single, weekly dose of HT is administered at the same time on Mondays for 8 weeks (recall that we defined a conventional RT schedule as 2×5 Gy for 8 weeks). For mild HT, we fix $\widetilde{\beta} = 0$ and account for increasing thermal doses by varying $\widetilde{\alpha}_{\text{V}} \in \{0.1, 0.3, 0.5\}$ and $\widetilde{\alpha}_{\text{RO2}} \in \{0.1, 0.3, 0.5\}$. For high HT, we fix $\widetilde{\alpha}_{\text{V}} = \widetilde{\alpha}_{\text{RO2}} = 0$ and vary $\widetilde{\beta} \in \{0.001, 0.003, 0.005, 0.007, 0.009, 0.01\}$.

For each virtual cohort and each treatment protocol, we solve Equations (4.12)–(4.17) numerically for $t \in (0, t^*]$, $t^* > 0$, using ODE45, a single step MATLAB built-in solver for non-stiff ODEs that is based on an explicit Runge-Kutta (4,5) formula, the Dormand-Prince pair [59]. For consistency with Chapter 3, we set $t^* = t_{\text{end}} + 10^6$, where t_{end} is the time at which the HT schedule ends, and we impose the initial conditions

$$\big(T(0), T_{\text{S}}(0), T_{\text{R}}(0), T_{\text{H}}(0), V(0), c(0)\big) = \big(T^*, 0, 0, 0, V_0, c^*\big), \tag{4.20}$$

where T^* and c^* are, respectively, the steady state tumour volume and oxygen concentration in the absence of treatment (see Chapter 2 and Figure 3.2). All remaining parameters are fixed at the values stated in Table 4.1, except κ_0, which takes values $\kappa_0 \in \{10^{-8}, 5\times10^{-8}, 10^{-7}, 5\times10^{-7}, 10^{-6}\}$.

For each simulation, we record $\bar{T}$, $\bar{T}_{\text{S}}$, $\bar{T}_{\text{R}}$, $\bar{T}_{\text{H}}$, $\bar{V}$ and $\bar{c}$, the mean values of each dependent variable over the last week of treatment. We also define the percent change in (mean) viable tumour cell, total cell and vascular volumes and (mean) oxygen concentration between the start and the end of treatment as follows:

$$\begin{aligned} \Delta^{\text{H}}_{\text{viable}} &= 100 \times \frac{\bar{T} - T_0}{T_0}, \quad \Delta^{\text{H}}_{\text{total}} = 100 \times \frac{\bar{\Sigma} - \Sigma_0}{\Sigma_0}, \\ \Delta^{\text{H}}_{\text{V}} &= 100 \times \frac{\bar{V} - V_0}{V_0}, \quad \Delta^{\text{H}}_{\text{c}} = 100 \times \frac{\bar{c} - c_0}{c_0}, \end{aligned} \tag{4.21}$$

where $\Sigma_0 = T_0 + V_0$ and $\bar{\Sigma} = \bar{T} + \bar{T}_{\text{S}} + \bar{T}_{\text{R}} + \bar{T}_{\text{H}} + \bar{V}$. We note that $\Delta^{\text{H}}_{\text{viable}}$ and $\Delta^{\text{H}}_{\text{total}}$, defined by Equations (4.21), are equivalent to $\Delta^{\text{R}}_{\text{viable}}$ and $\Delta^{\text{R}}_{\text{total}}$ defined by Equations (3.15) in Chapter 3 for RT treatments. Unless otherwise stated, for brevity, we henceforth refer to the relative changes (increases and decreases) in tumour cell and vascular volumes and

oxygen levels, as defined in (4.21), as changes (increases and decreases) in tumour cell and vascular volumes and oxygen levels.

4.4 Investigating tumour responses to mild HT

We begin by assessing tumour responses to mild HT. Figure 4.3 shows the short-term response of three tumours in NL, BS and SL regimes to mild HT ($\widetilde{\alpha}_{\mathrm{V}} = \widetilde{\alpha}_{\mathrm{RO2}} = 0.3$). When HT is applied, each tumour experiences a spike in oxygen levels, whose duration approximately coincides with the duration of the effects of mild HT. For the NL and BS tumours, the oxygen concentration drops transiently below baseline and then returns to baseline, whereas the SL tumour's oxygen levels return to baseline immediately. Correspondingly, the values of Δ_c^{H} for the NL and BS tumours are smaller than for the SL tumour (0.616% and 1.83%, respectively, vs. 3.15%). These differences can be explained by the increase in the rate at which NL and BS tumours consume oxygen for proliferation as they grow into free space in response to the spike in oxygen levels. By contrast, the rate at which the SL tumour consumes oxygen for proliferation remains zero as it lacks space for growth.

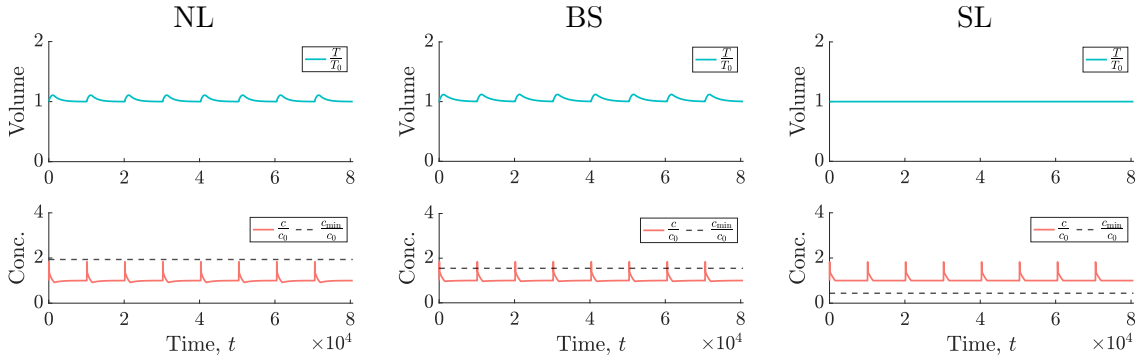


Figure 4.3: For mild HT ($\widetilde{\alpha}_{\mathrm{V}} = \widetilde{\alpha}_{\mathrm{RO2}} = 0.3$), we solve Equations (4.12)–(4.17) for $t \in (0, 8 \times 10^4]$ subject to initial conditions (4.20). We set $(q_1, q_3, V_0) = (1.59, 6.17, 5 \times 10^{-4})$ (NL), $(q_1, q_3, V_0) = (1.08, 6.19, 5 \times 10^{-3})$ (SL) and $(q_1, q_3, V_0) = (1.24, 6.29, 2.75 \times 10^{-3})$ (BS). Each tumour experiences a transient increase in oxygen levels, which is associated with a transient increase in tumour volume for the tumours in the NL and BS regimes.

Table 4.2 states the median and (min – max) values of $\Delta_{\mathrm{viable}}^{\mathrm{H}}$ and $\Delta_{\mathrm{c}}^{\mathrm{H}}$ for each virtual cohort. We see that tumours in monostable regimes (NL and SL) experience modest increases in oxygen levels, c. The NL tumours also undergo modest increases in viable tumour volume, T; this is not observed for SL tumours. Further, tumours in the BS regime experience increases in both c and T, as for the NL tumours. While the median values of $\Delta_{\mathrm{viable}}^{\mathrm{H}}$ and $\Delta_{\mathrm{c}}^{\mathrm{H}}$ for the BS cohort are consistent with those observed in the monostable cohorts, the maximum values indicate that certain tumours experience much larger increases in c and T. Figure 4.4 shows that these outliers correspond to tumours which grow towards, and reach, their larger SL steady state during treatment.

Regime	NL	SL	BS
$\Delta^{\mathrm{H}}_{\mathrm{viable}}(\%)$	2.71 (0.270 – 2.91)	0	4.16 (3.32 – 82.3)
$\Delta^{\mathrm{H}}_{\mathrm{c}}(\%)$	0.608 (0.479 – 2.96)	3.16 (1.13 – 3.20)	1.64 (1.03 – 3.34×10^3)

Table 4.2: Table summarising the median and (minimum – maximum) values of $\Delta^{\mathrm{H}}_{\mathrm{viable}}$ and $\Delta^{\mathrm{H}}_{\mathrm{c}}$ in the NL, SL and BS virtual populations. Increases in the viable volume and oxygen concentration are typically modest, except for certain tumours in the BS cohort, which experience significantly larger increases in T and c.

To understand long-term tumour responses to mild HT, we perform a steady state analysis of the system (4.12)–(4.17). In the absence of RT ($R \equiv 0$) and high HT ($\beta \equiv 0$), $T_{\mathrm{S}} \equiv T_{\mathrm{R}} \equiv T_{\mathrm{H}} \equiv 0$ and $V \equiv V_0$. Since we also have $\alpha_{\mathrm{V}} \equiv \alpha_{\mathrm{RO2}} \equiv 0$ after mild HT, it is straightforward to show that the steady state solutions of the system (4.12)–(4.17) are identical to those in the absence of treatment (see Chapter 2). In particular, given $T(0) = T^*$, tumours in monostable regimes when treatment starts will return to their original volume, $\Sigma_0 = T^* + V_0$. Tumours in the BS regime either return to their original NL steady state or switch to their SL steady state (see Figure 4.4a). Figure 4.4b shows that most tumours in the BS cohort remain NL following mild HT. Further, those tumours that switch to the SL steady state lie close to the boundary between BS and SL regimes ($V_{\mathrm{d}} \lesssim 1$), as for RT treatments.

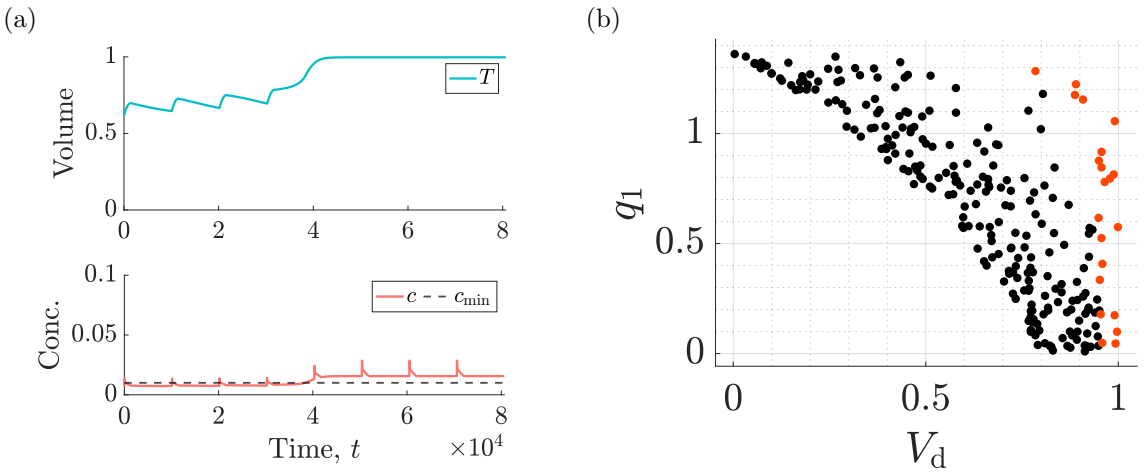


Figure 4.4: (a) For mild HT ($\widetilde{\alpha}_{\mathrm{V}} = \widetilde{\alpha}_{\mathrm{RO2}} = 0.3$), we solve Equations (4.12)–(4.17) for $t \in (0, 8\times10^4]$ subject to initial conditions (4.20). We set $(q_1, q_3, V_0) = (0.877, 5.72, 2.75\times10^{-3})$. The increases in T and c in response to mild HT enable the tumour to evolve to its SL steady state in the 4^{th} week of treatment. (b) For the virtual BS tumour population and mild HT ($\widetilde{\alpha}_{\mathrm{V}} = \widetilde{\alpha}_{\mathrm{RO2}} = 0.3$), the scatter plot shows the (q_1, V_{d}) pairs that correspond to tumours that switch (red) and do not switch (black) steady state. The former are characterised by larger values of V_{d}.

The qualitative response to mild HT ($\widetilde{\alpha}_{\mathrm{V}} = \widetilde{\alpha}_{\mathrm{RO2}} = 0.3$) does not change when $\widetilde{\alpha}_{\mathrm{V}}$ and $\widetilde{\alpha}_{\mathrm{RO2}}$ are varied (see Appendix B). We conclude that mild HT is unlikely to significantly

radiosensitise tumours in any growth regime as it typically induces only small increases in oxygen levels and any large increases are coupled with large increases in tumour volume. In particular, mild HT may worsen tumour responses to RT for tumours in NL and BS regimes by driving increases in tumour volume. We will confirm these hypotheses in Chapter 5 using our model of tumour growth and combined treatment response.

4.5 Investigating tumour responses to high HT

In this section, we investigate the response of the three virtual tumour populations to fractionated high HT. We fix the angiogenic rate $\kappa_0 = 10^{-7}$ and, for each regime, consider the short- and long-term tumour responses to conventional high HT ($\widetilde{\beta} = 0.005$). We determine the average response in each virtual cohort and focus on how the values of the oxygen consumption rates for maintenance and proliferation, q_1 and q_3, influence tumour sensitivity to high HT. We then investigate the impact of the high HT dose rate, $\widetilde{\beta}$, and the angiogenic rate, κ_0, on tumour responses.

4.5.1 Short-term tumour responses

Monostable regimes. Figure 4.5 shows typical responses of NL and SL tumours to high HT ($\widetilde{\beta} = 0.005$). The viable tumour cell volume and vascular volume of both tumours decrease during treatment, the changes being more pronounced for the NL tumour. Lower oxygen levels in the NL tumour mean that the proliferation rate is lower and the rate of hypoxic cell death is larger. Consequently, the net growth of the NL tumour between HT fractions is smaller and there is a larger reduction in the viable volume. With a smaller relative viable volume when HT is applied (from week 2 onwards), the NL tumour also accumulates a smaller proportion of dead material than the SL tumour. The damage-associated angiogenic response is, therefore, smaller in the NL than SL tumour, explaining the larger decrease in the vascular volume, V.

Figure 4.5 also shows that the oxygen concentration, c, remains approximately constant for the NL tumour and decreases such that $c < c_{\min}$ for the SL tumour. Since a decrease in V reduces the oxygen supply, while a decrease in T reduces the tumour's overall oxygen consumption rate, the balance between these processes will determine the oxygen concentration. T_0 and V_0 are substantially smaller for the NL tumour ($T_0 = 0.0477$, $V_0 = 0.0005$) than the SL tumour ($T_0 = 0.995$, $V_0 = 0.005$), which means the absolute changes in T and V are smaller. In particular, we note that the NL tumour remains in an NL regime, with $V \leq V_{\mathrm{N}}$ throughout treatment, whereas the SL tumour transitions from the SL to the NL regime, with $V \leq V_{\mathrm{N}}$ by the end of treatment. This leads to a reduction in oxygen supply which exceeds the reduction in oxygen consumption rates.

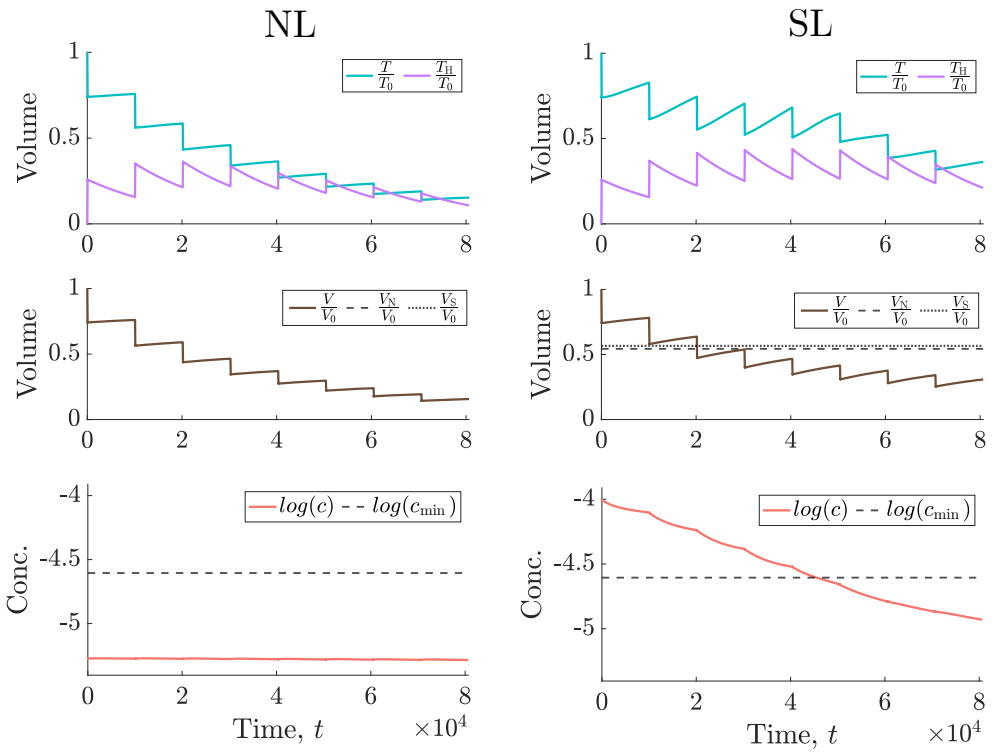


Figure 4.5: For high HT ($\widetilde{\beta} = 0.005$), we solve Equations (4.12)–(4.17) for $t \in (0, 8 \times 10^4]$ subject to initial conditions (4.20). We set $(V_0, q_1, q_3) = (0.0005, 2.18, 4.11)$ and $(V_0, q_1, q_3) = (0.005, 0.605, 3.85)$ for the NL and SL tumours, respectively. In both cases, the vascular, viable tumour cell and total tumour volumes decrease over time, with larger relative reductions for the NL tumour.

Figure 4.6 shows the distributions of $\Delta^{\mathrm{H}}_{\mathrm{viable}}$, $\Delta^{\mathrm{H}}_{\mathrm{total}}$ and $\Delta^{\mathrm{H}}_{\mathrm{V}}$ following conventional high HT, for the NL and SL tumour cohorts. The specific responses shown in Figure 4.5 are representative of the average responses of the NL and SL populations. In particular, while NL and SL tumours typically respond well to high HT, NL tumours respond better, with smaller average values of $\Delta^{\mathrm{H}}_{\mathrm{viable}}$, $\Delta^{\mathrm{H}}_{\mathrm{total}}$ and $\Delta^{\mathrm{H}}_{\mathrm{V}}$. Further, only a few outliers respond less well to high HT in the NL cohort, whereas the distribution for SL tumours is bimodal. This indicates that certain values of q_1 and q_3 within the NL and SL regimes affect tumour sensitivity to high HT.

In light of this, we now investigate the influence of the oxygen consumption rates for maintenance and proliferation, q_1 and q_3, on tumour responses to high HT in the NL and SL cohorts. The scatter plots in Figure 4.7 show that, in the NL tumour population, low values of q_1 and q_3 are associated with smaller reductions in viable cell and vascular volumes, while higher values of q_1 and/or q_3 are associated with larger reductions in viable cell and vascular volumes. The trends for the changes in total tumour volume are the same (result omitted for brevity). We investigate this further by considering the response to high HT of tumours defined by the parameter sets B_1, D_1, E_1 and F_1 (see Figure 4.7 and Table 4.3).

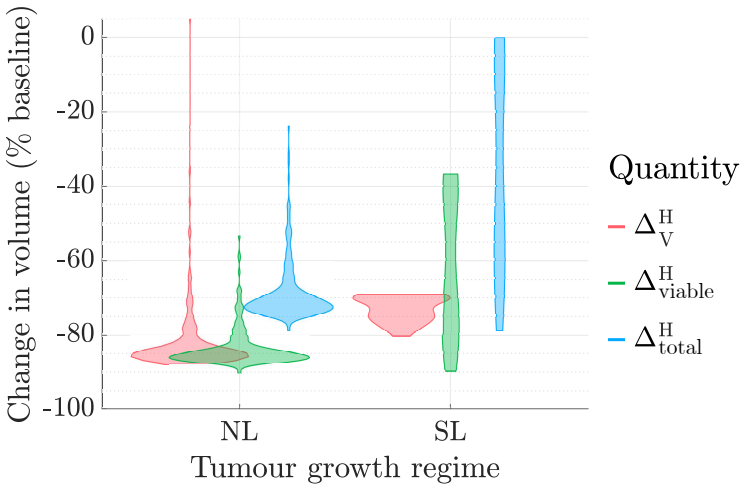


Figure 4.6: For virtual cohorts of NL and SL tumours, the violin plots show the distributions of $\Delta_{\mathrm{V}}^{\mathrm{H}}$, $\Delta_{\mathrm{viable}}^{\mathrm{H}}$ and $\Delta_{\mathrm{total}}^{\mathrm{H}}$. Most tumours in the NL and SL cohorts undergo large reductions in vascular, viable tumour cell and total tumour volumes, and these changes are typically larger for NL tumours. In the NL cohort, several outliers experience much smaller reductions in their vascular, viable tumour cell and total tumour volumes. By contrast, in the SL cohort, we distinguish two groups, which respectively experience smaller and larger reductions in these volumes.

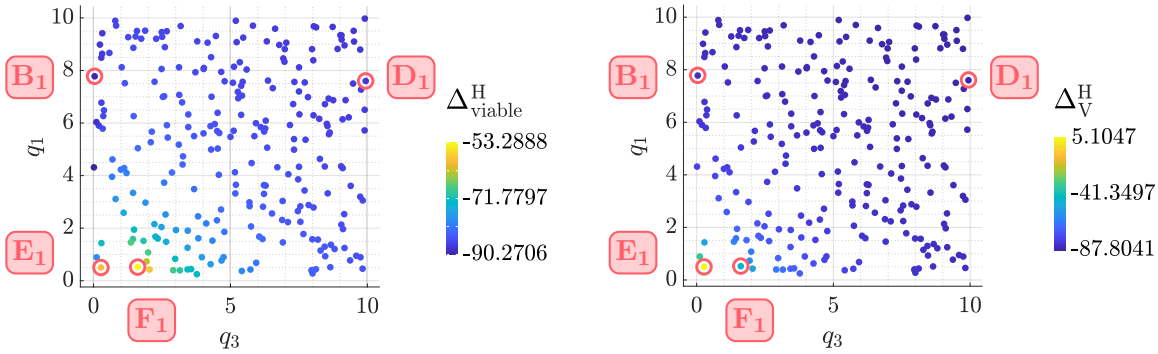


Figure 4.7: The scatter plots show the values of $\Delta_{\mathrm{viable}}^{\mathrm{H}}$ and $\Delta_{\mathrm{V}}^{\mathrm{H}}$ for each (q_1, q_3) pair used to generate the set of virtual NL tumours. $\Delta_{\mathrm{viable}}^{\mathrm{H}}$ and $\Delta_{\mathrm{V}}^{\mathrm{H}}$ decrease as q_1 and q_3 increase.

Figure 4.8 shows that the changes in T and T_{H} following the first few fractions of high HT are approximately the same for tumours B_1, D_1, E_1 and F_1, although E_1 experiences an increase in V while B_1, D_1 and F_1 experience reductions. This can be understood by noting that the initial volume of tumour E_1 is at least twice that of tumours B_1, D_1 and F_1. Consequently, its

Tumour	q_1	q_3
B_1	7.78	4.01×10^{-2}
D_1	7.60	9.94
E_1	5.03×10^{-1}	2.72×10^{-1}
F_1	5.24×10^{-1}	1.61

Table 4.3: Parameter sets B_1, D_1, E_1 and F_1 corresponding to the representative NL tumours. Note that B_1 and D_1 were previously defined in Chapter 3 via Table 3.3.

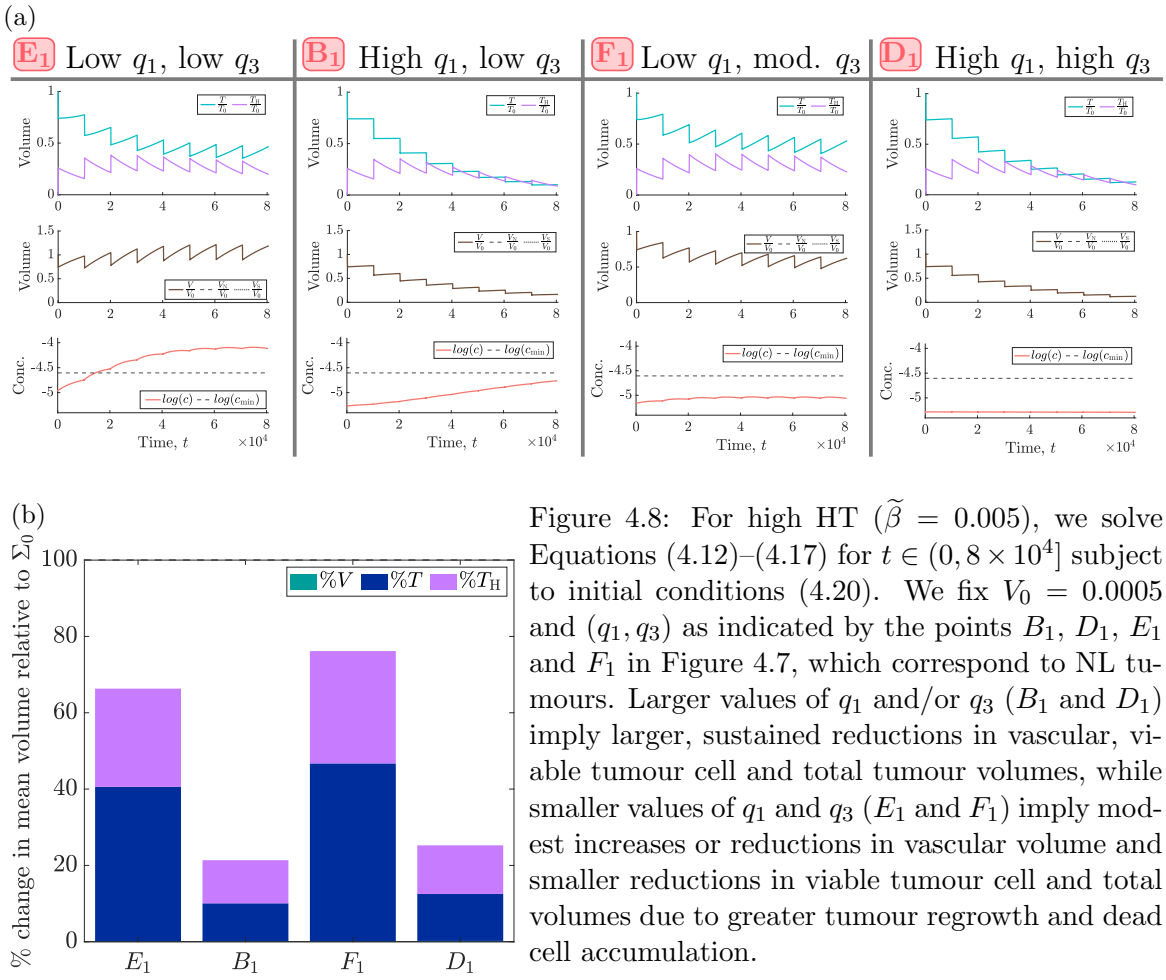


Figure 4.8: For high HT ($\widetilde{\beta} = 0.005$), we solve Equations (4.12)–(4.17) for $t \in (0, 8 \times 10^4]$ subject to initial conditions (4.20). We fix $V_0 = 0.0005$ and (q_1, q_3) as indicated by the points B_1, D_1, E_1 and F_1 in Figure 4.7, which correspond to NL tumours. Larger values of q_1 and/or q_3 (B_1 and D_1) imply larger, sustained reductions in vascular, viable tumour cell and total tumour volumes, while smaller values of q_1 and q_3 (E_1 and F_1) imply modest increases or reductions in vascular volume and smaller reductions in viable tumour cell and total volumes due to greater tumour regrowth and dead cell accumulation.

post-HT dead cell volume is larger and, hence, the extent of damage-associated vascular growth outweighs the vascular damage. As V increases, oxygen levels in tumour E_1 increase so that $c > c_{\min}$ by the end of the second week of treatment. Thereafter, there is no cell death due to hypoxia and, despite having low q_3, E_1 grows between HT fractions, maintaining a larger viable volume and accumulating more dead material than tumours B_1 and D_1. Tumour F_1 maintains a larger viable volume and accumulates more dead material than tumours E_1, B_1 and D_1, despite experiencing a reduction in V, as higher oxygen levels and a moderate value of q_3 enable greater tumour regrowth between fractions. By contrast, the net growth of the viable volume and the accumulation of dead material in tumours B_1 and D_1 are limited by reduced cell proliferation due to low q_3 (B_1) and/or low oxygen levels (B_1, D_1).

Overall, we have shown that high values of q_1 and/or q_3 characterise the best NL responders as they ensure limited tumour regrowth between HT fractions due to low oxygen levels, and low tumour cell proliferation rates when q_3 is low.

The scatter plots in Figure 4.10 show the values of $\Delta^{\mathrm{H}}_{\mathrm{viable}}$ and $\Delta^{\mathrm{H}}_{\mathrm{V}}$ for the (q_1, q_3) pairs

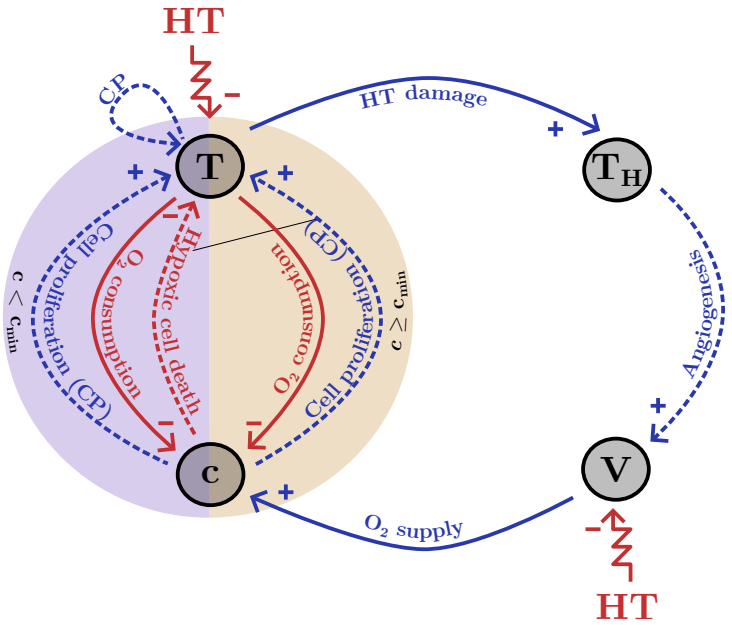


Figure 4.9: Schematic showing the causal relationships between undamaged and high HT-damaged tumour cells, the vasculature and the oyxgen concentration, T, T_{H}, V and c, respectively, according to the model (4.12)–(4.17). Positive causal links are in blue, while negative causal links are in red. Full curves represent direct links, while dashed curves represent indirect links.

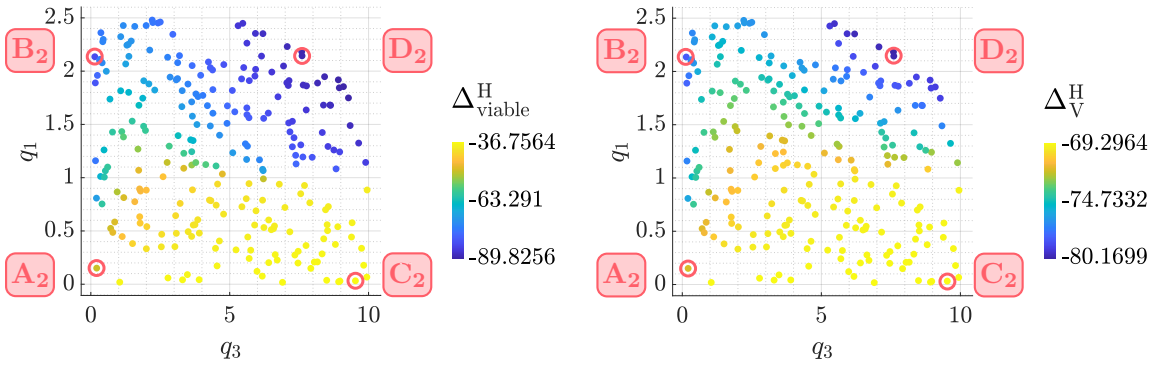


Figure 4.10: The scatter plots show the values of $\Delta^{\mathrm{H}}_{\mathrm{viable}}$ and $\Delta^{\mathrm{H}}_{\mathrm{V}}$ for each (q_1, q_3) pair used to generate the set of virtual SL tumours. Smaller values of $\Delta^{\mathrm{H}}_{\mathrm{viable}}$ and $\Delta^{\mathrm{H}}_{\mathrm{V}}$ are obtained for high values of q_1 combined with low or high values of q_3.

that define the SL virtual population. SL tumour responses are most sensitive to the value of the oxygen consumption rate for maintenance, q_1, with larger values associated with greater reductions in viable tumour cell and vascular volumes. When q_1 is large, these reductions are enhanced for small and large values of the oxygen consumption rate for proliferation, q_3. By contrast, when q_1 is small, only small values of q_3 enhance these reductions. As for NL tumours, we now consider the responses to high HT of four representative tumours defined by parameter sets $A_2 - D_2$ (see Figure 4.10 and Table 4.4).

Figure 4.11 reveals that low values of q_1 (A_2 and C_2) are associated with higher oxygen levels throughout treatment and, as a result, higher net growth rates, for all values of q_3. In particular, the smaller reductions in viable tumour cell volume for tumours A_2 and C_2, compared to tumours B_2 and D_2, can be explained by their larger regrowth between fractions. In turn, as depicted in the schematic in Figure 4.9, the greater viable tumour cell volume in tumours A_2 and C_2 explains the greater damaged cell accumulation and, thus, the smaller decrease in vascular volume.

As they are characterised by high values of q_1, tumours B_2 and D_2 have baseline oxygen levels that are close to the hypoxic threshold, $c_{\min}$. For tumour B_2, c increases gradually throughout treatment as the reduction in overall oxygen consumption rates exceeds the reduction in oxygen supply caused by a smaller vascular volume. Despite the increase in c, tumour regrowth between fractions is limited, allowing for a sustained reduction in viable volume, which we attribute to the low value of q_3. Like tumours A_2 and C_2, tumour D_2 regrows after the first HT fraction due to a high value of q_3. It experiences a substantial reduction in viable volume between the second and third fractions and, finally, a sustained decrease in viable volume. For tumour D_2, the decrease in V, coupled with high oxygen consumption rates, leads to a gradual decrease in c with $c < c_{\min}$ from the second HT fraction onwards. Consequently, nutrient insufficiency contributes to cell death and limits net tumour regrowth, as does low tumour cell proliferation when c is low. Together with HT-induced cell death, these processes underpin the large reduction in viable and total volumes observed for D_2.

Tumour	q_1	q_3
A_2	1.51×10^{-1}	2.10×10^{-1}
B_2	2.14	1.43×10^{-1}
C_2	3.21×10^{-2}	9.53
D_2	2.14	7.61

Table 4.4: Parameter sets A_2, B_2, C_2 and D_2 corresponding to the representative SL tumours.

We also note that tumours A_2 and C_2 have $V > V_{\mathrm{N}}$ throughout treatment, while tumours B_2 and D_2 have $V < V_{\mathrm{N}}$ from the first fraction onwards. In other words, A_2 and C_2 remain in the SL regime, while B_2 and D_2 enter the NL regime. We anticipate that the time evolution of the vascular volume post-treatment will determine the steady state volume attained by a tumour at long times: we return to this in Section 4.5.2.

Overall, we have shown that limited tumour cell proliferation between HT fractions and cell death due to hypoxia can contribute to the increased efficacy of HT for certain tumours in the SL cohort. Their relative contributions depend on the values of q_1 and q_3: when q_1 is large and q_3 is small, limited tumour cell proliferation between fractions (due to small q_3) ensures a sustained reduction in viable and total cell volumes and, when q_1 and q_3 are both large, hypoxic cell death and limited tumour cell proliferation between fractions (due

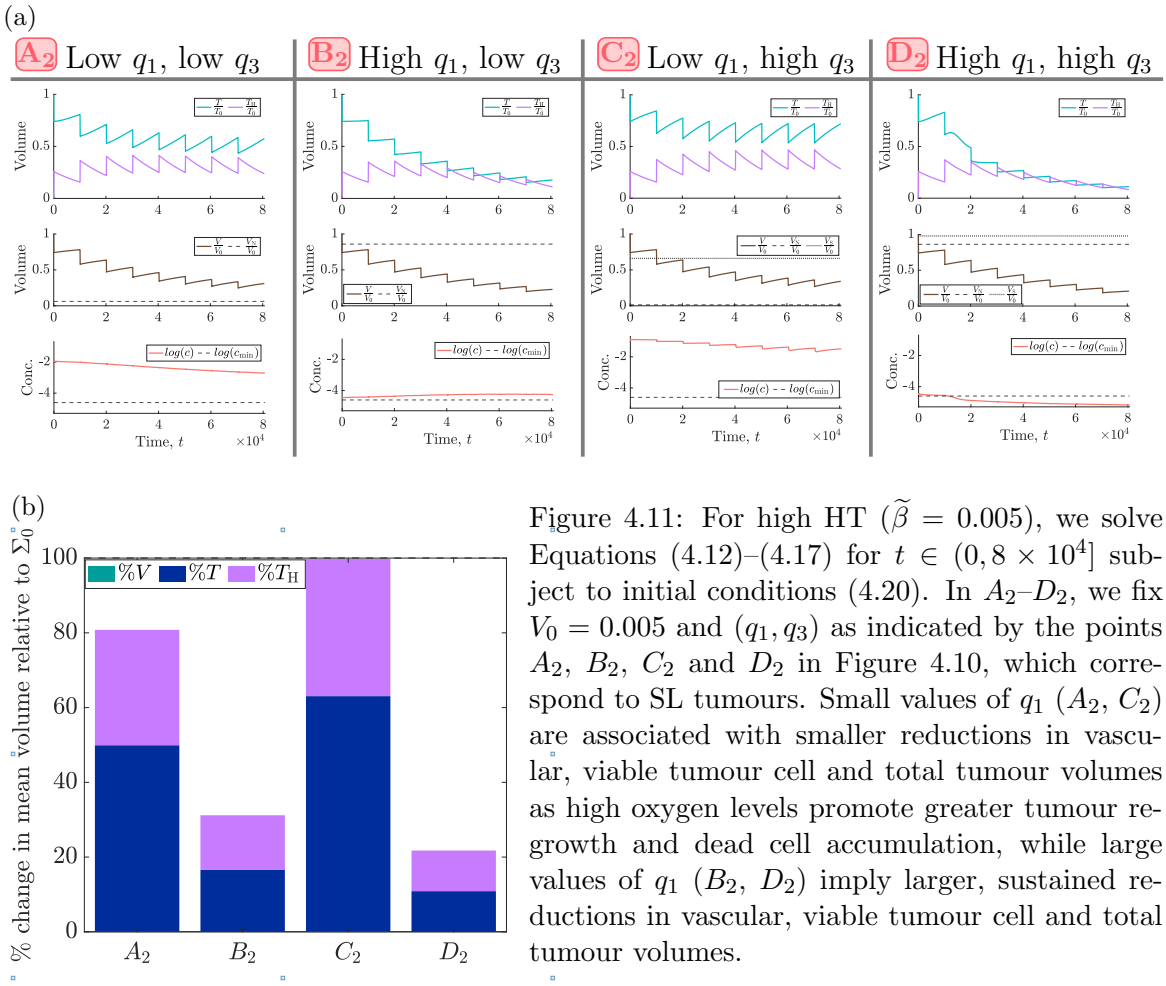


Figure 4.11: For high HT ($\widetilde{\beta} = 0.005$), we solve Equations (4.12)–(4.17) for $t \in (0, 8 \times 10^4]$ subject to initial conditions (4.20). In A_2–D_2, we fix $V_0 = 0.005$ and (q_1, q_3) as indicated by the points A_2, B_2, C_2 and D_2 in Figure 4.10, which correspond to SL tumours. Small values of q_1 (A_2, C_2) are associated with smaller reductions in vascular, viable tumour cell and total tumour volumes as high oxygen levels promote greater tumour regrowth and dead cell accumulation, while large values of q_1 (B_2, D_2) imply larger, sustained reductions in vascular, viable tumour cell and total tumour volumes.

to low oxygen levels and despite large q_3) ensure large reductions in viable and total cell volumes.

Bistable regimes. Figure 4.12a shows the response of a tumour in the BS regime to high HT. It undergoes large reductions in viable tumour cell and vascular volumes as HT-induced damage outweighs tumour and vascular regrowth between fractions. As for the response of the NL tumour shown in Figure 4.5, the sustained reduction in viable volume limits the accumulation of damaged material, which, in turn, limits the damage-induced angiogenic response (see the schematic in Figure 4.9). In contrast to the aforementioned NL tumour, the tumour in the BS regime has larger baseline oxygen levels. Further, since V decreases so that $V < V_{\mathrm{N}}$ after the final fraction, the tumour is driven into the NL regime at the end of treatment and it exhibits greater reductions in oxygen levels during high HT.

The results in Figure 4.12b indicate that all tumours in the BS cohort respond well to conventional high HT. There is little variability in $\Delta^{\mathrm{H}}_{\mathrm{viable}}$, $\Delta^{\mathrm{H}}_{\mathrm{total}}$ and $\Delta^{\mathrm{H}}_{\mathrm{V}}$ in the BS virtual cohort, implying that the behaviour shown in Figure 4.12a is representative of the entire

virtual population. Indeed, tumours in the BS regime respond significantly better to high HT than RT (compare Figure 3.11a and Figure 4.12b).

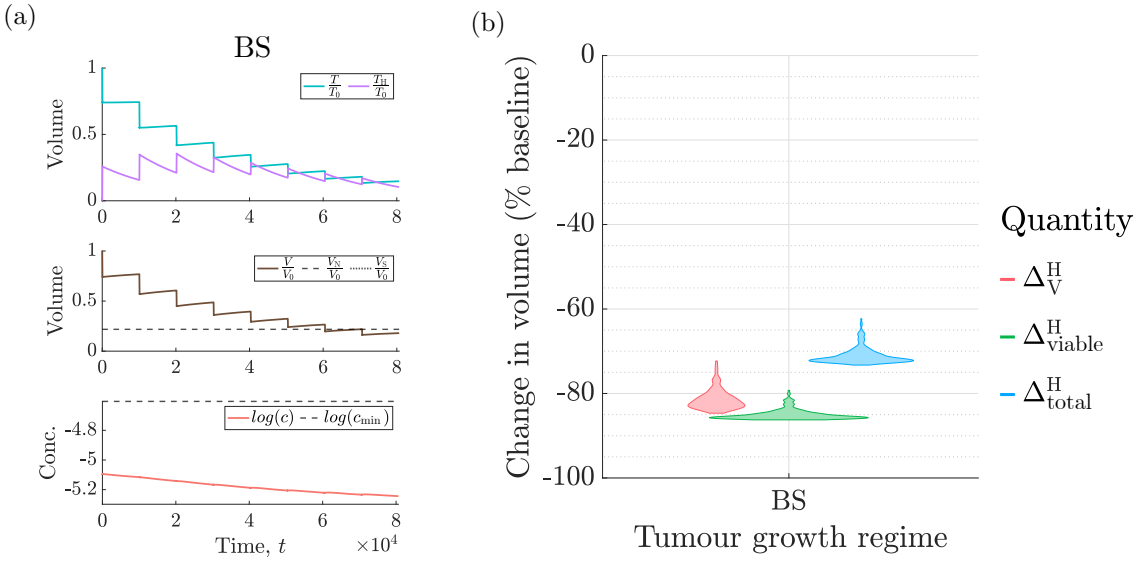


Figure 4.12: For high HT ($\widetilde{\beta} = 0.005$), we solve Equations (4.12)–(4.17) for $t \in (0, 8 \times 10^4]$ subject to initial conditions (4.20). We set $(V_0, q_1, q_3) = (0.00275, 0.297, 9.14)$ so that the tumour exhibits behaviour typical of the BS cohort. (b) Violin plots representing the distributions of Δ_V^H, Δ_{viable}^H and Δ_{total}^H for the BS virtual cohort. All tumours in the BS cohort respond well to high HT, with low variability across the cohort.

4.5.2 Post-HT tumour dynamics

In the previous section, we discussed the short-term response to high HT of tumours in monostable (NL and SL) and bistable regimes. We now investigate the long-term response to high HT by studying post-treatment tumour growth dynamics and, in particular, the tumour steady states attained following treatment.

Steady state analysis. We first perform a steady state analysis of the system (4.12)–(4.17) to understand the potential long-term effects of high HT. In the absence of RT and mild HT, we set $R \equiv 0$ and $\alpha_V \equiv \alpha_{RO2} \equiv 0$, and we have $T_S \equiv T_R \equiv 0$. Additionally, setting $\widetilde{\beta} = 0$ to indicate the completion of high HT, we seek steady state solutions of the following system:

$$\frac{dT}{dt} = q_2 cT(1 - \Sigma) - \delta_1(c_{\min} - c)H(c_{\min} - c)T, \tag{4.22}$$

$$\frac{dT_H}{dt} = -\eta_H T_H, \tag{4.23}$$

$$\frac{dV}{dt} = \kappa_0 T_H, \tag{4.24}$$

$$\frac{dc}{dt} = g(1 - c)V - q_1 Tc + q_3 Tc(1 - \Sigma). \tag{4.25}$$

Denoting the post-treatment steady state values by $T^{*,\text{post}}$, $T_{\text{H}}^{*,\text{post}}$, $V^{*,\text{post}}$ and $c^{*,\text{post}}$, we note that Equations (4.23)–(4.24) for T_{H} and V decouple. Further, integrating (4.23)–(4.24) for $t \geq t_{\text{end}}$, where t_{end} is the time at which HT ends, we have

$$T_{\text{H}}(t) = T_{\text{H}}(t_{\text{end}})e^{-\eta_{\text{H}}(t-t_{\text{end}})}, \tag{4.26}$$

$$V(t) = V(t_{\text{end}}) + \frac{\kappa_0}{\eta_{\text{H}}} T_{\text{H}}(t_{\text{end}}) \left(1 - e^{-\eta_{\text{H}}(t-t_{\text{end}})}\right). \tag{4.27}$$

In particular,

$$T_{\text{H}}(t) \to 0 \text{ as } t \to +\infty, \tag{4.28}$$

$$V(t) \to V(t_{\text{end}}) + \frac{\kappa_0}{\eta_{\text{H}}} T_{\text{H}}(t_{\text{end}}) \text{ as } t \to +\infty. \tag{4.29}$$

Equations (4.27) and (4.29) indicate that, following high HT, the vascular volume increases monotonically to a value which is proportional to the damaged cell volume at the end of treatment, the constant of proportionality being the ratio of the timescales for damaged cell degradation and angiogenesis. Therefore, if a tumour experiences an increases in vascular volume during HT, it will also attain a greater vascular volume post-treatment. By contrast, if a tumour experiences a decrease in vascular volume during HT, its post-treatment vascular volume may be smaller or larger than pre-treatment, depending on the timescales for damaged cell degradation and angiogenesis.

Now, since $T_{\text{H}}^{*,\text{post}} = 0$, it follows that $c^{*,\text{post}}$ and $T^{*,\text{post}}$ are solutions of the following system:

$$0 = q_2^* c^{*,\text{post}} T^{*,\text{post}}(1 - \Sigma^{*,\text{post}}) - \delta_1^*(c_{\min}^* - c^{*,\text{post}})H(c_{\min}^* - c^{*,\text{post}})T^{*,\text{post}}, \tag{4.30}$$

$$0 = g^*(1 - c^{*,\text{post}})V^{*,\text{post}} - q_1^* c^* T^{*,\text{post}} - q_3^* c^{*,\text{post}} T^{*,\text{post}}(1 - \Sigma^{*,\text{post}}), \tag{4.31}$$

where $\Sigma^{*,\text{post}} = T^{*,\text{post}} + V^{*,\text{post}}$. It is straightforward to show that the solutions of the system (4.30)–(4.31) are identical to the steady state solutions in the absence of treatment with $V^{*,\text{post}}$ substituted for V_0 (see Chapter 2).

The steady state analysis indicates that high HT preserves the steady states and growth regimes observed in the absence of treatment, while allowing tumours to move between regimes and evolve to new steady states depending on $V^{*,\text{post}}$. In what follows, we investigate how high HT affects the tumour steady states attained in each regime, in order to assess its efficacy.

Characterising post-HT steady states in each regime. In Chapter 2, we defined threshold vascular volumes, $V_{\text{N}}(q_1)$ and $V_{\text{S}}(q_1, q_3)$, below and above which only the NL and SL steady states exist, respectively. If the oxygen consumption rate for proliferation, q_3, is sufficiently large compared to the oxygen consumption rate for maintenance, q_1, then $V_{\text{N}} < V_{\text{S}}$ and there is a bistable regime in which the NL and SL steady states co-exist for

$V_N < V_0 < V_S$. Otherwise, $V_N = V_S$ and steady state solutions are unique. The preceding steady state analysis, therefore, implies that, following high HT, a tumour characterised by fixed (q_1, q_3) lies in the NL regime if $0 < V^{*,\text{post}} \leq V_N$, in the SL regime if $V^{*,\text{post}} \geq V_S$, and in the BS regime if $V_N < V^{*,\text{post}} < V_S$.

Pre-HT regime	Post-HT regime	$T^{*,\text{post}} < T^{*,pre}$?
NL	NL	Yes[1]
	BS	No
	SL	No
BS	NL	Yes
	BS	Yes[1,3]
	SL	No
SL	NL	Yes
	BS	Yes[3]
	SL	Yes[2]

[1] If $V^{*,\text{post}} < V_0$.
[2] If $V^{*,\text{post}} > V_0$.
[3] If the tumour evolves to its NL steady state.

Table 4.5: Table summarising the conditions under which the steady states of tumours in the NL, SL and BS cohorts following high HT are smaller than those attained in the absence of treatment.

Figure 2.4 in Chapter 2, showed further that, for fixed (q_1, q_3), the NL steady state tumour volume increases with V_0 and is always smaller than the SL steady state tumour volume, which decreases marginally with V_0. We can use these results to define conditions on $V^{*,\text{post}}$ for which the post-treatment steady state volume of a given tumour is smaller than its pre-treatment steady state volume. For instance, the steady state volumes of tumours in the NL cohort decrease following high HT if and only if they remain in the NL regime, with $V^{*,\text{post}} < V_0 < V_N$. Table 4.5 details the conditions on $V^{*,\text{post}}$ for each growth regime.

Remark 4.5.1. In section 4.5.1, we saw that, for specific tumours in the NL and SL virtual populations, a larger (smaller) reduction in vascular volume, V, coincides with a smaller (larger) accumulation of damaged material, T_H. It is possible to show numerically that this holds for tumours across the NL, SL and BS virtual cohorts (result omitted for brevity). Given Equation (4.27) for $V^{*,\text{post}}$, this implies that, for fixed η_H and κ_0, the greater the reduction in V during treatment, the smaller the steady state vascular volume post-treatment, $V^{*,\text{post}}$.

Figure 4.13 shows the post-treatment growth regimes of the NL, SL and BS virtual cohorts. All tumours in the NL virtual population remain NL, with only one tumour increasing in steady state volume. This corresponds to tumour E_1 (in Figure 4.8), which

exhibited an increase in V during treatment. In particular, all the tumours which exhibited a decrease in V during treatment have $V^{*,\text{post}} < V_0$.

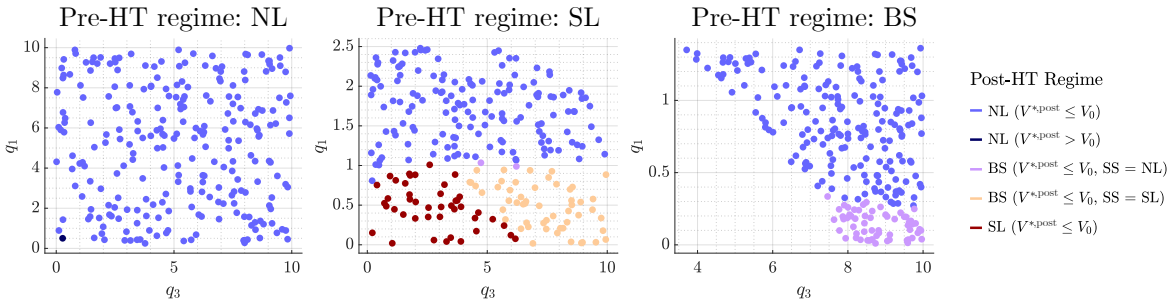


Figure 4.13: The scatter plots show the post-treatment growth regime for the virtual NL, SL and BS tumours. Most tumours in each virtual cohort attain smaller steady state volumes following high HT.

Approximately 60% of tumours originally in the SL cohort lie in the NL or BS regimes post-HT and undergo a reduction in steady state tumour volume as they attain NL steady states. These tumours, which are characterised by higher values of q_1 (e.g., tumours B_2 and D_2 in Figure 4.11), experienced larger than average reductions in V during treatment and, as such, had lower values of $V^{*,\text{post}}$. All other tumours in the SL cohort lie in SL or BS regimes post-HT, with $V^{*,\text{post}} \leq V_0$, and their steady state volume increases marginally as they attain an SL equilibrium. These tumours, which are characterised by lower values of q_1 (e.g., tumours A_2 and C_2 in Figure 4.11), experienced smaller than average reductions in V during treatment and, therefore, have higher values of $V^{*,\text{post}}$. We also see that tumours that enter the BS regime have high values of q_3, while those that remain in the SL regime have low values of q_3. This is because $V_{\text{S}}(q_1, q_3)$, the threshold value of V that separates SL and BS regimes, increases with q_3 (recall Figure 2.3 in Chapter 2), i.e., a smaller reduction in vascular volume from V_0 to $V^{*,\text{post}}$ is required to enter the BS regime when q_3 is larger.

Lastly, all tumours that are initially in the BS regime decrease in steady state volume as they lie in NL or BS regimes, have $V^{*,\text{post}} \leq V_0$ and attain an NL steady state post-high HT. This is consistent with the observation that all tumours in the BS virtual cohort exhibited large decreases in V, with low inter-tumoural variability during HT. We note further that lower values of q_1 are associated with tumours that remain in the BS regime, while higher values of q_1 are associated with tumours that move into the NL regime. This is because $V_{\text{N}}(q_1)$, the threshold value of V that separates BS and NL regimes, increases with q_1 (recall Figure 2.3 in Chapter 2), i.e., a smaller reduction from V_0 to $V^{*,\text{post}}$ is required to enter the NL regime when q_1 is larger.

Figure 4.13 also indicates that most tumours in the SL virtual cohort which transition to the BS regime in response to high HT evolve to an SL steady state, whereas tumours in the BS virtual cohort which remain in the BS regime evolve to an NL steady state. Given

$T(0) = T^*$, tumours in the SL cohort can transition from the basin of attraction of the SL steady state to that of the NL steady state if they experience a sufficiently large reduction in viable volume. By contrast, given $T(0) = T^*$ (where T^* corresponds to their NL steady state), tumours in the BS cohort may transition from the basin of attraction of the NL steady state to that of the SL steady state if they experience a sufficiently large increase in viable volume. Recalling that high HT reduces the viable tumour volume for all tumours in the BS and SL virtual populations (Section 4.5.1), tumours which remain in the BS regime following high HT always evolve to their NL steady state. For tumours in the SL cohort, Figure 4.14 shows that a sufficiently large reduction in viable volume to switch steady state can be achieved if the tumour becomes hypoxic during treatment, hypoxic cell death is induced and cell proliferation is limited.

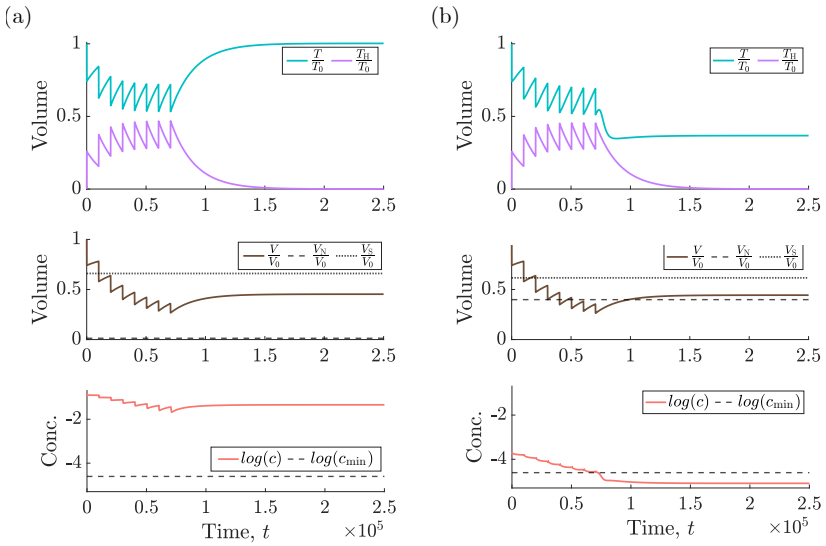


Figure 4.14: For high HT ($\widetilde{\beta} = 0.005$), we solve Equations (4.12)–(4.17) for $t \in (0, 8 \times 10^4]$ subject to initial conditions (4.20). We set (a) $(V_0, q_1, q_3) = (0.005, 0.0321, 9.53)$ and (b) $(V_0, q_1, q_3) = (0.005, 0.989, 6.21)$. Both SL tumours are in the BS regime following treatment. The tumour in (a) reaches its SL steady state, while the tumour in (b) reaches its NL steady state.

Taken together, these results suggest that tumours which respond well to high HT in the short-term (Section 4.5.1) will also respond well in the long-term (and conversely). We note that this finding follows from our choice to neglect, for simplicity, angiogenesis and vascular remodelling in the absence of treatment; we will return to this in the Discussion.

4.5.3 Sensitivity of tumour responses to the thermal dose

Short-term tumour responses. In Figure 4.15, we show how the value of $\widetilde{\beta}$, which is a proxy for thermal dose, influences tumour responses to high HT across the three virtual cohorts. Across the NL and BS cohorts, larger values of $\widetilde{\beta}$ lead to greater reductions in the

viable and total tumour cell volumes and the vascular volume. In particular, for the NL cohort, choosing $\widetilde{\beta}$ sufficiently large (i.e., $\widetilde{\beta} \geq 0.007$) ensures that the outliers, which exhibit increases in V at lower doses (recall tumour E_1 in Figure 4.8), have a positive response to treatment. For the SL cohort, increasing $\widetilde{\beta}$ markedly increases the treatment response, with most tumours experiencing responses similar to those of the NL and BS cohorts. We conclude that short-term tumour responses to high HT are enhanced for larger values of $\widetilde{\beta}$ in all regimes.

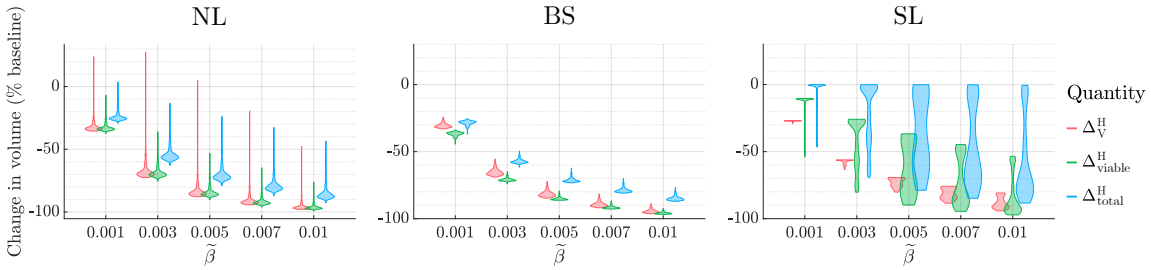


Figure 4.15: For the NL, BS and SL virtual tumour populations, we show how the distributions of $\Delta^{\mathrm{H}}_{\mathrm{V}}$, $\Delta^{\mathrm{H}}_{\mathrm{viable}}$ and $\Delta^{\mathrm{H}}_{\mathrm{total}}$ change as $\widetilde{\beta} \in \{0.001, 0.003, 0.005, 0.007, 0.01\}$ varies. The median values of $\Delta^{\mathrm{H}}_{\mathrm{V}}$, $\Delta^{\mathrm{H}}_{\mathrm{viable}}$ and $\Delta^{\mathrm{H}}_{\mathrm{total}}$ decrease as $\widetilde{\beta}$ increases.

Post-HT dynamics. Since increasing $\widetilde{\beta}$ enhances the efficacy of high HT and, in particular, leads to larger reductions in vascular volumes during treatment, we obtain greater reductions in steady state vascular volumes as $\widetilde{\beta}$ increases (by Remark 4.5.1). Figure 4.16 shows that, as a result, the number of tumours that attain a smaller post-treatment steady state tumour volume of NL type increases with $\widetilde{\beta}$. Further, since $V^{*,\mathrm{post}}$ decreases as $\widetilde{\beta}$ increases and the NL steady state tumour volume decreases with $V^{*,\mathrm{post}}$, the reductions in steady state volume increase with $\widetilde{\beta}$. This implies that long-term tumour responses to high HT are also improved by larger values of $\widetilde{\beta}$.

4.5.4 Sensitivity of tumour responses to the rate of angiogenesis

Short-term tumour responses. Figure 4.17 shows how the value of the rate of angiogenesis, κ_0, influences tumour responses to high HT when $\widetilde{\beta} = 0.005$ across the three virtual populations. Values of $\kappa_0 \leq 10^{-7}$ are associated with larger reductions in vascular volume during treatment. For the NL and BS virtual cohorts, this contributes to larger reductions in viable and total cell volumes as κ_0 decreases. In particular, for the NL cohort, a sufficiently small value of κ_0 (i.e., $\kappa_0 \leq 5 \times 10^{-8}$) results in all tumours having a positive response to treatment (similarly to sufficiently large $\widetilde{\beta}$). For the SL virtual cohort, as κ_0 decreases, there is a shift in the bimodal distributions of $\Delta^{\mathrm{H}}_{\mathrm{viable}}$ and $\Delta^{\mathrm{H}}_{\mathrm{total}}$ observed for $\kappa_0 = 10^{-7}$ towards unimodal distributions, whose median values lie close to those for the NL and BS cohorts (similarly to increasing $\widetilde{\beta}$).

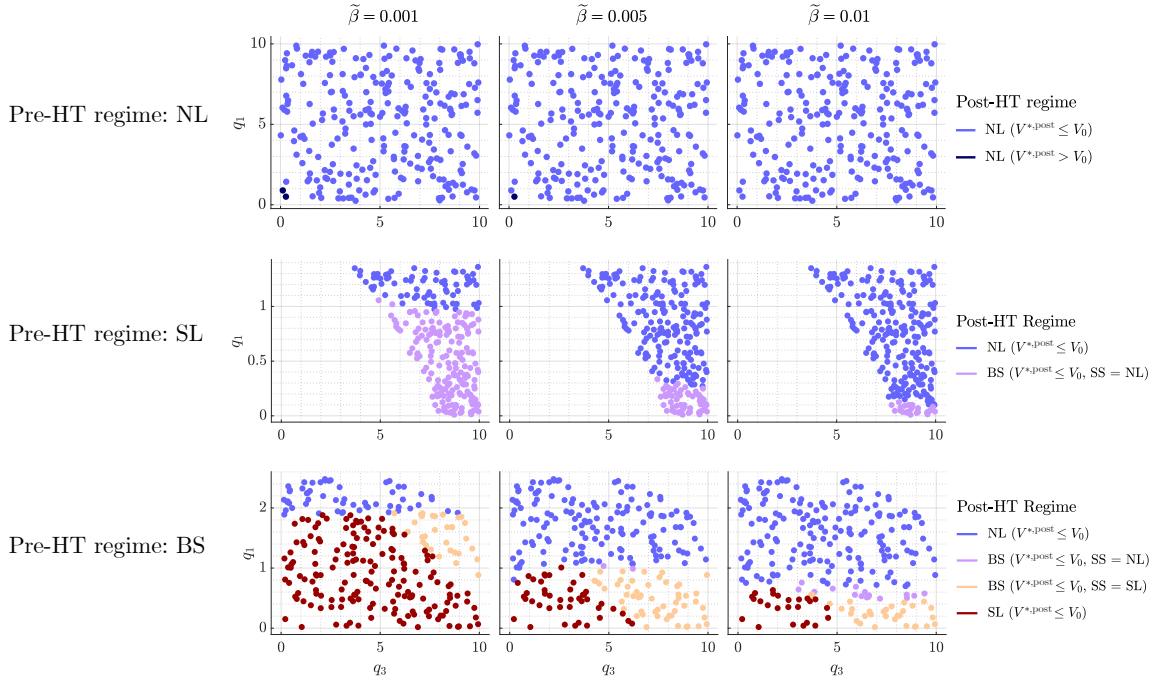


Figure 4.16: The scatter plots show how the post-treatment growth regimes for each (q_1, q_3) pair used to generate the set of virtual NL, SL and BS tumours, change as $\widetilde{\beta} \in \{0.001, 0.005, 0.01\}$ varies. The number of tumours which evolve to a smaller, NL steady state increases as $\widetilde{\beta}$ increases.

By contrast, values of $\kappa_0 > 10^{-7}$ are associated with smaller reductions, and increases, in vascular volume during treatment. In particular, for κ_0 sufficiently large, most tumours experience an increase in vascular volume during treatment, regardless of cohort. For the NL and BS virtual cohorts, sufficiently large increases in V lead to increases in the intratumoural oxygen levels so that $c > c_{\text{min}}$ (similarly to tumour E_1 in Figure 4.8). With no cell death due to hypoxia, the tumour regrows between high HT fractions. If this regrowth exceeds the high HT cell kill, then the tumours evolve to much larger volumes as they expand to fill the available free space. For the SL virtual population, viable and total volumes always decrease in response to high HT, since these tumours occupy all available space when treatment starts. However, the reductions in viable and total tumour burden are smaller for larger values of κ_0. This is because increases in V increase c so that $c \gg c_{\text{min}}$. Consequently, all SL tumours have greater net growth rates, regardless of the magnitude of q_3. This increases tumour regrowth between fractions and leads to greater accumulation of dead material.

Post-HT growth dynamics. As for higher values of $\widetilde{\beta}$, lower values of κ_0 are associated with larger reductions in vascular volume during treatment. Therefore, as κ_0 decreases, we observe an increase in both the number of tumours from each virtual cohort whose steady

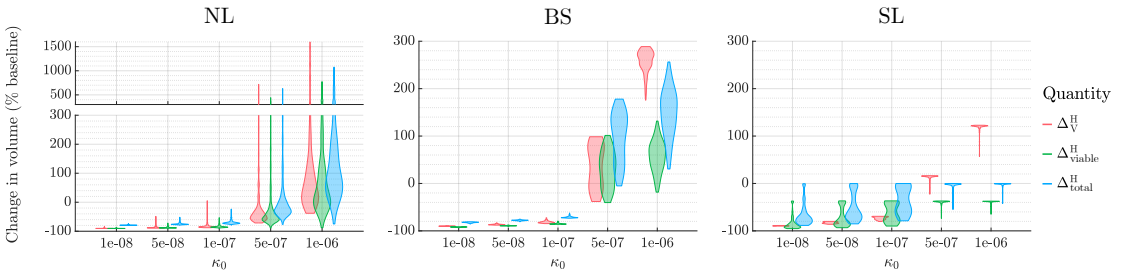


Figure 4.17: For the NL, BS and SL virtual tumour populations, we show how the distributions of $\Delta^{\mathrm{H}}_{\mathrm{V}}$, $\Delta^{\mathrm{H}}_{\mathrm{viable}}$ and $\Delta^{\mathrm{H}}_{\mathrm{total}}$ change as $\kappa_0 \in \{10^{-8}, 5\times10^{-8}, 10^{-7}, 5\times10^{-7}, 10^{-6}\}$ varies. The median values of $\Delta^{\mathrm{H}}_{\mathrm{V}}$, $\Delta^{\mathrm{H}}_{\mathrm{viable}}$ and $\Delta^{\mathrm{H}}_{\mathrm{total}}$ increase as κ_0 increases.

state tumour volume decreases because they attain a smaller, NL steady state (see Figure 4.18) and the reduction in steady state tumour volume.

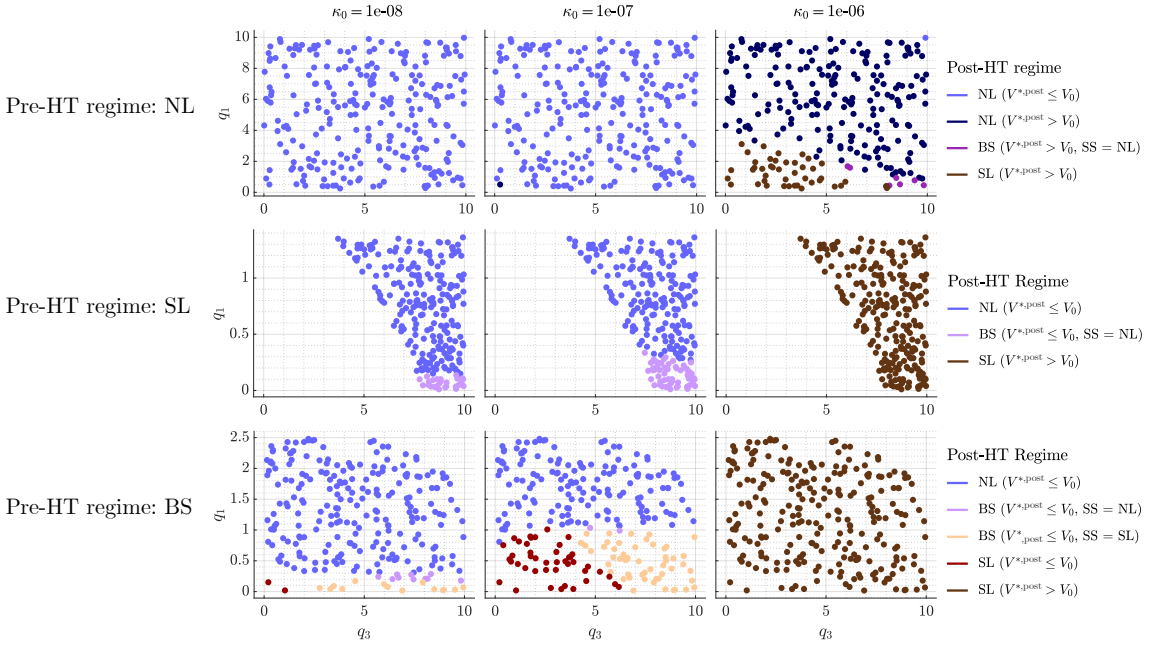


Figure 4.18: The scatter plots show how the post-treatment growth regimes for each (q_1, q_3) pair used to generate the virtual NL, SL and BS tumours, change as $\kappa_0 \in \{10^{-8}, 10^{-7}, 10^{-6}\}$ varies. The number of tumours which evolve to a smaller, NL steady state decreases as κ_0 increases. In particular, for $\kappa_0 = 10^{-6}$, the steady state volume of all but one tumour in the NL and BS cohorts increase.

By contrast, higher values of κ_0 are associated with smaller reductions, and increases, in vascular volume during treatment. Since any increase in V during treatment implies that $V^{*,\mathrm{post}} > V_0$, Figure 4.18 shows that the number of tumours in the NL and BS regimes (pre-HT) that decrease in steady state volume by attaining a smaller, NL steady state decreases as κ_0 increases. In particular, for $\kappa_0 = 10^{-6}$, the equilibrium volume of only one tumour in the NL cohort decreases following treatment as it remains in the NL regime, with $V^{*,\mathrm{post}} \leq V_0$. All tumours in the BS cohort attain a larger SL steady state as they enter the

SL regime post-high HT. Figure 4.18 also shows that for $\kappa_0 = 10^{-6}$, all tumours in the SL cohort achieve modest reductions in their steady state volumes, as they remain in the SL regime, with $V^{*,\text{post}} > V_0$. In this case, reductions in tumour steady state volumes occur when κ_0 is high, but these reductions are much smaller than for low κ_0.

Overall, these results indicate that high HT can be very effective for tumours in all regimes as long as their angiogenic response is sufficiently weak. If the angiogenic response is strong, then most tumours in the NL and BS cohorts respond poorly to treatment, while all tumours in the SL cohort have a reduced, but still positive, response.

4.6 Discussion

Building on the work discussed in Chapters 2 and 3, this chapter focussed on investigating tumour responses to hyperthermia. sWe incorporated HT into the model presented in Chapter 3 and distinguished between the effects of mild HT, which re-oxygenates the tumour via vasodilation and a reduction in the rates of oxygen consumption by tumour cells, and high HT, which causes cell and vascular damage, induces a damage-associated angiogenic response and inhibits DNA repair mechanisms. Using the NL, SL and BS virtual cohorts from Chapter 3, we studied the response of tumours in each regime to a range of fractionated mild and high HT protocols.

We found that the re-oxygenation effects of mild HT are typically negligible across the three virtual cohorts. For tumours in the NL and BS regimes, which have free space to grow into when treatment starts, increases in oxygen levels give rise to increases in tumour volume. In particular, the large increases in oxygenation observed for some tumours in the BS cohort are coupled with large increases in tumour volume; these tumours switch from the basin of attraction of their NL steady state to that of their SL steady state during mild HT and evolve to their SL steady state post-treatment. In this way, mild HT can be deleterious for tumours in the NL and BS regimes. These results suggest that mild HT is unlikely to significantly radiosensitise any tumours and may even worsen the RT response of tumours in the NL and BS regimes. We test these hypotheses in the following chapter.

In contrast to mild HT, high HT can be highly effective at reducing tumour burden, provided that the damage-induced angiogenic response is sufficiently weak. Indeed, most tumours in the three virtual cohorts respond well to high HT in the short-term as they experience reductions in viable and total tumour cell and vascular volumes. The largest reductions are typically observed in the NL and BS cohorts, while tumours in the SL cohort typically experience smaller reductions. The enhanced response of tumours in the NL and BS cohorts can be explained by their lower oxygen levels and smaller tumour cell and vascular volumes when treatment starts. Together, they imply smaller tumour cell and vascular regrowth between HT fractions and, thus, lead to a greater, sustained reduction

in overall tumour burden. We also noted that these short-term responses are enhanced by thermal dose, i.e., larger values of the high HT cell death rate, $\widetilde{\beta}$, lead to larger reductions in tumour burden during high HT.

As for our study of RT response, by identifying the parameter regions which give rise to the best and worst responders in the NL and SL virtual cohorts, we identified mechanisms that may explain successful high HT. For NL tumours, the combination of HT cell kill with limited tumour regrowth between fractions maximises HT efficacy, while, for SL tumours, HT efficacy is maximised by combinations of HT cell kill with limited tumour growth or hypoxia-induced cell kill. The additional SL-specific mechanism is due to the higher baseline oxygen levels for SL tumours, which experience a sharp increase in hypoxia-driven cell death if their oxygen levels drop below the hypoxic threshold, $c_{\min}$, during treatment. These findings illustrate the impact of different growth control mechanisms on tumour responses to high HT and, more generally, the importance of considering them when simulating tumour responses to treatment.

Our findings also indicate that long-term tumour responses are largely determined by short-term tumour responses across the three regimes, with the best responders in the short-term corresponding to the best responders in the long-term (and conversely). In particular, given a sufficiently weak angiogenic response, most tumours in the three cohorts experience reductions in steady state tumour volume post-high HT. In addition, the few tumours whose steady state tumour volume increases post-treatment correspond to tumours which experienced the smallest reductions in viable cell and vascular volumes within their cohort. A final implication is that the long-term reductions in tumour burden also increase with $\widetilde{\beta}$. We note that these results depend on our simplifying assumption that only high HT affects the vascular volume. By neglecting the co-evolution of the vasculature with tumour cells in the absence of treatment in response to angiogenesis and vascular remodelling, we do not fully capture all possible pre/post-treatment vascular changes, which could significantly alter our results. As such, the long-time model dynamics should be interpreted with caution.

Finally, when there is instead a strong, damage-induced, angiogenic response, most tumours in the NL and BS cohorts respond poorly to high HT, while all tumours in the SL cohort have a reduced, but still positive, response to treatment. The deleterious effect of high HT for tumours in the NL and BS regimes follows as their vascular volumes increase during HT. This increases oxygen levels and enables them to grow to much larger viable and total cell volumes during, and following, treatment, as they expand into the available free space. Tumours in the SL cohort occupy the entire space when treatment starts and, therefore, only experience reductions in viable and total tumour volumes. This is another example of how different growth arrest mechanisms influence tumour responses to HT.

In this chapter, we characterised tumour responses to mild and high HT across the NL, SL and BS growth regimes. In doing so, we established that mild HT is unlikely to radiosensitise any tumours, while high HT has the potential to act as a potent radiosensitiser across all three regimes. In the following chapter, we leverage our understanding of tumour responses to RT and HT from Chapters 3 and 4 to assess tumour responses to combinations of RT and HT. Our aim is to determine which treatment (RT, HT or RT + HT) and dosing regimen maximise the reduction in tumour burden across the three growth regimes.

Chapter 5

Investigating the influence of growth arrest mechanisms on tumour responses to combinations of radiotherapy and hyperthermia

5.1 Introduction

In Chapters 3 and 4, we investigated tumour responses to radiotherapy (RT) and hyperthermia (HT) in nutrient limited (NL), space limited (SL) and bistable (BS) regimes. For each cohort, we characterised typical tumour responses to these two treatments as well as tumour responses across the cohort. In doing so, we identified tumours which have strongly positive or negative responses to RT and HT and proposed biological processes that may underlie these extremal responses. In this chapter, we leverage our understanding of tumour responses to RT and HT alone to assess tumour responses to combinations of RT and HT.

While a number of clinical trials [43] have shown a significant improvement in tumour control and overall patient survival when RT and HT are combined, compared to RT alone, we still do not fully understand the biological mechanisms underpinning the success of combined treatment [15]. Key questions that we seek to elucidate in this chapter are the following:

- Does mild or high HT confer the greater improvement in RT response when RT and HT are combined?
- Can we characterise tumours which respond best to RT, HT and combined treatment? What does this tell us about the tumours that are most responsive to combined treatment?
- When combined treatment is best, which dosing regimen (i.e., RT fraction dose and frequency, HT fraction dose, order and delay between RT and HT) maximises its

efficacy?

Following the methodology outlined in Section 5.2, we use the model of tumour growth and response to RT and HT presented in Chapter 4 to compare tumour responses to fractionated RT, HT and their combination across the NL, SL and BS virtual tumour populations introduced in Chapter 3. Consistent with the results from Chapter 4, in Section 5.3, we show that mild HT does not significantly enhance any tumour responses to RT.

In Section 5.4, we focus on understanding short-term tumour responses to combinations of high HT and RT. We saw in Chapter 4 that short-term tumour responses to high HT determine the corresponding long-term tumour responses. In addition, we saw in Chapter 3 that RT only affects the long-term behaviour of tumours in the BS regime when they experience increases in viable volume during treatment. Since we find (see Section 5.4.3) that all BS tumours experience reductions in viable volume during combined treatment, RT does not affect their long-term behaviour. We conclude that the long-term response to combined treatment of all tumours is determined by high HT and is, in turn, governed by their short-term response. Combined with the fact that long-time model dynamics should be treated with caution (due to the omission of the effects of angiogenesis and RT on the vasculature), this explains why we only study short-term tumour responses to combinations of high HT and RT. For each virtual cohort (Sections 5.4.1–5.4.3), we characterise the interactions between conventional RT and high HT treatments, discuss how these interactions vary with the dosing regimen and, finally, determine the best treatment and dosing regimen pair for each tumour.

5.2 Methods

In this chapter, we aim to investigate whether combining HT and RT enhances tumour responses compared to HT and/or RT alone in the nutrient limited, space limited and bistable virtual cohorts introduced in Chapter 3. To do so, we compare tumour responses to a range of so-called equivalent RT, HT and RT + HT fractionation schedules, which we define below.

5.2.1 The treatment schedules under consideration

We define combination treatments that are consistent with the RT and HT treatments considered in Chapters 3 and 4. We assume that, for the duration of a combination treatment, a single, weekly dose of HT is administered at the same time on Mondays and $\delta_{\mathrm{H}} = 60\,\mathrm{min}$ is the duration of HT. The first weekly RT fraction is applied immediately after HT so that $t_{\mathrm{R}} = t_{\mathrm{H}} + \delta_{\mathrm{H}} + 1$, where t_{H} and t_{R} are the times at which the most recent HT and RT fractions, respectively, were administered. We coordinate RT and HT in this

way as mild HT effects are strongest when HT is applied immediately before RT and high HT effects are not significantly influenced by the order of, or the delay between, RT and HT (see Appendix C.2).

Treatment	$\widetilde{\alpha}_{\mathrm{V}} = \widetilde{\alpha}_{\mathrm{RO2}}(-)$	$\widetilde{\beta}(-)$	$D\,(\mathrm{Gy})$	$N_{\mathrm{frac}}(-)$
mild HT ± RT	$\{0.1, 0.3, 0.5\}$	0	$[\![0, 5]\!]$	$\{1, 3, 5\}$
high HT ± RT	0	$10^{-3} \times \{1, 3, 5, 7, 9, 10\}$	$[\![0, 5]\!]$	$\{1, 3, 5\}$

Table 5.1: Summary of parameters and values characterising the combinations of mild HT and RT and high HT and RT considered.

Subsequent RT fractions are applied at the same time of day as the HT treatment (i.e., treatment starts at the same time on each dosing day), at equally spaced time intervals during Monday to Friday. We distinguish between mild and high HT by letting $\widetilde{\alpha}_{\mathrm{V}}$, $\widetilde{\alpha}_{\mathrm{RO2}}$ and $\widetilde{\beta}$ take the values in Table 5.1 and we define the RT schedule by letting the dose amount, D, and the number of weekly RT fractions, N_{frac}, take the values in Table 5.1. Finally, the duration of each combination treatment, N_{wks} (weeks), is determined so that the total radiation dose administered is 80 Gy (or the closest multiple of D to 80 Gy).

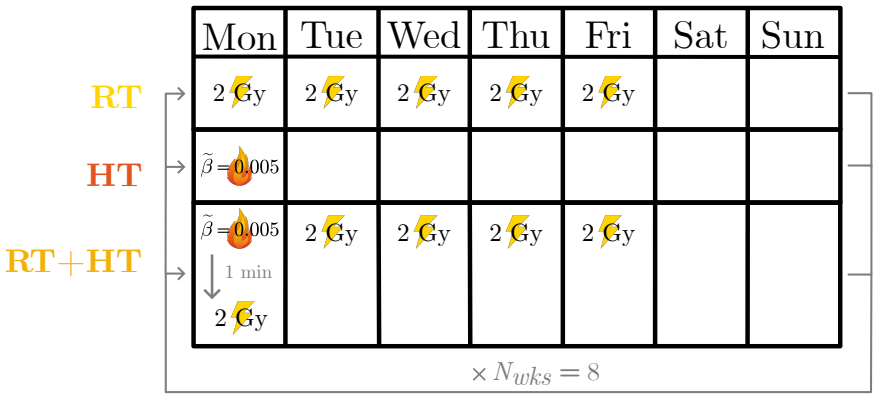


Figure 5.1: Schematic showing the equivalent RT, HT and RT + HT fractionation schedules when combining a conventional RT schedule comprising 5 × 2 Gy for 8 weeks and a conventional HT schedule with $\widetilde{\beta} = 0.005$.

For each combination treatment, the equivalent RT treatment retains all the properties of the combination treatment, except that we set $\widetilde{\alpha}_{\mathrm{V}} \equiv \widetilde{\alpha}_{\mathrm{RO2}} \equiv \widetilde{\beta} \equiv 0$ and apply the first weekly RT fraction when the first weekly HT fraction would have been applied. Similarly, the equivalent HT treatment retains all properties of the combination treatment, except that we set $R \equiv 0$. The schematic in Figure 5.1 depicts equivalent RT, HT and RT + HT fractionation schedules for a conventional RT schedule comprising 5 × 2 Gy for 8 weeks and a conventional high HT schedule with $\widetilde{\beta} = 0.005$.

5.2.2 Numerical methods

For each virtual cohort and each treatment (RT, HT or RT + HT) protocol, we solve Equations (4.12)–(4.17) numerically for $t \in (0, t^*]$, $t^* > 0$, using ODE45, a single step MATLAB built-in solver for non-stiff ordinary differential equations that is based on an explicit Runge-Kutta (4,5) formula, the Dormand-Prince pair [59]. For consistency with Chapters 3 and 4, we set $t^* = t_{\text{end}} + 10^6$, where t_{end} is the time at which the treatment schedule ends, and we impose the initial conditions

$$\big(T(0), T_{\text{S}}(0), T_{\text{R}}(0), T_{\text{H}}(0), V(0), c(0)\big) = \big(T^*, 0, 0, 0, V_0, c^*\big), \tag{5.1}$$

where T^* and c^* are, respectively, the steady state tumour volume and oxygen concentration in the absence of treatment (see Chapter 2 and Figure 3.2). All remaining RT and HT parameters are fixed at the values stated in Tables 3.1 and 4.1, respectively, except κ_0, which we fix at 10^{-7}. Tumour responses to combinations of RT and high HT for smaller and larger values of κ_0 can be explained by considering results from Chapters 3 and 4 alongside those presented in this chapter; see Appendix C.3.

Quantities of interest As in Chapters 3 and 4, we record $\bar{T}$, $\bar{T}_{\text{S}}$, $\bar{T}_{\text{R}}$, $\bar{T}_{\text{H}}$, $\bar{V}$ and $\bar{c}$, the mean values of each dependent variable over the last week of treatment, for each simulation. We then define the percent change in (mean) viable tumour cell, total cell and vascular volumes and (mean) oxygen concentration between the start and the end of treatment as follows:

$$\begin{aligned} \Delta^X_{\text{viable}} &= 100 \times \frac{(\bar{T} + \bar{T}_{\text{S}}) - T_0}{T_0}, \quad \Delta^X_{\text{total}} = 100 \times \frac{\bar{\Sigma} - \Sigma_0}{\Sigma_0}, \\ \Delta^X_{\text{V}} &= 100 \times \frac{\bar{V} - V_0}{V_0}, \quad \Delta^X_{\text{c}} = 100 \times \frac{\bar{c} - c_0}{c_0}, \end{aligned} \tag{5.2}$$

where $X = \text{R}$ for RT, $X = \text{H}$ for HT, $X = \text{R} + \text{H}$ for RT + HT, $\Sigma_0 = T^* + V_0$ and $\bar{\Sigma} = \bar{T} + \bar{T}_{\text{S}} + \bar{T}_{\text{R}} + \bar{T}_{\text{H}} + \bar{V}$. We note that, for $X = \text{R}$ and $X = \text{H}$, the quantities defined in Equations (5.2) are equivalent to those defined in Equations (3.15) and (4.21), respectively.

5.2.3 Comparing equivalent RT, HT and RT+HT treatments

For each (RT, HT, RT + HT) triplet, comprising a combination treatment and its equivalent RT and HT schedules, we compare the treatments in terms of efficacy using the following rules:

1. A treatment is considered ineffective and is excluded from consideration if and only if

$$\max\left\{\Delta^X_{\text{viable}},\ \Delta^X_{\text{total}},\ \Delta^X_{\text{V}}\right\} > 0, \tag{5.3}$$

for $X \in \{\text{R}, \text{H}, \text{R+H}\}$.

2. The combination treatment is considered more effective than RT or HT if and only if

$$\Delta^{\mathrm{R+H}}_{\mathrm{viable}} < \Delta^{X}_{\mathrm{viable}}, \quad \Delta^{\mathrm{R+H}}_{\mathrm{total}} < \Delta^{X}_{\mathrm{total}}, \quad \text{and} \quad \Delta^{\mathrm{R+H}}_{\mathrm{V}} < \Delta^{X}_{\mathrm{V}}, \tag{5.4}$$

for $X = \mathrm{R}$ or $X = \mathrm{H}$, respectively.

3. HT is considered more effective than RT (and conversely) if and only if

$$\begin{aligned} & \Delta^{\mathrm{H}}_{\mathrm{viable}} < \Delta^{\mathrm{R}}_{\mathrm{viable}}, \quad \text{and} \quad \Delta^{\mathrm{H}}_{\mathrm{total}} < \Delta^{\mathrm{R}}_{\mathrm{total}}, \\ \text{or} \quad & \Delta^{\mathrm{H}}_{\mathrm{viable}} > \Delta^{\mathrm{R}}_{\mathrm{viable}}, \quad \text{and} \quad |\Delta^{\mathrm{H}}_{\mathrm{total}} - \Delta^{\mathrm{R}}_{\mathrm{total}}| > |\Delta^{\mathrm{R}}_{\mathrm{viable}} - \Delta^{\mathrm{H}}_{\mathrm{viable}}|, \\ \text{or} \quad & \Delta^{\mathrm{H}}_{\mathrm{total}} > \Delta^{\mathrm{R}}_{\mathrm{total}} \quad \text{and} \quad |\Delta^{\mathrm{H}}_{\mathrm{viable}} - \Delta^{\mathrm{R}}_{\mathrm{viable}}| > |\Delta^{\mathrm{R}}_{\mathrm{total}} - \Delta^{\mathrm{H}}_{\mathrm{total}}|. \end{aligned} \tag{5.5}$$

Rule 1 guarantees that we only consider treatments with positive tumour responses. While our model does not account for adverse side-effects of RT and HT, we assume that combined treatment has a higher probability of causing intolerable effects than HT or RT alone, which we assume have an equal probability of causing intolerable side-effects. Consequently, rule 2 implies that combined treatment must improve the reductions in vascular, viable and total volumes observed for RT and HT alone to be considered more effective, while rule 3 implies that HT is more effective than RT if it leads to a greater combined reduction in viable and total volumes (and conversely). We finally note that, for effective HT and combination treatments, we have $\Delta^{\mathrm{R+H}}_{\mathrm{V}} < \Delta^{\mathrm{R}}_{\mathrm{V}}$ and $\Delta^{\mathrm{H}}_{\mathrm{V}} < \Delta^{\mathrm{R}}_{\mathrm{V}}$ since $\Delta^{\mathrm{R}}_{\mathrm{V}} = 0$ for RT.

5.2.4 Determining the 'best' treatment and dosing regimen pair

For each tumour in the NL, SL and BS virtual cohorts, we seek to identify the treatment and dosing regimen pair, among those under consideration here, which maximises treatment outcome, i.e., maximises the reduction in tumour burden while implicitly accounting for potentially increased adverse side-effects for combined treatment compared to HT or RT alone. We implement the latter in two ways.

First, we introduce a maximum tolerated dose (MTD) for high HT, which, by analogy with RT, should exist but, to our knowledge, has not been reported in the literature. Here, we implicitly assume that mild HT has negligible side-effects when applied alone [78]. For a high HT fraction dose $\widetilde{\beta}$ and treatment duration N_{wks}, we quantify the total high HT dose administered as

$$\beta_{\mathrm{total}} = \widetilde{\beta} N_{\mathrm{wks}}, \tag{5.6}$$

and assess the treatment and dosing regimen pair that maximises the reduction in tumour burden for high HT and combined treatments satisfying $\beta_{\mathrm{total}} \leq 0.08$. This maximal total thermal dose is double the total thermal dose for the conventional high HT schedule studied in Chapter 4 ($\widetilde{\beta} = 0.005$ for 8 weeks), which enables us to study a range of high HT schedules while mitigating over-exposure.

Second, for each tumour and each (RT, HT, RT + HT) triplet, we determine the most effective treatment as described above, with a minor modification. Under the preceding assumption that combined treatment has a higher probability of causing intolerable side-effects than HT and RT alone, we determine the 'best' treatment and dosing regimen pair by imposing a stronger condition for combined treatment to be considered more effective than HT and RT alone. In particular, not only must rule 2 in Section 5.2.3 be satisfied, but RT + HT must lead to a 'significant' improvement in treatment efficacy compared to HT and RT alone. In particular, we require

$$\Delta^{\mathrm{R+H}}_{\mathrm{viable}} + 10 < \min\left(\Delta^{\mathrm{R}}_{\mathrm{viable}}, \Delta^{\mathrm{H}}_{\mathrm{viable}}\right) \quad \text{or} \quad \Delta^{\mathrm{R+H}}_{\mathrm{total}} + 10 < \min\left(\Delta^{\mathrm{R}}_{\mathrm{total}}, \Delta^{\mathrm{H}}_{\mathrm{total}}\right). \tag{5.7}$$

In other words, combined treatment is best if and only if it induces reductions in viable or total volumes that are at least 10% larger than HT and RT alone. We do not impose such a condition on the reduction in vascular volume as $V \ll \Sigma$ and, therefore, it has a smaller impact on tumour burden.

Remark 5.2.1. The choice of a 10% increase in the reduction in viable or total volumes for combined treatment vs. HT or RT alone in Equation (5.7) influences which treatment is considered best: for values larger than 10%, fewer tumours will respond best to combined treatment, while for values smaller than 10%, a greater number of tumours will respond best to combined treatment (see Appendix C.4). This highlights the importance of accounting for adverse side-effects of different treatments in order to quantify when combined treatment is worthwhile. We return to this in the Discussion in Chapter 7.

After identifying the best treatment for each (RT, HT, RT + HT) triplet, we rank the (best) treatment and dosing regimen pairs from smallest to largest value of $\Delta_{\mathrm{viable}} + \Delta_{\mathrm{total}}$, i.e., the combined reduction in viable and total volumes. Here, we once more exclude Δ_{V} as the vascular volume has a limited influence on tumour burden. If a RT or HT schedule minimises $\Delta_{\mathrm{viable}} + \Delta_{\mathrm{total}}$, then we have found the best treatment and dosing regimen pair. If a RT + HT schedule minimises $\Delta_{\mathrm{viable}} + \Delta_{\mathrm{total}}$, then we check whether there are any RT or HT dosing schedules satisfying, for $X = \mathrm{R}$ or $X = \mathrm{H}$, respectively,

$$\Delta^{X}_{\mathrm{viable}} < \Delta^{\mathrm{best}}_{\mathrm{viable}} + 10 \quad \text{and} \quad \Delta^{X}_{\mathrm{total}} < \Delta^{\mathrm{best}}_{\mathrm{total}} + 10, \tag{5.8}$$

where $\Delta^{\mathrm{best}}_{\mathrm{viable}}$ and $\Delta^{\mathrm{best}}_{\mathrm{total}}$ are the values of $\Delta^{\mathrm{R+H}}_{\mathrm{viable}}$ and $\Delta^{\mathrm{R+H}}_{\mathrm{total}}$ for the combined treatment which minimises $\Delta_{\mathrm{viable}} + \Delta_{\mathrm{total}}$. Such HT or RT treatments induce reductions in both viable and total volumes that are at least 10% larger than combined treatment. If there are no such pairs, then we conclude that the RT + HT schedule found in the original ranking is the best treatment and dosing regimen pair. Otherwise, we rank the new set of (HT and RT) treatment and dosing regimen pairs from smallest to largest value of $\Delta_{\mathrm{viable}} + \Delta_{\mathrm{total}}$. The new pair which minimises $\Delta_{\mathrm{viable}} + \Delta_{\mathrm{total}}$ is then deemed the best.

5.3 Investigating tumour responses to combined mild HT and RT

In this section, we study tumour responses to combinations of mild HT and RT. We showed, in Chapter 4, that mild HT alone increases the viable and total volumes of tumours in the NL and BS cohorts, but has no effect for tumours in the SL cohort. Mild HT alone is, therefore, ineffective and we focus on whether tumour re-oxygenation due to mild HT can enhance tumour responses to RT.

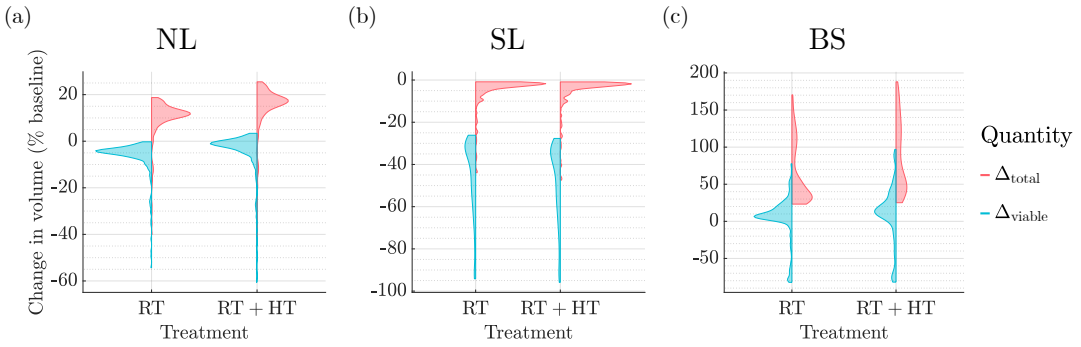


Figure 5.2: For the combination of a conventional RT schedule and mild HT ($\widetilde{\alpha}_{\text{V}} = \widetilde{\alpha}_{\text{RO2}} = 0.3$), the violin plots compare the distributions of $\Delta^{\text{R}}_{\text{viable}}$ and $\Delta^{\text{R}}_{\text{total}}$ to the distributions of $\Delta^{\text{R+H}}_{\text{viable}}$ and $\Delta^{\text{R+H}}_{\text{total}}$ for the virtual cohorts of (a) NL, (b) SL and (c) BS tumours. Most tumours in the NL cohort experience larger reductions in viable volume and smaller increases in total volume for RT alone, while most tumours in the SL cohort experience slightly greater reductions in viable and total volumes for combined treatment. Most tumours in the BS cohort experience smaller increases in viable and total volumes for RT alone.

Figure 5.2 shows that mild HT typically worsens tumour responses to RT in the NL cohort, with most tumours experiencing smaller reductions, or increases, in viable volume and larger increases in total volume following combined treatment. Further, the few NL tumours which benefit from mild HT experience reductions in viable and total volumes which are, at most, 6% larger than those for RT alone. By contrast, mild HT modestly enhances the RT efficacy for most tumours in the SL regime; they experience reductions in viable and total cell volumes, which are, at most, 5% larger than those for RT alone. For the BS regime, as in the NL regime, mild HT typically worsens tumour responses to RT: most tumours experience larger increases in total and viable volumes following combined treatment.

In addition, while some tumours in the BS regime experience greater reductions in viable volume following combined treatment, they also experience greater increases in total volume. These tumours evolve to their SL steady state during treatment, which leads to increases in intratumoural oxygen levels, RT cell kill, and the dead cell volume. Most of these tumours also evolve to their SL steady state during RT alone. Therefore, they experience a modest

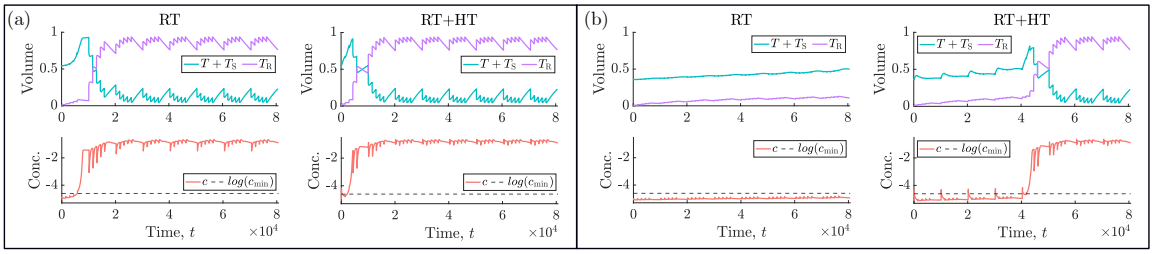


Figure 5.3: For a conventional RT schedule, alone and in combination with weekly mild HT ($\widetilde{\alpha}_V = \widetilde{\alpha}_{RO2} = 0.3$), we solve Equations (4.12)–(4.17) for $t \in (0, 8 \times 10^4]$ subject to initial conditions (5.1). We set $V_0 = 0.00275$, and (a) $(q_1, q_3) = (0.0455, 7.94)$ and (b) $(q_1, q_3) = (0.0471, 9.71)$. In (a), a modestly greater reduction in viable volume is observed for the combined treatment as mild HT modestly increases oxygen levels and RT cell kill. In (b), a significantly greater reduction in viable volume and increase in total volume are observed for combined treatment: re-oxygenation by mild HT enables the tumour to reach its SL steady state during treatment, which leads to increased rates of RT cell kill, oxygen levels and dead cell accumulation.

increase in RT cell kill due to re-oxygenation induced by mild HT, which results in a small increase in the reduction in viable volume compared to RT alone (see Figure 5.3a). The remaining tumours only evolve to their SL steady state during combined treatment and, therefore, experience more significant increases in RT cell kill (see Figure 5.3b), and large reductions in viable volume.

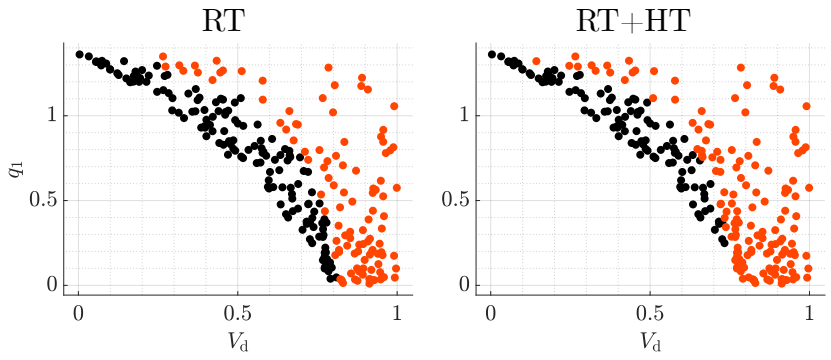


Figure 5.4: For the virtual BS population, the scatter plots show the (q_1, V_d) pairs that correspond to tumours that switch (red) and do not switch (black) steady state following a conventional RT schedule, alone and combined with mild HT ($\widetilde{\alpha}_V = \widetilde{\alpha}_{RO2} = 0.3$). Combining RT with mild HT does not prevent tumours switching between steady states and may even enable more tumours to switch steady state.

We have previously shown that neither RT nor mild HT affect the long-time tumour steady states in the NL and SL regimes, which means that combinations of mild HT and RT are unlikely to do so either. However, tumours in the BS regime may transition from the basin of attraction of their NL steady state to that of their SL steady state during treatment (i.e., they may switch steady state). We find that, as with RT alone, two types of tumours switch to the SL steady state following combined treatment: tumours which reach their SL

steady state during treatment and experience the greatest reductions in viable volume (e.g., Figure 5.3) and tumours which experience the greatest increases in viable volume as they evolve towards, but fail to reach, their SL steady state during treatment. Guided by Figure 5.2, we expect that all tumours which switched steady state following RT alone will do so following combined treatment and that a greater number of tumours will switch from the NL to the SL steady state following treatment. This is confirmed in Figure 5.4.

Recall that our criterion for combined treatment to outperform RT alone is that the reductions in viable or total volumes must be at least 10% larger than for RT (Section 5.2.4). The preceding results suggest that mild HT fails to significantly radiosensitise any of the virtual tumours under consideration here. In addition, mild HT can worsen the RT response of tumours in the NL and BS regimes. Our model, therefore, does not support the use of mild HT in combination with RT.

5.4 Investigating tumour responses to combined high HT and RT

In this section, we investigate tumour responses to combinations of RT and high HT. For each virtual cohort, we first compare tumour responses to a conventional RT schedule (5×2 Gy for 8 weeks), a conventional high HT schedule ($\widetilde{\beta} = 0.005$) and their combination. This enables us to characterise the interactions between RT and high HT across each cohort. We then investigate the impact of the dosing regimen, i.e., the RT dose rate, R, the number of weekly RT fractions, N_{frac}, and the high HT dose rate, $\widetilde{\beta}$, on the interactions between RT and high HT. Finally, we determine the 'best' treatment and dosing regimen, as defined in Section 5.2.4, for each tumour. We consider the NL cohort, followed by the SL cohort and finally the BS cohort as we observe different behaviours in each case. For the remainder of this section, unless otherwise stated, we refer to high HT as HT.

5.4.1 Nutrient limited regimes

5.4.1.1 Characterising interactions between conventional HT and RT

Figure 5.5 shows that all tumours in the NL virtual population respond well when conventional RT and HT schedules are combined, with all tumours experiencing reductions in vascular, viable cell and total tumour volumes. Comparing the distributions for each treatment suggests that HT has a greater influence on combined treatment response than RT across the cohort; in other words, HT is *dominant* and *drives* the combined treatment response. In particular, treatments which include HT (i.e., HT and RT + HT) elicit a significantly stronger response than RT alone. Comparing HT to RT + HT, we further see that most tumours experience greater reductions in vascular and viable cell volumes, but

smaller reduction in total volume, following combined treatment. Given our definition of the most effective treatment (Section 5.2.3), this implies that HT may be more effective than RT + HT for most NL tumours.

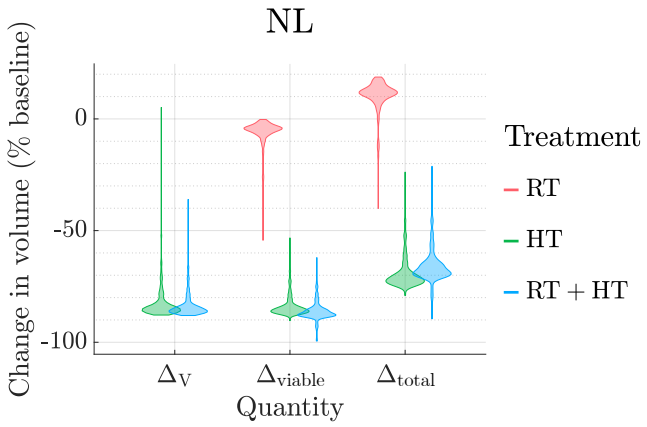
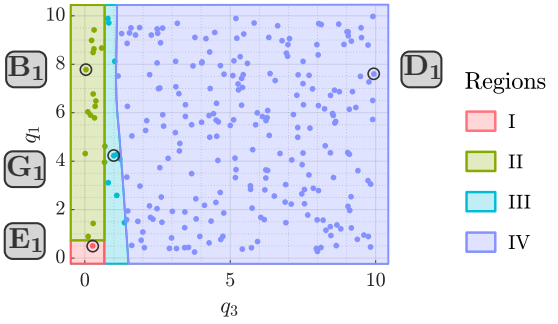


Figure 5.5: For the virtual NL cohort, the violin plots compare the distributions of Δ^X_V, Δ^X_{viable} and Δ^X_{total} for $X \in \{R, H, R+H\}$. Combined treatment response is significantly stronger than RT response and similar to HT response. On average, combined treatment appears to induce larger reductions in vascular and viable volumes and smaller reductions in total volume than HT alone.

In order to understand how HT and RT interact and when their combination enhances tumour response compared to RT or HT alone, we now determine the most effective treatment among conventional RT, conventional HT and their combination across the cohort.



Regions	HT	RT	HT + RT
I	✗	✓	✓ ✓ ✓
II	✓ ✓	✓	✓ ✓ ✓
III	✓ ✓	✗	✓ ✓ ✓
IV	✓ ✓ ✓	✗	✓ ✓

Figure 5.6: Scatter plot of the (q_1, q_3) pairs used to generate the NL virtual cohort that shows the regions in which HT and RT may interact in different ways. The table indicates, for each region, whether tumours respond positively (✓) or negatively (✗) to RT, HT and RT + HT. When multiple treatments have a positive effect within a region, we rank their efficacy using the number of check marks, with a larger number indicating higher efficacy. While combined treatment is most effective for NL tumours with low values of q_3, HT alone is typically most effective.

Figure 5.6 shows that combined treatment is most effective for NL tumours in regions I, II and III, which are characterised by low values of the oxygen consumption rate for

proliferation, q_3. We saw in Chapters 3 and 4 that, in region II, tumours respond well to both RT and HT alone. As a result, the two treatments combine additively (see Appendix C.1.1). Also from Chapters 3 and 4, we know that, in region I, tumour responses to RT and HT are, respectively, positive and negative, and conversely in region III. Therefore, for combined treatment to be most effective in these regions, RT and HT must combine synergistically. Indeed, Figure 5.7 shows that RT enhances the HT response of tumour E_1 (region I) in three ways. First, it reduces the vascular volume (compared to an increase for HT alone) as the total cell kill produces less HT-induced damage than HT alone and, thus, a weaker angiogenic response. Second, RT contributes to net cell death as low q_3 limits regrowth between fractions. Third, the sustained reduction in viable volume and low tumour regrowth lead to slower dead cell accumulation than for HT alone and, thus, a larger reduction in total volume. Similarly, Figure 5.7 also shows that, for tumour G_1 (region III), combining HT and RT overcomes the negative effects of RT (i.e., the increase in total volume) and elicits a better response than both RT and HT alone. This follows from HT- and RT-induced cell death combining so that G_1 experiences faster, and greater, reductions in viable and total volumes than for both RT and HT alone.

Returning to Figure 5.6, we find that, in region IV, HT alone is the most effective treatment. As in region III, tumours in region IV experience increases in total volume during RT because the accumulation of dead material exceeds the reduction in viable material (see Chapter 3). However, these increases are more pronounced in region IV than in region III (recall Figure 3.5). Consequently, despite the strongly positive response to HT alone for tumours in region IV (see Chapter 4), combining HT and RT slows the reduction in total volume such that $|\Delta_{\text{total}}^{\text{R+H}}| < |\Delta_{\text{total}}^{\text{H}}|$. In other words, combined treatment does not increase the reduction in total volume due to HT alone (see Appendix C.1.1).

In summary, most tumours in the NL cohort have a much stronger, positive response to HT than RT, which has negative effects when $q_3 \gtrsim 1$. As a result, we find that HT is the most effective treatment for a majority of the NL cohort (region IV). That said, RT + HT can be the most effective treatment when positive RT and HT effects combine additively (region II), and when RT and HT combine synergistically, overcoming negative HT or RT effects (regions I and III, respectively).

5.4.1.2 The influence of dosing regimen on interactions between HT and RT

Having determined tumour responses to the combination of conventional HT and RT, we now assess the impact of the thermal dose, $\widetilde{\beta}$, the RT dose rate, R, and the number of weekly RT fractions, N_{frac}, on the interactions between HT and RT.

Figure 5.8 shows that, as $\widetilde{\beta}$ increases and the effects of HT are enhanced, the threshold value of the oxygen consumption rate for proliferation, q_3 below which NL tumours respond

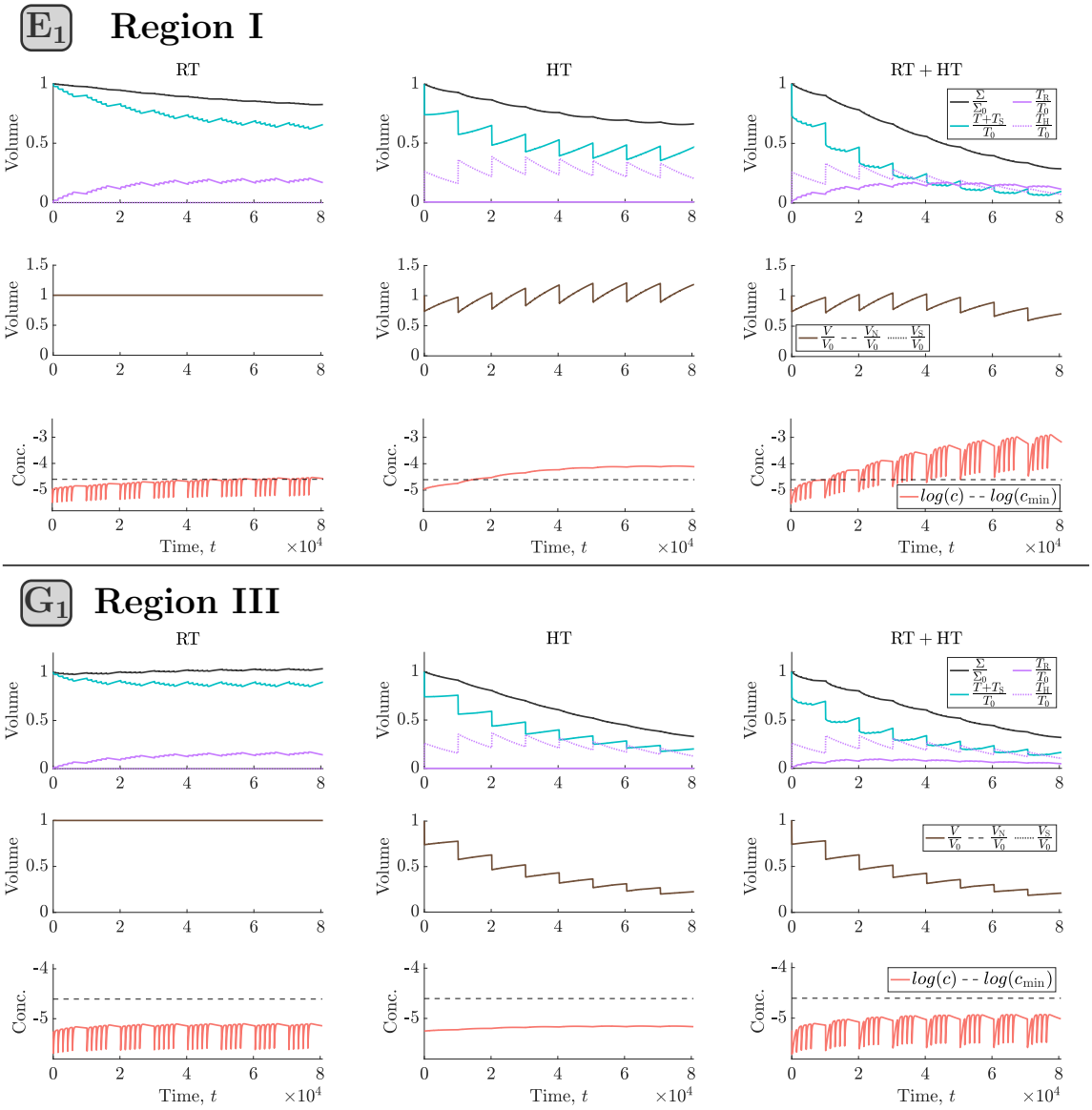


Figure 5.7: For conventional RT and HT schedules, alone and combined, we solve Equations (4.12)–(4.17) for $t \in (0, 8 \times 10^4]$ subject to initial conditions (4.20). In E_1 and G_1, we fix $V_0 = 0.0005$ and (q_1, q_3) as indicated by the points E_1 and G_1 in Figure 5.6. Regions I and III are defined in Figure 5.6. HT and RT combine synergistically for both tumours, overcoming negative HT (E_1) or RT (G_1) effects.

best to HT+RT increases (for a fixed value of the oxygen consumption rate for maintenance, q_1) and, thus, the number of tumours that respond best to combined treatment increases. Here, stronger, positive HT effects enable combined treatment to overcome negative RT effects and elicit a better response than both RT and HT alone (as for tumour G_1 in Figure 5.7). We observe the opposite effect as $\widetilde{\beta}$ decreases. In particular, if HT effects are sufficiently weak, some tumours may respond best to RT alone, e.g., tumour E_1.

As N_{frac} and R decrease, we observe the same qualitative behaviour as when $\widetilde{\beta}$ increases

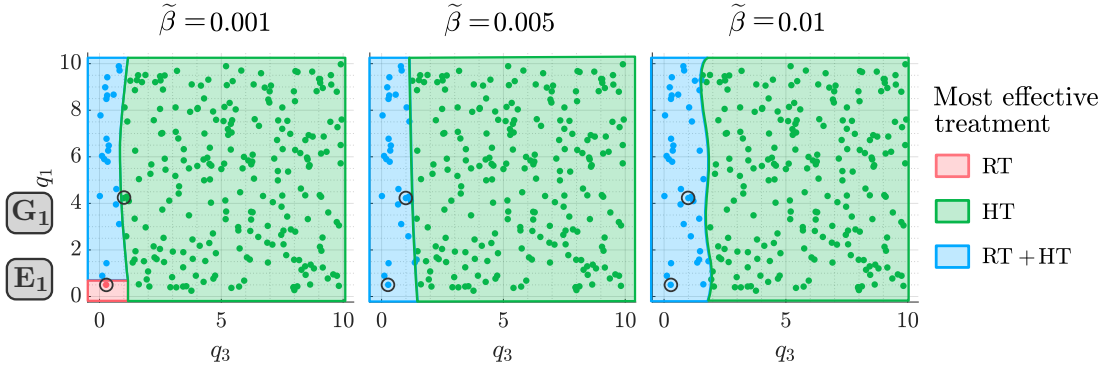


Figure 5.8: Scatter plots of the (q_1, q_3) pairs used to generate the NL virtual cohort showing the regions in which RT, HT and RT + HT are most effective for $\widetilde{\beta} \in \{0.001, 0.005, 0.01\}$, $R = 0.2$ and $N_{\text{frac}} = 5$. As $\widetilde{\beta}$ increases, the number of tumours for which combined treatment is most effective increases, and conversely. In particular, RT alone can be most effective if the thermal dose is sufficiently low.

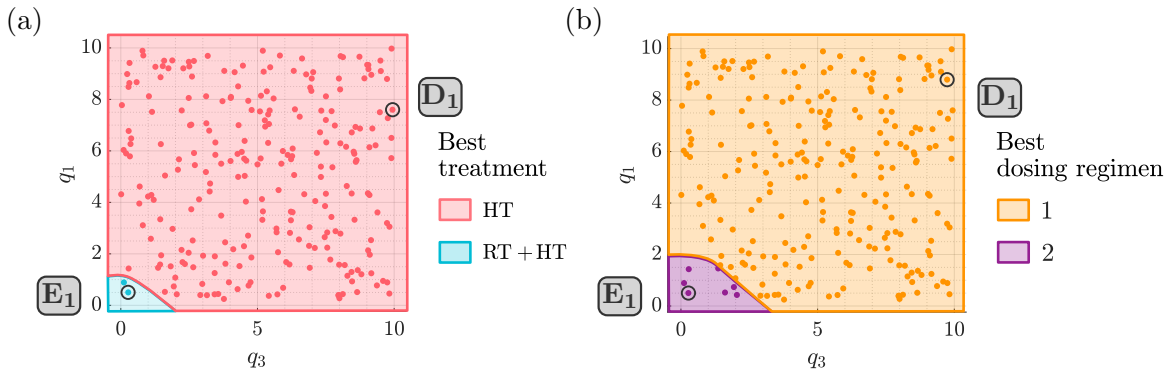
(see Appendix C.1.2). We saw, in Chapter 3, that smaller values of N_{frac} and R lead to smaller increases in total volume during RT. They also mean longer combined treatment schedules and a greater number of HT treatments, i.e., a greater total thermal dose, β_{total}. Therefore, decreasing N_{frac} and/or R can increase the number of tumours that respond best to HT + RT by increasing the efficacy of HT while reducing negative RT effects.

We conclude that, while increasing the total thermal dose increases the efficacy of HT and HT + RT, the interactions between HT and RT described in Section 5.4.1.1 are not affected by the dosing regimen. In particular, HT alone is typically the most effective treatment in the NL cohort as negative RT effects worsen HT response when the two treatments are combined.

5.4.1.3 Determining the treatment and dosing regimen which maximise tumour response

Having compared tumour responses to RT, HT and their combination for each dosing regimen considered, we now assess which treatment and dosing regimen pairs lead to the best outcome across the NL cohort. Recall that combined treatment is considered better than RT or HT alone if it elicits a reduction in viable or total volumes that is at least 10% larger than RT or HT alone, respectively (see Section 5.2.4).

Consistent with Sections 5.4.1.1 and 5.4.1.2, Figure 5.9 shows that most NL tumours respond best to HT alone, with only two tumours characterised by low values of q_3 and q_1 responding best to RT + HT. In particular, combined treatment only outperforms HT alone when response to HT alone is limited and response to RT alone is strongly positive, and the two treatments act synergistically (i.e., the other synergistic and additive interactions identified in Section 5.4.1.1 lead to RT + HT being negligibly better than HT alone).



Dosing regimen	$\widetilde{\beta}$	β_{total}	R	N_{frac}
1	Low	Maximal	Low	Low
2	High	Maximal	Low	High

Figure 5.9: Scatter plots showing the best (a) treatment and (b) dosing regimen (as defined in Section 5.2.4) for the (q_1, q_3) pairs used to generate the NL virtual cohort, where the dosing regimens are qualitatively defined in the table. Most NL tumours respond best to HT alone and the best dosing regimen depends on how effective HT is when applied alone. When HT response is limited (purple), larger HT fractions applied over a shorter time period maximise treatment efficacy, whereas, when HT response is strongly positive (orange), lower HT fractions applied over a longer time period are best.

Further, we identify two main types of dosing schedules, both of which maximise the total thermal dose:

1. Long HT treatments with low thermal doses per fraction;

2. Short treatments with high thermal doses per fraction and low RT doses applied at high frequency (for RT + HT).

Tumours that respond best to dosing regimen 1 have a strongly positive response to HT alone as limited tumour regrowth enables larger reductions in vascular and viable volumes (see Chapter 4). While these tumours respond well to HT schedules of both type 1 and 2, a larger number of low-dose HT fractions typically enables a more gradual, but larger, reduction in tumour burden (see the responses of tumour D_1 in Figure 5.10). Tumours that respond best to dosing regimen 2 have a more limited or poor response to HT alone as higher tumour regrowth means smaller reductions in vascular and viable volumes (see Chapter 4). In this case, low-dose HT and infrequent RT fractions lead to increases in vascular, viable and total volumes as tumour regrowth outweighs net cell death. By contrast, high-dose HT and frequent RT fractions, respectively, increase cell death and limit weekly tumour regrowth, enabling large reductions in vascular and viable volumes. For instance, see the responses of tumour E_1 in Figure 5.11.

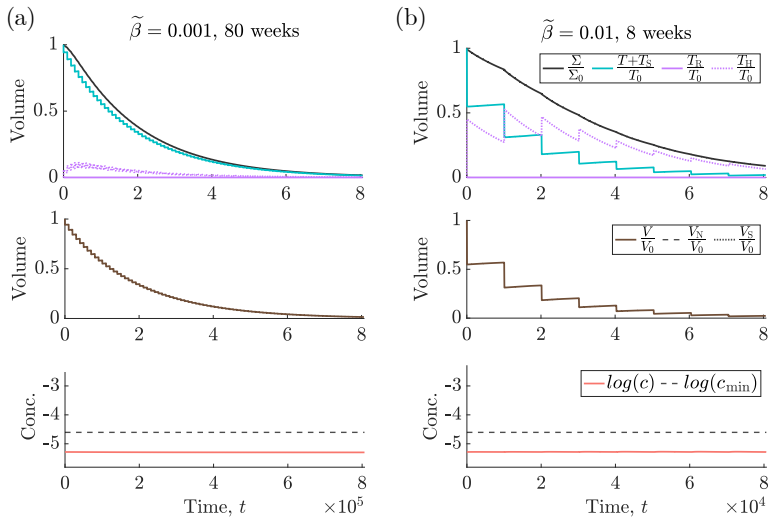


Figure 5.10: We solve Equations (4.12)–(4.17) for (a) $t \in (0, 8\times10^5]$ and (b) $t \in (0, 8\times10^4]$ subject to initial conditions (4.20). We fix the thermal dose (a) $\widetilde{\beta} = 0.001$ or (b) $\widetilde{\beta} = 0.01$, and simulate HT alone for (a) 80 weeks or (b) 8 weeks. We fix $V_0 = 0.0005$ and $(q_1, q_3) = (7.60, 9.94)$ as indicated by the point D_1 in Figure 5.9. A lower thermal dose applied over a longer period yields more gradual, but overall larger, reductions in viable, total and vascular volumes.

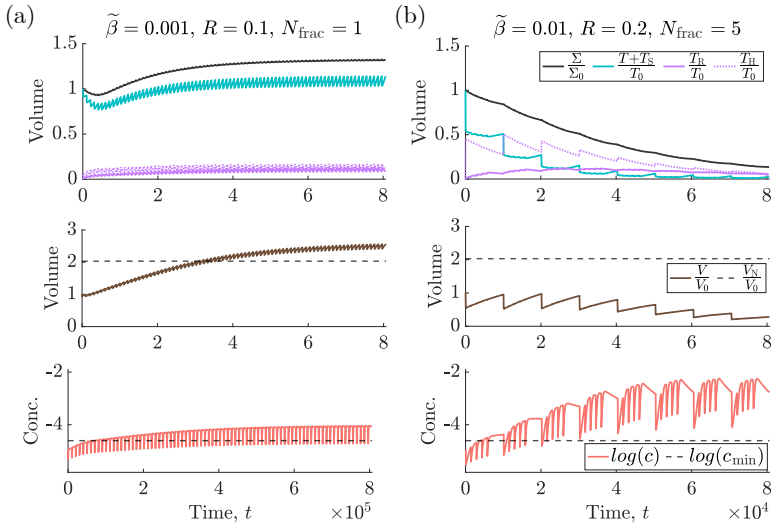


Figure 5.11: We solve Equations (4.12)–(4.17) for (a) $t \in (0, 8\times10^5]$ and (b) $t \in (0, 1.5\times10^5]$ subject to initial conditions (4.20). We fix the RT dose rate (a) $R = 0.1$ or (b) $R = 0.2$ and thermal dose (a) $\widetilde{\beta} = 0.001$ or (b) $\widetilde{\beta} = 0.01$, and simulate (a) once weekly RT fractions on Mondays for 80 weeks or (b) daily RT fractions, Monday to Friday, for 8 weeks. We fix $V_0 = 0.0005$ and $(q_1, q_3) = (0.503, 0.272)$ as indicated by the point E_1 in Figure 5.9 and Table 4.3. A larger thermal dose is necessary to obtain sustained reductions in viable, total and vascular volumes.

5.4.2 Space limited regimes

5.4.2.1 Characterising interactions between conventional HT and RT

Figure 5.12 shows that tumours in the SL cohort also respond well to combined treatment. Indeed, most SL tumours respond better to treatments involving HT, with the largest average reductions in vascular, viable cell and total tumour volumes achieved for RT + HT. However, differences in the efficacy of the three treatments for specific tumours are less clear from the violin plots in Figure 5.12 than for the NL cohort. In order to determine when combined treatment outperforms HT and/or RT alone, we now compare individual tumour responses to conventional RT, conventional HT and their combination across the SL cohort.

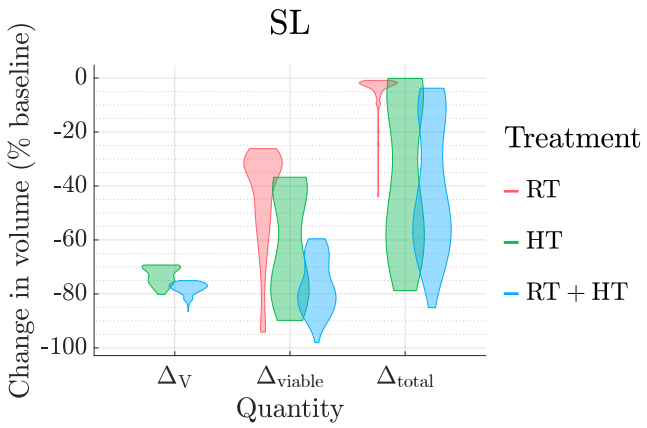
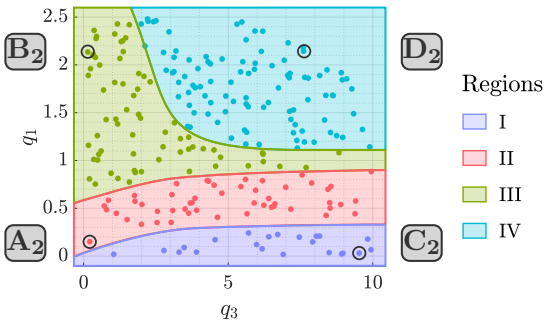


Figure 5.12: For the virtual SL cohort, the violin plots compare the distributions of Δ_V^X, Δ_{viable}^X and Δ_{total}^X for $X \in \{R, H, R+H\}$. All tumours respond well to combined treatment, which typically leads to larger reduction in vascular, viable and total volumes.

Figure 5.13 shows that HT alone is most effective for tumours in region IV, which are characterised by high values of the oxygen consumption rates for maintenance and proliferation, q_1 and q_3. From Chapters 3 and 4, we know that such tumours have a limited response to RT (due to increases in total volume), but strongly positive response to HT. As for NL tumours with high q_3, we find that combined treatment fails to elicit a larger reduction in total volume than HT alone as RT slows this reduction, worsening HT response (see Appendix C.1.3).

Further, RT alone is most effective for tumours in region I, which are characterised by the lowest values of q_1. We saw, in Chapters 3 and 4, that such tumours have a strongly positive response to RT, but limited response to HT (due to fast tumour regrowth). As shown for tumour C_2 in Figure 5.14, combined treatment is less effective than RT alone for tumours in region I because it does not lead to a smaller reduction in viable volume than RT alone. In particular, HT-induced vascular damage reduces oxygen levels and, thus, RT cell



Regions	HT	RT	HT + RT
I	✓ ✓	✓ ✓ ✓	✓
II	✓	✓ ✓	✓ ✓ ✓
III	✓ ✓	✓	✓ ✓ ✓
IV	✓ ✓ ✓	✓	✓ ✓

Figure 5.13: Scatter plot of the (q_1, q_3) pairs used to generate the SL virtual cohort that shows the regions in which HT and RT may interact in different ways. The table defines these regions by indicating, for each region, whether tumours respond positively (check mark) or negatively (cross) to RT, HT and RT + HT. When multiple treatments have a positive effect within a region, we rank their efficacy using the number of check marks, with a larger number indicating higher efficacy. Treatments involving HT are most effective for tumours with higher values of q_1, and HT alone is most effective when q_3 is also high. By contrast, treatments involving RT are most effective for tumours with lower values of q_3, RT alone is most effective for the smallest values of q_1 when q_3 is high.

kill rates. Combined with fast tumour regrowth between fractions and over the weekend break, this slows the reduction in viable volume and can even enable net growth of the viable volume during combined treatment (as for C_2).

Finally, Figure 5.13 shows that combined treatment is the most effective for SL tumours in regions II and III. Comparison of Figures 3.7 and 4.10 from Chapters 3 and 4, respectively, indicates that tumour responses to RT and HT in these regions are limited to moderate. More specifically, RT responses are moderate when q_1 and/or q_3 are low (e.g., tumours A_2 and B_2) and limited otherwise, while HT responses are moderate when q_1 is large (e.g., tumour B_2), and limited otherwise (e.g., tumour A_2). We find that HT and RT act additively when responses to both treatments are moderate (i.e., tumour B_2; see Appendix C.1.3) and synergistically otherwise (i.e., tumour A_2). For example, Figure 5.14 shows how HT enhances RT response for tumour A_2: HT cell kill and reduced oxygen levels due to HT-induced vascular damage, respectively, increase total cell death and limit cell proliferation. As a result, combined treatment enables faster and larger reductions in viable and total volumes than RT alone.

Overall, combining RT and HT is not beneficial for tumours which have a strongly positive response to RT and limited response to HT, and conversely. Instead, as for the NL cohort, combined treatment is most effective for tumours which have a limited to moderate response to RT and HT, with additive interactions when responses to both RT and HT are moderate, and synergistic interactions otherwise.

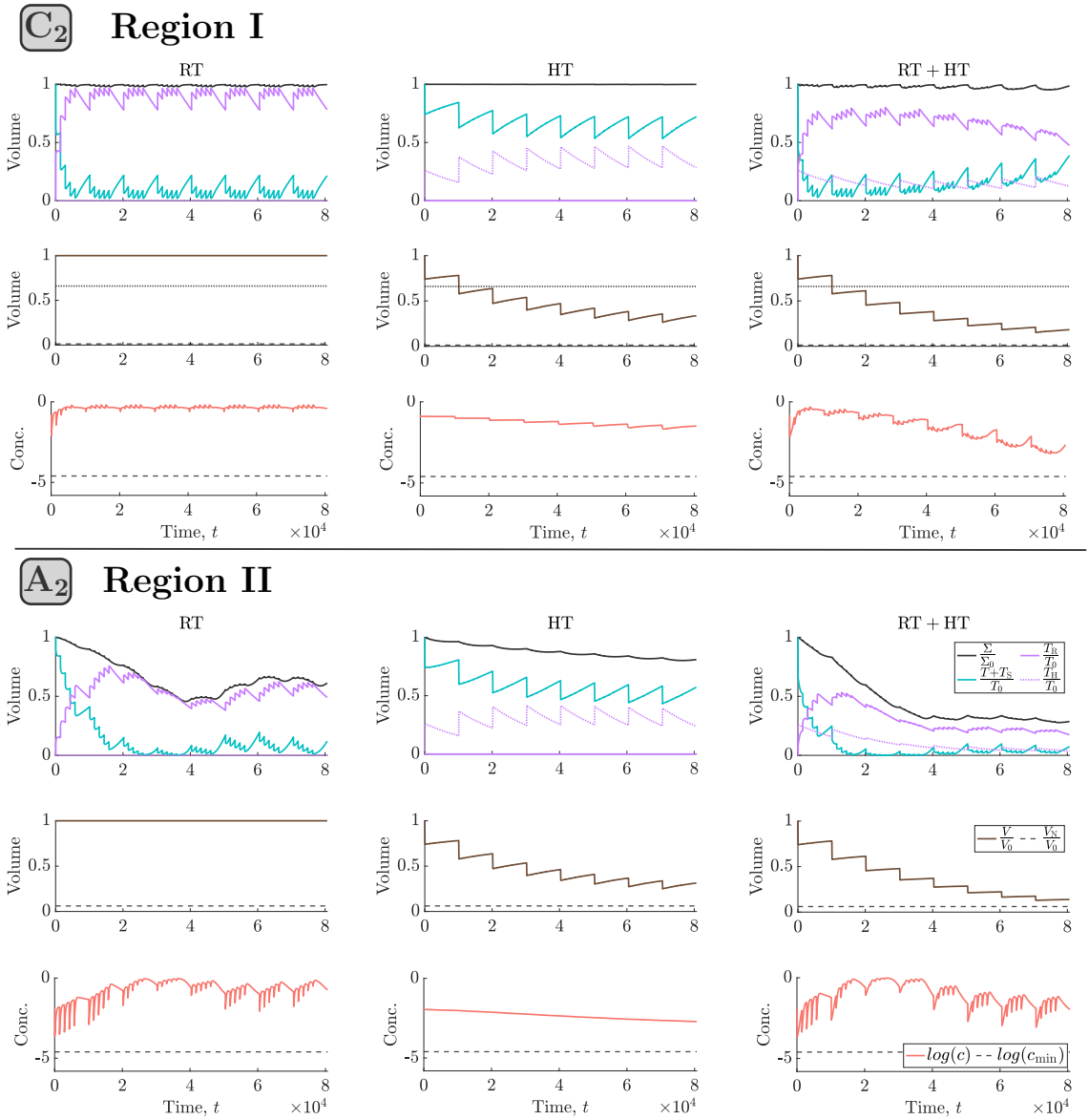


Figure 5.14: For conventional RT and HT schedules, alone and combined, we solve Equations (4.12)–(4.17) for $t \in (0, 8 \times 10^4]$ subject to initial conditions (4.20). In A_2 and C_2, we fix $V_0 = 0.005$ and (q_1, q_3) as indicated by the points A_2 and C_2 in Figure 5.13 and Table 4.4 in Chapter 4. Regions I and II are defined in Figure 5.13. For tumour C_2, HT worsens RT response when combined, whereas, for tumour A_2, HT and RT act synergistically when combined.

5.4.2.2 The influence of dosing regimen on interactions between HT and RT

By varying the thermal dose, $\widetilde{\beta}$, the RT dose rate, R, and the number of weekly RT fractions, N_{frac}, we investigate how the interactions between RT and HT depend on the dosing regimen.

As R increases, the efficacy of RT increases, while the efficacy of HT decreases (since the combined treatment schedule is shorter and fewer HT fractions are applied). Figure

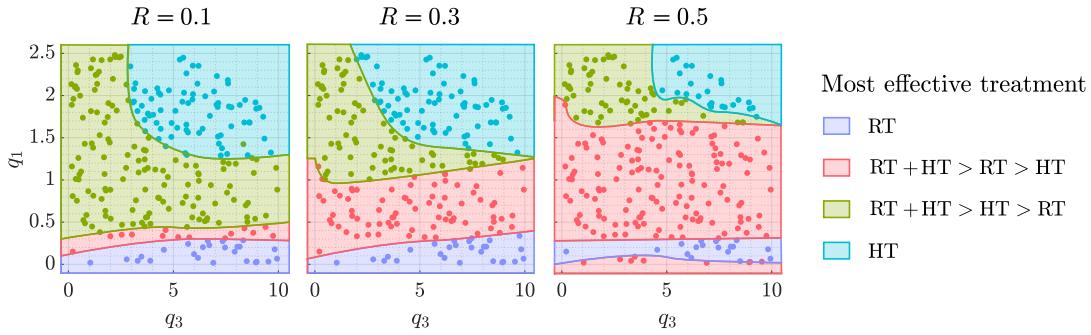


Figure 5.15: Scatter plots of the (q_1, q_3) pairs used to generate the SL virtual cohort showing the regions in which RT, HT and RT+HT are most effective for $R \in \{0.1, 0.3, 0.5\}$, $\widetilde{\beta} = 0.005$ and $N_{\text{frac}} = 5$. The number of tumours for which combined treatment is most effective is largest for $R = 0.5$ and second largest for $R = 0.1$.

5.15 shows that, as a result, the value of the oxygen consumption rate for maintenance, q_1, below which RT alone is more effective than HT alone increases with R. In particular, when $R = 0.5$, most SL tumours respond better to RT than HT, whereas, when $R = 0.1$, most SL tumours respond better to HT than RT.

Now, given q_1, the value of the oxygen consumption rate for proliferation, q_3, above which HT alone is most effective increases as R increases from 0.3 to 0.5. This is because stronger RT responses can more easily improve weaker HT responses when the two treatments are combined. Consequently, the region in which HT alone is most effective is smaller when $R = 0.5$ than when $R = 0.3$. Further, the region in which RT alone is most effective is also smaller when $R = 0.5$ than when $R = 0.3$. Indeed, if a tumour's baseline oxygen levels are sufficiently high, then the HT-induced reduction in RT cell kill rates during the second half of a longer schedule (recall the combined treatment response of tumour C_2 in Figure 5.14) no longer arises during the shorter schedule associated with $R = 0.5$. Thus, for tumours characterised by the lowest values of q_1 (and, thus, highest baseline oxygen levels), combined treatment achieves larger reductions in both viable and total volumes than RT alone when R is large.

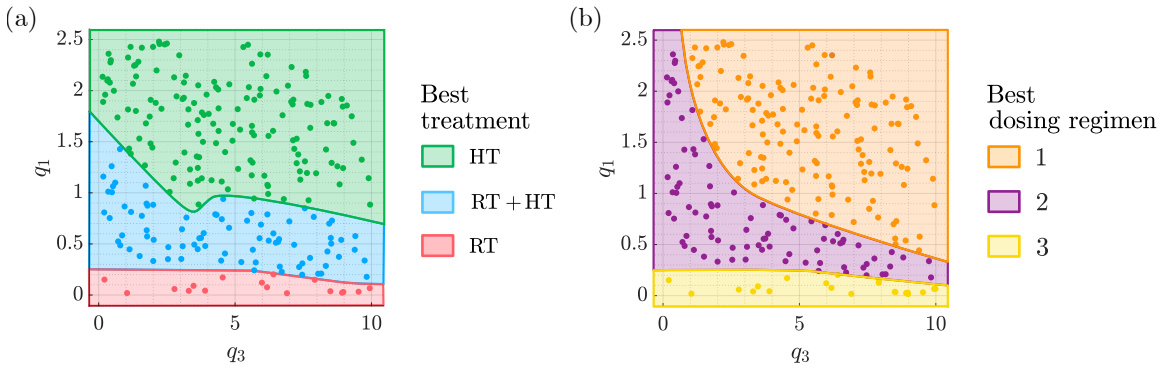
As the regions in which RT and HT alone are most effective become smaller when R increases from 0.3 to 0.5, we find that the efficacy of combined treatment increases for large R. Similar arguments can be used to explain why the efficacy of combined treatment also increases for small R, where HT response is enhanced compared to RT response.

When $\widetilde{\beta}$ is large, and when N_{frac} is small, we observe the same qualitative behaviour as when R is small (see Appendix C.1.4). Similarly, when $\widetilde{\beta}$ is small, we observe the same qualitative behaviour as when R is large (see Appendix C.1.4). Our findings, therefore, indicate that the number of tumours for which combined treatment is most effective increases both as RT is enhanced compared to HT (i.e., for large R and low $\widetilde{\beta}$) and as HT is enhanced compared to RT (i.e., for small R, large $\widetilde{\beta}$ and small N_{frac}).

5.4.2.3 Determining the treatment and dosing regimen which maximise tumour response

We finally assess which treatment and dosing regimen pairs lead to the best outcome across the SL cohort.

Figure 5.16 shows that, as for the NL cohort, tumours in the SL cohort which respond better to HT than RT (high q_1) are best treated with HT alone. In particular, the additive interactions of HT and RT observed for high q_1 and low q_3 across dosing regimens (see Figure 5.15) offer a negligible improvement compared to HT alone. Similarly, SL tumours which respond much better to RT than HT (low q_1) are better treated with RT alone. This means that the synergistic interactions between HT and RT observed for low q_1 for certain dosing regimens (see Figure 5.15) also only modestly improve responses to RT. Our results, therefore, suggest that combined treatment should only be used for tumours with moderate to limited responses to RT and HT alone, for which significant synergistic interactions arise.



Dosing regimen	$\widetilde{\beta}$	$\widetilde{\beta}_{\text{total}}$	R	N_{frac}
1	Low	Maximal	Low	Low
2	High	Maximal	Low	High
3	-	-	High	High

Figure 5.16: Scatter plots showing the best (a) treatment and (b) dosing regimen (as defined in Section 5.2.4) for the (q_1, q_3) pairs used to generate the SL virtual cohort, where the dosing regimens are qualitatively defined in the table. Tumours with particularly positive responses to RT or HT alone respond best to RT or HT alone, respectively, while tumours with a moderate or limited response to RT and HT alone respond best to combined treatment. When RT alone is best, high RT fractions applied at high frequency maximise treatment efficacy. When HT or combined treatment is best, high HT fractions applied over a shorter time period, for moderate HT and RT responders, or low HT fractions applied over a longer time period, for particularly good HT responders and poor RT responders, should be applied, with low RT fractions for combined treatment.

Further, we identify three types of dosing schedules:

1. Long treatments with low thermal doses per fraction, and low RT fraction doses and

frequency (for RT + HT);

2. Short treatments with high thermal doses per fraction, and low RT fraction doses and high RT fraction frequency (for RT + HT);

3. Short RT treatments with high fraction doses and frequency.

The dosing regimens of type 1 and 2 are analogous to those defined for the NL cohort. Both maximise the total thermal dose: longer, low-dose HT is used for tumours with a stronger HT response; shorter, high-dose HT is used for tumours with a weaker HT response. By contrast, the type 3 dosing regimen is tailored to tumours that respond best to RT alone and, therefore, is the one which maximises RT response (as defined in Section 3.4.2.3).

5.4.3 Bistable regimes

Figure 5.17 reveals that, even though RT has a deleterious effect for tumours in the BS virtual population, all tumours in this cohort respond well to combined treatment. Further, the distributions of $\Delta_{\mathrm{V}}^{\mathrm{R+H}}$, $\Delta_{\mathrm{viable}}^{\mathrm{R+H}}$ and $\Delta_{\mathrm{total}}^{\mathrm{R+H}}$ are similar to the distributions of $\Delta_{\mathrm{V}}^{\mathrm{H}}$, $\Delta_{\mathrm{viable}}^{\mathrm{H}}$ and $\Delta_{\mathrm{total}}^{\mathrm{H}}$, with slightly smaller average values of $\Delta_{\mathrm{V}}^{\mathrm{R+H}}$ and $\Delta_{\mathrm{viable}}^{\mathrm{R+H}}$, and slightly larger average values of $\Delta_{\mathrm{total}}^{\mathrm{R+H}}$. This suggests that HT alone is typically most effective for tumours in the BS cohort, as combined treatment fails to elicit a larger reduction in total volume than HT alone.

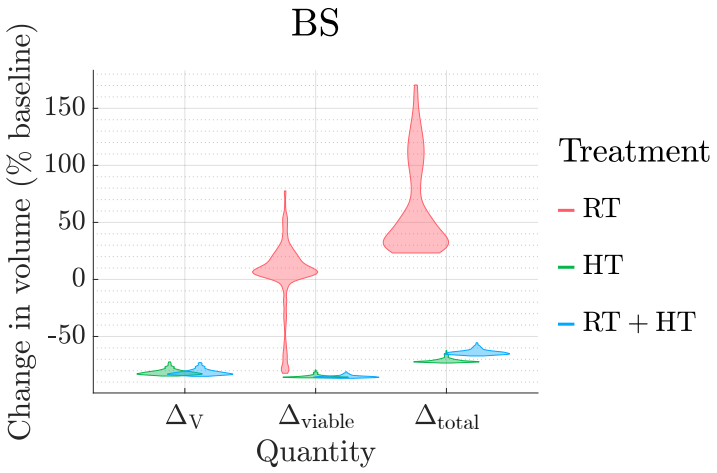


Figure 5.17: For the virtual BS cohort, the violin plots compare the distributions of Δ_{V}^{X}, $\Delta_{\mathrm{viable}}^{X}$ and $\Delta_{\mathrm{total}}^{X}$ for $X \in \{\mathrm{R}, \mathrm{H}, \mathrm{R+H}\}$. Combined treatment response is significantly stronger than RT response and similar to HT response. On average, combined treatment appears to induce slightly larger reductions in vascular and viable volumes and smaller reductions in total volume than HT alone.

Comparison of tumour responses to conventional RT, HT and RT + HT across the BS cohort confirms that all tumours in the BS cohort experience the largest reductions in

viable, total and vascular volume for HT alone. Figure 5.18 shows that, in the BS regime, as for NL tumours with strongly positive responses to HT and poor responses to RT (e.g., tumour G_1), a tumour's negative RT response can inhibit its positive response to HT when the two treatments are combined. Here, RT reduces the net cell death in the first week of treatment (as the tumour grows between RT fractions) and the tumour experiences an increase in total volume due to accumulation of RT-damaged material. This delays the reduction in total volume during RT + HT and results in a larger total volume by the end of the combined treatment schedule.

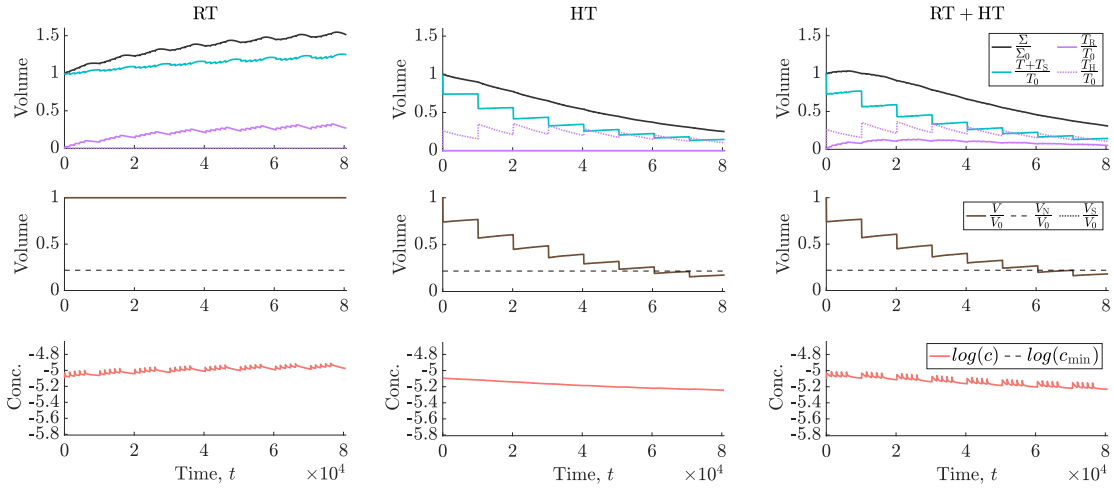


Figure 5.18: For conventional RT and HT schedules, alone and combined, we solve Equations (4.12)–(4.17) for $t \in (0, 8 \times 10^4]$ subject to initial conditions (4.20). We set $(V_0, q_1, q_3) = (0.00275, 0.297, 9.14)$ so that the tumour exhibits behaviour typical of the BS cohort. The negative RT response of this tumour worsens the positive HT response when the two treatments are combined.

We further find that, while the dosing regimen can impact the efficacy of each treatment, HT remains the most effective treatment across the BS cohort for all $\widetilde{\beta}$, R and N_{frac} values tested (result not shown for brevity). It follows that tumours in the BS regime should be treated with HT alone and, as for NL and SL tumours which have a strongly positive response to HT alone (e.g., NL tumour G_1 in Figure 5.10), a long treatment with low thermal dose per fraction maximises the reduction in tumour burden (result not shown for brevity).

5.5 Discussion

In this chapter, we concluded our study on the influence of nutrient and space limited growth arrest mechanisms on tumour responses to radiotherapy and hyperthermia. We used the model from Chapter 4 to compare tumour responses to a range of RT, HT and combined treatment schedules across the nutrient limited, space limited and bistable virtual

cohorts studied in Chapters 3 and 4. In so doing, we can now provide answers to the key questions outlined in Section 5.1.

Consistent with the findings presented in Chapter 4, we confirmed that mild HT does not significantly enhance tumour responses to RT. In particular, while the addition of mild HT leads to a modest improvement in the RT response of SL tumours, it typically worsens the RT response of tumours in NL and BS regimes. By contrast, high HT can significantly improve tumour responses to RT, provided that the HT-induced angiogenic response is sufficiently weak. This finding highlight the importance of treatment-induced changes in the vasculature when predicting treatment response (see the Discussion in Chapter 7).

Regime	q_1	q_3	Response to RT	Response to high HT	Best treatment	Best dosing regimen
NL	Low	Low	✓	✗	RT + HT	2
	Low	Mod.	✗	✓	HT	2
	Low	High	✗	✓✓	HT	1
	High	Low	✓	✓✓	HT	1
	High	High	✗	✓✓	HT	1
SL	Low	All	✓✓	∼	RT	3
	Mod.	Low	✓	∼	RT + HT	2
	Mod.	High	∼	✓	RT + HT	1
	High	Low	✓	✓	HT	2
	High	High	∼	✓✓	HT	1
BS	All	All	✗	✓✓	HT	1

Table 5.2: For each regime, we summarise how the treatment and dosing regimen pairs that maximise treatment efficacy depend on tumour responses to RT and high HT alone. Two green check marks (✓✓) indicate a strong, positive response, one green check mark (✓) indicates a moderate response, an orange tilde (∼) indicates a limited response and a red cross (✗) indicates a negative response.

Assuming κ_0 is sufficiently small, we now detail key results relating to combinations of high HT and RT, which are summarised in Table 5.2. Most tumours respond better to combined treatment than RT alone, the exception being tumours in the SL regime which have the strongest positive response to RT alone (and weakest response to high HT alone). For these tumours, combining high HT and RT either worsens treatment outcome as a smaller reduction in viable volume than RT alone is achieved, or negligibly improves treatment outcome by eliciting a modest ($< 10\%$) increase in the reduction in viable volume due to RT alone. Further, tumours in each regime which have strongly positive responses to high HT alone and weaker (moderate to negative) responses to RT alone respond best to high HT alone. In particular, combined treatment elicits a smaller, or modestly larger,

reduction in total volume than high HT for these tumours. Consistent with these findings, high HT and RT only have significant synergistic interactions for (1) tumours that have a poor or limited response to high HT and moderate response to RT, and (2) tumours that have a limited response to RT and moderate response to HT.

As shown in Table 5.2, the above findings imply that most of the NL cohort and all of the BS cohort respond best to high HT alone, with only a few NL tumours responding best to combined treatment. By contrast, in the SL cohort, there is a more even split between tumours which respond best to RT, high HT and combined treatment. In this way, our model supports clinical evidence suggesting that not all tumours will respond better to combined treatment than RT alone. Our model also provides insight into why certain tumours may not respond better to combined treatment than RT (i.e., well-oxygenated SL tumours with low q_1), and also which tumours may respond best to high HT alone (NL tumours with high q_1 and/or q_3, BS tumours and SL tumours with high q_1).

The latter result is of particular interest since HT is typically viewed as an adjuvant treatment, rather than a primary treatment [15]. This is because the few clinical trials investigating tumour responses to HT alone found that high HT has a limited efficacy when applied alone [165]. It would, therefore, be useful to investigate whether the differences between these clinical results and our model predictions are due to limitations of treatment methods, which may fail to heat an entire tumour to the target temperature [187], or an overestimation of high HT effects in our model.

Moreover, we distinguished between three types of dosing regimens that can maximise the reduction in tumour burden:

1. Long treatments with low thermal doses per fraction, and low RT fraction doses and frequency (for RT + HT);

2. Short treatments with high thermal doses per fraction, and low RT fraction doses and high RT fraction frequency (for RT + HT);

3. Short RT treatments with high fraction doses and frequency.

Importantly, we found that there is not a one-to-one correspondence between the best treatment and the best dosing regimen for treatments involving high HT. For instance, two tumours which respond best to high HT and combined treatment, respectively, may both respond best to a dosing regimen of type 1. Indeed, our model predicts that, when HT or RT + HT is the best treatment, the best dosing regimen depends only on tumour responses to high HT alone (see Table 5.2).

Overall, the results presented in this chapter suggest that a one-size-fits-all approach to the design of combined high HT and RT treatments is not appropriate for tumours in the

NL and SL cohorts. Indeed, we found inter-tumour variability in terms of the most effective treatment, and also the dosing regimen that maximises treatment efficacy. By contrast, all tumours in the BS cohort respond best to the same high HT schedule.

In Chapters 2–5, we showed that nutrient and space limited mechanisms of growth arrest can significantly influence tumour growth and responses to RT and HT. More generally, our results have highlighted the importance of taking these growth control mechanisms into account when investigating tumour dynamics under treatment. With tumour invasion being a hallmark of cancer [97], a logical next step would be to probe the impact of growth arrest mechanisms on tumour invasion into healthy tissue. With a view to doing so in the future, the following chapter focusses on the in-depth analysis of a simple, spatially-resolved model of tumour invasion into extracellular matrix.

Chapter 6

Travelling wave analysis of a model of tumour invasion with degenerate, cross-dependent diffusion

6.1 Introduction

The preceding chapters focussed on studying a spatially-uniform ordinary differential equation (ODE) model of tumour growth and response to radiotherapy and hyperthermia. While this modelling framework generated many interesting results, it neglected both spatial effects and interactions between tumour tissue and healthy tissue. However, the invasion of a primary tumour into healthy tissue and its spread throughout the body is a key hallmark of cancer [97], which is intrinsically space-dependent. Spatially-resolved models are, therefore, needed to describe tumour invasion and, as discussed in Section 1.5, a number of approaches have been proposed. This includes reaction-diffusion (R-D) partial differential equation (PDE) models, such as the pioneering Gatenby-Gawlinski model [83] introduced in Section 1.5.1.

By assuming that healthy tissue, comprising healthy cells and/or extracellular matrix (ECM), acts as a barrier to tumour cell invasion, the Gatenby-Gawlinksi model and its variations include a degenerate, cross-diffusion term in the equation for the tumour cell density. This key common feature is of mathematical interest due to its impact on the existence and properties of travelling wave solutions (TWS) of the aforementioned models. We saw in Section 1.5.2 that comprehensive results on the existence of TWS for models of tumour invasion comprising R-D PDEs remain limited, with the existence of TWS typically supported by numerical simulations and partial analytical results [27, 51, 63, 74, 107, 158, 169, 238]. To the best of our knowledge, a first rigorous proof of the existence of a form of weak TWS was recently produced by Gallay and Mascia [82] for the following reduced

version of the Gatenby-Gawlinski model, where N and M, respectively, denote the tumour cell and healthy cell densities:

$$\begin{cases} \dfrac{\partial M}{\partial t} = M(1 - M - \alpha N), \\ \dfrac{\partial N}{\partial t} = \dfrac{\partial}{\partial x}\left[D_{\mathrm{N}}(1-M)\dfrac{\partial N}{\partial x}\right] + \beta N(1-N). \end{cases} \tag{6.1}$$

In this chapter, we propose a new minimal R-D PDE model (Section 6.2) which captures key features of the tumour invasion process, including degenerate, cross-dependent diffusion, and is also analytically tractable. In Section 6.3.1, we define the constant profile, constant speed TWS associated with our model, prove preliminary results and derive the ODE system that the TWS must satisfy. In brief, we seek two types of TWS. Both types represent invasive fronts of tumour tissue into ECM, which represents healthy tissue, but they differ according to whether the density of ECM far ahead of the wave front is maximal or not. For the former, we prove the existence and uniqueness of TWS for all positive propagation speeds using the shooting argument developed by Gallay and Mascia [82] (Section 6.3.2). For the latter, we expand this shooting argument to prove the existence and uniqueness of TWS for propagation speeds greater than or equal to a strictly positive minimum value (Section 6.3.2). Motivated by our numerical simulations and partial analytical results, we make a conjecture that characterises this minimum wave speed (Section 6.3.2). In Section 6.4, we present numerical simulations of our model which support and complement the preceding analytical results.

The work presented in this chapter has been published in the following paper:
Colson, C., Sánchez-Garduño, F., Byrne, H. M., Maini, P. K. and Lorenzi, T, 2021. Travelling-wave analysis of a model of tumour invasion with degenerate, cross-dependent diffusion. Proceedings of the Royal Society A, 477(2256), 20210593.

6.2 The mathematical model

In this section, we present the minimal model of tumour invasion that we use to study nonlinear, degenerate diffusion. There is increasing evidence that phenotypically heterogeneous tumours can contain sub-populations of cells with different traits, e.g., matrix-degrading cells and acid-producing cells [233]. Here, we make the simplifying assumption that the healthy tissue compartment comprises solely ECM, disregarding healthy cells, and focus on the interactions of ECM-degrading tumour cells and ECM. Applying conservation of mass to the tumour cell and ECM densities, which we denote by $N(x,t)$ and $M(x,t)$,

respectively, for $(x,t) \in \mathbb{R} \times (0,+\infty)$, we propose the following system of PDEs:

$$\begin{cases} \dfrac{\partial N}{\partial t} = \underbrace{\dfrac{\partial}{\partial x}\left[D_{\mathrm{N}}\left(1-\dfrac{M}{M_{\max}}\right)\dfrac{\partial N}{\partial x}\right]}_{\text{tumour cell movement}} + \underbrace{\rho\left(1-\dfrac{N}{K}\right)N}_{\text{tumour growth}}, \\ \dfrac{\partial M}{\partial t} = \underbrace{-kMN}_{\text{ECM degradation}}. \end{cases} \tag{6.2}$$

We assume that the tumour grows logistically, with maximum growth rate, ρ, and carrying capacity, K. Further, the ECM acts as a physical barrier that inhibits tumour cell movement, but not proliferation. Thus, following Gatenby and Gawlinski [83] and others [154, 157, 233], we suppose that the random motility coefficient of the tumour cells is a monotonically decreasing function of the ECM density in order to model the way in which the ECM hinders tumour cell movement. The random motility coefficient of tumour cells in the absence of ECM is denoted by D_{N} and the ECM density that inhibits all tumour cell movement is denoted by $M_{\max}$. Finally, we neglect ECM production and assume it is degraded at a rate that is proportional to the local tumour cell density, with constant of proportionality k. The associated mass-action term in Equation (6.2) reflects the localised nature of matrix degradation.

To reduce the number of free parameters in the system and facilitate the analysis that follows, we non-dimensionalise Equation (6.2) by introducing the following scalings:

$$\hat{t} = \rho t, \quad \hat{x} = \sqrt{\frac{\rho}{D_{\mathrm{N}}}}x, \quad \hat{N} = \frac{N}{K}, \quad \hat{M} = \frac{M}{M_{\max}}. \tag{6.3}$$

Dropping hats for notational convenience, we obtain the following system:

$$\begin{cases} \dfrac{\partial N}{\partial t} = \dfrac{\partial}{\partial x}\left[(1-M)\dfrac{\partial N}{\partial x}\right] + (1-N)N, \\ \dfrac{\partial M}{\partial t} = -\kappa MN, \end{cases} \tag{6.4}$$

where $\kappa = \frac{K}{\rho}k$.

We note that system (6.4) is similar to the reduced version of the Gatenby-Gawlinski model from Moschetta and Simeoni [169], given by Equation 6.1 and studied by Gallay and Mascia [82], and the reduced model of melanoma invasion from Browning et al. [27] studied by El-Hachem et al. [63]. In particular, while the models differ with regard to the reaction terms used to model production and degradation of the ECM and tumour cell densities, each model shares the same degeneracy in the cross-diffusion term, which is the focus of this chapter.

Gallay and Mascia [82] rigorously proved the existence of a weak form of TWS for any positive wave speed, $c > 0$, for the system 6.1 in [169]. These TWS represent the invasion of tumour tissue into healthy tissue, where the density of healthy tissue ahead of the wave front

is at carrying capacity. El Hachem et al. [63] performed a numerical study which suggests that such TWS also exist for the model in [27] for any positive wave speed. Their numerical results also indicated the existence of another type of TWS for the model in [27] for wave speeds above a strictly positive minimum value. These TWS differ from the former in that the density of healthy tissue ahead of the wave front is below carrying capacity. Finally, El-Hachem et al. [63] described the dependence of the minimum wave speed of this second type of TWS on the rescaled degradation rate of healthy tissue, which we denote by κ: the minimum wave speed is constant if κ is below some threshold value, κ^* say, which is yet to be determined, and increases with κ for $\kappa \geq \kappa^*$.

In this chapter, we rigorously prove the existence of both aforementioned types of TWS for system (6.4) by applying and extending the shooting argument developed by Gallay and Mascia [82]. As in [63] and [82], we will find that the first type of TWS exists for all $c > 0$, and that there is a strictly positive minimum wave speed for the second type of TWS. We will see that this minimum wave speed for TWS of system (6.4) can be qualitatively characterised in the same way as that for equivalent TWS of the model in [27]. However, given κ, the values of this minimum wave speed for TWS of system (6.4) and of the system in [27] are not the same. An additional contribution of our work compared to that in [63] is that we propose an expression for κ^* for system (6.4), not reported in [63] for the model in [27].

6.3 Travelling wave analysis

6.3.1 The travelling wave problem

6.3.1.1 Preliminaries

We seek constant profile, constant speed TWS of system (6.4) by introducing the travelling wave coordinate $\xi = x - ct$. We require the wave speed $c > 0$ so that the tumour invades the ECM from left to right in the spatial domain. Substituting the ansatz $N(x,t) = \mathcal{N}(\xi)$ and $M(x,t) = \mathcal{M}(\xi)$ into system (6.4), we deduce that TWS must satisfy the following ODE system:

$$\begin{cases} \dfrac{\mathrm{d}}{\mathrm{d}\xi}\left((1-\mathcal{M})\dfrac{\mathrm{d}\mathcal{N}}{\mathrm{d}\xi}\right) + c\dfrac{\mathrm{d}\mathcal{N}}{\mathrm{d}\xi} + (1-\mathcal{N})\mathcal{N} = 0, & \text{(6.5a)} \\ c\dfrac{\mathrm{d}\mathcal{M}}{\mathrm{d}\xi} - \kappa\mathcal{M}\mathcal{N} = 0. & \text{(6.5b)} \end{cases}$$

The TWS we seek connect spatially homogeneous steady states of system (6.4) and, equivalently, steady states of system (6.5a)–(6.5b). Thus, our TWS must satisfy one of the

following sets of asymptotic conditions:

$$\lim_{\xi\to-\infty}(\mathcal{N}(\xi),\mathcal{M}(\xi))=(1,0),\ \lim_{\xi\to+\infty}(\mathcal{N}(\xi),\mathcal{M}(\xi))=(0,1), \tag{6.6}$$

$$\lim_{\xi\to-\infty}(\mathcal{N}(\xi),\mathcal{M}(\xi))=(1,0),\ \lim_{\xi\to+\infty}(\mathcal{N}(\xi),\mathcal{M}(\xi))=(0,\bar{\mathcal{M}})\text{ with }\bar{\mathcal{M}}\in[0,1). \tag{6.7}$$

In other words, far behind the wave, the tumour density is at carrying capacity and the ECM has been fully degraded, whereas, far ahead of the wave, the tumour density is zero and the ECM density is either at carrying capacity (i.e., $\mathcal{M}=1$) or at any value $\mathcal{M}\in[0,1)$. As noted previously, the first equation in system (6.4) is a degenerate parabolic equation since the cross-diffusion coefficient $D(M)=1-M$ is zero when $M=1$. The existence of global classical solutions of this PDE system and the corresponding ODE system (6.5a)–(6.5b) is, therefore, unclear in cases where $M=1$ or, correspondingly, where $\mathcal{M}=1$. As a result, we define a weak TWS in a manner similar to that in which a propagation front was defined in [82].

Definition 6.3.1. The triple $(\mathcal{N},\mathcal{M};c)$ is called a weak TWS for system (6.4) if

1. $(\mathcal{N},\mathcal{M})\in C(\mathbb{R},[0,1])\times C(\mathbb{R},[0,1])$ and $(1-\mathcal{M})\frac{\mathrm{d}\mathcal{N}}{\mathrm{d}\xi}\in L^2(\mathbb{R})$;
2. $(\mathcal{N},\mathcal{M})$ is a weak solution of (6.5a)–(6.5b), i.e., for all $(\phi,\psi)\in C^1(\mathbb{R})\times C^1(\mathbb{R})$ with compact support

$$\int_{\mathbb{R}}\left\{\left[c\mathcal{N}+(1-\mathcal{M})\frac{\mathrm{d}\mathcal{N}}{\mathrm{d}\xi}\right]\frac{\mathrm{d}\phi}{\mathrm{d}\xi}-(1-\mathcal{N})\mathcal{N}\phi\right\}\mathrm{d}\xi=0, \tag{6.8}$$

$$\int_{\mathbb{R}}\mathcal{M}\left\{c\frac{\mathrm{d}\psi}{\mathrm{d}\xi}+\kappa\mathcal{N}\psi\right\}\mathrm{d}\xi=0; \tag{6.9}$$

3. one of the pairs of asymptotic conditions given by (6.6) and (6.7), respectively, are satisfied.

We refer to $(\mathcal{N},\mathcal{M})$ as the travelling wave profile and c as the propagation speed.

Note. Henceforth, unless otherwise stated, we refer to weak TWS in the sense of Definition 6.3.1 as TWS.

If $(\mathcal{N},\mathcal{M};c)$ is a TWS for system (6.4), then we can show that $\mathcal{N}(1-\mathcal{N})\in L^1(\mathbb{R})$ and $c>0$. The proof is identical to that of Lemma 2.1 in [82] and, thus, we omit it. The following lemma states that, if $(\mathcal{N},\mathcal{M};c)$ is a TWS for system (6.4), then $\mathcal{N}$ and $\mathcal{M}$ are non-negative and bounded and, thus, the TWS is biologically realistic.

Lemma 6.3.1. *If $(\mathcal{N},\mathcal{M};c)$ is a weak TWS, in the sense of Definition 6.3.1, that satisfies the asymptotic conditions* (6.7) *for $\bar{\mathcal{M}}\in(0,1)$, then there exists a unique point $\bar{\xi}\in\mathbb{R}\cup\{+\infty\}$ such that*

1. $\mathcal{N}, \mathcal{M} \in C^\infty((-\infty, \bar{\xi}))$ *and* $0 < \mathcal{N}(\xi) < 1$, $0 < \mathcal{M}(\xi) < \bar{\mathcal{M}}$ *for* $\xi < \bar{\xi}$*;*

2. If $\bar{\xi} < +\infty$*, then* $\mathcal{N}(\xi) = 0$ *and* $\mathcal{M}(\xi) = \bar{\mathcal{M}}$ *for all* $\xi \geq \bar{\xi}$*.*

Proof. Suppose $(\mathcal{N}, \mathcal{M}; c)$ is a weak TWS for system (6.4) in the sense of Definition 6.3.1. We first prove the regularity result for $\mathcal{N}, \mathcal{M}$. Since $\mathcal{M}$ is a weak solution of (6.4), then, by (6.9), its weak derivative is $\frac{\kappa}{c}\mathcal{M}\mathcal{N}$. We have that $\mathcal{M}$ and $\mathcal{N}$ are continuous in $\mathbb{R}$, which implies the weak derivative of $\mathcal{M}$ is continuous in $\mathbb{R}$ since $\kappa, c > 0$. It follows that $\mathcal{M}$ is continuously differentiable in $\mathbb{R}$ and, hence, $\mathcal{M}$ is a classical solution to (6.5b). $\mathcal{N}$ is a weak solution of the ODE (6.5a) posed on $I \coloneqq (-\infty, \bar{\xi})$. Using the Elliptic Regularity theorem and Sobolev Embedding theorem, we can show that $\mathcal{N} \in C^2(I)$ since $\mathcal{N}(1 - \mathcal{N}) \in L^1(\mathbb{R})$. This means that $\mathcal{N}$ is a classical solution of (6.5a) on I. Using a bootstrap argument, it is then straightforward to prove that $\mathcal{N}$ and $\mathcal{M}$ are smooth on I.

We now prove the strict bounds on $\mathcal{N}$ and $\mathcal{M}$ on I. If there exists $\xi^* \in \mathbb{R}$ such that $\mathcal{M}(\xi^*) = 0$, then the ODE (6.5b) implies that $\mathcal{M}$ is identically zero for all $\xi \geq \xi^*$. This contradicts the requirement that $\mathcal{M}$ tends to $\bar{\mathcal{M}} > 0$ as $\xi \to +\infty$, so we must have $\mathcal{M}(\xi) > 0$ for all $\xi \in \mathbb{R}$. Since $\mathcal{M}$ converges to zero as $\xi \to -\infty$, we know that $\mathcal{M}(\xi) < \bar{\mathcal{M}}$ for $\xi < 0$ with $|\xi|$ large. Therefore, we either have $\mathcal{M}(\xi) < \bar{\mathcal{M}}$ for all $\xi \in \mathbb{R}$ and we set $\bar{\xi} = +\infty$, or there exists a unique $\bar{\xi} \in \mathbb{R}$ such that $\mathcal{M}(\bar{\xi}) = \bar{\mathcal{M}}$ and $\mathcal{M}(\xi) < \bar{\mathcal{M}}$ for any $\xi < \bar{\xi}$. Uniqueness follows from the fact that $\mathcal{M}$ is increasing for positive $\mathcal{N}$.

It is straightforward to show that $\mathcal{N}$ cannot have a non-degenerate minimum in I that is equal to zero, without being identically zero in I, which would contradict the requirement that $\mathcal{N}$ converges to 1 as $\xi \to -\infty$. Similarly, $\mathcal{N}$ cannot have a non-degenerate maximum in I that is equal to 1, without being identically equal to 1 on this interval. If $\bar{\xi} = +\infty$, this contradicts the requirement that $\mathcal{N}$ converges to 0 as $\xi \to +\infty$. If $\bar{\xi} < +\infty$, this means that $\frac{\mathrm{d}\mathcal{M}}{\mathrm{d}\xi}(\bar{\xi}) = \frac{\kappa}{c}\bar{\mathcal{M}} > 0$ and $\mathcal{M}(\xi) \geq \bar{\mathcal{M}}$ for $\xi \geq \bar{\xi}$ close to $\bar{\xi}$. Since $\mathcal{M}$ is increasing for positive $\mathcal{N}$, the former inequality contradicts the requirement that $\mathcal{M}$ tends to $\bar{\mathcal{M}}$ as $\xi \to +\infty$. We must therefore have $\mathcal{N}(\xi) < 1$ for all $\xi \in I$.

To prove *2*, we suppose $\bar{\xi} < +\infty$. By assumption, $\mathcal{M}$ tends to $\bar{\mathcal{M}}$ as $\xi \to +\infty$ and, by definition of $\bar{\xi} < +\infty$, $\mathcal{M}(\bar{\xi}) = \bar{\mathcal{M}}$. Now, $\mathcal{M}$ is increasing with $\mathcal{N} > 0$ and $\mathcal{M} > 0$, so the asymptotic condition for $\mathcal{M}$ can only be satisfied if $\mathcal{M}(\xi) = \bar{\mathcal{M}}$ and $\mathcal{N}(\xi) = 0$ for all $\xi \geq \bar{\xi}$. □

Remark 6.3.1. The case of TWS that satisfy the asymptotic conditions (6.7) for $\bar{\mathcal{M}} = 0$ is not considered in Lemma 6.3.1. By definition, such solutions satisfy $\lim_{\xi \to \pm\infty} \mathcal{M}(\xi) = 0$ for $\mathcal{N} \geq 0$, which is only possible if $\mathcal{M} \equiv 0$ on $\mathbb{R}$ since $\mathcal{M}$ is increasing for $\mathcal{N}, \mathcal{M} > 0$. In this case, system (6.5a)–(6.5b) reduces to the Fisher-KPP equation, which has been extensively studied [77, 127, 174]. It is known that the Fisher-KPP equation admits classical TWS that

satisfy the asymptotic conditions $\lim_{\xi\to-\infty}\mathcal{N}(\xi)=1$, $\lim_{\xi\to+\infty}\mathcal{N}(\xi)=0$ and $\lim_{\xi\to\pm\infty}\frac{\mathrm{d}\mathcal{N}}{\mathrm{d}\xi}(\xi)=0$ for all $c\geq 2$. This result, therefore, holds for TWS of (6.5a)–(6.5b) satisfying the asymptotic conditions (6.7) for $\bar{\mathcal{M}}=0$.

A version of Lemma 6.3.1 for TWS that satisfy the asymptotic conditions (6.6) follows similarly [82]. These results highlight that the solutions we seek are classical solutions of system (6.5a)–(6.5b) on intervals of the form $(-\infty,\bar{\xi})$. Further, if $\bar{\xi}=+\infty$, then the TWS are here called *smooth*. In contrast, if $\bar{\xi}<+\infty$, then Lemma 6.3.1 implies that we have a corner point at $\bar{\xi}$ and the TWS are here called *sharp*.

6.3.1.2 Desingularisation of the ODE system

Definition 6.3.1 describes two types of TWS of system (6.5a)–(6.5b), which differ in the asymptotic conditions they satisfy at infinity. One type of solution converges to $(\mathcal{N},\mathcal{M})=(0,1)$ at infinity. Therefore, we need to elucidate the behaviour of solutions as they approach $\mathcal{M}=1$, which is precisely when system (6.5a)–(6.5b) is *singular*. A common approach to simplify the analysis is to remove this singularity by re-parametrising the system. Given a solution $(\mathcal{N},\mathcal{M})$ of system (6.5a)–(6.5b) satisfying either (6.6) or (6.7), we introduce a new independent variable $y=\Phi(\xi)$ defined such that

$$\frac{\mathrm{d}y}{\mathrm{d}\xi}\equiv\Phi'(\xi)=\frac{1}{1-\mathcal{M}(\xi)}\ \forall\xi\in\mathbb{R}. \tag{6.10}$$

Further introducing the following dependent variables:

$$n(y)=\mathcal{N}(\Phi^{-1}(y)),\quad m(y)=\mathcal{M}(\Phi^{-1}(y)),\quad y\in\mathbb{R}, \tag{6.11}$$

we can apply the chain rule and use (6.10) to find that, for $0\leq m\leq 1$, the trajectories satisfy the following ODE system, for $y\in\mathbb{R}$:

$$\begin{cases}\dfrac{\mathrm{d}^2n}{\mathrm{d}y^2}+c\dfrac{\mathrm{d}n}{\mathrm{d}y}+(1-n)n(1-m)=0, & \text{(6.12a)}\\[2ex] \dfrac{\mathrm{d}m}{\mathrm{d}y}-\dfrac{\kappa}{c}m(1-m)n=0. & \text{(6.12b)}\end{cases}$$

In line with the asymptotic conditions (6.6) and (6.7), we require one of the following to hold:

$$\lim_{y\to-\infty}(n(y),m(y))=(1,0),\ \lim_{y\to+\infty}(n(y),m(y))=(0,1), \tag{6.13}$$

$$\lim_{y\to-\infty}(n(y),m(y))=(1,0),\ \lim_{y\to+\infty}(n(y),m(y))=(0,\bar{m})\text{ with }\bar{m}\in[0,1). \tag{6.14}$$

Importantly, system (6.12a)–(6.12b) is topologically equivalent to system (6.5a)–(6.5b) for $(\mathcal{N},\mathcal{M})\in(0,1)^2$. This follows from the fact that (6.11) defines a homeomorphism that maps the orbits of (6.5a)–(6.5b) onto the orbits of (6.12a)–(6.12b), while preserving their

orientation – Equation (6.10) implies that y is an increasing function of ξ for all $0 \leq \mathcal{M} < 1$. We also observe that, in contrast to system (6.5a)–(6.5b), system (6.12a)–(6.12b) has an additional continuum of steady states of the form $(n, m) = (\bar{n}, 1)$, $\bar{n} \in (0, 1]$. These are not spatially homogeneous steady states of the original PDE system (6.4), so we do not consider them as asymptotic conditions in the context of TWS.

We finally obtain a system of three first order ODEs by introducing the additional variable $p = \frac{\mathrm{d}n}{\mathrm{d}y}$ and, using primes to denote derivatives with respect to y, we have

$$\begin{cases} n' = p, & \text{(6.15a)} \\ p' = -cp - (1-n)n(1-m), & \text{(6.15b)} \\ m' = \dfrac{\kappa}{c} m(1-m)n. & \text{(6.15c)} \end{cases}$$

In the following section, we set up a framework, first proposed in [82] for a different system, to study two distinct types of solutions of (6.15a)–(6.15c). First, those that remain in the region $\mathcal{D}_1$, defined as

$$\mathcal{D}_1 \coloneqq \{(n, p, m) \in \mathbb{R}^3 \mid m \in (0, 1), n \in (0, 1), p \in (-\infty, 0)\}, \tag{6.16}$$

and that satisfy $\lim\limits_{y \to -\infty} (n(y), p(y), m(y)) = (1, 0, 0)$, $\lim\limits_{y \to +\infty} (n(y), p(y), m(y)) = (0, 0, 1)$. Second, for $\bar{m} \in (0, 1)$, those that remain in the region $\mathcal{D}_{\bar{m}}$, defined similarly to (6.16) as

$$\mathcal{D}_{\bar{m}} \coloneqq \{(n, p, m) \in \mathbb{R}^3 \mid m \in (0, \bar{m}), n \in (0, 1), p \in (-\infty, 0)\}, \tag{6.17}$$

and that satisfy $\lim\limits_{y \to -\infty} (n(y), p(y), m(y)) = (1, 0, 0)$, $\lim\limits_{y \to +\infty} (n(y), p(y), m(y)) = (0, 0, \bar{m})$.

6.3.2 The existence and uniqueness of travelling wave solutions

In this section, we study the existence of TWS. To do so, we apply the shooting argument developed by Gallay and Mascia [82]. The crucial difference between Gallay and Mascia's model and system (6.4) is that the latter has an additional continuum of steady states of the form $(0, \bar{M})$, $\bar{M} \in (0, 1)$. We find that the results of [82] for TWS connecting the equilibrium points $(1, 0, 0)$ and $(0, 0, 1)$ apply, with minor modifications, to the TWS of system (6.15a)–(6.15c) that satisfy the same asymptotic conditions (6.6). For completeness, full proofs are, nonetheless, provided for all of the key results, except when they require no modification at all; in such cases we simply state the corresponding results. For TWS of system (6.15a)–(6.15c) that satisfy the asymptotic conditions (6.7), we further develop the shooting argument to obtain new results.

6.3.2.1 Local analysis of the equilibrium point $(1,0,0)$: defining the shooting parameter

The TWS of interest satisfy $\lim_{y\to-\infty}(n(y),p(y),m(y)) = (1,0,0)$. We therefore study the behaviour of solutions of (6.15a)–(6.15c) in a neighbourhood of the equilibrium point $P_1 \coloneqq (1,0,0)$ by performing a linear stability analysis. The Jacobian matrix at P_1 reduces to

$$J\big|_{(1,0,0)} = \begin{bmatrix} 0 & 1 & 0 \\ 1 & -c & 0 \\ 0 & 0 & \frac{\kappa}{c} \end{bmatrix},$$

and it has the following eigenvalues and eigenvectors:

$$\lambda_1 = \frac{-c-\sqrt{c^2+4}}{2}, \quad \lambda_2 = \frac{-c+\sqrt{c^2+4}}{2}, \quad \lambda_3 = \frac{\kappa}{c}, \tag{6.18}$$

$$\vec{v}_1 = \left(\frac{c-\sqrt{c^2+4}}{2}, 1, 0\right)^\top, \quad \vec{v}_2 = \left(\frac{c+\sqrt{c^2+4}}{2}, 1, 0\right)^\top, \quad \vec{v}_3 = (0,0,1)^\top. \tag{6.19}$$

Since λ_1 is negative and λ_2 and λ_3 are positive, P_1 is a three-dimensional hyperbolic saddle point with a two-dimensional unstable manifold, which locally is a plane through P_1 generated by the eigenvectors $\vec{v}_2$ and $\vec{v}_3$. There is also a one-dimensional stable manifold which locally is a straight line spanned by the eigenvector $\vec{v}_1$. Trajectories defined by (6.15a)–(6.15c) that leave P_1 must do so via the two-dimensional unstable manifold at P_1. We, therefore, compute asymptotic expansions of all solutions of (6.15a)–(6.15c) in a neighbourhood of P_1 that lie on the unstable manifold. Requiring that $n \in (0,1)$ and $p < 0$, so that solutions leaving P_1 remain in $\mathcal{D}_1$, we obtain the following result.

Lemma 6.3.2. *Fix $c > 0$. For any $\alpha \geq 0$, the system* (6.15a)–(6.15c) *has a unique solution such that, as $y \to -\infty$,*

$$\begin{aligned} n(y) &= 1 - e^{\lambda_2 y} + \mathcal{O}(e^{(\lambda_2+\mu)y}), \\ p(y) &= -\lambda_2 e^{\lambda_2 y} + \mathcal{O}(e^{(\lambda_2+\mu)y}), \\ m(y) &= \alpha e^{\lambda_3 y} + \mathcal{O}(e^{(\lambda_3+\mu)y}), \end{aligned} \tag{6.20}$$

where λ_2 and λ_3 are given by (6.18) *and $\mu = \min(\lambda_2, \lambda_3) > 0$.*

Remark 6.3.2. The free parameter, α, arises because the form taken by the unstable manifold at P_1 does not impose any condition on m. In a sense, the choice of α is a choice of how fast m increases from 0 and, accordingly, α will influence the value that m attains at $y = +\infty$. We illustrate this in Figure 6.1. In addition, by Remark 6.3.1, it is clear that $\alpha = 0$ is the unique value of the shooting parameter such that the solution of (6.15a)–(6.15c) that satisfies (6.20) stays in a region where $n \in (0,1)$, $p < 0$ and $m = 0$ and satisfies the asymptotic conditions (6.14) for $\bar{m} = 0$.

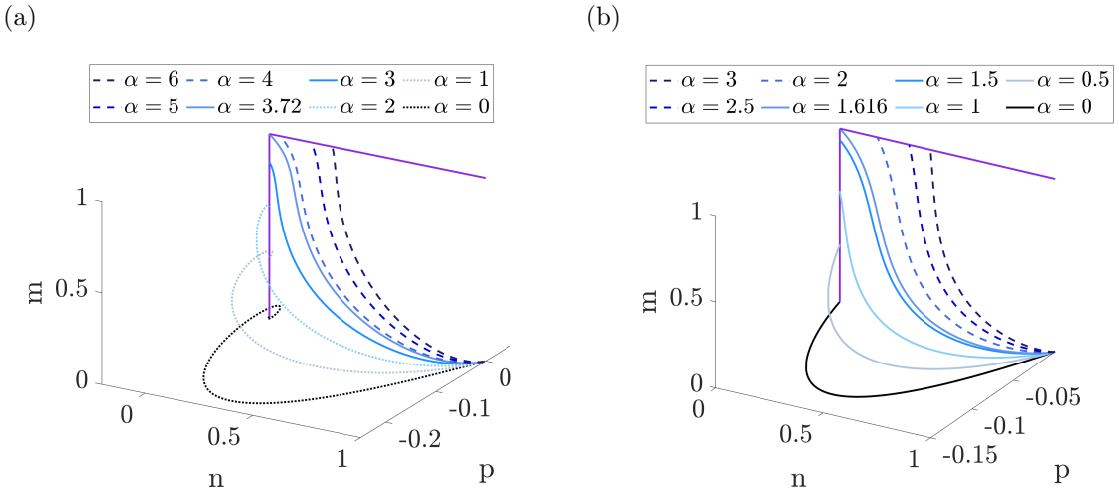


Figure 6.1: Solutions of (6.15a)–(6.15c) subject to asymptotic conditions (6.20) for different values of the shooting parameter α, $\kappa = 1$ and (a) $c = 1$ or (b) $c = 2$. The purple lines are the two continua of steady states of the system (6.15a)–(6.15c), given by $(0, 0, \bar{m})$, $\bar{m} \in [0, 1]$, and $(\bar{n}, 0, 1)$, $\bar{n} \in [0, 1]$, respectively. Since $(n, m) = (\bar{n}, 1)$, $\bar{n} \in [0, 1)$, are not spatially homogeneous steady states of (6.4), the dashed curves represent solutions that are not TWS of (6.4). The dotted curves represent physically unrealistic solutions for which the n-component becomes negative. The values m and n attain at infinity appear to increase monotonically (between 0 and 1) with α.

Now, the idea is to view solutions of (6.15a)–(6.15c) that satisfy (6.20) as functions of α, which we define to be our shooting parameter, and c, which is the wave speed. In particular, we denote by $(n_{\alpha,c}, p_{\alpha,c}, m_{\alpha,c})$ the unique solution of (6.15a)–(6.15c) satisfying (6.20). Our first result is the following.

Lemma 6.3.3. *If the solution $(n_{\alpha,c}, p_{\alpha,c}, m_{\alpha,c})$ is defined on some interval $J := (-\infty, y_0)$, with $y_0 \in \mathbb{R}$, and satisfies $n_{\alpha,c}(y) > 0$ for all $y \in J$, then $(n_{\alpha,c}(y), p_{\alpha,c}(y), m_{\alpha,c}(y)) \in \mathcal{D}_1$ for all $y \in J$.*

Proof. Suppose that $(n_{\alpha,c}, p_{\alpha,c}, m_{\alpha,c})$ is defined on $J := (-\infty, y_0)$, $y_0 \in \mathbb{R}$, and satisfies $n_{\alpha,c}(y) > 0$ for all $y \in J$. We need to check that we also have $n_{\alpha,c}(y) < 1$, $p_{\alpha,c}(y) < 0$ and $0 < m_{\alpha,c}(y) < 1$ for all $y \in J$.

Since $n_{\alpha,c}(y) > 0$ for all $y \in J$, the right-hand side of (6.15c) is strictly positive unless $m_{\alpha,c}(y) = 0$ or $m_{\alpha,c}(y) = 1$, which means $m_{\alpha,c}$ is strictly increasing between 0 and 1. By construction, $m_{\alpha,c}(y) = 0$ only at $y = -\infty$, so $m_{\alpha,c}(y) > 0$ for all $y \in J$. Then, we can integrate (6.15c) from the first $\bar{y} \in \mathbb{R}$ such that $m_{\alpha,c}(\bar{y}) > 0$ to any $y \leq y_0$ to obtain

$$m_{\alpha,c}(y) = \frac{1}{\frac{1-m_{\alpha,c}(\bar{y})}{m_{\alpha,c}(\bar{y})} \exp\left(-\frac{\kappa}{c}\int_{\bar{y}}^{y} n_{\alpha,c}(s)\mathrm{d}s\right) + 1},$$

which yields $m_{\alpha,c}(y) < 1$ for all $y \leq y_0$. We therefore have $m_{\alpha,c}(y) < 1$ for all $y \in J$.

Suppose that $p_{\alpha,c}(y)$ is not strictly negative for all $y \in J$. Then, there exists $y_1 < y_0 \in J$ such that $p_{\alpha,c}(y_1) = 0$ and $p_{\alpha,c}(y) < 0$ for all $y \in (-\infty, y_1)$. Since $n'_{\alpha,c} = p_{\alpha,c}$, $\lim_{y\to-\infty} n_{\alpha,c}(y) = 1$ and $n_{\alpha,c}(y) > 0$ for all $y \in J$, we have $0 < n_{\alpha,c}(y) < 1$ for all $y \in (-\infty, y_1)$. Then, $p'_{\alpha,c}(y_1) = -(1 - n_{\alpha,c}(y_1))n_{\alpha,c}(y_1)(1 - m_{\alpha,c}(y_1)) < 0$, as we have already shown that $m_{\alpha,c}(y) < 1$ for all $y \in J$. This means that there is a strict, non-degenerate maximum for $n_{\alpha,c}$ at y_1, which contradicts the fact that $n_{\alpha,c}(y)$ is strictly decreasing in a left-neighbourhood of y_1. We, therefore, must have $p_{\alpha,c}(y) < 0$ for all $y \in J$, which finally implies that $n_{\alpha,c}(y) < 1$ for all $y \in J$. □

Given Lemma 6.3.3, we introduce the following variable for any $\alpha > 0$ and $c > 0$:

$$T(\alpha, c) \coloneqq \sup\{y_0 \in \mathbb{R} \mid n_{\alpha,c}(y) > 0 \text{ for all } y < y_0\} \in \mathbb{R} \cup \{+\infty\}. \tag{6.21}$$

Then, Lemma 6.3.3 implies that only one of the following holds:

- $T(\alpha, c) < +\infty$, so $n_{\alpha,c}(T(\alpha, c)) = 0$ and $p_{\alpha,c}(T(\alpha, c)) < 0$. In this case, $n_{\alpha,c}(y)$ becomes negative for some $y > T(\alpha, c)$ and $(n_{\alpha,c}, p_{\alpha,c}, m_{\alpha,c})$ does not represent a valid TWS; we disregard these values of the shooting parameter α.
- $T(\alpha, c) = +\infty$, which means that we have a global solution which stays in $\mathcal{D}_1$ for all $y \in \mathbb{R}$. We are interested in finding TWS for these values of α.

Remark 6.3.3. Given $\bar{m} \in (0, 1)$, Lemma 6.3.3 provides a condition under which solutions of (6.15a)–(6.15c) that satisfy (6.20) remain in $\mathcal{D}_1$, but not necessarily in $\mathcal{D}_{\bar{m}} \subset \mathcal{D}_1$. In particular, even if $n_{\alpha,c}(y) > 0$ for all $y \in J$, a solution can leave $\mathcal{D}_{\bar{m}}$. In that case, for a solution of (6.15a)–(6.15c) that satisfies (6.20) to converge to $(0, 0, \bar{m})$ as $y \to +\infty$, we must have $n(y) < 0$ for some values of y (since m is increasing for positive n). Therefore, searching for solutions that satisfy $T(\alpha, c) = +\infty$ is a necessary condition for the existence of physically realistic TWS that converge to $(0, 0, \bar{m})$ as $y \to +\infty$, but not a sufficient one (m may not attain the value $\bar{m}$ for positive n).

6.3.2.2 Monotonicity of solutions with respect to the shooting parameter

A key component of our analysis is that solutions of system (6.15a)–(6.15c) satisfying (6.20) are monotonic functions of the shooting parameter, α, provided $n > 0$. This result can be formulated as follows:

Lemma 6.3.4. *Fix $c > 0$. If $\alpha_2 > \alpha_1 > 0$, then $T(\alpha_2, c) \geq T(\alpha_1, c)$ and the solutions of* (6.15a)–(6.15c) *defined by* (6.20) *satisfy*

$$n_{\alpha_2,c}(y) > n_{\alpha_1,c}(y), \quad m_{\alpha_2,c}(y) > m_{\alpha_1,c}(y), \tag{6.22}$$

for all $y \in (-\infty, T(\alpha_1, c))$.

Proof. Fix $c > 0$ and $\alpha_2 > \alpha_1 > 0$. In the rest of the proof, we denote $n_i = n_{\alpha_i,c}$ and $m_i = m_{\alpha_i,c}$, for $i = 1, 2$.

The first step in this proof is to show that the following inequalities

$$n_{\alpha_2,c}(y) > n_{\alpha_1,c}(y), \quad m_{\alpha_2,c}(y) > m_{\alpha_1,c}(y), \tag{6.23}$$

hold for $y \in (-\infty, y_1)$ for some $y_1 < 0$ sufficiently large and negative. Since this has been proved in [82], we assume 6.23 holds.

The second part of this proof involves showing that $T(\alpha_1, c) \leq T(\alpha_2, c)$ and that inequalities (6.23) hold for all $y \in (-\infty, T(\alpha_1, c))$, where $T(\alpha, c)$ is defined in Equation (6.21).

Suppose for a contradiction that there exists $y_2 < \min(T(\alpha_1, c), T(\alpha_2, c))$ such that inequalities (6.23) hold on the interval $[y_1, y_2)$ but at least one of them becomes an equality at $y = y_2$. We have that

$$n_i'' + cn_i' + g_i n_i = 0, \quad \text{where} \quad g_i = (1 - n_i)(1 - m_i).$$

Since $0 < n_1(y) < n_2(y) < 1$ and $0 < m_1(y) < m_2(y) < 1$ for $y \in [y_1, y_2)$, we know that $0 < g_2(y) < g_1(y)$ for $y \in [y_1, y_2)$. Now, the ratio $\rho(y) = n_2(y)/n_1(y)$ satisfies the following second order ODE:

$$\rho''(y) + \left(c + \frac{2n_1'(y)}{n_1(y)}\right)\rho'(y) + (g_2(y) - g_1(y))\rho(y) = 0, \quad y \in (y_1, y_2). \tag{6.24}$$

Using results from the first part of the proof (see [82]), we know that $\rho(y_1) > 1$ and $\rho'(y_1) > 0$. From (6.24), we note that ρ cannot have a positive maximum in (y_1, y_2), so ρ must be increasing for $y \in (y_1, y_2)$, i.e., $\rho(y) \geq \rho(y_1) > 1$ for $y \in [y_1, y_2)$. Taking the limit as $y \to y_2$, we find that $\rho(y_2) > 1$ and, therefore, $n_2(y) > n_1(y)$ for $y \in [y_1, y_2]$.

We still need to show that we cannot have $m_2(y_2) = m_1(y_2)$. We know that, for $i = 1, 2$,

$$m_i'(y) = \frac{\kappa}{c} m_i(y)(1 - m_i(y))n_i(y), \tag{6.25}$$

for $y \in [y_1, y_2]$. By assumption, $0 < n_1(y) < n_2(y) < 1$ and $0 < m_1(y) < m_2(y) < 1$ for $y \in [y_1, y_2)$, so we can integrate (6.25) from y_1 to $y \leq y_2$ to obtain the following:

$$\frac{m_i(y)}{1 - m_i(y)} = \frac{m_i(y_1)}{1 - m_i(y_1)} \exp\left(\frac{\kappa}{c}\int_{y_1}^{y} n_i(s)\mathrm{d}s\right), \; i = 1, 2. \tag{6.26}$$

In particular,

$$\frac{m_2(y_2)}{1 - m_2(y_2)}\frac{1 - m_1(y_2)}{m_1(y_2)} = \frac{m_2(y_1)}{1 - m_2(y_1)}\frac{1 - m_1(y_1)}{m_1(y_1)} \exp\left(\frac{\kappa}{c}\int_{y_1}^{y_2} (n_2(s) - n_1(s))\mathrm{d}s\right). \tag{6.27}$$

Since $0 < n_1(y) < n_2(y) < 1$ for $y \in [y_1, y_2)$, the exponential term in (6.27) is larger than one. Since we also have $0 < m_1(y) < m_2(y) < 1$ for $y \in [y_1, y_2)$, we obtain the following inequalities:

$$\frac{m_2(y_2)}{1 - m_2(y_2)}\frac{1 - m_1(y_2)}{m_1(y_2)} > \frac{m_2(y_1)}{1 - m_2(y_1)}\frac{1 - m_1(y_1)}{m_1(y_1)} > 1. \tag{6.28}$$

This implies that $m_2(y_2) > m_1(y_2)$.

We have, therefore, shown that both inequalities (6.23) hold at $y = y_2$ and we have reached the desired contradiction, which implies that inequalities (6.23) hold for all $y \in (-\infty, \min(T(\alpha_1, c), T(\alpha_2, c)))$. We must then also have $T(\alpha_1, c) \leq T(\alpha_2, c)$. Otherwise, $n_2(T(\alpha_2, c)) = 0 < n_1(T(\alpha_2, c))$ and, by continuity, we must have $n_{2,c}(y) = n_{1,c}(y)$ for some $y < T(\alpha_2, c)$, which we just showed was impossible. □

Lemma 6.3.4 shows that, for fixed $c > 0$, $T(\alpha, c)$ is an increasing function of α. Since we seek TWS that satisfy $T(\alpha, c) = +\infty$, we define the following critical value of α, which depends on c:

$$\alpha_0(c) \coloneqq \inf\{\alpha > 0 \mid T(\alpha, c) = +\infty\} \in [0, +\infty) \cup \{+\infty\}. \tag{6.29}$$

We then characterise α_0 as a function of c in the following lemma.

Lemma 6.3.5. *If $c \geq 2$, then $\alpha_0(c) = 0$. If $0 < c < 2$, then $0 < \alpha_0(c) < +\infty$.*

Proof. Let $c \geq 2$. To show that $\alpha_0(c) = 0$, we must prove that $T(\alpha, c) = +\infty$ for all $\alpha > 0$. On any interval of the form $(-\infty, y_0]$, $y_0 \in \mathbb{R}$, solutions $(n_{\alpha,c}, p_{\alpha,c}, m_{\alpha,c})$ of (6.15a)–(6.15c) that satisfy the asymptotic conditions (6.20) depend continuously on α, uniformly in y. It is then straightforward to show that, as $\alpha \to 0$, the solution $(n_{\alpha,c}, p_{\alpha,c}, m_{\alpha,c})$ of (6.15a)–(6.15c) converges uniformly on compact intervals to $(n, n', 0)$, where n is the solution of the Fisher-KPP equation

$$n'' + cn' + (1 - n)n = 0, \tag{6.30}$$

subject to the asymptotic conditions

$$\lim_{y \to -\infty} n(y) = 1, \quad \lim_{y \to +\infty} n(y) = 0, \quad \lim_{y \to \pm\infty} n'(y) = 0. \tag{6.31}$$

It is known that this solution satisfies $n(y) > 0$ for all $y \in \mathbb{R}$ for $c \geq 2$. By Lemma 6.3.4, we also know that $n_{\alpha,c}(y)$ is an increasing function of α, so, for any $\alpha > 0$, we must have $n_{\alpha,c}(y) > n(y) > 0$ for all $y \in \mathbb{R}$. Therefore, $T(\alpha, c) = +\infty$ for all $\alpha > 0$, as required.

Let $0 < c < 2$. It is known that the solution to the Fisher-KPP equation (6.30) subject to the asymptotic conditions (6.31) goes negative for such c, which means that there exists $\bar{y} \in \mathbb{R}$ such that $n(\bar{y}) < 0$. Since the solution $(n_{\alpha,c}, p_{\alpha,c}, m_{\alpha,c})$ of (6.15a)–(6.15c) converges uniformly on compact intervals to $(n, n', 0)$, where n is the solution of (6.30) subject to (6.31), we can choose $\alpha > 0$ sufficiently small such that $n_{\alpha,c}(\bar{y}) < 0$. In this case, $T(\alpha, c) < +\infty$ and this implies that $\alpha_0(c) > 0$.

To show that $\alpha_0(c) < +\infty$, we need to prove that there exists $\alpha > 0$ sufficiently large such that $T(\alpha, c) = +\infty$. We begin by introducing $y_0 = (\ln \alpha)/\lambda_3$ and consider the following

shifted asymptotic expansions of $(n_{\alpha,c}, p_{\alpha,c}, m_{\alpha,c})$ at $y \to -\infty$:

$$\begin{aligned}\bar{n}(y) &= n_{\alpha,c}(y - y_0) = 1 - \beta e^{\lambda_2 y} + \mathcal{O}(e^{(\lambda_2+\mu)y}),\\ \bar{p}(y) &= p_{\alpha,c}(y - y_0) = -\lambda_2 \beta e^{\lambda_2 y} + \mathcal{O}(e^{(\lambda_2+\mu)y}),\\ \bar{m}(y) &= m_{\alpha,c}(y - y_0) = e^{\lambda_3 y} + \mathcal{O}(e^{(\lambda_3+\mu)y}),\end{aligned} \tag{6.32}$$

where $\beta = \alpha^{-\lambda_2/\lambda_3}$. On any interval of the form $(-\infty, y_0]$, these functions converge uniformly to $(1, 0, \chi)$ as $\beta \to 0$, where χ is the unique solution of the following differential equation:

$$\chi' = \frac{\kappa}{c}\chi(1 - \chi), \tag{6.33}$$

normalised so that $\chi(y) \to e^{\lambda_3 y} + \mathcal{O}(e^{2\lambda_3 y})$ as $y \to -\infty$. Clearly, χ is increasing and converges to 1 as $y \to +\infty$.

By the uniform convergence of $(\bar{n}, \bar{p}, \bar{m})$ to $(1, 0, \chi)$ as $\beta \to 0$ on $(-\infty, y_0]$, for any $\epsilon > 0$, there exists $\beta^* > 0$ sufficiently small such that

$$\bar{n}(y) \geq 1 - \epsilon, \quad \bar{p}(y) \geq -\epsilon, \quad \bar{m}(y) \geq \chi - \epsilon/2, \quad y \in (-\infty, y_0], \tag{6.34}$$

and these inequalities hold for all $0 < \beta \leq \beta^*$. In addition, as χ converges to 1 as $y \to +\infty$, we can find $y^* \in \mathbb{R}$ such that $\chi(y) \geq 1 - \epsilon/2$ for $y \geq y^*$.

For any $0 < \epsilon < 1$, it is therefore possible to choose $\beta > 0$ small enough and $y_1 = -(\ln \beta)/\lambda_2 \in \mathbb{R}$ large enough such that

$$\bar{n}(y) \geq 1 - \epsilon, \quad \bar{p}(y) \geq -\epsilon, \ \forall y \in (-\infty, y_1], \quad \bar{m}(y_1) \geq 1 - \epsilon. \tag{6.35}$$

We set $\epsilon = 1/(2K)$, where

$$K = 1 + \frac{1}{c} + \frac{2}{\kappa} > 1. \tag{6.36}$$

We can, therefore, find β and y_1 such that (6.35) holds for this ϵ. Then, the idea for the rest of this proof is to show that we have $\bar{n}(y) \geq 1 - \epsilon K = 1/2$ for all $y \in [y_1, +\infty)$, which would imply that there exists $\alpha < +\infty$ such that $T(\alpha, c) = +\infty$, as required.

Suppose, for a contradiction, that we can find $y > y_1$ such that $\bar{n}(y) < 1/2$. Then, there must exist $y_2 > y_1$ such that $\bar{n}(y_2) = 1/2$ and $\bar{n}(y) \geq 1/2$ for all $y \in (-\infty, y_2]$. Since $\bar{n}(y) \geq 1/2$ for $y \in [y_1, y_2]$, $\bar{m}$ satisfies the following for $y \in [y_1, y_2]$:

$$\bar{m}' = \frac{\kappa}{c}(1 - \bar{m})\bar{m}\bar{n} \geq \frac{\kappa}{2c}(1 - \bar{m})\bar{m}. \tag{6.37}$$

We recall that, by assumption, $\bar{m}(y_1) \geq 1 - \epsilon$ and, therefore, we can integrate (6.37) from y_1 to $y \in (y_1, y_2]$ to obtain

$$\frac{\bar{m}(y)}{1 - \bar{m}(y)} \geq \frac{\bar{m}(y_1)}{1 - \bar{m}(y_1)} e^{\left(\frac{\kappa}{2c}(y - y_1)\right)} \geq \frac{1 - \epsilon}{\epsilon} e^{\left(\frac{\kappa}{2c}(y - y_1)\right)}. \tag{6.38}$$

From (6.38), we can show that $1 - \bar{m}(y) \leq 2\epsilon e^{-\left(\frac{\kappa}{2c}(y-y_1)\right)}$ for $y \in [y_1, y_2]$. Moreover, since $\bar{n}(y) \geq 1/2$ for $y \in [y_1, y_2]$, we can see that $\bar{n}(y)$ satisfies the following inequality for $y \in [y_1, y_2]$:

$$\bar{n}''(y) + c\bar{n}'(y) + \epsilon e^{-\left(\frac{\kappa}{2c}(y-y_1)\right)} \geq \bar{n}''(y) + c\bar{n}'(y) + (1 - \bar{n}(y))\bar{n}(y)(1 - \bar{m}(y)) = 0. \quad (6.39)$$

We integrate this inequality with respect to y from y_1 to any $y \in (y_1, y_2]$ and, assuming that $c - \kappa/(2c) \neq 0$, we obtain

$$\bar{n}'(y) \geq \bar{n}'(y_1)e^{-c(y-y_1)} - \frac{\epsilon}{c - \kappa/(2c)}\left(e^{-(\kappa/(2c))(y-y_1)} - e^{-c(y-y_1)}\right). \quad (6.40)$$

This inequality can be integrated a second time to finally obtain

$$\begin{aligned}
\bar{n}(y) &\geq \bar{n}(y_1) + \bar{n}'(y_1)\frac{1 - e^{-c(y-y_1)}}{c} - \frac{\epsilon}{c - \kappa/(2c)}\left(\frac{1 - e^{-(\kappa/(2c))(y-y_1)}}{\kappa/(2c)} + \frac{-1 + e^{-c(y-y_1)}}{c}\right), \\
&> \bar{n}(y_1) + \frac{1}{c}\bar{n}'(y_1) - \frac{\epsilon}{c\kappa/(2c)}, \\
&\geq 1 - \epsilon - \frac{\epsilon}{c} - \frac{2\epsilon}{\kappa} = 1 - K\epsilon = 1/2,
\end{aligned} \quad (6.41)$$

where the second (strict) inequality relies on the fact that $\bar{n}(y_1) \geq 1 - \epsilon$ and $\bar{n}'(y_1) \geq -\epsilon$, by assumption. In particular, (6.41) implies that $\bar{n}(y_2) > 1/2$, which contradicts our assumption that $\bar{n}(y_2) = 1/2$. We therefore have that $\bar{n}(y) \geq 1/2$ holds for all $y \in [y_1, +\infty)$, as required.

In the case where $c - \kappa/(2c) = 0$, a similar proof follows, taking $\epsilon = 1/(2K)$, where $K = 1 + 1/c + 1/c^2 > 1$. We note that equations (6.37)–(6.39) still hold and, integrating (6.39) with respect to y from y_1 to any $y \in (y_1, y_2]$, we obtain

$$\bar{n}'(y) \geq \bar{n}'(y_1)e^{-c(y-y_1)} - \epsilon(y - y_1)e^{-c(y-y_1)}. \quad (6.42)$$

Integrating this inequality once more, we find

$$\begin{aligned}
\bar{n}(y) &\geq \bar{n}(y_1) + \bar{n}'(y_1)\frac{1 - e^{-c(y-y_1)}}{c} + \epsilon\left(\frac{(y - y_1)e^{-c(y-y_1)}}{c} + \frac{e^{-c(y-y_1)} - 1}{c^2}\right), \\
&> \bar{n}(y_1) + \frac{1}{c}\bar{n}'(y_1) - \frac{\epsilon}{c^2}, \\
&\geq 1 - \epsilon - \frac{\epsilon}{c} - \frac{\epsilon}{c^2} = 1 - K\epsilon = 1/2,
\end{aligned} \quad (6.43)$$

where the second (strict) inequality relies on the fact that $\bar{n}(y_1) \geq 1 - \epsilon$ and $\bar{n}'(y_1) \geq -\epsilon$, by assumption. This proves the desired contradiction for $c - \kappa/(2c) = 0$.

To conclude, we have shown that $T(\alpha, c) = +\infty$ for $\alpha > 0$ large enough (equivalently $\beta > 0$ small enough). □

Lemma 6.3.5 ensures that, for all $c > 0$, there exist some values of α for which $T(\alpha, c) = +\infty$ and, thus, for all $c > 0$, there exist some TWS. It remains to elucidate the behaviour of solutions at infinity to determine which TWS exist for each $c > 0$.

Remark 6.3.4. The proof of Lemma 6.3.5 relies on showing that, for any $0 < c < 2$, we can choose $\alpha(c) > 0$ sufficiently large such that there exists a solution of system (6.15a)–(6.15c) that satisfies (6.20), remains in region $\mathcal{D}_1$ and converges to $(\bar{n}, 0, 1)$ as $y \to +\infty$, with $\bar{n} \in (0, 1)$. Such solutions are not TWS, but their existence will be crucial in proving the existence of the TWS we seek.

6.3.2.3 The behaviour of solutions at infinity

By Lemma 6.3.5, we know that, for any $c > 0$, there exist solutions of system (6.15a)–(6.15c) that satisfy (6.20) and remain in region $\mathcal{D}_1$ for all $y \in \mathbb{R}$. It remains to characterise the behaviour of these solutions as $y \to +\infty$, and, in so doing, to establish whether they are TWS. Denoting the limits of components of the solution at infinity as

$$n_\infty(\alpha, c) \coloneqq \lim_{y\to+\infty} n_{\alpha,c}(y), \quad m_\infty(\alpha, c) \coloneqq \lim_{y\to+\infty} m_{\alpha,c}(y), \quad p_\infty(\alpha, c) \coloneqq \lim_{y\to+\infty} p_{\alpha,c}(y),$$

we introduce the following lemma.

Lemma 6.3.6. *If $T(\alpha, c) = +\infty$, then the following limits exist:*

$$n_\infty(\alpha, c) \in [0, 1), \quad m_\infty(\alpha, c) \in [0, 1] \quad \textit{and} \quad p_\infty(\alpha, c) = 0. \tag{6.44}$$

Moreover, if $m_\infty(\alpha, c) \in [0, 1)$, then $n_\infty(\alpha, c) = 0$, and, if $n_\infty(\alpha, c) \in (0, 1)$, then $m_\infty(\alpha, c) = 1$.

Proof. Suppose that $T(\alpha, c) = +\infty$. Then, by Lemma 6.3.3, the solution $(n_{\alpha,c}, p_{\alpha,c}, m_{\alpha,c})$ of (6.15a)–(6.15c) that satisfies (6.20) stays in region $\mathcal{D}_1$, defined by (6.16), for all $y \in \mathbb{R}$. This implies that $n_{\alpha,c}(y) > 0$ and $n'_{\alpha,c}(y) = p_{\alpha,c}(y) < 0 \ \forall y \in \mathbb{R}$ and, as $n_{\alpha,c}$ satisfies (6.20), we also have $n_{\alpha,c}(y) < 1 \ \forall y \in \mathbb{R}$. This means that n is strictly decreasing and bounded above and below by 1 and 0, respectively, in $\mathbb{R}$ and, thus, $n_\infty(\alpha, c) \in [0, 1)$ exists. Since $p_{\alpha,c} \coloneqq n'_{\alpha,c}$, the latter implies that $p_\infty(\alpha, c)$ exists and $p_\infty(\alpha, c) = 0$; otherwise $n_{\alpha,c}(y)$ cannot converge to a finite limit as $y \to +\infty$. Moreover, by the definition of $\mathcal{D}_1$, we have that $0 < m_{\alpha,c}(y) < 1 \ \forall y \in \mathbb{R}$ and, since $n_{\alpha,c}(y) > 0 \, \forall y \in \mathbb{R}$, this implies that $m'_{\alpha,c}(y) = \frac{\kappa}{c} m_{\alpha,c}(y)(1 - m_{\alpha,c}(y)) n_{\alpha,c}(y) > 0 \, \forall y \in \mathbb{R}$. Hence, $m_{\alpha,c}$ is strictly increasing and bounded above and below by 1 and 0, respectively, in $\mathbb{R}$, and thus $m_\infty(\alpha, c) \in (0, 1]$ exists. Finally, if the components of $(n_\infty(\alpha, c), p_\infty(\alpha, c), m_\infty(\alpha, c))$ exist, then this must be an equilibrium of (6.15a)–(6.15c). The final statement of the lemma follows. □

Lemma 6.3.6 defines the possible limits of solutions $(n_{\alpha,c}, p_{\alpha,c}, m_{\alpha,c})$ of (6.15a)–(6.15c) that satisfy (6.20) and remain in region $\mathcal{D}_1$. We must now determine for which values of $c > 0$ we can find $\alpha(c) > 0$ such that the corresponding solution $(n_{\alpha,c}, p_{\alpha,c}, m_{\alpha,c})$:

1. remains in $\mathcal{D}_1$ and converges to $(0, 0, 1)$ as $y \to +\infty$, or,

2. for each $\bar{m} \in (0, 1)$, remains in $\mathcal{D}_{\bar{m}}$ and converges to $(0, 0, \bar{m})$ as $y \to +\infty$.

We consider these cases separately in the two sections that follow.

6.3.2.4 Solutions converging to the equilibrium point $(0, 0, 1)$

In this section, we show that, for each $c > 0$, there exists a unique value of $\alpha > 0$ such that the solution $(n_{\alpha,c}, p_{\alpha,c}, m_{\alpha,c})$ of system (6.15a)–(6.15c) satisfying (6.20) remains in region $\mathcal{D}_1$ and converges to the equilibrium point $P_2 \coloneqq (0, 0, 1)$ as $y \to +\infty$. This then allows us to draw conclusions about the existence and uniqueness of TWS that satisfy the asymptotic conditions (6.6).

By Remark 6.3.4, we have that, for any $c > 0$, there exists $\alpha(c) > 0$ sufficiently large such that the solution of system (6.15a)–(6.15c) satisfying (6.20) remains in region $\mathcal{D}_1$ and satisfies $m_\infty = 1$. We can, therefore, define

$$\alpha_1(c) \coloneqq \inf \{\alpha > \alpha_0(c) \mid m_\infty(\alpha, c) = 1\} \in [0, +\infty) \cup \{+\infty\}, \tag{6.45}$$

and prove the following result.

Lemma 6.3.7. *For any $c > 0$, we have $0 < \alpha_1(c) < +\infty$.*

Proof. Fix $c > 0$. By Remark 6.3.4, we know that there exists $\alpha = \alpha(c) < +\infty$ large enough such that $m_\infty(\alpha, c) = 1$ and, hence, $\alpha_1(c) < +\infty$. If $0 < c < 2$, then we know by Lemma 6.3.5 that $\alpha_0(c) > 0$ and, therefore, by the definition of $\alpha_1(c)$, we must have $\alpha_1(c) \geq \alpha_0(c) > 0$.

If $c \geq 2$, then suppose, for a contradiction, that $\alpha_1(c) = 0$. A linear stability analysis about the equilibrium point $(0, 0, \bar{m}_1)$ with $\bar{m}_1 \in [0, 1)$ shows that it is non-hyperbolic, with two negative eigenvalues λ_1, λ_2 and one zero eigenvalue λ_3:

$$\lambda_{1,2} = \frac{-c \pm \sqrt{c^2 - 4(1 - \bar{m})}}{2}, \quad \lambda_3 = 0. \tag{6.46}$$

Therefore, by the Centre Manifold Theorem, in a small, open neighbourhood of $(0, 0, \bar{m}_1)$ with $\bar{m}_1 \in [0, 1)$, there exists a two-dimensional stable manifold, spanned by the eigenvectors $\vec{v}_{1,2}$ corresponding to $\lambda_{1,2}$. In this neighbourhood, there also exists a one-dimensional centre manifold spanned by $\vec{v}_3 = (0, 0, 1)^\top$, which comprises the family of equilibria $(0, 0, \bar{m}_2)$ with $\bar{m}_2$ sufficiently close to $\bar{m}_1$. Therefore, for fixed $0 < \epsilon < 1$, we can find a neighbourhood Ω

of $(0,0,0)$ that is foliated by two-dimensional stable leaves over a one-dimensional centre manifold, composed of points of the form $(0,0,\bar{m})$ with $0 \leq \bar{m} < \epsilon$. Then, any solution that enters Ω converges to $(0,0,\bar{m})$ as $y \to +\infty$ for some $\bar{m}$ that satisfies $0 \leq \bar{m} < \epsilon$.

Now, by Remark 6.3.2, $\alpha_1(c) = 0$ implies that $(n_\infty(\alpha_1(c),c), p_\infty(\alpha_1(c),c), m_\infty(\alpha_1(c),c)) = (0,0,0)$. Thus, we can find $\bar{y} \in \mathbb{R}$ large enough such that $(n_{\alpha_1(c),c}(y), p_{\alpha_1(c),c}(y), m_{\alpha_1(c),c}(y)) \in \Omega$ for all $y \geq \bar{y}$. By continuity of solutions with respect to α, we can find $\delta > 0$ such that $(n_{\alpha,c}(\bar{y}), p_{\alpha,c}(\bar{y}), m_{\alpha,c}(\bar{y})) \in \Omega$ for any $0 < \alpha < \delta$. This implies that, for any such α, $(n_{\alpha,c}(y), p_{\alpha,c}(y), m_{\alpha,c}(y))$ converges to $(0,0,\bar{m}) \in \Omega$ as $y \to +\infty$. Since $0 \leq \bar{m} < \epsilon$ by our choice of Ω, there exists $0 < \alpha < \delta$ such that $0 \leq m_\infty(\alpha,c) < \epsilon$. However, since $\alpha_1(c) = 0$, we must have $m_\infty(\alpha,c) = 1$ for all $\alpha > 0$ and we have reached the desired contradiction. □

Lemma 6.3.7 ensures that, for any $c > 0$ and $\alpha \geq \alpha_1(c)$, the solution $(n_{\alpha,c}, p_{\alpha,c}, m_{\alpha,c})$ of (6.15a)–(6.15c), subject to the asymptotic conditions (6.20), stays in region $\mathcal{D}_1$ and satisfies $(n_\infty(\alpha,c), p_\infty(\alpha,c), m_\infty(\alpha,c)) = (n_\infty(\alpha,c), 0, 1)$, where $n_\infty(\alpha,c) \in [0,1)$. We would now like to show that, for any $c > 0$, there exists a unique $\alpha \geq \alpha_1(c)$ such that $n_\infty(\alpha,c) = 0$.

For the rest of this section, we suppose that $\alpha \geq \alpha_1(c)$. A linear stability analysis at the equilibrium point P_2 shows that P_2 is non-hyperbolic, with one negative eigenvalue and two zero eigenvalues. Therefore, at P_2, we have a one-dimensional stable manifold, $\mathcal{W}_S \subset \mathbb{R}^3$, generated by the eigenvector $\vec{v}_1 = (1/c, 1, 0)^\top$ associated with $\lambda_1 = -c$. We also have a two-dimensional centre manifold, $\mathcal{W}_C \subset \mathbb{R}^3$, which is tangent at P_2 to the subspace spanned by the eigenvectors $\vec{v}_2 = (1,0,0)^\top$ and $\vec{v}_3 = (0,0,1)^\top$ associated with $\lambda_2 = \lambda_3 = 0$. Solutions of (6.15a)–(6.15c) that satisfy (6.20) and remain in a small enough neighbourhood of P_2 for all sufficiently large $y > 0$ converge to $\mathcal{W}_C$. Therefore, in order to study the dynamics around P_2, we perform a nonlinear local stability analysis. We begin by transforming system (6.15a)–(6.15c) into normal form by introducing the following variables:

$$\tilde{n}(y) = n(y) + p(y)/c, \quad \tilde{p}(y) = p(y), \quad \tilde{m}(y) = 1 - m(y), \tag{6.47}$$

which satisfy the following system:

$$\begin{cases} \dfrac{\mathrm{d}\tilde{n}}{\mathrm{d}y} = -\dfrac{1}{c}\tilde{m}\left(\tilde{n} - \dfrac{\tilde{p}}{c}\right)\left(1 - \tilde{n} + \dfrac{\tilde{p}}{c}\right), & \text{(6.48a)} \\ \dfrac{\mathrm{d}\tilde{p}}{\mathrm{d}y} = -c\tilde{p} - \tilde{m}\left(\tilde{n} - \dfrac{\tilde{p}}{c}\right)\left(1 - \tilde{n} + \dfrac{\tilde{p}}{c}\right), & \text{(6.48b)} \\ \dfrac{\mathrm{d}\tilde{m}}{\mathrm{d}y} = -\dfrac{\kappa}{c}\tilde{m}(1-\tilde{m})\left(\tilde{n} - \dfrac{\tilde{p}}{c}\right). & \text{(6.48c)} \end{cases}$$

Then, we know that, in a neighbourhood of the origin, the centre manifold can be described by a function $\mathcal{P}(\tilde{n},\tilde{m})$ such that $(\tilde{n},\tilde{p},\tilde{m}) \in \mathcal{W}_C$ if and only if $\tilde{p} = \mathcal{P}(\tilde{n},\tilde{m})$, where

$$\mathcal{P}(\tilde{n},\tilde{m}) = -\frac{1}{c}\tilde{n}\tilde{m}(1 + \mathcal{O}(|\tilde{n}| + |\tilde{m}|)). \tag{6.49}$$

Using this expression for the centre manifold in a neighbourhood of the origin, we must now prove that there is a solution of system (6.48a)–(6.48c) converging to the centre manifold $\mathcal{W}_C$ that converges to the origin as $y \to +\infty$. We are interested in solutions (n, p, m) of (6.15a)–(6.15c) that satisfy (6.20) and remain in region $\mathcal{D}_1$ for all $y \in \mathbb{R}$. Equivalently, we seek solutions $(\tilde{n}, \tilde{p}, \tilde{m})$ of (6.48a)–(6.48c) that satisfy (6.20) and lie on a manifold $\mathcal{W}_C^+ \subset \mathcal{W}_C$, where

$$\mathcal{W}_C^+ = \{(\tilde{n}, \tilde{p}, \tilde{m}) \in \mathcal{W}_C \mid \tilde{n}, \tilde{m} > 0\}. \tag{6.50}$$

The following lemma characterises such solutions that converge to the origin as $y \to +\infty$.

Lemma 6.3.8. *Up to translations in the variable y, there exists a unique solution of* (6.48a)–(6.48c) *that satisfies the asymptotic conditions* (6.20)*, lies on the centre manifold $\mathcal{W}_C^+$, and whose components converge to zero as $y \to +\infty$, such that*

$$\tilde{n}(y) = \frac{c}{\kappa y} + \mathcal{O}\left(\frac{1}{y^2}\right) \quad \textit{and} \quad \tilde{m}(y) = \frac{c}{y} + \mathcal{O}\left(\frac{1}{y^2}\right). \tag{6.51}$$

Proof. We will begin by proving that a solution $(\tilde{n}, \tilde{p}, \tilde{m})$ of the following system:

$$\begin{cases} \dfrac{\mathrm{d}\tilde{n}}{\mathrm{d}y} = -\dfrac{1}{c}\tilde{m}\left(\tilde{n} - \dfrac{\tilde{p}}{c}\right)\left(1 - \tilde{n} + \dfrac{\tilde{p}}{c}\right), & \text{(6.52a)} \\ \dfrac{\mathrm{d}\tilde{p}}{\mathrm{d}y} = -c\tilde{p} - \tilde{m}\left(\tilde{n} - \dfrac{\tilde{p}}{c}\right)\left(1 - \tilde{n} + \dfrac{\tilde{p}}{c}\right), & \text{(6.52b)} \\ \dfrac{\mathrm{d}\tilde{m}}{\mathrm{d}y} = -\dfrac{\kappa}{c}\tilde{m}(1 - \tilde{m})\left(\tilde{n} - \dfrac{\tilde{p}}{c}\right), & \text{(6.52c)} \end{cases}$$

subject to the asymptotic conditions (6.20) and whose components converge to zero as $y \to +\infty$ exists on $\mathcal{W}_C^+$. We introduce the ansatz

$$\tilde{n}(y) = \frac{a}{y} f(\ln y), \quad \tilde{m}(y) = \frac{b}{y} g(\ln y), \quad z = \ln y, \tag{6.53}$$

where $a \coloneqq c/\kappa$ and $b \coloneqq c$. For $\tilde{n}$ and $\tilde{m}$ evolving according to (6.52a) and (6.52c), with $\tilde{p} = \mathcal{P}(\tilde{n}, \tilde{m})$, the functions f and g satisfy

$$\begin{cases} \dfrac{\mathrm{d}f}{\mathrm{d}z} = f - \dfrac{1}{c}\dfrac{b}{a} g\left(af - e^z \dfrac{\mathcal{P}}{c}\right)\left(1 - e^{-z} af + \dfrac{\mathcal{P}}{c}\right), & \text{(6.54a)} \\ \dfrac{\mathrm{d}g}{\mathrm{d}z} = g + \dfrac{\kappa}{c} g(1 - be^{-z} g)\left(-af + e^z \dfrac{\mathcal{P}}{c}\right). & \text{(6.54b)} \end{cases}$$

Now, we recall that

$$\mathcal{P}(\tilde{n}, \tilde{m}) = -\frac{1}{c}\tilde{n}\tilde{m}(1 + \mathcal{O}(|\tilde{n}| + |\tilde{m}|)). \tag{6.55}$$

Hence, from (6.53), we have

$$\left|\mathcal{P}(\tilde{n},\tilde{m})\right| = \left| - e^{-2z}\frac{c}{\kappa}fg\right| \leq e^{-2z}\frac{c}{\kappa}|f||g|. \tag{6.56}$$

Since f and g are bounded for all $z \in \mathbb{R}$, $\mathcal{P}$ converges to 0 as $z \to +\infty$ and we can similarly show that $e^z\mathcal{P}$ converges to 0 as $z \to +\infty$. Therefore, system (6.54a)–(6.54b) converges, as $z \to +\infty$, to

$$\begin{cases} \dfrac{\mathrm{d}f}{\mathrm{d}z} = f - gf = f(1-g), & \text{(6.57a)} \\ \dfrac{\mathrm{d}g}{\mathrm{d}z} = g - gf = g(1-f). & \text{(6.57b)} \end{cases}$$

This system has a unique, strictly positive fixed point $(f^*, g^*) = (1, 1)$ and it can easily be verified through a linear stability analysis that this fixed point is hyperbolic with eigenvalues $\lambda_1 = 1, \lambda_2 = -1$. Therefore, there exists a one-dimensional stable manifold along which solutions to (6.54a)–(6.54b) can converge to $(1, 1)$ as $z \to +\infty$ and they satisfy $|f(z) - 1| + |g(z) - 1| = \mathcal{O}(e^{-z})$ in this limit. We can, therefore, conclude that there exists a solution of (6.52a)–(6.52c) subject to the asymptotic conditions (6.20), on $\mathcal{W}_C^+$, whose components converge to $(0, 0)$ as $y \to +\infty$, such that

$$\tilde{n}(y) = \frac{c}{\kappa y} + \mathcal{O}\left(\frac{1}{y^2}\right) \quad \text{and} \quad \tilde{m}(y) = \frac{c}{y} + \mathcal{O}\left(\frac{1}{y^2}\right), \quad \text{as } y \to +\infty. \tag{6.58}$$

We must now prove uniqueness of the above solution. We will do so by proving that any arbitrary positive solution to (6.52a)–(6.52c) on the centre manifold $\mathcal{W}_C^+$ that converges to the origin as $y \to +\infty$ must satisfy the asymptotic condition (6.58). This means that there exists $y_1 > 0$ large enough such that the chosen arbitrary solution coincides with the constructed solution for all $y \in [y_1, +\infty)$. This precisely implies that the arbitrary solution chosen coincides with the constructed solution on the centre manifold, from which uniqueness follows.

For ease of notation, we write the evolution of $\tilde{n}$ and $\tilde{m}$ on $\mathcal{W}_C^+$ as follows:

$$\begin{cases} \dfrac{\mathrm{d}\tilde{n}}{\mathrm{d}y} = -\dfrac{1}{c}\tilde{m}\left(\tilde{n} - \dfrac{\mathcal{P}(\tilde{n},\tilde{m})}{c}\right)\left(1 - \tilde{n} + \dfrac{\mathcal{P}(\tilde{n},\tilde{m})}{c}\right) = \mathcal{G}(\tilde{n},\tilde{m}), & \text{(6.59a)} \\ \dfrac{\mathrm{d}\tilde{m}}{\mathrm{d}y} = -\dfrac{\kappa}{c}\tilde{m}(1-\tilde{m})\left(\tilde{n} - \dfrac{\mathcal{P}(\tilde{n},\tilde{m})}{c}\right) = \mathcal{H}(\tilde{n},\tilde{m}). & \text{(6.59b)} \end{cases}$$

The solution $(\tilde{n}, \tilde{m})$ constructed above satisfies $\tilde{n} = \Phi(\tilde{m})$ in some ϵ-neighbourhood of the origin, where $\epsilon > 0$ and $\Phi : (0, \epsilon) \to \mathbb{R}^+$ is a C^k function satisfying the following functional relation for $w \in (0, \epsilon)$:

$$\mathcal{G}(\Phi(w), w) = \Phi'(w)\mathcal{H}(\Phi(w), w). \tag{6.60}$$

In particular, the solution $(\tilde{n}, \tilde{m})$ satisfies (6.58), so we have $\Phi(w) = w/\kappa + \mathcal{O}(w^2)$ as $w \to 0$.

Now, consider any arbitrary positive solution $(\tilde{n}, \tilde{m})$ of (6.59a)–(6.59b) that converges to the origin as $y \to +\infty$. Using (6.59a)–(6.59b), we find

$$\frac{\mathrm{d}}{\mathrm{d}y}(\tilde{n} - \Phi(\tilde{m})) = \mathcal{G}(\tilde{n}, \tilde{m}) - \Phi'(\tilde{m})\mathcal{H}(\tilde{n}, \tilde{m}). \tag{6.61}$$

Using (6.60) and adding and subtracting $\mathcal{G}(\Phi(\tilde{m}), \tilde{m}) = \Phi'(\tilde{m})\mathcal{H}(\Phi(\tilde{m}), \tilde{m})$ to the right-hand side of (6.61), we obtain

$$\frac{\mathrm{d}}{\mathrm{d}y}(\tilde{n} - \Phi(\tilde{m})) = \mathcal{G}(\tilde{n}, \tilde{m}) - \mathcal{G}(\Phi(\tilde{m}), \tilde{m}) - \Phi'(\tilde{m})(\mathcal{H}(\tilde{n}, \tilde{m}) - \mathcal{H}(\Phi(\tilde{m}), \tilde{m})). \tag{6.62}$$

Now, we note that, by the Fundamental Theorem of Calculus for line integrals,

$$\begin{cases} \mathcal{G}(\tilde{n}, \tilde{m}) - \mathcal{G}(\Phi(\tilde{m}), \tilde{m}) = \int_{\Phi(\tilde{m})}^{\tilde{n}} \partial_1 \mathcal{G}(s, \tilde{m})\mathrm{d}s, \\ \Phi'(\tilde{m})(\mathcal{H}(\tilde{n}, \tilde{m}) - \mathcal{H}(\Phi(\tilde{m}), \tilde{m})) = \Phi'(\tilde{m}) \int_{\Phi(\tilde{m})}^{\tilde{n}} \partial_1 \mathcal{H}(s, \tilde{m})\mathrm{d}s, \end{cases} \tag{6.63}$$

where we have denoted the derivative with respect to the first variable, $\tilde{n}$, by ∂_1. Finally, using (6.63) and reparametrising the curve from $(\Phi(\tilde{m}), \tilde{m})$ to $(\tilde{n}, \tilde{m})$, Equation (6.62) yields

$$\frac{\mathrm{d}}{\mathrm{d}y}(\tilde{n} - \Phi(\tilde{m})) = \Delta(\tilde{n}, \tilde{m})(\tilde{n} - \Phi(\tilde{m})), \tag{6.64}$$

where

$$\Delta(\tilde{n}, \tilde{m}) \coloneqq \int_0^1 \left(\partial_1 \mathcal{G}\left((1-t)\Phi(\tilde{m}) + t\tilde{n}, \tilde{m}\right) - \Phi'(\tilde{m})\partial_1 \mathcal{H}\left((1-t)\Phi(\tilde{m}) + t\tilde{n}, \tilde{m}\right)\right) \mathrm{d}t. \tag{6.65}$$

Using (6.55) and (6.59a)–(6.59b), it is straightforward to find the following asymptotic expansion of $\Delta(\tilde{n}, \tilde{m})$ as $(\tilde{n}, \tilde{m}) \to (0, 0)$:

$$\Delta(\tilde{n}, \tilde{m}) = \frac{\tilde{m}}{c}\left(\frac{1-\kappa}{\kappa}\tilde{m} + \tilde{n}\right)(1 + \mathcal{O}(|\tilde{n}| + |\tilde{m}|)). \tag{6.66}$$

In particular, if $0 < \kappa \leq 1$, then $\Delta(\tilde{n}, \tilde{m}) > 0$ for sufficiently small $(\tilde{n}, \tilde{m})$ on $\mathcal{W}_C^+$. Now, we can choose $y_1 > 0$ sufficiently large (to ensure that $(\tilde{n}, \tilde{m})$ is sufficiently small) and integrate (6.64) from y_1 to y_2 to obtain

$$\tilde{n}(y_2) - \Phi(\tilde{m}(y_2)) = \exp\left(\int_{y_1}^{y_2} \Delta(\tilde{n}(y), \tilde{m}(y))\mathrm{d}y\right)(\tilde{n}(y_1) - \Phi(\tilde{m}(y_1))), \tag{6.67}$$

from which we have that $|\tilde{n}(y_2) - \Phi(\tilde{m}(y_2))| \geq |\tilde{n}(y_1) - \Phi(\tilde{m}(y_1))|$, whenever $0 < \kappa \leq 1$. By assumption, $(\tilde{n}, \tilde{m})$ converges to $(0, 0)$ as $y \to +\infty$, i.e., $\tilde{n}$ and $\Phi(\tilde{m})$ both converge to 0 as $y \to +\infty$. Therefore, the left-hand side of the above inequality converges to zero as $y_2 \to +\infty$, which implies that, if $0 < \kappa \leq 1$, then $\tilde{n}(y_1) = \Phi(\tilde{m}(y_1))$ for all sufficiently large $y_1 > 0$. We can then conclude that, if $0 < \kappa \leq 1$, then any positive solution $(\tilde{n}, \tilde{m})$ to (6.59a)–(6.59b) on the centre manifold, which converges to the origin as $y \to +\infty$, coincides, up to a translation in y, with the solution constructed in the first part of the proof.

We can similarly show that we have uniqueness for $\kappa > 1$. The solution $(\tilde{n}, \tilde{m})$ constructed in the first part of the proof satisfies $\tilde{m} = \Psi(\tilde{n})$ in some ϵ-neighbourhood of the origin, where $\epsilon > 0$ and $\Psi : (0, \epsilon) \to \mathbb{R}^+$ is a C^k function satisfying the following functional relation for $w \in (0, \epsilon)$:

$$\mathcal{H}(w, \Psi(w)) = \Psi'(w)\mathcal{G}(w, \Psi(w)). \tag{6.68}$$

In particular, the solution $(\tilde{n}, \tilde{m})$ satisfies (6.58), so we have $\Psi(w) = \kappa w + \mathcal{O}(w^2)$ as $w \to 0$.

Now, consider again any arbitrary positive solution $(\tilde{n}, \tilde{m})$ of (6.59a)–(6.59b) that converges to the origin as $y \to +\infty$. Similarly to the derivation of (6.64), we find

$$\frac{\mathrm{d}}{\mathrm{d}y}(\tilde{m} - \Psi(\tilde{n})) = \Delta(\tilde{n}, \tilde{m})(\tilde{m} - \Psi(\tilde{n})), \tag{6.69}$$

where, denoting the derivative with respect to the second variable, $\tilde{m}$, by ∂_2, we have

$$\Delta(\tilde{n}, \tilde{m}) = \int_0^1 \left(\partial_2\mathcal{H}\left(\tilde{n}, (1-t)\Psi(\tilde{n}) + t\tilde{m}\right) - \Psi'(\tilde{n})\partial_2\mathcal{G}\left(\tilde{n}, (1-t)\Phi(\tilde{m}) + t\tilde{n}, \tilde{m}\right)\right) \mathrm{d}t. \tag{6.70}$$

Using (6.55) and (6.59a)–(6.59b), it is straightforward to find the following asymptotic expansion of $\Delta(\tilde{n}, \tilde{m})$ as $(\tilde{n}, \tilde{m}) \to (0, 0)$:

$$\Delta(\tilde{n}, \tilde{m}) = \frac{\kappa}{c}\tilde{n}((\kappa - 1)\tilde{n} + \tilde{m})(1 + \mathcal{O}(|\tilde{n}| + |\tilde{m}|)). \tag{6.71}$$

In particular, if $\kappa > 1$, then $\Delta(\tilde{n}, \tilde{m}) > 0$ for sufficiently small $(\tilde{n}, \tilde{m})$ on $\mathcal{W}_C^+$. Now, integrating (6.69) from y_1 to y_2 for $y_1 > 0$ sufficiently large, we obtain

$$\tilde{m}(y_2) - \Psi(\tilde{n}(y_2)) = \exp\left(\int_{y_1}^{y_2} \Delta(\tilde{n}(y), \tilde{m}(y))\mathrm{d}y\right)(\tilde{m}(y_1) - \Psi(\tilde{n}(y_1))), \tag{6.72}$$

from which we have that $|\tilde{m}(y_2) - \Psi(\tilde{n}(y_2))| \geq (\tilde{m}(y_1) - \Psi(\tilde{n}(y_1)))|$, whenever $\kappa > 1$. By assumption, $(\tilde{n}, \tilde{m})$ converges to $(0, 0)$ as $y \to +\infty$, i.e., $\tilde{m}$ and $\Psi(\tilde{n})$ both converge to 0 as $y \to +\infty$. Therefore, the left-hand side of the above inequality converges to zero as $y_2 \to +\infty$, which implies that, if $\kappa > 1$, then $\tilde{m}(y_1) = \Psi(\tilde{n}(y_1))$ for all sufficiently large $y_1 > 0$. Therefore, if $\kappa > 1$, then any positive solution $(\tilde{n}, \tilde{m})$ to (6.59a)–(6.59b) on the centre manifold $\mathcal{W}_C^+$, converging to the origin as $y \to +\infty$, coincides, up to a translation in y, with the solution constructed in the first part of the proof.

We have now proved the uniqueness of the solution to (6.59a)–(6.59b) that converges to the origin as $y \to +\infty$ and satisfies the asymptotic conditions (6.58). □

Lemma 6.3.8 establishes the existence of at least one solution of (6.15a)–(6.15c) that satisfies (6.20), stays in region $\mathcal{D}_1$ and converges to $(0, 0, 1)$ as $y \to +\infty$. Furthermore, this solution is uniquely determined on the centre manifold $\mathcal{W}_C^+$. Given that any solution of (6.15a)–(6.15c) that satisfies (6.20), stays in region $\mathcal{D}_1$ and converges to $(0, 0, 1)$ as $y \to +\infty$ must do so via $\mathcal{W}_C^+$ and, given the monotonicity result of Lemma 6.3.4, it is easy to prove the following lemma.

Lemma 6.3.9. *Given any $c > 0$, there exists at most one value $\alpha \geq \alpha_1(c)$ of the shooting parameter such that the solution $(n_{\alpha,c}(y), p_{\alpha,c}(y), m_{\alpha,c}(y))$ of* (6.15a)–(6.15c) *satisfying the asymptotic properties in Lemma 6.3.2 converges to $P_2 = (0, 0, 1)$ as $y \to +\infty$.*

The proof of Lemma 6.3.9 is identical to that of Lemma 2.13 in [82] and is, therefore, omitted.

Exploiting the continuity of solutions with respect to the shooting parameter, α, we can extend Lemma 6.3.9 to determine the unique value of α, given $c > 0$, for which the solution $(n_{\alpha,c}(y), p_{\alpha,c}(y), m_{\alpha,c}(y))$ of (6.15a)–(6.15c) that satisfies (6.20) converges to $(0, 0, 1)$ as $y \to +\infty$. For the proof of the following result, we refer the reader to the proof of Lemma 2.14 in [82].

Lemma 6.3.10. *Given any $c > 0$, if $\alpha = \alpha_1(c)$, then the solution $(n_{\alpha,c}(y), p_{\alpha,c}(y), m_{\alpha,c}(y))$ of* (6.15a)–(6.15c) *satisfying the asymptotic properties in Lemma 6.3.2 converges to $P_2 = (0, 0, 1)$ as $y \to +\infty$.*

Using Lemma 6.3.10 and reversing the change of variables (6.10), it is straightforward to construct a unique (up to translation) solution $(\mathcal{N}(\xi), \mathcal{M}(\xi)) = (n(\Phi(\xi)), m(\Phi(\xi)))$ of system (6.5a)–(6.5b) that satisfies the asymptotic conditions (6.6). This leads to our first main result, which can be proved as in [82].

Theorem 6.3.11. *Fix $\kappa > 0$. For any $c > 0$, system* (6.4) *has a smooth weak TWS $(\mathcal{N}, \mathcal{M}; c)$ connecting $(1, 0)$ and $(0, 1)$. This solution is unique (up to translation), and $\mathcal{N}$ and $\mathcal{M}$ are monotonically strictly decreasing and increasing functions of $x - ct = \xi \in \mathbb{R} \cup \{-\infty, +\infty\}$, respectively.*

6.3.2.5 Solutions converging to the equilibrium point $(0, 0, \bar{m})$ with $\bar{m} \in [0, 1)$

In this section, we consider solutions of system (6.15a)–(6.15c) subject to (6.20) that stay in region $\mathcal{D}_{\bar{m}} \subset \mathcal{D}_1$ and converge to $(0, 0, \bar{m})$ for $\bar{m} \in (0, 1)$ as $y \to +\infty$. Using arguments similar to those for the previous case, we can show that, for all $\bar{m} \in [0, 1)$, there exists a strictly positive, real-valued wave speed above which the solutions we seek exist and are unique. We will refer to this wave speed as the *minimum wave speed* and we will observe that it depends on κ, the rescaled degradation rate of ECM. In particular, given $\kappa > 0$, we denote the minimum wave speed by $c^*_\kappa(\bar{m})$ for each $\bar{m} \in [0, 1)$. This will enable us to draw some conclusions on the existence and uniqueness of TWS that satisfy the asymptotic conditions (6.7).

At this stage, we have no information about the possible values of $c^*_\kappa(\bar{m})$ for $\bar{m} \in (0, 1)$ and $\kappa > 0$. More specifically, given $\kappa > 0$, we currently have $c^*_\kappa(\bar{m}) \in \mathbb{R}^*_+$ for each $\bar{m} \in (0, 1)$. For $\bar{m} = 0$, by Remark 6.3.1, it is straightforward to show that $c^*_\kappa(0) = 2$ for all $\kappa > 0$. To

characterise the minimum wave speed for $\bar{m} \in (0,1)$, we begin by proving a non-existence result.

Lemma 6.3.12. *Fix $\kappa > 0$ and $\bar{m} \in (0,1)$. If $0 < c < 2\sqrt{1-\bar{m}}$, then there is no $\alpha' \in [\alpha_0(c), +\infty)$ such that the solution $(n_{\alpha',c}, p_{\alpha',c}, m_{\alpha',c})$ of (6.15a)–(6.15c) that satisfies the asymptotic properties in Lemma 6.3.2 converges to $(0,0,\bar{m})$ as $y \to +\infty$.*

Proof. Fix $\kappa > 0$ and $\bar{m} \in (0,1)$ and suppose that $0 < c < 2\sqrt{1-\bar{m}}$. We suppose, for a contradiction, that there exists $\alpha' \in [\alpha_0(c), +\infty)$ such that the solution $(n_{\alpha',c}, p_{\alpha',c}, m_{\alpha',c})$ of (6.15a)–(6.15c) that satisfies (6.20) converges to $(0,0,\bar{m})$ as $y \to +\infty$. By the definition of $\alpha_0(c)$, this implies that $(n_{\alpha',c}, p_{\alpha',c}, m_{\alpha',c})$ stays in region $\mathcal{D}_1$ for all $y \in \mathbb{R}$. Now, we can choose $\epsilon > 0$ small enough such that $0 < c < 2\sqrt{(1-\bar{m}-\epsilon)(1-\epsilon)}$ and we can also find $\bar{y}$ sufficiently large such that $n_{\alpha',c}(y) < \epsilon$ and $m_{\alpha',c}(y) < \bar{m} + \epsilon$ for all $y \geq \bar{y}$. Solutions of the constant coefficient second order ODE

$$n'' + cn' + (1-\bar{m}-\epsilon)(1-\epsilon)n = 0,$$
$$\text{with} \quad \lim_{y\to-\infty} n(y) = 1, \quad \lim_{y\to+\infty} n(y) = 0, \quad \lim_{y\to\pm\infty} n'(y) = 0,$$

have infinitely many zeros in $(\bar{y}, +\infty)$ (since its characteristic equation has complex roots). Since $(1-\bar{m}-\epsilon)(1-\epsilon) < (1-m_{\alpha',c}(y))(1-n_{\alpha',c}(y))$ for all $y \in (\bar{y}, +\infty)$, Sturm's Comparison Theorem implies that $n_{\alpha',c}(y)$ must also have infinitely many zeros in $(\bar{y}, +\infty)$. Therefore, $(n_{\alpha',c}, p_{\alpha',c}, m_{\alpha',c})$ exits region $\mathcal{D}_1$ (and $\mathcal{D}_{\bar{m}}$), contradicting the assumption that $\alpha' \geq \alpha_0(c)$. □

Given $\kappa > 0$ and $\bar{m} \in (0,1)$, if the minimum wave speed, $c^*_\kappa(\bar{m})$, exists, then Lemma 6.3.12 yields a lower bound for $c^*_\kappa(\bar{m})$. More specifically, for all $\kappa > 0$ and $\bar{m} \in (0,1)$, $c^*_\kappa(\bar{m}) \geq 2\sqrt{(1-\bar{m})}$.

Lemma 6.3.13. *Fix $\kappa > 0$. If $c \geq 2$, then, for all $\bar{m} \in (0,1)$, there exists a unique $\alpha \in (\alpha_0(c), \alpha_1(c))$ such that the solution of (6.15a)–(6.15c) satisfying the asymptotic properties in Lemma 6.3.2 converges to $(0,0,\bar{m})$ as $y \to +\infty$.*

Proof. Fix $\kappa > 0$ and suppose that $c \geq 2$. By Lemmas 6.3.5 and 6.3.7, we know that $0 = \alpha_0(c) < \alpha_1(c)$. Then, by the definition of $\alpha_0(c)$, we have that, for any $\alpha \in (\alpha_0(c), \alpha_1(c))$, $T(\alpha, c) = +\infty$, and the solution $(n_{\alpha,c}, p_{\alpha,c}, m_{\alpha,c})$ of (6.15a)–(6.15c) satisfying (6.20) stays in the region $\mathcal{D}_1$ for all $y \in \mathbb{R}$ by Lemma 6.3.3. Then, by Lemma 6.3.6, we know that, for every $\alpha \in (\alpha_0(c), \alpha_1(c))$, the limits $n_\infty(\alpha, c)$, $p_\infty(\alpha, c)$, $m_\infty(\alpha, c)$ exist. In addition, by the monotonicity of $n_{\alpha,c}$ and $m_{\alpha,c}$ with respect to α (see Lemma 6.3.4) and the fact that $(n_\infty(\alpha_1(c), c), m_\infty(\alpha_1(c), c)) = (0,1)$ by Lemma 6.3.10, we must have

$$0 = n_\infty(\alpha_0(c), c) \leq n_\infty(\alpha, c) \leq n_\infty(\alpha_1(c), c) = 0,$$
$$0 = m_\infty(\alpha_0(c), c) \leq m_\infty(\alpha, c) \leq m_\infty(\alpha_1(c), c) = 1.$$

We recall that $\alpha_0(c) = 0$ and $\alpha_1(c)$ are the unique values of the shooting parameter for which the solution of (6.15a)–(6.15c) that satisfies (6.20) remains in region $\mathcal{D}_1$ and converges to $(0,0,0)$ and $(0,0,1)$ as $y \to +\infty$, respectively. Therefore, we find that, for every $\alpha \in (\alpha_0(c), \alpha_1(c))$, the limits for $(n_{\alpha,c}, p_{\alpha,c}, m_{\alpha,c})$ as $y \to +\infty$ must satisfy

$$n_\infty(\alpha, c) = 0, \quad m_\infty(\alpha, c) \in (0,1) \quad \text{and} \quad p_\infty(\alpha, c) = 0. \tag{6.73}$$

We will now prove that the mapping $\alpha \mapsto m_\infty(\alpha, c)$ is continuous and strictly increasing on $[\alpha_0(c), \alpha_1(c)]$. Choose α', α'' such that $\alpha_0(c) < \alpha' < \alpha'' < \alpha_1(c)$. Suppose, for a contradiction, that

$$\lim_{y\to+\infty} m_{\alpha',c}(y) = m_\infty(\alpha', c) = \bar{m} = m_\infty(\alpha'', c) = \lim_{y\to+\infty} m_{\alpha'',c}(y).$$

Irrespective of the asymptotic conditions (6.20), we can solve equation (6.15c) for $y \in \mathbb{R}$ and impose $\lim_{y\to+\infty} m(y) = \bar{m} \in (0,1)$ to obtain

$$m(y) = \left[1 + \frac{1-\bar{m}}{\bar{m}} \exp\left(\frac{\kappa}{c}\int_y^{+\infty} n(s)\mathrm{d}s\right)\right]^{-1}. \tag{6.74}$$

Any solution for which $\lim_{y\to+\infty} m(y) = \bar{m} \in (0,1)$ must therefore take the form (6.74). Thus, $m_{\alpha',c}$ and $m_{\alpha'',c}$ take the form (6.74), with n replaced by $n_{\alpha',c}$ and $n_{\alpha'',c}$, respectively. Now, by Lemma 6.3.4, we know that $m_{\alpha',c}(y) < m_{\alpha'',c}(y)$ for all $y \in \mathbb{R}$ since $\alpha' < \alpha''$. We, therefore, have, for any $y \in \mathbb{R}$,

$$\left[1 + \frac{1-\bar{m}}{\bar{m}} \exp\left(\frac{\kappa}{c}\int_y^{+\infty} n_{\alpha',c}(s)\mathrm{d}s\right)\right]^{-1} < \left[1 + \frac{1-\bar{m}}{\bar{m}} \exp\left(\frac{\kappa}{c}\int_y^{+\infty} n_{\alpha'',c}(s)\mathrm{d}s\right)\right]^{-1}, \tag{6.75}$$

$$\Rightarrow \int_y^{+\infty} (n_{\alpha',c}(s) - n_{\alpha'',c}(s))\mathrm{d}s > 0. \tag{6.76}$$

Since $\big(n_{\alpha',c}(y) - n_{\alpha'',c}(y)\big) < 0$ for all $y \in \mathbb{R}$ by Lemma 6.3.4, the inequality (6.76) cannot hold and we have reached a contradiction. Since we have that $m_\infty(\alpha', c) \leq m_\infty(\alpha'', c)$, by monotonicity of solutions with respect to α, and that $m_\infty(\alpha', c) \neq m_\infty(\alpha'', c)$, by the above argument, we conclude that $m_\infty(\alpha', c) < m_\infty(\alpha'', c)$. This proves that the mapping $\alpha \mapsto m_\infty(\alpha, c)$ is strictly increasing on $(\alpha_0(c), \alpha_1(c))$. Using the fact that $\alpha_0(c)$ and $\alpha_1(c)$ are, respectively, the unique values of the shooting parameter for which the solution of (6.15a)–(6.15c) given by Lemma 6.3.2 converges to $(0,0,0)$ and $(0,0,1)$ as $y \to +\infty$, we have that $\alpha \mapsto m_\infty(\alpha, c)$ is strictly increasing on $[\alpha_0(c), \alpha_1(c)]$.

We now prove that the mapping $\alpha \mapsto m_\infty(\alpha, c)$ is continuous on $[\alpha_0(c), \alpha_1(c)]$. For fixed $\alpha' \in [\alpha_0(c), \alpha_1(c))$, (6.73) implies that $n_\infty(\alpha', c) = 0$, $p_\infty(\alpha', c) = 0$ and $m_\infty(\alpha', c) = \bar{m}_1 \in [0,1)$. In the proof of Lemma 6.3.7, we performed a linear stability analysis about the equilibrium point $(0, 0, \bar{m}_1)$ for $\bar{m}_1 \in [0,1)$. We showed that, for fixed $\epsilon > 0$, we

can find a neighbourhood Ω of $(0,0,\bar{m}_1)$ that is foliated by two-dimensional stable leaves over a one-dimensional centre manifold, which comprises equilibria of the form $(0,0,\bar{m})$ for $|\bar{m}-\bar{m}_1|<\epsilon$. Then, any solution that enters Ω converges to $(0,0,\bar{m})$ as $y\to+\infty$ for some $\bar{m}$ that satisfies $|\bar{m}-\bar{m}_1|<\epsilon$. Since $(n_{\alpha',c}(y),p_{\alpha',c}(y),m_{\alpha',c}(y))$ converges to $(0,0,\bar{m}_1)$ as $y\to+\infty$, we can find $\bar{y}\in\mathbb{R}$ large enough such that $(n_{\alpha',c}(y),p_{\alpha',c}(y),m_{\alpha',c}(y))\in\Omega$ for all $y\geq\bar{y}$. By continuity of solutions with respect to α, we can find $\delta>0$ such that $(n_{\alpha'',c}(\bar{y}),p_{\alpha'',c}(\bar{y}),m_{\alpha'',c}(\bar{y}))\in\Omega$ for any $\alpha''\in[\alpha_0(c),\alpha_1(c))$ such that $|\alpha'-\alpha''|<\delta$. This implies that, for any such α'', $(n_{\alpha'',c}(y),p_{\alpha'',c}(y),m_{\alpha'',c}(y))$ converges to $(0,0,\bar{m}_2)\in\Omega$ as $y\to+\infty$, for some $\bar{m}_2\neq\bar{m}_1$ (since $m_\infty(\alpha,c)$ is strictly increasing with α). By our choice of Ω, $|\bar{m}_2-\bar{m}_1|<\epsilon$, i.e., $|m_\infty(\alpha'',c)-m_\infty(\alpha',c)|<\epsilon$ for any $\alpha''\in[\alpha_0(c),\alpha_1(c))$ such that $|\alpha'-\alpha''|<\delta$. This proves continuity of the mapping $\alpha\mapsto m_\infty(\alpha,c)$ on $[\alpha_0(c),\alpha_1(c))$.

We finally show continuity at $\alpha_1(c)$. We fix $\epsilon>0$ and note that, since $m_\infty(\alpha_1(c),c)=1$, we can find $\bar{y}\in\mathbb{R}$ large enough such that $|m_{\alpha_1(c),c}(y)-1|<\epsilon/2$ for all $y\geq\bar{y}$. By continuity of solutions with respect to α, we can find $\delta>0$ such that $|m_{\alpha',c}(\bar{y})-m_{\alpha_1(c),c}(\bar{y})|<\epsilon/2$ for any $\alpha'\in[\alpha_0(c),\alpha_1(c)]$ satisfying $|\alpha'-\alpha_1(c)|<\delta$, i.e., for any $\alpha'\in(\alpha_1(c)-\delta,\alpha_1(c)]$. Therefore, we have that $|m_{\alpha',c}(\bar{y})-1|<\epsilon$ for any $\alpha'\in(\alpha_1(c)-\delta,\alpha_1(c)]$. Moreover, for any $\alpha'\in(\alpha_1(c)-\delta,\alpha_1(c)]$, the function $m_{\alpha',c}(y)$ is strictly increasing for all $y\in\mathbb{R}$ and bounded above by 1, so $m_\infty(\alpha',c)\in(m_{\alpha',c}(\bar{y}),1]$. In particular, for any $\alpha'\in(\alpha_1(c)-\delta,\alpha_1(c)]$, we have $|m_\infty(\alpha',c)-1|=|m_\infty(\alpha',c)-m_\infty(\alpha_1(c),c)|<\epsilon$. This proves continuity of the mapping $\alpha\mapsto m_\infty(\alpha,c)$ at $\alpha_1(c)$.

We have now shown that the mapping $\alpha\mapsto m_\infty(\alpha,c)$ is strictly increasing and continuous on $[\alpha_0(c),\alpha_1(c)]$. Since $m_\infty(\alpha_0(c),c)=0$ and $m_\infty(\alpha_1(c),c)=1$, application of the Intermediate Value Theorem enables us to conclude that, for any $\bar{m}\in(0,1)$, there exists a unique $\alpha\in(\alpha_0(c),\alpha_1(c))$ such that $m_\infty(\alpha,c)=\bar{m}$. □

Remark 6.3.5. Using a similar proof to the above, we can generalise Lemma 6.3.13 to obtain the following result. Given $\kappa,c>0$, suppose that there exists a unique value of the shooting parameter, $\alpha\in[\alpha_0(c),\alpha_1(c))$, such that the solution $(n_{\alpha,c},p_{\alpha,c},m_{\alpha,c})$ of (6.15a)–(6.15c) satisfies (6.20) and converges to $(0,0,\bar{m})$ as $y\to+\infty$ for some $\bar{m}\in[0,1)$. Then, for all $\bar{m}'\in(\bar{m},1)$, there exists a unique value of the shooting parameter, $\alpha'\in(\alpha,\alpha_1(c))$, for which the solution of (6.15a)–(6.15c) that satisfies (6.20) stays in $\mathcal{D}_{\bar{m}'}$ and converges to $(0,0,\bar{m}')$ as $y\to+\infty$.

Lemma 6.3.13 implies that, for all $\bar{m}\in(0,1)$, the minimum wave speed, $c^*_\kappa(\bar{m})$, exists and is bounded above by 2. Then, given $\bar{m}\in[0,1)$, for any $c\geq c^*_\kappa(\bar{m})$, we can define

$$\alpha_{\bar{m}}(c)\coloneqq\{\alpha\geq\alpha_0(c)\mid m_\infty(\alpha,c)=\bar{m}\}\in[\alpha_0(c),\alpha_1(c)). \tag{6.77}$$

We now improve the upper bound on $c^*_\kappa(\bar{m})$ for $\bar{m} \in (0,1)$ by formulating a conjecture. We consider the following generalised Fisher-KPP equation with reaction term, g, of Fisher-KPP type:

$$\begin{aligned} &n'' + cn' + g(n) = 0, \\ \text{with} \quad &\lim_{y\to-\infty} n(y) = 1, \quad \lim_{y\to+\infty} n(y) = 0, \quad \lim_{y\to\pm\infty} n'(y) = 0. \end{aligned} \tag{6.78}$$

One typically seeks TWS such that n is monotonically decreasing, in which case we can invert $n(y)$ to obtain a function $Y(n)$, $n \in [0,1]$. Considering the new variable $P(n) \coloneqq n'(Y(n))$, we obtain the following first order boundary value problem (BVP):

$$\begin{cases} P' = -c - \dfrac{g(n)}{P}, \\ P(0) = 0, \end{cases} \tag{6.79}$$

subject to $P(1) = 0$, $P(n) < 0$ $\forall n \in (0,1)$. Studying TWS of (6.78) and solutions of (6.79), subject to their respective asymptotic and boundary conditions, is equivalent [149]. Moreover, it is known that if $g''(n) < 0 \forall n \in [0,1]$, then (6.79) subject to $P(1) = 0$, $P(n) < 0$ $\forall n \in (0,1)$ has a unique solution if $c \geq 2\sqrt{g'(0)}$ [76, 190, 254]. Therefore, TWS of (6.78) exist and are unique if $c \geq 2\sqrt{g'(0)}$.

Returning to our original problem, by introducing $P(n) \coloneqq n'(Y(n))$ and $M(n) \coloneqq m(Y(n))$, we view the system (6.15a)–(6.15c) subject to the conditions (6.7) as the following BVP:

$$\begin{cases} P' = -c - \dfrac{(1-n)n(1-M(n))}{P}, \\ M' = \dfrac{\kappa}{c}\dfrac{M(1-M)N}{P}, \\ P(0) = 0,\ M(0) = \bar{m}, \end{cases} \tag{6.80}$$

subject to the additional conditions

$$P(n) < 0, \quad 0 < M(n) < \bar{m}\ \forall n \in (0,1), \quad P(1) = M(1) = 0. \tag{6.81}$$

It is possible to show that $g(n) = (1-n)n(1-M(n))$ is of Fisher-KPP type for $0 \leq M \leq \bar{m} < 1$ and that $g''(0) < 0$ if $\kappa \leq \kappa^*(\bar{m})$ (see the Supplementary Material of [44]), where

$$\kappa^*(\bar{m}) \coloneqq \frac{1-\bar{m}}{\bar{m}} \quad \forall \bar{m} \in (0,1). \tag{6.82}$$

We conjecture that, if $\kappa \leq \kappa^*(\bar{m})$, then $g''(n) < 0$ $\forall n \in [0,1]$. By the preceding result for the generalised Fisher-KPP equation, this would imply that, given $0 < \kappa \leq \kappa^*(\bar{m})$, the system (6.15a)–(6.15c) subject to the conditions (6.7) has unique TWS for $c \geq 2\sqrt{g'(0)} = 2\sqrt{1-\bar{m}}$. Now, given $\kappa > 0$, we let $m^*(\kappa) \coloneqq \frac{1}{\kappa+1}$. Noting that $0 < \kappa \leq \kappa^*(\bar{m})$ if and only if $0 < \bar{m} \leq m^*(\kappa)$, we formulate the following conjecture.

Conjecture 1. *Fix $\kappa > 0$ and $\bar{m} \in (0, m^*(\kappa)]$. Given $c \geq 2\sqrt{1-\bar{m}}$, there exists a unique $\alpha' \in [\alpha_0(c), \alpha_1(c))$ such that the solution $(n_{\alpha',c}, p_{\alpha',c}, m_{\alpha',c})$ of (6.15a)–(6.15c) that satisfies the asymptotic properties in Lemma 6.3.2 converges to $(0, 0, \bar{m})$ as $y \to +\infty$. In particular, if $c = 2\sqrt{1-\bar{m}}$, then $\alpha' = \alpha_0(c)$.*

Conjecture 1 implies that, given $\kappa > 0$, there are values of $\bar{m} \in (0, 1)$ such that the solutions of (6.15a)–(6.15c) that satisfy the asymptotic conditions (6.7) behave similarly to solutions of a generalised Fisher-KPP equation with reaction term $g(n) = (1-n)n(1-\bar{m})$. In particular, the minimum wave speed for these TWS is defined similarly to that of a generalised Fisher-KPP equation, i.e., it is the smallest value of $c > 0$ such that $(0, 0, \bar{m})$ is a stable node, and not a stable spiral, for system (6.15a)–(6.15c). In addition, using Lemmas 6.3.12 and 6.3.13 and Conjecture 1, we make the hypothesis that, if $\bar{m} \in (m^*(\kappa), 1)$ or, equivalently, if $\kappa > \kappa^*(\bar{m})$, then the minimum wave speed for TWS that converge to $(0, 0, \bar{m})$ as $y \to +\infty$ should satisfy $c^*_\kappa(\bar{m}) \in \left(2\sqrt{1-\bar{m}}, 2\right)$. In other words, in these cases, we expect that there is another mechanism that can lead to $n(y) < 0$, $y \in \mathbb{R}$, even if $(0, 0, \bar{m})$ is a stable node for the system (6.15a)–(6.15c).

The preceding hypothesis and Conjecture 1 are supported by numerical simulations of the PDE system (6.4) and ODE system (6.15a)–(6.15c) (for numerical methods; see Section 6.4.1). In Figure 6.2, we show that solutions of system (6.4) subject to the initial conditions (6.91) with $\bar{M} \in [0, 1]$ evolve into travelling waves with constant propagation speed (see Figure 6.3 in Section 6.4.2 for corresponding travelling wave profiles). We observe that, for $0 < \kappa \leq \kappa^*(\bar{M})$, this speed is independent of κ, and, calculating the slopes of these lines, we find that it is approximately equal to $2\sqrt{1-\bar{M}}$. Additionally, when $\kappa > \kappa^*(\bar{M})$, we observe that the wave speed selected by the PDE model increases with κ. We also solved numerically the system (6.15a)–(6.15c), subject to the asymptotic conditions (6.20), for the same values of $\kappa > \kappa^*(\bar{M})$ and the respective values of the propagation speed estimated using the solutions of the PDE system (results not shown). We observed that, given $\kappa > \kappa^*(\bar{M})$, the wave speed selected by the PDE appears to correspond to the smallest wave speed such that the solution (n, p, m) of the system (6.15a)–(6.15c), subject to (6.20), satisfies $n(y) > 0\ \forall y \in \mathbb{R}$ and converges to $(0, 0, \bar{m})$, $\bar{m} = \bar{M}$.

Now, suppose Conjecture 1 is true. Then, given $\kappa > 0$, for each $\bar{m} \in [0, m^*(\kappa)]$ and $c \geq 2\sqrt{1-\bar{m}}$, $\alpha_{\bar{m}}(c)$ as defined by (6.77) exists and is the unique α' mentioned in the statement of Conjecture 1. Using Remark 6.3.5 and Conjecture 1, the subsequent result follows naturally (we omit the proof for brevity).

Lemma 6.3.14. *Suppose Conjecture 1 is true and fix $\kappa > 0$. If $c \geq 2\sqrt{1-m^*(\kappa)}$, then, for all $\bar{m} \in (m^*(\kappa), 1)$, there exists a unique $\alpha \in (\alpha_{m^*(\kappa)}(c), \alpha_1(c))$ such that the solution of (6.15a)–(6.15c) that satisfies the asymptotic properties in Lemma 6.3.2 converges to $(0, 0, \bar{m})$ as $y \to +\infty$.*

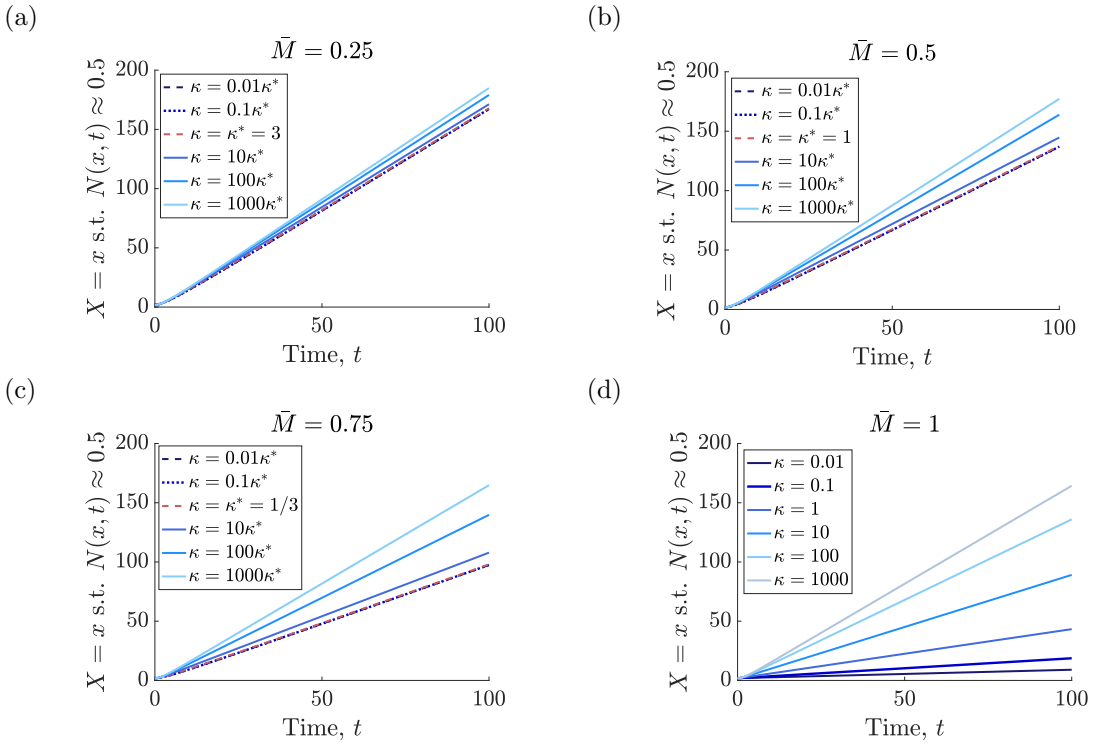


Figure 6.2: We solve system (6.4) on the 1D spatial domain, $x \in \mathcal{X} := [0, 200]$, and impose the initial conditions (6.91) with (a) $\bar{M} = 0.25$, (b) $\bar{M} = 0.5$, (c) $\bar{M} = 0.75$ and (d) $\bar{M} = 1$. Each plot represents $X(t)$ such that $N(X(t), t) = 0.5$ for $t \in (0, 100]$ when (a)–(c) $\kappa \in \kappa^* \times \{0.01, 0.1, 1, 10, 100, 1000\}$, where κ^* is defined by (6.82), and (d) $\kappa \in \{0.01, 0.1, 1, 10, 100, 1000\}$. We see that the front travels with a constant propagation speed that increases monotonically with κ.

This lemma allows us to obtain a sharper upper bound on the minimum wave speed for solutions of (6.15a)–(6.15c) subject to (6.20) that converge to $(0, 0, \bar{m})$ as $y \to +\infty$, where $\bar{m} \in (m^*(\kappa), 1)$. We now summarise what we can conclude about the minimum wave speed $c^*_\kappa(\bar{m})$.

Lemma 6.3.15. *Suppose Conjecture 1 is true. Given $\kappa > 0$, the minimum wave speed $c^*_\kappa(\bar{m})$ is a monotonically decreasing function on $[0, 1)$, such that*

$$c^*_\kappa(\bar{m}) \begin{cases} = 2\sqrt{1-\bar{m}}, & \text{if } \bar{m} \in [0, m^*(\kappa)]\,, \\ \in \left[2\sqrt{1-\bar{m}}, 2\sqrt{1-m^*(\kappa)}\right], & \text{if } \bar{m} \in (m^*(\kappa), 1)\,. \end{cases} \tag{6.83}$$

Proof. Fix $\kappa > 0$. Suppose, for a contradiction, that c^*_κ is not a monotonically decreasing function of $\bar{m}$ on $[0, 1)$. Then, we can find $0 \leq \bar{m}' < \bar{m}'' < 1$ such that $c^*_\kappa(\bar{m}') < c^*_\kappa(\bar{m}'')$. Now, choose $c \in (c^*_\kappa(\bar{m}'), c^*_\kappa(\bar{m}''))$. Then, there exists a solution of (6.15a)–(6.15c) that satisfies the asymptotic conditions (6.20), stays in region $\mathcal{D}_{\bar{m}'}$ and converges to $(0, 0, \bar{m}')$ as $y \to +\infty$, but there does not exist a solution of (6.15a)–(6.15c) that satisfies the asymptotic conditions (6.20), stays in region $\mathcal{D}_{\bar{m}''}$ and converges to $(0, 0, \bar{m}'')$ as $y \to +\infty$. As

$\bar{m}'' \in (\bar{m}', 1)$, Remark 6.3.5 gives us a contradiction, hence c_κ^* is a decreasing function of $\bar{m}$ on $[0, 1)$.

From Lemma 6.3.12 and Conjecture 1, we know that the minimum wave speed for all $\bar{m} \in [0, m^*(\kappa)]$ is $c_\kappa^*(\bar{m}) = 2\sqrt{1-\bar{m}}$. Since c_κ^* is a decreasing function of $\bar{m}$ on $[0, 1)$, we must have $c_\kappa^*(\bar{m}) \leq 2\sqrt{1-m^*(\kappa)}$ for any $\bar{m} \in (m^*(\kappa), 1)$. Finally, by Lemma 6.3.12, we know that $c_\kappa^*(\bar{m}) \geq 2\sqrt{1-\bar{m}}$ for any $\bar{m} \in (m^*(\kappa), 1)$. This completes the proof. □

While we do not have a complete characterisation of the minimum wave speed for all $\kappa > 0$ and $\bar{m} \in (0, 1)$, we can now state our second main result.

Theorem 6.3.16. *Suppose Conjecture 1 is true. Given $\kappa > 0$, for any $\bar{\mathcal{M}} \in [0, 1)$, there exists a minimum wave speed $c_\kappa^*(\bar{\mathcal{M}})$ defined by* (6.83) *such that:*

1. *For $0 < c < c_\kappa^*(\bar{\mathcal{M}})$, system* (6.4) *has no weak TWS $(\mathcal{N}, \mathcal{M}; c)$ connecting $(1, 0)$ and $(0, \bar{\mathcal{M}})$.*

2. *For $c \geq c_\kappa^*(\bar{\mathcal{M}})$, system* (6.4) *has a smooth weak TWS $(\mathcal{N}, \mathcal{M}; c)$ connecting $(1, 0)$ and $(0, \bar{\mathcal{M}})$. Moreover, this solution is unique (up to translation) and $\mathcal{N}, \mathcal{M}$ are monotonically strictly decreasing and increasing functions of $x - ct = \xi \in \mathbb{R} \cup \{-\infty, +\infty\}$, respectively.*

Proof. We first prove item *2.* Fix $\bar{\mathcal{M}} \in [0, 1)$ and let $\bar{m} = \bar{\mathcal{M}}$. Given any $c \geq c_\kappa^*(\bar{m})$, we choose $\alpha = \alpha_{\bar{m}}(c) \in [\alpha_0(c), \alpha_1(c))$. Then, the solution $(n_{\alpha,c}, p_{\alpha,c}, m_{\alpha,c})$ of (6.15a)–(6.15c) satisfying the asymptotic conditions (6.20) converges to $(0, 0, \bar{m})$ as $y \to +\infty$. Similarly to the proof of Theorem 6.3.11 in [82], we now reverse the change of variables from ξ to y given by

$$\frac{\mathrm{d}y}{\mathrm{d}\xi} \equiv \Phi'(\xi) = \frac{1}{1 - \mathcal{M}(\xi)} \ \forall \xi \in \mathbb{R}, \tag{6.84}$$

or, equivalently,

$$\frac{\mathrm{d}\xi}{\mathrm{d}y} \equiv (\Phi^{-1})'(y) = 1 - m(y) \ \forall y \in \mathbb{R}. \tag{6.85}$$

More specifically, we define

$$\xi(y) = \Phi^{-1}(y) = y - \int_{-\infty}^{y} m(s)\mathrm{d}s \ \forall y \in \mathbb{R}. \tag{6.86}$$

Since we want to define $\xi(y)$ as $y \to \pm\infty$ and we already have an asymptotic expansion of m as $y \to -\infty$ in (6.20), we only need to compute an asymptotic expansion of m as $y \to +\infty$.

We saw in the proof of Lemma 6.3.13 that $(n_{\alpha,c}, p_{\alpha,c}, m_{\alpha,c})$ approaches $(0, 0, \bar{m})$ via a two-dimensional stable manifold. Computing a general asymptotic expansion of solutions of (6.15a)–(6.15c) in a neighbourhood of $(0, 0, \bar{m})$ that lie on this stable manifold, we find

that there must exist $C_1, C_2 \in \mathbb{R}$ such that $n \in (0,1)$, $p < 0$ and $m \in (0, \bar{m})$ (i.e., such that the solution remains in $\mathcal{D}_{\bar{m}}$) and, as $y \to +\infty$, $(n_{\alpha,c}(y), p_{\alpha,c}(y), m_{\alpha,c}(y))$ satisfies

$$\begin{aligned} n_{\alpha,c}(y) &= C_1 \left(\frac{c\nu_1}{\kappa(1-\bar{m})\bar{m}} \right) e^{\nu_1 y} + C_2 \left(\frac{c\nu_2}{\kappa(1-\bar{m})\bar{m}} \right) e^{\nu_2 y} + \mathcal{O}(e^{2\nu_1 y}), \\ p_{\alpha,c}(y) &= C_1 \left(\frac{-c^2\nu_1}{\kappa(1-\bar{m})\bar{m}} - \frac{c}{\kappa\bar{m}} \right) e^{\nu_1 y} + C_2 \left(\frac{-c^2\nu_2}{\kappa(1-\bar{m})\bar{m}} - \frac{c}{\kappa\bar{m}} \right) e^{\nu_2 y} + \mathcal{O}(e^{2\nu_1 y}), \\ m_{\alpha,c}(y) &= \bar{m} + C_1 e^{\nu_1 y} + C_2 e^{\nu_2 y} + \mathcal{O}(e^{2\nu_1 y}), \end{aligned} \tag{6.87}$$

where

$$\nu_1 = \frac{-c + \sqrt{c^2 - 4(1-\bar{m})}}{2}, \quad \nu_2 = \frac{-c - \sqrt{c^2 - 4(1-\bar{m})}}{2}.$$

Using (6.20) and (6.87), we can now define $\xi(y)$ as $y \to \pm\infty$ in the following way:

$$\xi = \Phi^{-1}(y) = \begin{cases} y - \frac{\alpha}{\lambda_3} e^{\lambda_3 y} + \mathcal{O}\left(e^{(\lambda_3+\mu)y}\right), & \text{as } y \to -\infty, \\ y(1-\bar{m}) - \frac{C_1}{\nu_1} e^{\nu_1 y} - \frac{C_2}{\nu_2} e^{\nu_2 y} + \mathcal{O}\left(e^{2\nu_1 y}\right), & \text{as } y \to +\infty. \end{cases} \tag{6.88}$$

From (6.88), it is clear that, as $y \to +\infty$, $\xi \to +\infty$. We therefore do not have sharp fronts for system (6.5a)–(6.5b) subject to the asymptotic conditions (6.7). By inverting (6.88), we obtain

$$y = \Phi(\xi) = \begin{cases} \xi + \frac{\alpha}{\lambda_3} e^{\lambda_3 \xi} + \mathcal{O}\left(e^{(\lambda_3+\mu)y}\right), & \text{as } \xi \to -\infty, \\ \frac{\xi}{1-\bar{m}} + \frac{C_1}{\nu_1(1-\bar{m})} e^{\frac{\nu_1 \xi}{(1-\bar{m})}} + \frac{C_2}{\nu_2(1-\bar{m})} e^{\frac{\nu_2 \xi}{(1-\bar{m})}} + \mathcal{O}\left(e^{(\nu_1+\nu_2)}\right), & \text{as } \xi \to +\infty. \end{cases} \tag{6.89}$$

We can now construct a solution of (6.5a)–(6.5b) which satisfies the asymptotic conditions (6.7) for $\bar{\mathcal{M}} = \bar{m}$ by defining $\mathcal{N}(\xi) = n_{\alpha,c}(\Phi(\xi))$ and $\mathcal{M}(\xi) = m_{\alpha,c}(\Phi(\xi))$. Since we know that $n'_{\alpha,c}(y) = n'_{\alpha,c}(\Phi(\xi)) < 0$ and $m'_{\alpha,c}(y) = m'_{\alpha,c}(\Phi(\xi)) > 0$ for all $y \in \mathbb{R}$, it is easy to see that $\frac{\mathrm{d}\mathcal{N}}{\mathrm{d}\xi} < 0$ and $\frac{\mathrm{d}\mathcal{M}}{\mathrm{d}\xi} > 0$ for all $\xi \in \mathbb{R}$. This shows that $\mathcal{N}$ and $\mathcal{M}$ are monotonically strictly decreasing and increasing in ξ, respectively. Finally, the uniqueness of the constructed solution follows from the uniqueness of the solution $(n_{\alpha,c}, p_{\alpha,c}, m_{\alpha,c})$.

We now prove item *1* by contradiction. Fix $\bar{\mathcal{M}} \in [0,1)$. Let $0 < c < c^*_\kappa(\bar{\mathcal{M}})$. Suppose that system (6.4) has a unique (up to translation) weak travelling wave solution $(\mathcal{N}, \mathcal{M}; c)$ connecting $(1,0)$ and $(0, \bar{\mathcal{M}})$, where $\mathcal{N}$ and $\mathcal{M}$ are monotonically strictly decreasing and increasing in $\xi = x - ct$, respectively. Then, we can construct a solution of (6.15a)–(6.15c) that satisfies the asymptotic conditions $\lim_{y\to-\infty}(n(y), p(y), m(y)) = (1,0,0)$, $\lim_{y\to+\infty}(n(y), p(y), m(y)) = (0,0,\bar{m})$ for $\bar{m} = \bar{\mathcal{M}}$ by defining $n(y) = \mathcal{N}(\Phi^{-1}(y))$, $p(y) = n'(y)$ and $m(y) = \mathcal{M}(\Phi^{-1}(y))$. Since $\mathcal{N}$ and $\mathcal{M}$ are monotonically strictly decreasing and increasing with respect to $\xi = \Phi^{-1}(y)$, it is easy to see that n and m are monotonically strictly decreasing and increasing with respect to y and that $p(y) < 0$ $\forall y \in \mathbb{R}$. This implies that there exists $\alpha = \alpha(c)$ such that the solution of (6.15a)–(6.15c) that satisfies (6.20) stays

in region $\mathcal{D}_{\bar{m}}$ and converges to $(0, 0, \bar{m})$ as $y \to +\infty$. Since $0 < c < c^*_\kappa(\bar{\mathcal{M}}) = c^*_\kappa(\bar{m})$, this contradicts the definition of the minimum wave speed. □

6.4 Numerical simulations: demonstration of analytical results

In this section, we present numerical solutions of the PDE model (6.4), which complement our travelling wave analysis.

6.4.1 Numerical methods and set-up

The PDE model. We solve the PDE model (6.4) numerically on the one-dimensional (1D) spatial domain $\mathcal{X} \coloneqq [0, L]$ with $L > 0$ using the method of lines. We discretise the spatial domain $\mathcal{X}$ using a uniform grid comprising P points and we discretise the equations using the following explicit central difference scheme, introduced in [233], to approximate the nonlinear diffusion terms:

$$\begin{aligned}\frac{\partial}{\partial x}\left(D(m)\frac{\partial n}{\partial x}\right) = \frac{1}{2(\delta_x)^2}\Bigg(&\left(D(m)\Big|_{r-1} + D(m)\Big|_r\right) n_{r-1} \\ &- \left(D(m)\Big|_{r-1} + 2D(m)\Big|_r + D(m)\Big|_{r+1}\right) n_r \\ &+ \left(D(m)\Big|_r + D(m)\Big|_{r+1}\right) n_{r+1}\Bigg),\end{aligned} \tag{6.90}$$

where $D(m) = 1 - m \ \forall m \in [0, 1]$, $|_r$ denotes evaluation at the r^{th} spatial grid point and $\delta_x = L/P$ is the spatial grid step (i.e., $x_r = r\delta_x$).

This spatial discretisation results in a system of $2P$ time-dependent ODEs, which we solve using ODE15s, a variable step, variable order MATLAB built-in solver for stiff ODEs that is based on the numerical differentiation formulas (NDF1-NDF5) [222]. Similarly to [233], we assume that the tumour has already spread to a position $x = \sigma < L$ in the tissue and we impose initial conditions that satisfy, for $\bar{M} \in [0, 1]$,

$$\begin{cases} N(x,0) = 1,\ M(x,0) = 0, & \text{if } 0 \le x < \sigma - \omega, \\ N(x,0) = \exp\left(1 - \frac{1}{1-\left(\frac{x-\sigma+\omega}{\omega}\right)^2}\right),\ M(x,0) = \bar{M}\left(1 - N(x,0)\right), & \text{if } \sigma - \omega \le x < \sigma, \\ N(x,0) = 0,\ M(x,0) = \bar{M}, & \text{if } \sigma \le x \le L. \end{cases} \tag{6.91}$$

Here, $0 < \omega < \sigma$ represents how sharp the initial boundary between the tumour and healthy tissue is. Initial conditions with compact support for N, such as those given by (6.91), are biologically relevant. We checked that the travelling waves profiles and wave speeds are preserved across different initial conditions with compact support for N. These results are omitted for brevity and can be found in the Supplementary Material of [44].

We complete the mathematical problem by imposing zero-flux boundary conditions for N at $x = 0$ and $x = L$. We set $L = 200$, $P = 2000$, $\sigma = 2$ and $\omega = 1$ for our simulations and run them for $t \in (0, 100]$. We verified the convergence in space of our numerical scheme and found that using a discretisation step size $\delta_x = L/P = 0.1$ ensures that the numerical results are only weakly affected by numerical diffusion (see the Supplementary Material of [44]).

The ODE models. We numerically solve the desingularised ODE system (6.15a)–(6.15c), subject to the asymptotic conditions (6.20), using ODE45. Further, to numerically solve the ODE system (6.5a)–(6.5b), we transform it into a system of three first order ODEs by introducing the additional variable $\mathcal{P} = (1 - \mathcal{M})\frac{\mathrm{d}\mathcal{N}}{\mathrm{d}\sim}$. In particular, we obtain the following non-desingularised system:

$$\begin{cases} \dfrac{\mathrm{d}\mathcal{N}}{\mathrm{d}\xi} = \dfrac{\mathcal{P}}{1-\mathcal{M}}, & \text{(6.92a)} \\ \dfrac{\mathrm{d}\mathcal{P}}{\mathrm{d}\xi} = -c\dfrac{\mathcal{P}}{1-\mathcal{M}} + (1-\mathcal{N})\mathcal{N} = 0, & \text{(6.92b)} \\ \dfrac{\mathrm{d}\mathcal{M}}{\mathrm{d}\xi} = \dfrac{\kappa}{c}\mathcal{M}\mathcal{N}. & \text{(6.92c)} \end{cases}$$

We then solve the system (6.92a)–(6.92c) using ODE15s, subject to asymptotic conditions equivalent to (6.20), with $\mathcal{N}(\xi)$, $\mathcal{P}(\xi)$ and $\mathcal{M}(\xi)$ replacing $n(y)$, $p(y)$, $m(y)$, respectively.

6.4.2 Travelling wave solutions

From Theorems 6.3.11 and 6.3.16, we know that system (6.4) has TWS connecting $(1, 0)$ and $(0, \bar{M})$, $\bar{M} \in [0, 1]$, for all $c > 0$ if $\bar{M} = 1$ and for all $c \geq c^*_\kappa(\bar{M})$, defined by (6.83), otherwise. Figure 6.3 shows that solutions of (6.4), subject to the initial conditions (6.91) for $\bar{M} \in \{0.25, 0.5, 0.75, 1\}$, evolve towards constant profile, constant speed travelling waves. Further, solving numerically the ODE model (6.5a)–(6.5b), subject to the appropriate asymptotic conditions, for c equal to the wave speed selected by the numerical solution of the PDE model, we find good agreement between the travelling wave profiles predicted by the PDE and ODE models (result not shown for brevity; see [44]). These numerical results support the existence of TWS as defined by Theorems 6.3.11 and 6.3.16.

6.4.3 Elucidating the wave speed that emerges in the PDE model

A characteristic feature of the well-studied Fisher-KPP model is that any non-negative initial condition with compact support will evolve towards a travelling front with speed equal to the minimum wave speed [77, 127, 174]. One may, therefore, question whether this result extends to more complex R-D systems that exhibit travelling waves. For our model, the results from Section 6.3.2.5 suggest that this holds for solutions of (6.4) subject

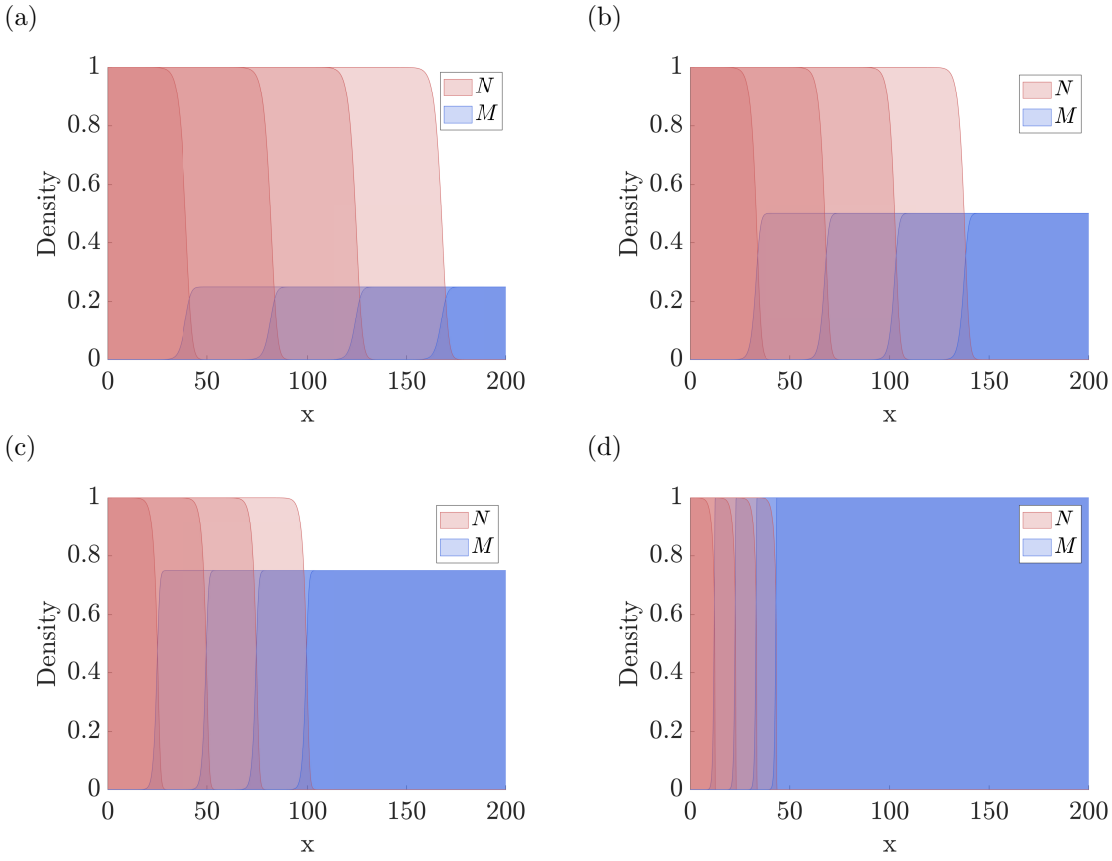


Figure 6.3: For $\kappa = 1$, we solve system (6.4) on the 1D spatial domain, $x \in \mathcal{X} = [0, 200]$, and impose initial conditions (6.91) with $\sigma = 2$, $\omega = 1$ and (a) $\bar{M} = 0.25$, (b) $\bar{M} = 0.5$, (c) $\bar{M} = 0.75$ and (d) $\bar{M} = 1$. We plot the respective solutions for $t \in \{25, 50, 75, 100\}$ and observe the emergence of a constant profile, constant speed TWS in all cases. The wave speed decreases as $\bar{M}$ increases.

to the initial conditions (6.91) for $\bar{M} \in [0, 1)$. In contrast, the results from Section 6.3.2.4 show that there is no strictly positive minimum wave speed for TWS of (6.4) that satisfies the asymptotic conditions (6.6). Yet, the solution of (6.4) subject to the initial conditions (6.91) for $\bar{M} = 1$ appears to evolve towards a travelling front with a strictly positive speed, as illustrated in Figure 6.3 for $\kappa = 1$ and Figure 6.2d for different values of κ. In this way, the solutions of the PDE system preferentially select a wave speed in a way that the corresponding ODE system does not.

Given different values of $\kappa > 0$, we calculated the speed of the travelling fronts that emerge for solutions of (6.4) subject to the initial conditions (6.91) with $\bar{M} \in [0, 1]$. Our numerical simulations suggest that the wave speed selected by the PDE model is a continuous, decreasing function of $\bar{M} \in [0, 1]$, as illustrated in Figure 6.4. This is consistent with Lemma 6.3.15 and our observation that the speed of travelling fronts that emerge for solutions of (6.4), subject to the initial conditions (6.91) with $\bar{M} \in [0, 1)$, appears to be equal to the minimum wave speed, $c^*_\kappa(\bar{M})$, defined by (6.83). This result is interesting because

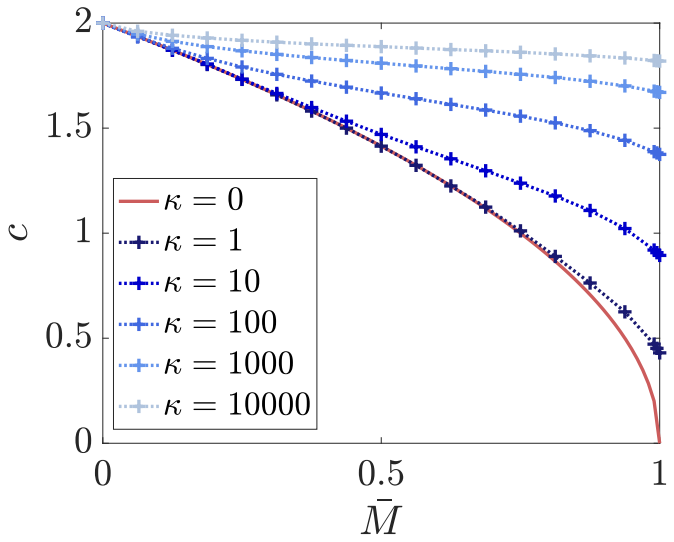


Figure 6.4: We solve system (6.4) on the 1D spatial domain, $x \in \mathcal{X} := [0, 200]$, and impose the initial conditions (6.91) for $\bar{M} \in [0, 1]$. We plot the speed of the travelling front that emerges for $\bar{M} \in \{0.0625j | j \in [\![1, 15]\!]\} \cup \{0.99, 1\}$ and observe that this speed is monotonically decreasing with $\bar{M}$, given $\kappa > 0$, and monotonically increasing with $\kappa > 0$, given $\bar{M} \in [0, 1]$.

the speed selected by the PDE model appears to be left-continuous at $\bar{M} = 1$, despite the fact that the minimum wave speed for the existence of TWS is not.

6.5 Discussion

In this chapter, we carried out a travelling wave analysis for a minimal model of tumour cell invasion into ECM. Our aim was to use this simpler model to gain insight into the existence of travelling wave solutions (TWS) for more complex reaction-diffusion PDE models of tumour invasion that include a degenerate cross-dependent diffusion term. For most of these models, results available in the literature on the existence of TWS largely rely on numerical results, which are typically complemented by partial analytical results. This has, for the most part, precluded a complete understanding of the existence of TWS.

We found that system (6.4) supports a continuum of TWS, which describe the invasion of ECM by tumour cells and differ according to the density of ECM far ahead of the front. More specifically, we distinguished between two types of TWS, the first connecting the spatially homogeneous steady states $(1, 0)$ and $(0, 1)$, and the second connecting the spatially homogeneous steady states $(1, 0)$ and $(0, \bar{M})$, for $\bar{M} \in [0, 1)$. This distinction follows from the degeneracy in (6.4) when $M = 1$.

As a first step, we proved the existence of TWS of the first type for any positive wave speed, $c > 0$. This result is interesting as it differs from most previous results for degenerate

diffusion in a scalar or multi-equation setting, where TWS exist if and only if the wave speed is greater than or equal to a strictly positive minimum wave speed [149, 213, 216]. It is important to note that this does not imply that a positive wave speed which is preferentially selected does not exist for solutions of (6.4) that connect $(1, 0)$ and $(0, 1)$. In fact, we saw in Section 6.4.3 that a strictly positive, κ-dependent wave speed appears to be selected by (6.4) subject to the initial conditions (6.91) with $\bar{M} = 1$.

We then proved that TWS of the second type exist if and only if the wave speed is greater than or equal to a strictly positive minimum wave speed, $c^*_\kappa(\bar{\mathcal{M}})$, defined by (6.83) for $\bar{\mathcal{M}} \in [0, 1)$. Given $\kappa > 0$, this minimum speed appears to be a monotonically decreasing, continuous function of $\bar{\mathcal{M}}$. In particular, we conjectured that, given $\kappa > 0$ and $m^*(\kappa) \coloneqq \frac{1}{\kappa+1}$, we can precisely define $c^*_\kappa(\bar{\mathcal{M}}) = 2\sqrt{1 - \bar{\mathcal{M}}}$ for $\bar{\mathcal{M}} \in [0, m^*(\kappa)]$. Similarly to the generalised Fisher-KPP equation, this minimum wave speed is the smallest $c > 0$ such that the equilibrium $(0, 0, \bar{m})$, with $\bar{m} = \bar{\mathcal{M}}$, of system (6.15a)–(6.15c) is a stable node and not a stable spiral. For $\bar{\mathcal{M}} \in (m^*(\kappa), 1)$ and consistent with (6.83), numerical simulations suggested that the wave speed selected by the PDE is strictly greater than $2\sqrt{1 - \bar{\mathcal{M}}}$. In this case, the equilibrium $(0, 0, \bar{m})$ of system (6.15a)–(6.15c) being a stable node is no longer a sufficient condition to ensure the positivity of the n-component of the TWS in the desingularised variables and, thus, of the $\mathcal{N}$-component of the TWS in the original variables. In other words, there exists an additional necessary condition for the positivity of the TWS, which remains to be determined. Further, this additional condition reflects the differences that can be in observed in systems of equations compared to scalar equations, which can be attributed to the higher dimensionality of the problem.

The methodology employed in this chapter to rigorously prove the existence of TWS for model (6.4) is applicable to models which differ from ours only in the reaction terms for the production and degradation of the ECM and tumour cell densities, e.g., model (6.1) (as shown by Gallay and Mascia [82]) and the model in [27]. This is because key properties of our argument (e.g., the monotonicity of solutions with respect to the shooting parameter, α) hold true given physically-realistic modifications to these reaction terms. By contrast, in the case of models which contain additional flux terms (i.e., chemotaxis or haptotaxis terms) to describe tumour cell movement, such as the model of volume-filling tumour cell invasion by Crossley et al. [49], these properties may be violated and a different approach is required.

The key motivation behind the work presented in this chapter was mathematical in nature as we primarily sought to rigorously prove the existence (and uniqueness) of TWS of the model (6.4) and to comprehensively characterise their minimum wave speed. That said, our results are also meaningful in their biological context, i.e., tumour invasion. Our results reveal that tumour cell invasion speeds may increase with tumour cell aggressivity

(represented by κ) and decrease with ECM integrity (represented by $\bar{M}$). While these trends are not surprising, the model (6.4) has sufficiently few parameters that its predictions can be tested against experimental data (e.g., *in vitro* invasion assays). In this way, the model (6.4) could provide biological insight, despite its simplicity. Further, the analytical tractability of the model makes it amenable to additional studies. For instance, given the largely exhaustive understanding that we have of the current model's behaviour, one can more easily assess the influence of, say, different cancer therapies or nutrient limited growth control on the model dynamics (see Discussion in Chapter 7).

Chapter 7

Conclusions and Future Work

Developing targeted and effective treatment strategies for patients is at the forefront of cancer research. Recently, there has been an increased focus on combination therapies, which aim to exploit anti-cancer effects while minimising adverse side-effects. In particular, experimental and clinical data have established hyperthermia (HT) as a promising candidate for enhancing the efficacy of radiotherapy (RT) [43, 187]. However, incomplete understanding of the interactions between RT and HT, coupled with high inter-tumour heterogeneity in sensitivity to these treatments, is hindering their joint use in the clinic.

In this thesis, we aimed to investigate how two distinct mechanisms of growth control may influence tumour dynamics when RT and HT are applied, alone and in combination, in order to shed light on their interactions and generate hypotheses that may explain some of the widely varying tumour behaviours observed clinically. To this end, we developed a comprehensive mathematical model of tumour growth and response to RT and HT. By systematically investigating different treatments (RT, HT and RT + HT), we produced experimentally testable predictions relating to the biological processes that may underpin positive and negative treatment outcomes and how RT and HT treatments should be combined.

A natural extension of the preceding work consists of assessing how the two mechanisms of growth control may impact tumour invasion in the absence and presence of treatment. Another goal of this thesis was, therefore, to study degenerate, cross-dependent diffusion, which is a key mathematical feature of most reaction-diffusion(-taxis) partial differential equation (PDE) models of tumour invasion into healthy tissue. To do so, we proposed a minimal model that captures the key components of tumour invasion while remaining analytically tractable, and carried out a rigorous travelling wave analysis.

In what follows, we summarise the key results of each chapter and outline possible avenues for future work.

7.1 Summary of work

In Chapter 2, we developed and analysed a new ordinary differential equation (ODE) model of tumour growth which distinguishes between nutrient limited growth arrest, where cell proliferation and cell death rates balance, and space limited growth arrest, where the cell proliferation rate converges to zero, with no cell death. Despite its simplicity, this model exhibits rich solution structure, and we identified three distinct growth regimes: nutrient limited (NL), space limited (SL) and bistable (BS), where both mechanisms of growth arrest coexist. The oxygen consumption rates for maintenance and proliferation, q_1 and q_3, and the vascular volume, V_0, have the greatest influence on the qualitative behaviour of the model and, in particular, the NL, SL and BS regimes lie in different regions of (q_1, q_3, V_0)-space. By distinguishing these regimes, the model lends itself to investigating how nutrient and space limited mechanisms of growth control may impact tumour responses to RT, HT and combined treatment.

Accordingly, in Chapter 3, we extended the model of tumour growth developed in Chapter 2 to include time-dependent tumour responses to RT, and we investigated how tumours in three NL, SL and BS virtual tumour populations respond to RT. We found that tumour responses in the monostable cohorts (NL and SL) can be distinguished from those of tumours in the BS cohort. More specifically, tumours in the NL and SL cohorts have a largely positive response to treatment, with SL tumours experiencing the largest reductions in tumour burden. By contrast, RT is deleterious for all tumours in the BS cohort. Probing deeper into the biological processes that may underlie positive and negative responses to RT, we found that, for NL tumours, positive tumour responses are due to limited tumour regrowth (associated with low values of q_3) while limited tumour regrowth and high RT cell kill (associated with low values of q_1) both play an important role for the positive response of SL tumours. In the BS regime, a tumour's proximity to the boundary between the BS and SL regions in (q_1, q_3, V_0)-space is indicative of its response to treatment, with tumours near this boundary exhibiting extremal responses and, in particular, experiencing the largest increases in tumour burden. A final key result of Chapter 3 relates to RT dosing schedules: for a fixed total dose, tumours in the SL cohort respond best to high fraction doses applied at high frequency (i.e., hitting the tumour as hard and as quickly as possible), while, counter-intuitively, tumours in the NL and BS cohort can benefit from lower fraction doses applied at lower frequency.

As a next step, in Chapter 4, we extended the model of tumour growth and RT response presented in Chapter 3 to incorporate time-dependent tumour responses to HT. We distinguished between mild HT, which we assumed re-oxygenates a tumour via vasodilation and a reduction in oxygen consumption rates, and high HT, which we assumed damages tumour

and endothelial cells, induces a damage-associated angiogenic response, and inhibits DNA repair mechanisms. By setting the radiation dose rate to zero in the model, so that the effect of RT could be neglected, Chapter 4 focussed on studying the response of tumours in the NL, SL and BS cohorts to HT. Our first result was that the effects of mild HT are typically negligible and may even be deleterious for some tumours in the NL and BS cohorts. This led us to conclude that mild HT is unlikely to cause significant radio-sensitisation when RT and HT are combined.

By contrast, high HT has a significantly stronger impact on tumour dynamics. We initially assumed all tumours have a moderate HT-induced angiogenic response (i.e., $\kappa_0 = 10^{-7}$). As for RT response, we distinguished tumours in the monostable regimes and the BS regime: most tumours respond well to high HT, however, the intra-cohort variability in tumour responses was higher in the monostable regimes compared to the BS regime, where all tumours have a particularly strong, positive response to high HT. Delving deeper into the variability observed in monostable regimes, we found that NL tumours with limited tumour regrowth due to a smaller volume at the start of treatment (associated with high values of q_1 and/or q_3) respond most positively to high HT, while SL tumours with limited tumour regrowth due to lower oxygen levels (associated with high values of q_1) respond most positively to high HT. In light of the findings from Chapter 3, this means that some NL tumours that respond best to RT (low q_1 and low q_3) have the worst response to high HT. Similarly, SL tumours that have the strongest RT response (low q_1) also have the weakest high HT response. The implications of these findings for combined treatment response were identified in Chapter 5 (see below). By studying the influence of increasing the weekly high HT fraction dose for a fixed treatment duration, i.e., increasing the total thermal dose, we found that all tumours benefit from a higher thermal dose.

Finally, we relaxed our assumption that all tumours have a moderate HT-induced angiogenic response and allowed the rate of angiogenesis, κ_0, to vary. In doing so, we showed that, the weaker the angiogenic response, the stronger the high HT response, and conversely. In particular, this means that, for tumours with a strong HT-induced angiogenic response, high HT response is poor and HT is less likely to enhance tumour responses to RT when the two treatments are combined.

Building on the work presented in Chapters 3 and 4, Chapter 5 used the model of tumour growth and response to RT and HT presented in Chapter 4 to study tumour responses to combinations of these two treatments. By comparing responses to RT, HT and combined treatment, we characterised the interactions between RT and HT across each virtual cohort. For each tumour, we also determined the treatment (RT, HT and RT + HT) and dosing regimen pair that leads to the 'best' outcome. Imposing maximum tolerable doses (MTDs) on RT and high HT treatment schedules and considering combined treatment to be best

if it induces reductions in viable or total tumour volume that are at least 10% larger than RT or high HT alone, the 'best' outcome was defined as the largest reduction in the sum of viable and total tumour volumes, i.e., the cumulative reduction in tumour burden.

Overall, we identified a number of cases in which combined treatment is not advisable. As predicted by the findings in Chapter 4, mild HT does not enhance tumour responses to RT and, when the HT-induced angiogenic response is sufficiently strong, high HT also does not (typically) enhance tumour responses to RT. Further, given a sufficiently weak HT-induced angiogenic response, tumours in the SL cohort which respond best to RT and worst to high HT (i.e., those characterised by low q_1) do not benefit from combined treatment. Similarly, any tumours which respond particularly well to high HT (i.e., the entire BS cohort, tumours in the NL cohort with high q_1 and/or high q_3 and tumours in the SL cohort with high q_1 and high q_3) do not benefit from combined treatment. In particular, this implies that RT and high HT only have significant synergistic interactions when responses to RT and high HT alone are moderate, limited or poor. A last important result from Chapter 5 relates to the dosing regimens that maximise treatment outcome. As seen in Chapter 3, for SL tumour responding best to RT alone, applying higher fraction doses at higher frequency maximises RT efficacy. By contrast, for tumours responding best to treatments that include high HT (i.e., high HT and high HT + RT), applying lower HT fraction doses over a longer time period maximises treatment efficacy when response to HT alone is stronger, while applying higher HT fraction doses over a shorter time period maximises treatment efficacy when response to HT alone is weaker.

With a view of extending the work presented in Chapters 2–5 to study the influence of growth arrest mechanisms on tumour growth via invasion, Chapter 6 focussed on the mathematical analysis of a simple reaction-diffusion PDE model of tumour invasion. Crucially, this model contains a degenerate, cross-dependent diffusion term, which is used by most reaction-diffusion(-taxis) PDE models of tumour invasion to describe the inhibition of tumour cell movement by the extracellular matrix (ECM). However, a rigorous understanding of the influence of this type of diffusion on the behaviour of travelling wave solutions (TWS) of such PDE models has been lacking. We, therefore, carried out a detailed travelling wave analysis of our model. We considered two types of invasive fronts of tumour tissue into ECM. These fronts differ according to whether or not the ECM density far ahead of the wave front is at carrying capacity. In the former case, we used a shooting argument developed by Gallay and Mascia [82] to prove the existence of a unique TWS for any positive propagation speed. In the latter case, we extended this argument to prove that there exists a unique TWS for any propagation speed greater than or equal to a strictly positive minimum wave speed. Complementing our travelling wave analysis with numerical results, we conjectured that the minimum wave speed increases and decreases monotonically with

the rescaled rate at which tumour cells degrade the ECM and the ECM density ahead of the front, respectively.

7.2 Future work

There are a number of possible extensions of the work presented in this thesis and we outline those we consider to be the most compelling.

7.2.1 Validation against experimental data

The modelling framework developed in Chapters 2–5 to investigate tumour responses to combinations of RT and HT generated a number of interesting results. In particular, while some of our findings support experimentally and clinically observed phenomena, e.g., that increases in tumour oxygen levels observed following mild HT do not significantly enhance tumour responses to RT, we also obtained more surprising findings that challenge certain common assumptions, e.g., that treating patients with the MTD is the best course of treatment. However, the absence of suitable experimental and/or clinical data has meant that our key findings remain to be tested, thus limiting their significance.

Therefore, calibrating our model using a variety of experimental data would help validate the theoretical predictions from Chapters 3–5. More specifically, we could use *in vitro* assays involving two-dimensional monolayers and/or three-dimensional multicellular spheroids in order to test our predictions for tumours in the NL and SL cohorts. Tumour cells grown as monolayers have access to ample nutrient and proliferate until they reach confluence [122]; they are, thus, space limited. Further, tumour spheroids grown in matrices formed of agarose gel or collagen can also be space limited as they reach an equilibrium as cell proliferation ceases, without cell death [103]. By contrast, tumour spheroids grown in free suspension reach an equilibrium when cell proliferation and cell death rates balance [47], making them nutrient limited.

Finally, if we can show that a tumour's growth regime can be determined from its initial response to RT or HT, then it should also be possible to use *in vivo* tumour data from mice treated with RT, HT and their combination to test model predictions across all three regimes.

7.2.2 Spatial modelling

Incorporating spatial structure into the modelling approach from Chapters 2–5 is another important extension. Indeed, *in vivo* tumours grow within healthy tissue and, as previously mentioned, the transition from vascular growth to invasion of the healthy tissue is a hallmark of cancer [98]. To describe invasion, which is an intrinsically spatial process,

a spatially-resolved approach becomes necessary. In addition, it is well-known that intra-tumoural oxygen levels are both temporally- and spatially-heterogeneous. In particular, it has been shown that spatial heterogeneity in tumour oxygenation can significantly influence intra-tumour phenotypic heterogeneity, tumour growth dynamics and response to different treatments [35, 41, 206, 253, 252]. The crucial role of oxygen in our model in terms of modulating both tumour growth and treatment response, thus, also motivates the extension to a spatial model.

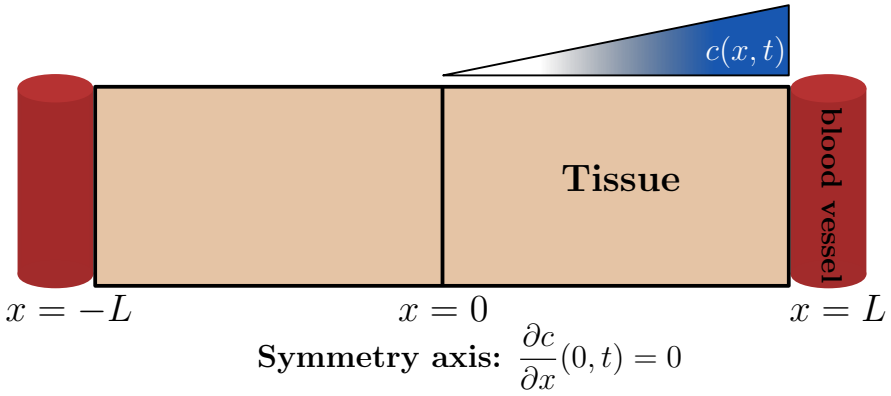


Figure 7.1: Schematic representation of the modified one-dimensional model of tumour growth via invasion. See text for details.

A first step would be to extend the simple PDE model of tumour invasion proposed in Chapter 6 so that it distinguishes between growth arrest due to competition for space and nutrient insufficiency. Following [35], we would assume that oxygen is supplied by two blood vessels at the boundaries of the domain $[-L, L]$ (see Figure 7.1) and consumed by tumour cells for proliferation and maintenance as it diffuses through the ECM and tumour tissue. The oxygen concentration, $c(x,t)$, would, therefore, be governed by a reaction-diffusion PDE of the form

$$\frac{\partial c}{\partial t} = D_c \frac{\partial^2 c}{\partial x^2} - q(c,N)N, \tag{7.1}$$

where $D_c > 0$ is the diffusion coefficient of oxygen and the function $q = q(c,N) > 0$ is the rate of oxygen consumption by tumour cells. We would also impose boundary conditions

$$c(L,t) = c_{max}, \quad \frac{\partial c}{\partial x}(0,t) = 0, \quad t > 0, \tag{7.2}$$

and initial conditions

$$c(x,0) = c_0(x), \quad x \in [0,L]. \tag{7.3}$$

Further, we would retain the assumption from Chapter 6 that tumour cells compete for space only with each other, and we would additionally assume that tumour cells consume oxygen for proliferation and maintenance and die due to nutrient insufficiency when the oxygen concentration drops below a certain threshold. Keeping all other assumptions the

same, the PDE system governing the evolution of the tumour cell and ECM densities, $N(x,t)$ and $M(x,t)$, would take the following form:

$$\begin{cases} \dfrac{\partial N}{\partial t} = \dfrac{\partial}{\partial x}\left[D_N\left(1-\dfrac{M}{M_{max}}\right)\dfrac{\partial N}{\partial x}\right] + [p(c,N)-d(c)]N, \\ \dfrac{\partial N}{\partial t} = -kMN, \end{cases} \tag{7.4}$$

where $p = p(c,N) \geq 0$ is the rate of tumour cell proliferation and $d = d(c) \geq 0$ is the rate of tumour cell death due to nutrient starvation. As in Chapter 6, we would impose no-flux boundary conditions

$$\frac{\partial N}{\partial x}(0,t) = \frac{\partial N}{\partial x}(L,t) = 0, \quad t > 0, \tag{7.5}$$

and initial conditions

$$n(x,0) = n_0(x), \quad m(x,0) = m_0(x) = 1 - n_0(x), \quad x \in [0,L]. \tag{7.6}$$

Finally, we would define the functional forms of q, p and d consistently with those in Chapter 2, i.e.,

$$\begin{cases} q(c,N) = q_1 c + q_3 c\left(1-\dfrac{N}{N_{max}}\right), \\ p(c,N) = q_2 c\left(1-\dfrac{N}{N_{max}}\right), \\ d(c) = \delta_1(c-c_{min})H(c-c_{min}), \end{cases} \tag{7.7}$$

where H is the Heaviside step-function. In this way, we would be able to compare the dynamics of this new spatially-resolved model of tumour growth via invasion to those of the well-mixed model of tumour growth presented in Chapter 2. Extending the PDE model comprising Equations 7.1 and 7.4 to include tumour responses to RT and HT would similarly offer a worthwhile comparison with the models presented in Chapters 3 and 4.

Using a spatial model with a Krogh-cylinder geometry for the vasculature, as described above, is only one of several options. For instance, another would be to assume the existence of multiple blood vessels distributed across the spatial domain and model the inflow of oxygen from blood vessels as point sources [252].

7.2.3 A more realistic depiction of angiogenesis in the presence and absence of treatment

To limit model complexity, our model of tumour growth and response to RT and HT neglected the remodelling of tumour vasculature in response to angiogenesis [38, 73] and RT [152, 153, 196, 232, 250] that is observed *in vivo*. However, the results in Chapters 2–5 clearly indicate that tumour growth dynamics as well as tumour responses to combined treatment in the short- and long-term depend critically on the pre-treatment level of vascularisation and HT-induced changes in vascularisation. In light of this finding, it would be interesting

to extend the model to view the vascular volume as a dynamic variable, which evolves in response to angiogenic cues [95], RT and HT. This would provide us with a more realistic description, not only of the co-evolution of the tumour cells and vasculature, but also of tumour responses to RT and HT. In particular, we would be able to make a more reliable assessment of long-time tumour dynamics in response to RT and HT.

7.2.4 Accounting for healthy tissue response to treatment

In Chapter 3, we found that the efficacy of RT for tumours in the SL regime typically increases with RT fraction dose and frequency. Similarly, we found in Chapters 4 and 5 that tumour responses to treatments comprising HT also typically improve with total thermal dose, i.e., the cumulative thermal dose over the course of treatment. Motivated by these results, we now propose a final extension of the modelling framework presented in Chapters 2–5 that would be worth exploring.

More specifically, it would be interesting to explicitly describe the damage to surrounding healthy tissue sustained during RT and HT and impose a maximum level of cumulative damage during treatment, above which toxicity is considered intolerable. For instance, different normal tissue complication probabilities (NTCPs) have been used to estimate the expected (patient- and organ-specific) adverse side-effects of given RT dosing schedules [99, 231] and optimise RT dosing schedules [110, 132]. Further, a number of mathematical models investigating RT-induced damage to healthy tissue have focussed on describing 'bystander effects' observed at low RT doses (e.g., see [23, 126, 143, 162, 178, 199]). These are secondary effects of radiation (e.g., DNA damage, cell death, DNA repair delays, mutation induction, genomic instabilities) found in cells exposed to radiation or located near irradiated regions [201, 200], which can cause greater tumour and healthy cell death than direct radiation at low RT fraction doses and should, therefore, be taken into consideration.

By combining ideas from the above work, we would be able to consider a trade-off between anti-tumour effects and adverse side-effects. This would allow us, not only to determine the dosing regimens for RT, HT and combined treatment that are physically realistic, but also to draw more meaningful comparisons between individual (RT and HT alone) and combined (RT + HT) treatments by identifying the treatment which maximises the reduction in tumour burden, while minimising healthy tissue damage.

7.3 Final remarks

We developed a novel ODE model of tumour growth that distinguishes between nutrient and space limited mechanisms of growth arrest and extended it to include tumour responses to radiotherapy and hyperthermia. We used this mathematical framework to systematically

investigate how the two distinct, aforementioned mechanisms of growth control may influence tumour responses to RT and HT, applied alone and in combination. In doing so, we produced a range of experimentally testable predictions relating to the biological mechanisms underlying the efficacy of these two treatments and how they should be combined. Further, we proposed and rigorously analysed a model of tumour invasion, obtaining new insights into a key mathematical feature of reaction-diffusion(-taxis) PDE models (i.e., degenerate, cross-dependent diffusion). This work also provides a natural extension of our ODE modelling framework to describe growth via invasion and spatial effects more generally. We believe that our modelling framework could help guide treatment protocol design by efficiently reducing the number of scenarios that could not feasibly be tested experimentally. Hence, it has the potential to support the establishment of HT as a legitimate, alternative therapy in the clinic.

Appendix A

Defining the parameters for our model of tumour growth and response to hyperthermia and radiotherapy

A.1 Defining the tumour growth parameters

In this section, we justify the dimensionless parameter choices summarised in Table 2.1, by referring to dimensional parameter values.

We first define a range of values for the vascular volume, V_0. Assuming that the average diameter of a cell is 20 µm, we estimate that the maximum number of cells that can occupy $1\,\text{mm}^3$ of space is 1.25×10^5 [7]. Now, the Krogh cylinder model shows that oxygen can diffuse up to $100 - 200\,\mu\text{m}$. Using the average cell size and cylindrical geometry, we estimate that a section of blood vessel of length 20 µm can supply oxygen to a number of cells in the range $[100, 300]$. In particular, given that the average diameter of a capillary is 8 µm [171] and using cylindrical geometry once again, we further estimate that $1 \times 10^{-6}\,\text{mm}^3$ of blood vessel can provide oxygen for a volume of cells in the range $[8 \times 10^{-4}, 2.4 \times 10^{-3}]\,\text{mm}^3$. Therefore, a biologically realistic range for V_0 such that the tumour may be sufficiently oxygenated is $[5 \times 10^{-4}, 5 \times 10^{-3}]$. Since tumour vasculature is usually less effective than healthy vasculature [33], we consider $V_0 \in (0, 5 \times 10^{-3}]$.

We now determine c_{min} and g. To do so, we first estimate $S_{\text{max}} = 10^{-6}\,\text{m}^3$ in accordance with the average size of vascular tumours in mice [75, 264]. Moreover, the average oxygen partial pressure in peripheral normal tissues is approximately $p_{\text{max}} = 38\,\text{mmHg}$ [182] and, therefore, using Henry's Law to convert p_{max} into a concentration, it is straightforward to calculate $c^*_{\text{max}} = 2.1 \times 10^{-3}\,\text{kg}\,\text{m}^{-3}$. Now, hypoxia is attained when oxygen levels fall below 8 mmHg [159]. Unlike normal tissue cells, tumour cells can survive in such hypoxic conditions and only start to die in severely hypoxic conditions, which range from 0.75 mmHg

to 0.075 mmHg depending on the tumour [159]. Hence, we take the average of these two values and, using Henry's Law again, we have $c^*_{\min} = 2.26 \times 10^{-5}\,\mathrm{kg\,m^{-3}}$. This implies that

$$c_{\min} = \frac{c^*_{\min}}{c^*_{\max}} = \frac{2.26}{2.1} \times 10^{-2} \approx 10^{-2}, \tag{A.1}$$

and we, therefore, set $c_{\min} = 10^{-2}$.

In addition, we expect that the rate of oxygen exchange per unit volume area of blood vessels, g^* ($\mathrm{m^{-3}\,min^{-1}}$), depends on a variety of factors, including the quality of the vascular network, which can lead to highly heterogeneous tumour perfusion rates [86], and surface areas of oxygen exchange. Since our model does not account for these details, we fix g^* so that, for average values of the oxygen consumption rates, we are in the SL regime for $V_0 \geq 5 \times 10^{-3}$ and we are in the NL or BS regime for $V_0 \leq 5 \times 10^{-4}$ (recall that, for $V_0 \in [5 \times 10^{-4}, 5 \times 10^{-3}]$, the vasculature should be sufficient to supply oxygen to the whole tumour).

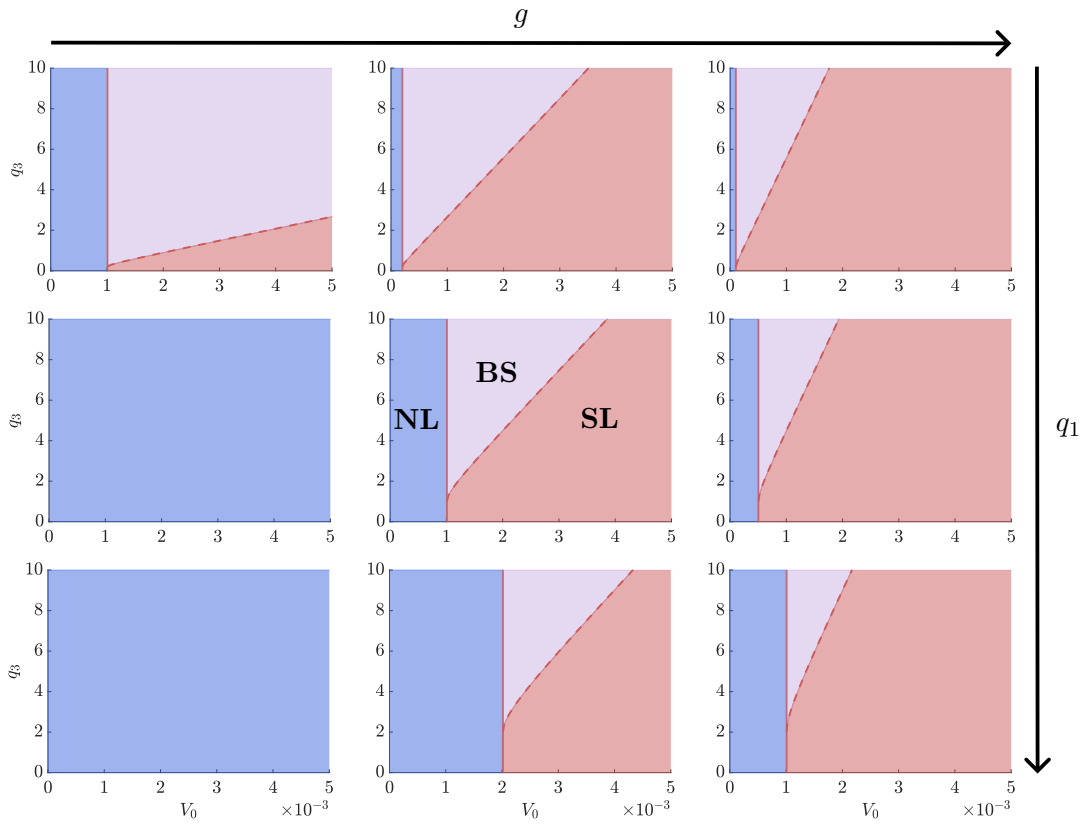


Figure A.1: Regions of existence of the NL and SL steady states of the system (2.5)–(2.6) in (V_0, q_3)-space for $q_1 \in \{0.1, 0.5, 1\}$ and $g \in \{1, 5, 10\}$. The solid and dashed red lines represent the boundaries between the three distinct regions.

Figure A.1 shows that values of $g \geq 5$ are appropriate and that the qualitative behaviour of the model (i.e., the existence of three growth regimes: NL for small values of V_0, SL for large values of V_0 and BS for moderate values of V_0 and large values of q_3) is not affected by

values of $g \geq 5$. Thus, we set $g = g^* S_{\max} \tau = 5$, which is equivalent to $g^* = 5 \times 10^6\,\mathrm{m}^{-3}\,\mathrm{min}^{-1}$ for a timescale $\tau = 1\,\mathrm{min}$.

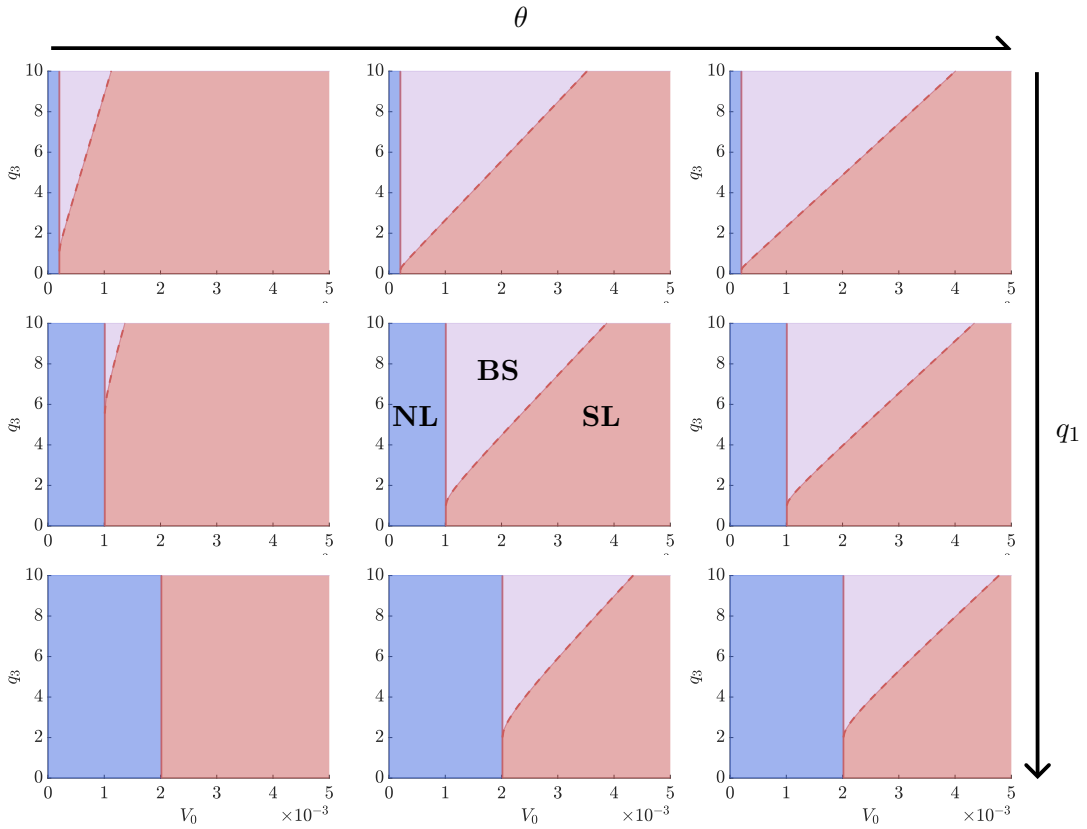


Figure A.2: Regions of existence of the NL and SL steady states of the system (2.5)–(2.6) in (V_0, q_3)-space for $q_1 \in \{0.1, 0.5, 1\}$ and $\delta_1 = \theta q_2$, where $\theta \in \{0.1, 1, 10\}$. The solid and dashed red lines represent the boundaries between the three distinct regions.

We now define the oxygen consumption rates, q_1 and q_3, the proliferation rate, q_2, the death rate, δ_1, and the conversion factor between q_2 and q_3, k. Biological observations suggest that the proliferation and death rates of tumour cells are highly correlated in some tumours: the larger the proliferation rate, the larger the death rate [135, 146, 247]. This suggests that these rates are proportional to each other and we make the simplifying assumption that the dimensionless parameters δ_1 and q_2 satisfy $\delta_1 = q_2$ in order to reduce the number of parameters in the model. Figure A.2 shows that this assumption does not affect the qualitative behaviour of the model described in Chapter 2 and, in particular, the three tumour growth regimes are preserved.

Now, we estimate δ_1^* $(\mathrm{m}^3\,\mathrm{kg}^{-1}\,\mathrm{min}^{-1})$ as

$$\delta_1^* \in \left(\frac{1.2 \times 10^{-6}\,\mathrm{min}^{-1}}{0.75 \times 2.1 \times 10^{-5}\,\mathrm{kg\,m}^{-3}}, \frac{1.2 \times 10^{-4}\,\mathrm{min}^{-1}}{0.75 \times 2.1 \times 10^{-5}\mathrm{kg\,m}^{-3}} \right), \tag{A.2}$$

where the numerators of both fractions correspond to death rates found in the literature [138, 217] and the denominator corresponds to the average oxygen concentration below $c_{\min}^*$

(this scaling allows us to obtain the correct units for δ_1^*). We then have

$$\delta_1^* \in \left(7.6 \times 10^{-2}\,\mathrm{m}^3\,\mathrm{kg}^{-1}\,\mathrm{min}^{-1}, 7.6\,\mathrm{m}^3\,\mathrm{kg}^{-1}\,\mathrm{min}^{-1}\right), \tag{A.3}$$

which we non-dimensionalise according to (2.8) to obtain

$$\delta_1 \in (1.6 \times 10^{-4}, 1.6 \times 10^{-2}). \tag{A.4}$$

Since $q_2 = \delta_1$ by assumption, we have

$$q_2 \in (1.6 \times 10^{-4}, 1.6 \times 10^{-2}). \tag{A.5}$$

Further, the value of k^* ($\mathrm{m}^6\ \mathrm{kg}^{-1}$), the conversion factor between q_3^* and q_2^*, is not readily available in the literature. Since cells consume oxygen significantly faster than they proliferate, we expect $q_2^* \ll q_3^*$, i.e., $k^* \ll 1$. We performed preliminary numerical simulations (result not shown for brevity) to find a value of k^* that gives realistic growth dynamics across parameter space. As a result, we fix $k^* = \frac{10^{-5}}{2.1}\ \mathrm{m}^6\ \mathrm{kg}^{-1}$ and this implies that

$$k = \frac{c^*_{\max}}{S_{\max}} k^* = \frac{2.1 \times 10^{-3} \times 10^{-5}\,\mathrm{kg\,m^{-3}m^6kg^{-1}}}{2.1 \times 10^{-6}\mathrm{m}^3} = 10^{-2}. \tag{A.6}$$

Combining Equations (A.5) and (A.6) gives us the following dimensionless range for $q_3 = q_2/k$:

$$q_3 \in (1.6 \times 10^{-2}, 1.6). \tag{A.7}$$

We further justify the range of values for q_3 by considering experimentally-determined values for the rate of oxygen consumption by cells. Wagner et al. [256] conducted their own experiments and reviewed results from other authors; they reported oxygen consumption rates in the range $6 \times 10^{-5} - 6 \times 10^{-3}\,\mathrm{kg\,m^{-3}\,min^{-1}}$. These constant consumption rates correspond to the oxygen uptake of cells in a well-oxygenated medium, i.e., where the rate of oxygen consumption is at its maximum. Given the volume of the tumours in their experiments and the maximal oxygen concentration they set, we can find the following estimate for the range of q_1^*:

$$q_1^* \in (2.1 \times 10^4, 2.1 \times 10^7)\,\mathrm{m^{-3}\,min^{-1}}. \tag{A.8}$$

Given (2.8) and $S_{\max} = 10^{-6}$, this implies that

$$q_1 \in (2.1 \times 10^{-2}, 21). \tag{A.9}$$

The range of values for q_1 in Equation (A.9) is determined using overall oxygen consumption rates which do not distinguish between consumption for proliferation and for maintenance. In practice, q_1 would, therefore, be smaller than the values in (A.9). In view of this, we recover the dimensionless parameter range for q_1 in Table 2.1 by rounding down the upper and lower bounds of the range in (A.9) to the closest order of magnitude. Consistent with the range for q_3 in Equation (A.7), we assume q_3 to be in the same range as q_1.

A.2 Defining the radiotherapy parameters

Parameters	Definition	Value(s) (units)	Source
ν	RT sub-lethal damage rate	$0.000 - 0.775\,\mathrm{Gy}^{-1}$	[176]
λ, λ_S	RT lethal damage rate	$0.104 - 1.091\,\mathrm{Gy}^{-1}$	[176]
μ	Repair rate constant	$3.2 \times 10^{-2} - 5 \times 10^{-3}\,\mathrm{min}^{-1}$	[229]
		$0.006\,\mathrm{min}^{-1}$, $0.011\,\mathrm{min}^{-1}$	[176]
η_R	Clearance rate of cells killed by RT	$5 \times 10^{-5}\,\mathrm{min}^{-1}$	[176]

Table A.1: List of dimensional RT response parameter values found in the literature, which we use to estimate dimensionless parameter values stated in Table 3.1.

A.3 Defining the hyperthermia parameters

Parameters	Definition	Value(s) (units)	Source
κ_0	Rate of angiogenesis	$0.223 - 0.8\,\mathrm{mm\,d}^{-1}$	[142]
		$0.144 - 0.6\,\mathrm{mm\,d}^{-1}$	[114]
μ_Λ	HT weighing factor	$[0, 5]$ (-)	[262]
k_1	Repair protein inactivation rate	$[0.1, 1]\,\mathrm{min}^{-1}$	[262]
k_2	Repair protein reactivation rate	$[0, 0.00167]\,\mathrm{min}^{-1}$	[262]

Table A.2: List of dimensional high HT response parameter values found in the literature, which we use to estimate dimensionless parameter values stated in Table 4.1.

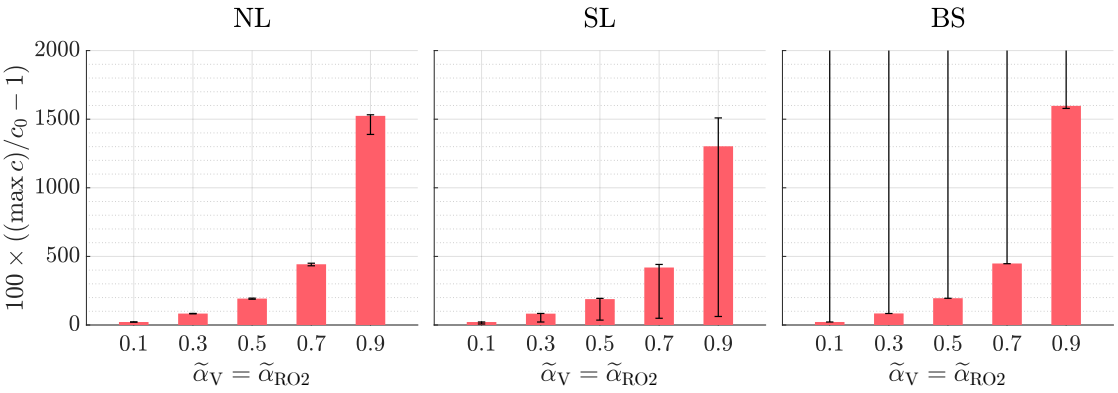


Figure A.3: For the NL, SL and BS cohorts, we show the median, minimum and maximum values of $100 \times (\max c/c_0 - 1)$ reached in the last week of an 8-week long mild HT schedule with $\widetilde{\alpha}_{\mathrm{V}} = \widetilde{\alpha}_{\mathrm{RO2}} \in \{0.1, 0.3, 0.5, 0.7, 0.9\}$. For the BS cohort, maximum values are greater than 2000% for all values of $\widetilde{\alpha}_{\mathrm{V}}$ and $\widetilde{\alpha}_{\mathrm{RO2}}$. Experimental evidence suggests that we can usually expect at most a 3-fold increase in the oxygen concentration due to mild HT [228]. Therefore, values of $\widetilde{\alpha}_{\mathrm{V}} = \widetilde{\alpha}_{\mathrm{RO2}} \leq 0.5$ are physically realistic, while values of $\widetilde{\alpha}_{\mathrm{V}} = \widetilde{\alpha}_{\mathrm{RO2}} > 0.5$ may lead to unrealistically large increases in tumour oxygenation.

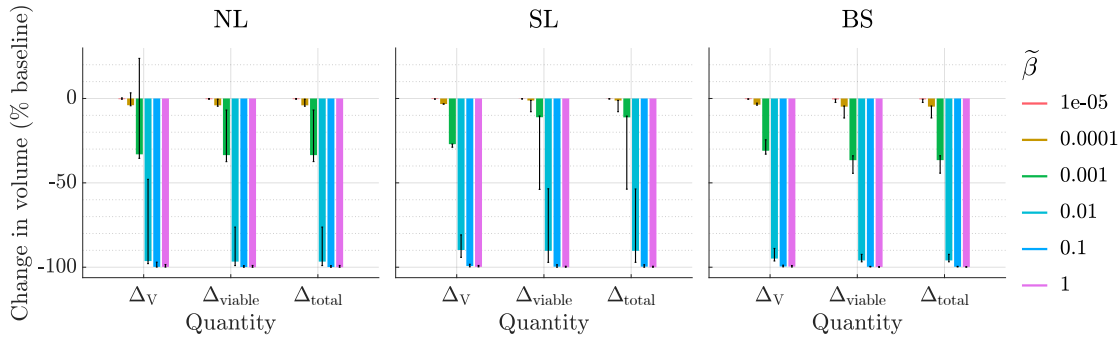


Figure A.4: For the NL, SL and BS cohorts, we show the median, minimum and maximum values of $\Delta^{\mathrm{H}}_{\mathrm{V}}$, $\Delta^{\mathrm{H}}_{\mathrm{viable}}$ and $\Delta^{\mathrm{H}}_{\mathrm{total}}$ in the last week of an 8-week long high HT schedule with $\widetilde{\beta} \in \{0.00001, 0.0001, 0.001, 0.01, 0.1, 1\}$. When $\widetilde{\beta} \leq 0.0001$, the effects of high HT are negligible, while, when $\widetilde{\beta} \geq 0.1$, high HT leads to nearly complete tumour eradication. Values of $\widetilde{\beta} \in [0.001, 0.01]$ are associated with more physically realistic values of $\Delta^{\mathrm{H}}_{\mathrm{viable}}$, $\Delta^{\mathrm{H}}_{\mathrm{total}}$ and $\Delta^{\mathrm{H}}_{\mathrm{V}}$ and greater inter-tumour variability. We, thus, choose $\widetilde{\beta} \in [0.001, 0.01]$ to be representative of a realistic range of high HT doses.

Appendix B

Tumour response to mild HT is not significantly affected by the values of $\widetilde{\alpha}_{\mathrm{V}}$ and $\widetilde{\alpha}_{\mathrm{RO2}}$

In this section, we show that tumour responses to mild HT in the NL, SL and BS virtual cohorts are qualitatively the same for all values of $\widetilde{\alpha}_{\mathrm{V}} = \widetilde{\alpha}_{\mathrm{RO2}} \in \{0.1, 0.3, 0.5\}$.

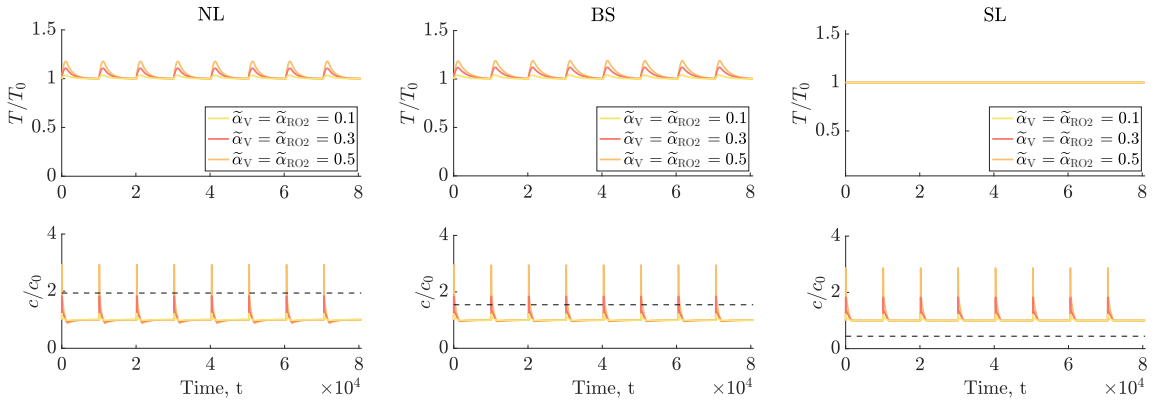


Figure B.1: For mild HT ($\widetilde{\alpha}_{\mathrm{V}} = \widetilde{\alpha}_{\mathrm{RO2}} \in \{0.1, 0.3, 0.5\}$), we solve Equations (4.12)–(4.17) for $t \in (0, 8 \times 10^4]$ subject to initial conditions (4.20). We set (NL) $(q_1, q_3, V_0) = (1.59, 6.17, 5 \times 10^{-4})$, (BS) $(q_1, q_3, V_0) = (1.24, 6.29, 2.75 \times 10^{-3})$ and (SL) $(q_1, q_3, V_0) = (1.08, 6.19, 5 \times 10^{-3})$. For all values of $\widetilde{\alpha}_{\mathrm{V}}$ and $\widetilde{\alpha}_{\mathrm{RO2}}$, the tumours experience transient increases in oxygen levels, which are associated with transient increases in tumour volume for the tumours in the NL and BS regimes. As $\widetilde{\alpha}_{\mathrm{V}}$ and $\widetilde{\alpha}_{\mathrm{RO2}}$ increase, the observed increases in c and T are enhanced.

For three NL, BS and SL tumours, Figure B.1 shows that the observed increases in oxygen levels and tumour volume during exposure to mild HT are enhanced as $\widetilde{\alpha}_{\mathrm{V}}$ and $\widetilde{\alpha}_{\mathrm{RO2}}$ increase. In spite of this, these tumours' qualitative response to mild HT remains the same across the different $\widetilde{\alpha}_{\mathrm{V}}$ and $\widetilde{\alpha}_{\mathrm{RO2}}$ values. The summary statistics in Table B.1 confirm that these results hold across the NL, BS and SL virtual cohorts. In terms of long-term tumour response, Figure B.2 shows that, while the number of tumours in the BS cohort

which switch to a SL steady state following mild HT increases with $\widetilde{\alpha}_{\mathrm{V}}$ and $\widetilde{\alpha}_{\mathrm{RO2}}$, most tumours in this cohort remain NL following mild HT. Further, the tumours that switch steady state are characterised by large values of V_{d}.

		$\Delta^{\mathrm{H}}_{\mathrm{viable}}$			$\Delta^{\mathrm{H}}_{\mathrm{c}}$		
Quantity	Regime	$\widetilde{\alpha}_{\mathrm{V}} = 0.1$	$\widetilde{\alpha}_{\mathrm{V}} = 0.3$	$\widetilde{\alpha}_{\mathrm{V}} = 0.5$	$\widetilde{\alpha}_{\mathrm{V}} = 0.1$	$\widetilde{\alpha}_{V} = 0.3$	$\widetilde{\alpha}_{\mathrm{V}} = 0.5$
Median	NL	0.869	2.71	4.46	0.0651	0.608	2.37
Min.		0.0899	0.270	0.424	0.0453	0.479	2.00
Max.		0.953	2.91	4.80	0.815	2.96	6.32
Median	BS	1.32	4.16	6.81	0.362	1.64	4.29
Min.		1.05	3.32	5.46	0.202	1.03	1.98
Max.		82.3	82.3	106	3290	3340	3420
Median	SL	0	0	0	0.888	3.16	6.55
Min.		-	-	-	0.359	1.13	1.98
Max.		-	-	-	0.896	3.20	6.66

Table B.1: Table summarising the median, minimum and maximum values of $\Delta^{\mathrm{H}}_{\mathrm{viable}}$ and $\Delta^{\mathrm{H}}_{\mathrm{c}}$ in the NL, SL and BS virtual populations for mild HT with $\widetilde{\alpha}_{\mathrm{V}} = \widetilde{\alpha}_{\mathrm{RO2}} \in \{0.1, 0.3, 0.5\}$. Across values of $\widetilde{\alpha}_{\mathrm{V}}$ and $\widetilde{\alpha}_{\mathrm{RO2}}$, the increases in the viable volume and oxygen concentration are typically modest, except for certain tumours in the BS regime, which experience significantly larger increases in T and c.

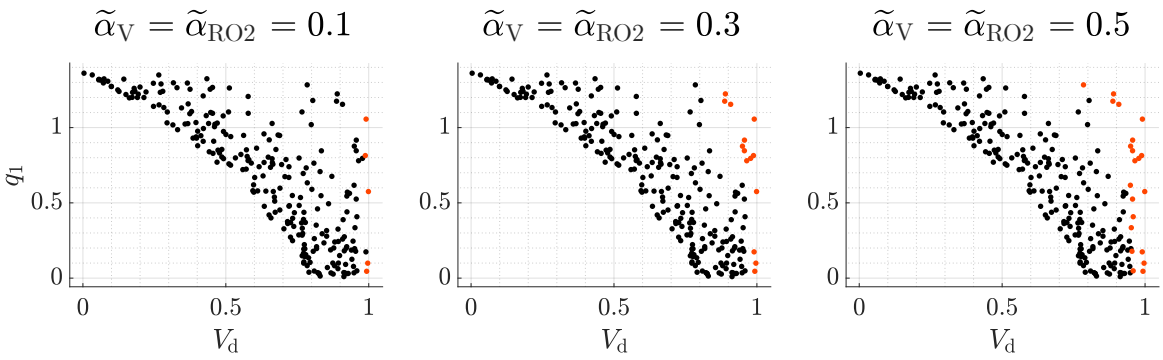


Figure B.2: For the virtual BS tumour population and mild HT ($\widetilde{\alpha}_{\mathrm{V}} = \widetilde{\alpha}_{\mathrm{RO2}} \in \{0.1, 0.3, 0.5\}$), the scatter plots show the (q_1, V_{d}) pairs that correspond to tumours that switch (red) and do not switch (black) steady state. The former are typically characterised by larger values of V_{d} and the number of tumours which switch steady state increases with $\widetilde{\alpha}_{\mathrm{V}}$ and $\widetilde{\alpha}_{\mathrm{RO2}}$.

Appendix C

Tumour response to RT+HT: additional numerical results

Here, we present numerical simulation results that support and complement the findings outlined in Chapter 5.

C.1 Comparing tumour responses to equivalent RT, HT and RT+HT protocols

C.1.1 Appendix for Section 5.4.1.1

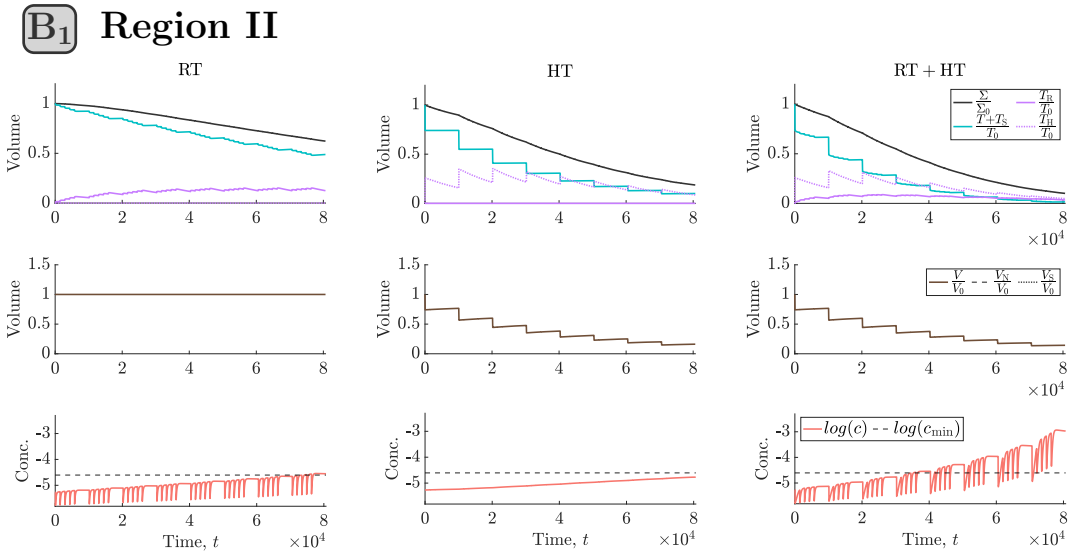


Figure C.1: For conventional RT and HT schedules, alone and combined, we solve Equations (4.12)–(4.17) for $t \in (0, 8 \times 10^4]$ subject to initial conditions (4.20). We fix $V_0 = 0.0005$ and $(q_1, q_3) = (7.78, 0.0401)$ corresponding to tumour B_1 in region II shown in Figure 5.6. This tumour responds well to both RT and HT alone and the two treatments combine additively.

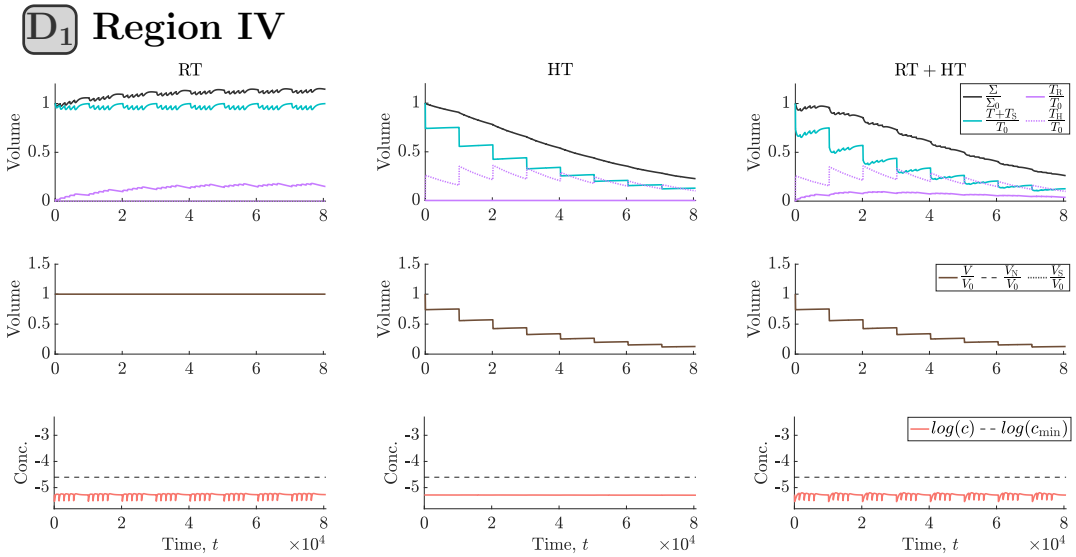


Figure C.2: For conventional RT and HT schedules, alone and combined, we solve Equations (4.12)–(4.17) for $t \in (0, 8 \times 10^4]$ subject to initial conditions (4.20). We fix $V_0 = 0.0005$ and $(q_1, q_3) = (7.60, 9.94)$ corresponding to tumour D_1 in region IV shown in Figure 5.6. This tumour responds best to HT alone as its response to RT alone is sufficiently poor that combined treatment leads to a smaller reduction in total volume than HT alone.

C.1.2 Appendix for Section 5.4.1.2

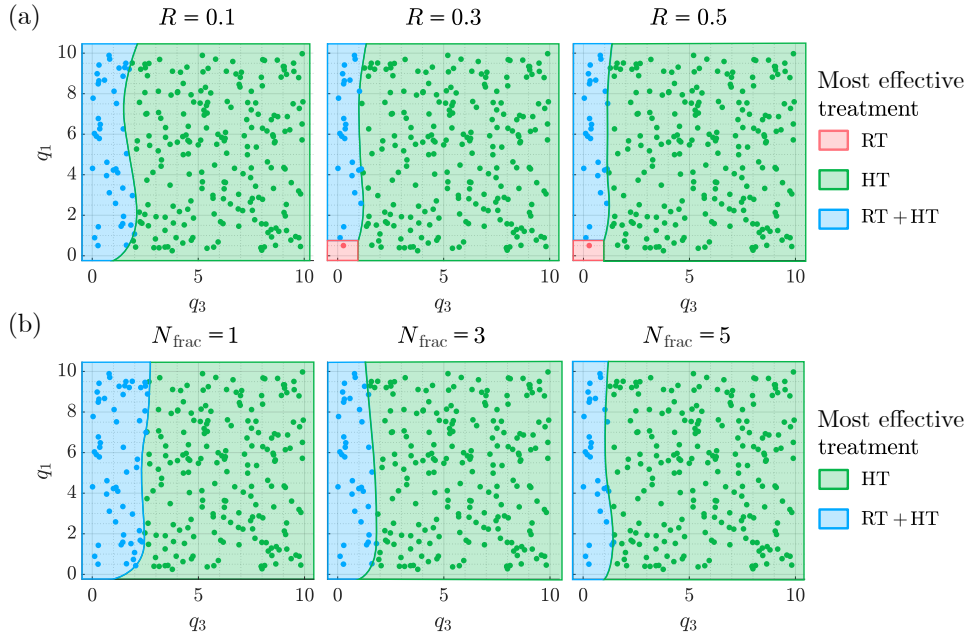


Figure C.3: Scatter plots of the (q_1, q_3) pairs that define the NL virtual cohort showing the regions in which RT, HT and RT + HT are most effective for (a) $R \in \{0.1, 0.3, 0.5\}$, $\widetilde{\beta} = 0.005$ and $N_{\text{frac}} = 5$ and (b) $R = 0.2$, $\widetilde{\beta} = 0.005$ and $N_{\text{frac}} \in \{1, 3, 5\}$. As R and N_{frac} decrease, treatments comprising HT (i.e., HT and RT + HT) are most effective for an increasing number of tumours. This is because the duration of these treatments increase when R and N_{frac} decrease, resulting in a larger total thermal dose.

C.1.3 Appendix for Section 5.4.2.1

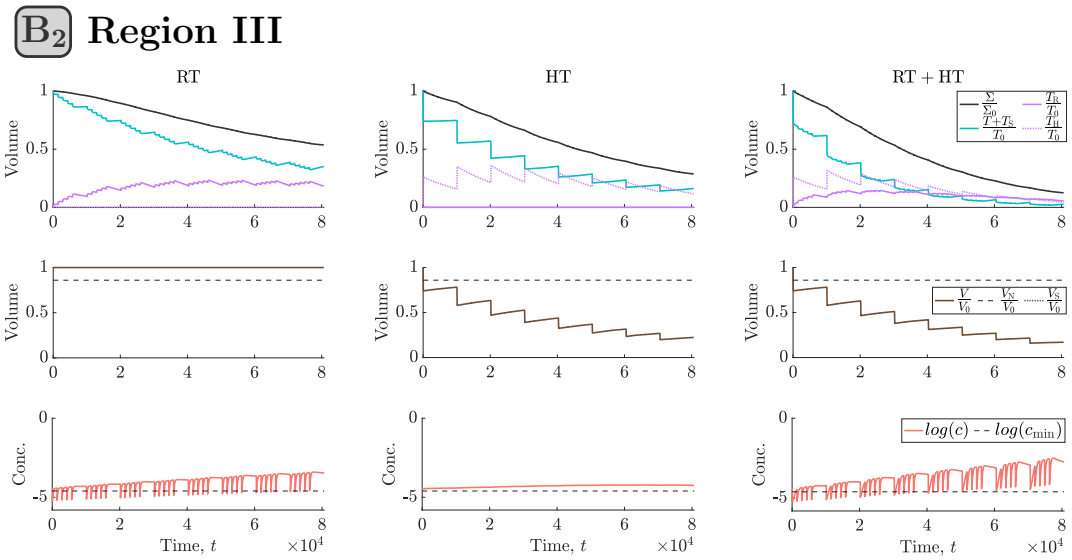


Figure C.4: For conventional RT and HT schedules, alone and combined, we solve Equations (4.12)–(4.17) for $t \in (0, 8 \times 10^4]$ subject to initial conditions (4.20). We fix $V_0 = 0.005$ and $(q_1, q_3) = (2.14, 0.143)$ corresponding to tumour B_2 in region III shown in Figure 5.13. This tumour responds well to both RT and HT alone and the two treatments combine additively.

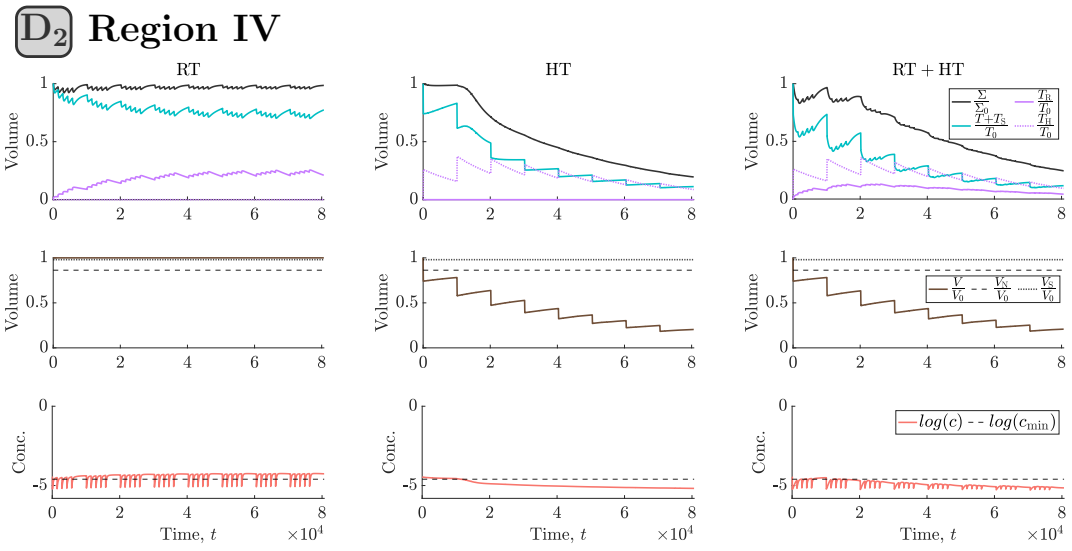


Figure C.5: For conventional RT and HT schedules, alone and combined, we solve Equations (4.12)–(4.17) for $t \in (0, 8 \times 10^4]$ subject to initial conditions (4.20). We fix $V_0 = 0.005$ and $(q_1, q_3) = (2.14, 7.60)$ corresponding to tumour D_2 in region IV shown in Figure 5.13. This tumour responds best to HT alone as its response to RT alone is sufficiently poor that combined treatment leads to a smaller reduction in total volume than HT alone.

C.1.4 Appendix for Section 5.4.2.2

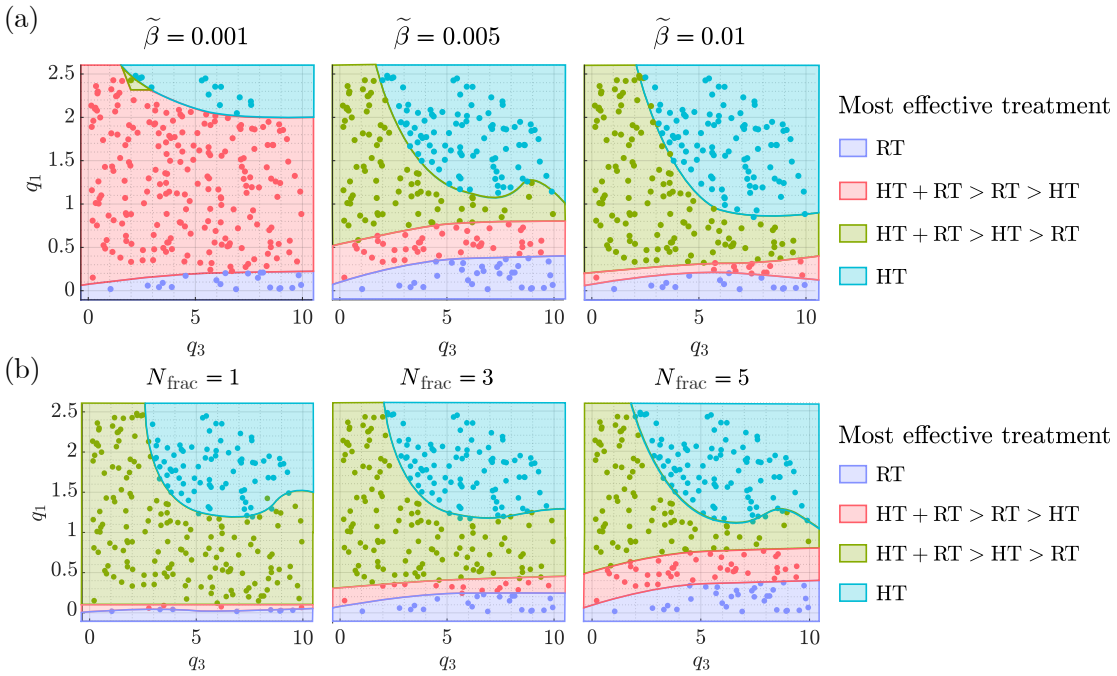


Figure C.6: Scatter plots of the (q_1, q_3) pairs used to generate the SL virtual cohort showing the regions in which RT, HT and RT + HT are most effective for (a) $R = 0.2$, $\widetilde{\beta} \in \{0.001, 0.005, 0.01\}$ and $N_{\text{frac}} = 5$ and (b) $R = 0.2$, $\widetilde{\beta} = 0.005$ and $N_{\text{frac}} \in \{1, 3, 5\}$. The efficacy of combined treatment increases when $\widetilde{\beta}$ is small because RT responses are enhanced compared to HT responses. The efficacy of combined treatment also increases when $\widetilde{\beta}$ is large and N_{frac} is small because HT responses are enhanced compared to RT responses.

C.2 The importance of how RT and HT are coordinated

To determine if the way in which RT and HT are coordinated has a significant impact on tumour responses to combinations of RT and HT, we consider the combination schedules defined in Section 5.2.1, with minor modifications. More specifically, we vary the order in which RT and HT are administered on Mondays and the delay between the two treatments, which we define to be 1 minute, 1 hour or 4 hours. These delays are motivated by those applied in clinical trials [102, 185, 245], as discussed in Section 1.3.3.2.

Figures C.7 and C.8 show that, for combinations of conventional RT and HT, the way in which RT and mild or high HT are coordinated typically has a small impact on tumour responses to combined treatment, with differences in $\Delta^{\text{R+H}}_{\text{viable}}$, $\Delta^{\text{R+H}}_{\text{total}}$ and $\Delta^{\text{R+H}}_{\text{V}}$ that are less than 10% for most tumours. That said, the effects of mild HT are strongest when HT is applied immediately before RT. These results extend to all combined treatment schedules.

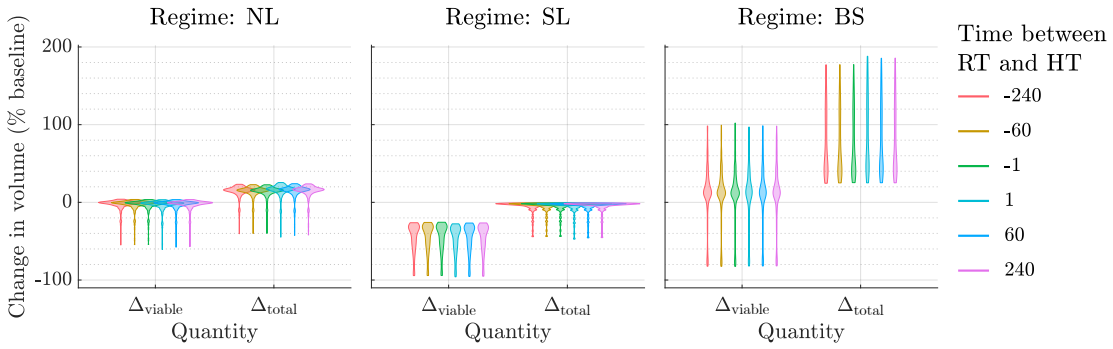


Figure C.7: For the NL, SL and BS cohorts and combinations of conventional RT ($5 \times 2\,\text{Gy}$ for 8 weeks) and mild HT ($\tilde{\alpha}_{\text{V}} = \tilde{\alpha}_{\text{RO2}} = 0.3$), the violin plots compare the distributions of $\Delta^{\text{R+H}}_{\text{viable}}$ and $\Delta^{\text{R+H}}_{\text{total}}$ across the different ways in which we coordinate RT and HT. Negative time between RT and HT refers to RT applied before HT, and conversely for positive time. The differences due to the way in which RT and mild HT are coordinated are below 10% for most tumours, with larger differences when HT is applied immediately before (vs. after) RT.

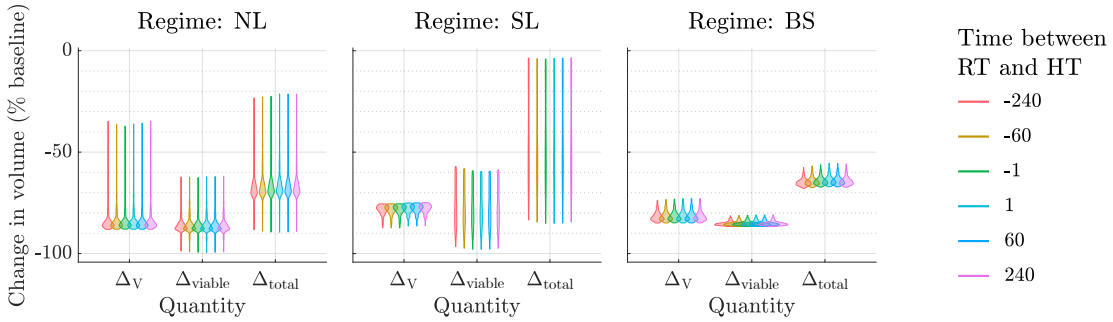


Figure C.8: For the NL, SL and BS cohorts and combinations of conventional RT ($5 \times 2\,\text{Gy}$ for 8 weeks) and high HT ($\widetilde{\beta} = 0.005$), the violin plots compare the distributions of $\Delta^{\text{R+H}}_{\text{viable}}$, $\Delta^{\text{R+H}}_{\text{total}}$ and $\Delta^{\text{R+H}}_{\text{V}}$ across the different ways in which we coordinate RT and HT. Negative time between RT and HT refers to RT applied before HT, and conversely for positive time. The differences due to the way in which RT and high HT are coordinated are negligible ($\leq 5\%$).

C.3 The influence of the rate of damage-induced angiogenesis, κ_0

To determine the influence of κ_0 on tumour responses to combinations of RT and high HT, we performed the numerical study outlined in Chapter 5 for $\kappa_0 = 10^{-8}$ and $\kappa_0 = 10^{-6}$. Figure C.9 summarises the key results from these additional studies by comparing the best treatment across the NL, SL and BS virtual cohorts when $\kappa_0 \in \{10^{-8}, 10^{-7}, 10^{-6}\}$.

Figure C.9 shows that, when $\kappa_0 = 10^{-8}$, most tumours respond best to high HT alone. This can be explained as follows. In Chapter 4, we saw that tumour responses to HT alone are significantly enhanced for $\kappa_0 = 10^{-8}$ (see Section 4.5.4). As a result, high HT responses will be significantly enhanced compared to RT responses and high HT will have

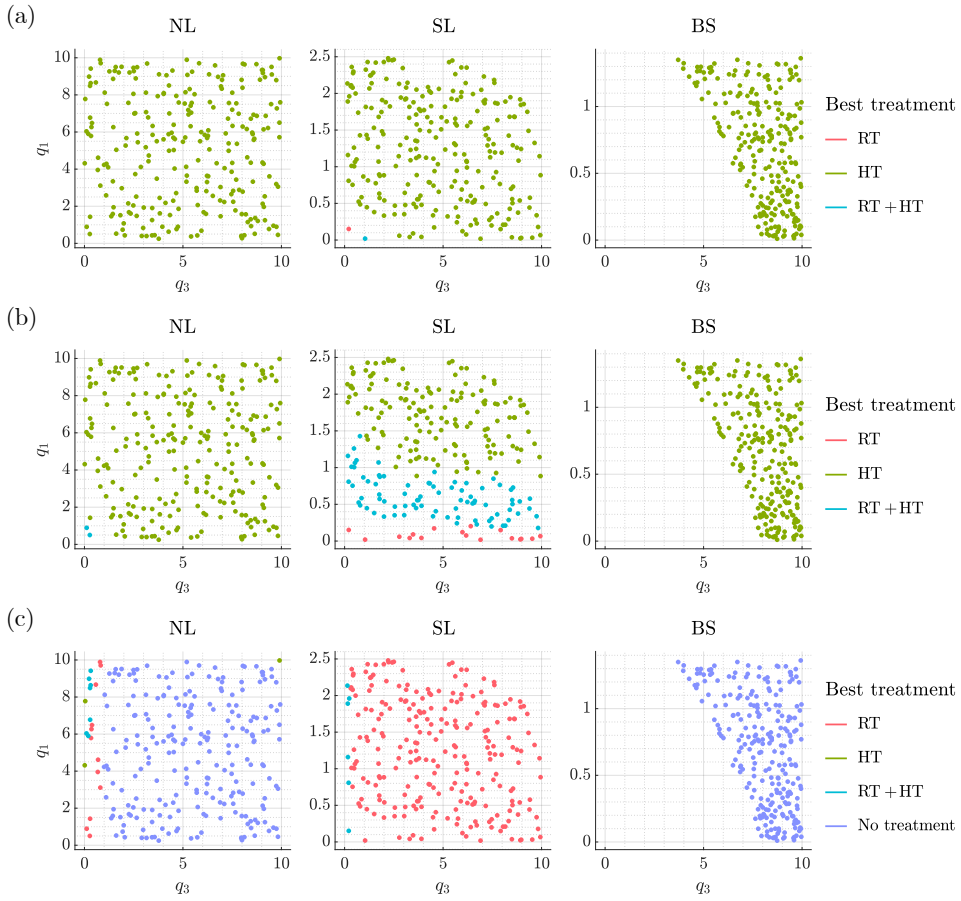


Figure C.9: Scatter plots showing how the best treatment (as defined in Section 5.2.4) for the (q_1, q_3) pairs used to generate the NL, SL and BS virtual cohorts varies with (a)–(c) $\kappa_0 \in \{10^{-8}, 10^{-7}, 10^{-6}\}$. High HT response is enhanced as κ_0 decreases, which results in a greater number of tumours responding best to high HT alone when $\kappa_0 = 10^{-8}$. By contrast, high HT response worsens as κ_0 increases, which results in a greater number of tumours either responding best to RT alone or having no preferred treatment, as all treatments are deleterious.

the dominant influence on tumour responses to combined treatment. From the results shown in Chapter 5, this implies that a greater number of tumours will respond best to high HT alone, since high HT (and combined treatment) is more likely to outperform RT and combined treatment is less likely to significantly improve upon high HT alone.

Further, Figure C.9 shows that, when $\kappa_0 = 10^{-6}$, most tumours either respond best to RT alone or there is no effective treatment. We can also explain this using results from Chapters 3 and 4. In Chapter 3, we saw that tumour responses to RT alone are limited in the NL cohort, especially when the oxygen consumption rate for proliferation, q_3, is large, deleterious in the BS cohort, and positive in the SL cohort (see Section 3.4). In addition, in Chapter 4, we saw that tumour responses to high HT alone are typically deleterious in the NL and BS cohorts and limited in the SL cohort when $\kappa_0 = 10^{-6}$ (see Section 4.5.4). This

means that, for the NL and BS cohorts, high HT will typically worsen tumour response to RT when the two treatments are combined. Thus, if RT alone elicits a positive response, it will typically be the best treatment and, otherwise, no treatment will be preferred. Finally, for the SL cohort, the limited efficacy of high HT alone when $\kappa_0 = 10^{-6}$ combined with the high efficacy of RT alone imply that RT alone will typically be the best treatment.

Overall, these results confirm the importance of understanding vascular dynamics during tumour growth and under treatment, as they greatly impact tumour responses to high HT, alone and combined with RT. As shown here, this can have significant consequences on the preferred treatment for a given tumour.

C.4 The influence of how we define the 'best' treatment

In Section 5.2.4, we outline our methodology for determining the 'best' treatment (and dosing regimen) for each tumour. In particular, we assume that combined treatment is best if and only if it induces reductions in viable or total volumes at least $P = 10\%$ larger than HT and RT alone. Here, we show how varying $P \in \{0, 10, 20\}\%$ impacts our assessment of the best treatment when considering combinations of RT and high HT.

Unsurprisingly, Figure C.10 shows that, as P increases and the condition for combined treatment to be best becomes stronger, fewer tumours respond best to combined treatment. In the NL cohort, where response to high HT alone is typically better than response to RT alone, this means that, as P increases, a larger number of tumours respond best to high HT alone. In the SL cohort, where higher values of the oxygen consumption rate for maintenance, q_1, are associated with positive high HT response and limited RT response, and conversely for lower values of q_1, we see that, as P increases, a greater number of tumours (with higher q_1) respond best to high HT alone and a greater number of tumours (with lower q_1) respond best to RT alone. Finally, in the BS cohort, where RT is deleterious and high HT is very effective, RT always worsens high HT response when combined, and high HT alone is best.

These results highlight the importance of quantifying when the additional, positive anti-cancer effects obtained by combining high HT and RT outweigh the additional, negative side-effects also obtained by combining high HT and RT. In particular, one should also model the effect of RT and HT on healthy tissue (see the Discussion in Chapter 7).

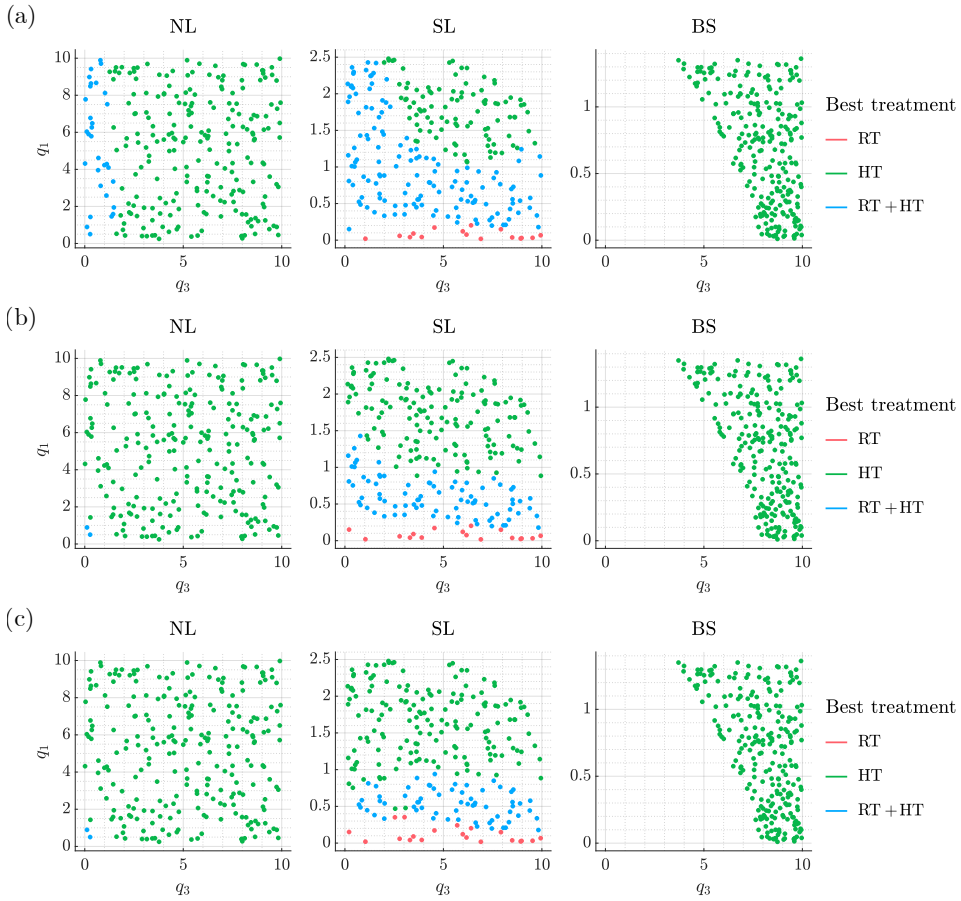


Figure C.10: Scatter plots showing how the best treatment for the (q_1, q_3) pairs used to generate the NL, SL and BS virtual cohorts varies with $P \in \{0, 10, 20\}\%$. (P is the minimum percent increase in the reduction in viable or total volumes for combined treatment compared to RT and high HT alone necessary for combined treatment to be considered better than RT and high HT alone.) As P increases, the number of tumours responding best to combined treatment decreases, while the number of tumours responding best to high HT alone increases (all cohorts) and the number of tumours responding best to RT alone increases (SL cohort).

References

[1] Kamran A Ahmed, Candace R Correa, Thomas J Dilling, Nikhil G Rao, Ravi Shridhar, Andy M Trotti, Richard B Wilder, and Jimmy J Caudell. Altered fractionation schedules in radiation treatment: a review. In *Seminars in Oncology*, volume 41, pages 730–750. Elsevier, 2014.

[2] Juan CL Alfonso and Lawrence Berk. Modeling the effect of intratumoral heterogeneity of radiosensitivity on tumor response over the course of fractionated radiation therapy. *Radiation Oncology*, 14(1):1–12, 2019. doi: 10.1186/s13014-019-1288-y.

[3] Juan CL Alfonso, Nick Jagiella, Luis Núnez, Miguel A Herrero, and Dirk Drasdo. Estimating dose painting 506 effects in radiotherapy: a mathematical model. *PloS One*, 9(2):e89380, 2014. doi: 10.1371/journal.pone.0089380.

[4] Alexander RA Anderson. A hybrid mathematical model of solid tumour invasion: the importance of cell adhesion. *Mathematical Medicine and Biology: a Journal of the IMA*, 22(2):163–186, 2005.

[5] Alexander RA Anderson, Mark AJ Chaplain, E Luke Newman, Robert JC Steele, and Alastair M Thompson. Mathematical modelling of tumour invasion and metastasis. *Computational and Mathematical Methods in Medicine*, 2(2):129–154, 2000.

[6] Robyn P Araujo and DL Sean McElwain. A history of the study of solid tumour growth: the contribution of mathematical modelling. *Bulletin of Mathematical Biology*, 66(5):1039–1091, 2004.

[7] Aleksandra Ardaševa, Alexander RA Anderson, Robert A Gatenby, Helen M Byrne, Philip K Maini, and Tommaso Lorenzi. Comparative study between discrete and continuum models for the evolution of competing phenotype-structured cell populations in dynamical environments. *Physical Review E*, 102(4):042404, 2020.

[8] Nicola J Armstrong, Kevin J Painter, and Jonathan A Sherratt. A continuum approach to modelling cell–cell adhesion. *Journal of Theoretical Biology*, 243(1):98–113, 2006.

[9] Colin Atkinson, Gerd EH Reuter, and CJ Ridler-Rowe. Traveling wave solution for some nonlinear diffusion equations. *SIAM Journal on Mathematical Analysis*, 12(6): 880–892, 1981.

[10] Mohammad Mahdi Attar, Mohammad Haghpanahi, Saeid Amanpour, and Mohammad Mohaqeq. Analysis of bioheat transfer equation for hyperthermia cancer treatment. *Journal of Mechanical Science and Technology*, 28(2):763–771, 2014.

[11] Stephen F Badylak, Charles F Babbs, Teresa M Skojac, William D Voorhees, and Ralph C Richardson. Hyperthermia-induced vascular injury in normal and neoplastic tissue. *Cancer*, 56(5):991–1000, 1985.

[12] Mariona Baliu-Piqué, Atanasio Pandiella, and Alberto Ocana. Breast cancer heterogeneity and response to novel therapeutics. *Cancers*, 12(11):3271, 2020.

[13] Manuel Bañobre-López, Antonio Teijeiro, and Jose Rivas. Magnetic nanoparticle-based hyperthermia for cancer treatment. *Reports of Practical Oncology & Radiotherapy*, 18(6):397–400, 2013.

[14] Gian Franco Baronzio, Erich Dieter Hager, Gian Franco Baronzio, Roberta Delia Seta, Mario D'Amico, Attilio Baronzio, Isabel Freitas, Giorgio Forzenigo, Alberto Gramaglia, and E Dieter Hager. Effects of local and whole body hyperthermia on immunity. *Hyperthermia in Cancer Treatment: A Primer*, pages 247–275, 2006.

[15] Zhaleh Behrouzkia, Zahra Joveini, Behnaz Keshavarzi, Nazila Eyvazzadeh, and Reza Zohdi Aghdam. Hyperthermia: how can it be used? *Oman Medical Journal*, 31 (2):89, 2016.

[16] Antonella Belfatto, Barbara Alicja Jereczek-Fossa, Guido Baroni, and Pietro Cerveri. Model-supported radiotherapy personalization: in silico test of hyper-and hypofractionation effects. *Frontiers in Physiology*, 9:1445, 2018. doi: 10.3389/fphys.2018.01445.

[17] Samuel Bernard and Hanspeter Herzel. Why do cells cycle with a 24 hour period? *Genome Informatics*, 17(1):72–79, 2006.

[18] Alexander B Bloom and Muhammad H Zaman. Influence of the microenvironment on cell fate determination and migration. *Physiological Genomics*, 46(9):309–314, 2014.

[19] Jesús J Bosque, Gabriel F Calvo, Víctor M Pérez-García, and María Cruz Navarro. The interplay of blood flow and temperature in regional hyperthermia: a mathematical approach. *Royal Society Open Science*, 8(1):201234, 2021.

[20] Jesús J Bosque, Gabriel F Calvo, and María Cruz Navarro. Modelling the effect of vascular status on tumour evolution and outcome after thermal therapy. *Applied Mathematical Modelling*, 110:207–240, 2022.

[21] James Henry Breasted. *The Edwin Smith Surgical Papyrus: published in facsimile and hieroglyphic transliteration with translation and commentary in two volumes*, volume 3. University of Chicago Press Chicago, 1930.

[22] Anne Bredel-Geissler, Ulrich Karbach, Stefan Walenta, Lutz Vollrath, and Wolfgang Mueller-Klieser. Proliferation-associated oxygen consumption and morphology of tumor cells in monolayer and spheroid culture. *Journal of Cellular Physiology*, 153(1): 44–52, 1992.

[23] David J Brenner, John B Little, and Rainer K Sachs. The bystander effect in radiation oncogenesis: II. a quantitative model. *Radiation Research*, 155(3):402–408, 2001.

[24] Chris JW Breward, Helen M Byrne, and Claire E Lewis. The role of cell-cell interactions in a two-phase model for avascular tumour growth. *Journal of Mathematical Biology*, 45(2):125–152, 2002.

[25] David M Brizel, Sean P Scully, John M Harrelson, Lester J Layfield, Richard K Dodge, Hal C Charles, Thaddeus V Samulski, Leonard R Prosnitz, and Mark W Dewhirst. Radiation therapy and hyperthermia improve the oxygenation of human soft tissue sarcomas. *Cancer Research*, 56(23):5347–5350, 1996.

[26] David M Brizel, Gregory S Sibley, Leonard R Prosnitz, Richard L Scher, and Mark W Dewhirst. Tumor hypoxia adversely affects the prognosis of carcinoma of the head and neck. *International Journal of Radiation Oncology* Biology* Physics*, 38(2):285–289, 1997.

[27] Alexander P Browning, Parvathi Haridas, and Matthew J Simpson. A bayesian sequential learning framework to parameterise continuum models of melanoma invasion into human skin. *Bulletin of Mathematical Biology*, 81(3):676–698, 2019.

[28] Sarah Brüningk, Gibin G Powathil, Peter Ziegenhein, Jannat Ijaz, Ian Rivens, Simeon Nill, Mark Chaplain, Uwe Oelfke, and Gail ter Haar. Combining radiation with hyperthermia: a multiscale model informed by in vitro experiments. *Journal of The Royal Society Interface*, 15(138):20170681, 2018.

[29] Sarah C Brüningk, Jannat Ijaz, Ian Rivens, Simeon Nill, Gail ter Haar, and Uwe Oelfke. A comprehensive model for heat-induced radio-sensitisation. *International Journal of Hyperthermia*, 34(4):392–402, 2018.

[30] Helen M Byrne. Mathematical biomedicine and modeling avascular tumor growth. 2012.

[31] Helen M Byrne, John R King, DL Sean McElwain, and Luigi Preziosi. A two-phase model of solid tumour growth. *Applied Mathematics Letters*, 16(4):567–573, 2003.

[32] Juan Campos, Pilar Guerrero, Óscar Sánchez, and Juan Soler. On the analysis of traveling waves to a nonlinear flux limited reaction-diffusion equation. In *Annales de l'IHP Analyse non linéaire*, volume 30, pages 141–155, 2013.

[33] Peter Carmeliet and Rakesh K Jain. Angiogenesis in cancer and other diseases. *Nature*, 407(6801):249–257, 2000. doi: 10.1038/35025220.

[34] Carlo Cattaneo. Sur une forme de l'equation de la chaleur eliminant la paradoxe d'une propagation instantantee. *Comptes Rendus de l'Académie des Sciences de Paris*, 247: 431–433, 1958.

[35] Giulia L Celora, Helen M Byrne, and Panayotis G Kevrekidis. Spatio-temporal modelling of phenotypic heterogeneity in tumour tissues and its impact on radiotherapy treatment. *Journal of Theoretical Biology*, 556:111248, 2023. doi: 10.1016/j.jtbi.2022.111248.

[36] KH Chadwick and HP Leenhouts. Molecular theory of cell survival. Technical report, Instituut voor Toepassing van Atoomenergie in de Landbouw, Wageningen . . . , 1973.

[37] Ibrahim M Chamseddine and Katarzyna A Rejniak. Hybrid modeling frameworks of tumor development and treatment. *Wiley Interdisciplinary Reviews: Systems Biology and Medicine*, 12(1):e1461, 2020.

[38] Mark AJ Chaplain. Avascular growth, angiogenesis and vascular growth in solid tumours: The mathematical modelling of the stages of tumour development. *Mathematical and Computer Modelling*, 23(6):47–87, 1996. doi: 10.1016/0895-7177(96)00019-2.

[39] Mark AJ Chaplain and Georgios Lolas. Mathematical modelling of cancer cell invasion of tissue: The role of the urokinase plasminogen activation system. *Mathematical Models and Methods in Applied Sciences*, 15(11):1685–1734, 2005.

[40] Mark AJ Chaplain, Miroław Lachowicz, Zuzanna Szymańska, and Dariusz Wrzosek. Mathematical modelling of cancer invasion: the importance of cell–cell adhesion and cell–matrix adhesion. *Mathematical Models and Methods in Applied Sciences*, 21(04): 719–743, 2011.

[41] Giulia Chiari, Giada Fiandaca, and Marcello Edoardo Delitala. Hypoxia-related radiotherapy resistance in tumours: treatment efficacy investigation in an eco-evolutionary perspective. *arXiv preprint arXiv:2306.10040*, 2023.

[42] Katrina F Chu and Damian E Dupuy. Thermal ablation of tumours: biological mechanisms and advances in therapy. *Nature Reviews Cancer*, 14(3):199–208, 2014.

[43] Nikola Cihoric, Alexandros Tsikkinis, Gerard van Rhoon, Hans Crezee, Daniel M Aebersold, Stephan Bodis, Marcus Beck, Jacek Nadobny, Volker Budach, Peter Wust, and Pirus Ghadjar. Hyperthermia-related clinical trials on cancer treatment within the ClinicalTrials. gov registry. *International Journal of Hyperthermia*, 31(6):609–614, 2015.

[44] Chloé Colson, Faustino Sánchez-Garduño, Helen M Byrne, Philip K Maini, and Tommaso Lorenzi. Travelling-wave analysis of a model of tumour invasion with degenerate, cross-dependent diffusion. *Proceedings of the Royal Society A*, 477(2256):20210593, 2021.

[45] Chloé Colson, Helen M Byrne, and Philip K Maini. Combining mechanisms of growth arrest in solid tumours: A mathematical investigation. *Bulletin of Mathematical Biology*, 84(8):1–24, 2022. doi: 10.1007/s11538-022-01034-2.

[46] Chloé Colson, Philip K Maini, and Helen M Byrne. Investigating the influence of growth arrest mechanisms on tumour responses to radiotherapy. *Bulletin of Mathematical Biology*, 85(8):1–33, 2023. doi: 10.1007/s11538-023-01171-2.

[47] Elisabete C Costa, André F Moreira, Duarte de Melo-Diogo, Vítor M Gaspar, Marco P Carvalho, and Ilídio J Correia. 3D tumor spheroids: an overview on the tools and techniques used for their analysis. *Biotechnology Advances*, 34(8):1427–1441, 2016.

[48] Vittorio Cristini, Xiangrong Li, John S Lowengrub, and Steven M Wise. Nonlinear simulations of solid tumor growth using a mixture model: invasion and branching. *Journal of Mathematical Biology*, 58:723–763, 2009.

[49] Rebecca M Crossley, Philip K Maini, Tommaso Lorenzi, and Ruth E Baker. Traveling waves in a coarse-grained model of volume-filling cell invasion: Simulations and comparisons. *Studies in Applied Mathematics*, 151(4):1471–1497, 2023.

[50] Stanley B Curtis. Lethal and potentially lethal lesions induced by radiation—a unified repair model. *Radiation Research*, 106(2):252–270, 1986. doi: 10.2307/3576798.

[51] Paige N Davis, Peter van Heijster, Robert Marangell, and Marianito R Rodrigo. Traveling wave solutions in a model for tumor invasion with the acid-mediation hypothesis. *Journal of Dynamics and Differential Equations*, pages 1–23, 2021.

[52] Adriana M De Mendoza, Soňa Michlíková, Johann Berger, Jens Karschau, Leoni A Kunz-Schughart, and Damian D McLeod. Mathematical model for the thermal enhancement of radiation response: Thermodynamic approach. *Scientific Reports*, 11 (1):5503, 2021.

[53] Arturo De Pablo and Ariel Sanchez. Travelling wave behaviour for a porous-Fisher equation. *European Journal of Applied Mathematics*, 9(3):285–304, 1998.

[54] Arturo de Pablo and Juan Luis Vázquez. Travelling waves and finite propagation in a reaction-diffusion equation. *Journal of Differential Equations*, 93(1):19–61, 1991.

[55] Morgan Delarue, Fabien Montel, Danijela Vignjevic, Jacques Prost, Jean-François Joanny, and Giovanni Cappello. Compressive stress inhibits proliferation in tumor spheroids through a volume limitation. *Biophysical Journal*, 107(8):1821–1828, 2014.

[56] Annaïck Desmaison, Céline Frongia, Katia Grenier, Bernard Ducommun, and Valérie Lobjois. Mechanical stress impairs mitosis progression in multi-cellular tumor spheroids. *PloS One*, 8(12):e80447, 2013.

[57] Mark W Dewhirst, Ellen Jones, Thaddeus V Samulski, Zeljko Vujaskovic, Chuan Li, and Leonard Prosnitz. Clinical hyperthermia. In *Holland-Frei Cancer Medicine. 6th edition*. BC Decker, 2003.

[58] Pia Domschke, Dumitru Trucu, Alf Gerisch, and Mark AJ Chaplain. Mathematical modelling of cancer invasion: implications of cell adhesion variability for tumour infiltrative growth patterns. *Journal of Theoretical Biology*, 361:41–60, 2014.

[59] John R Dormand and Peter J Prince. A family of embedded Runge-Kutta formulae. *Journal of Computational and Applied Mathematics*, 6(1):19–26, 1980. doi: 10.1016/0771-050X(80)90013-3.

[60] Pavel Drábek and Peter Takac. Travelling waves in the Fisher-KPP equation with nonlinear diffusion and a non-lipschitzian reaction term. *arXiv preprint arXiv:1803.10306*, 2018.

[61] Dirk Drasdo and Stefan Höhme. A single-cell-based model of tumor growth in vitro: monolayers and spheroids. *Physical Biology*, 2(3):133, 2005. doi: 10.1088/1478-3975/2/3/001.

[62] Grzegorz Dudziuk, Weronika Wronowska, Anna Gambin, Zuzanna Szymańska, and Mikołaj Rybiński. Biologically sound formal model of hsp70 heat induction. *Journal of Theoretical Biology*, 478:74–101, 2019.

[63] Maud El-Hachem, Scott W McCue, and Matthew J Simpson. Travelling wave analysis of cellular invasion into surrounding tissues. *Physica D: Nonlinear Phenomena*, 428: 133026, 2021.

[64] Pernille B Elming, Brita S Sørensen, Arlene L Oei, Nicolaas AP Franken, Johannes Crezee, Jens Overgaard, and Michael R Horsman. Hyperthermia: The optimal treatment to overcome radiation resistant hypoxia. *Cancers*, 11(1):60, 2019.

[65] Bahman Emami, Gilbert H Nussbaum, Randall K TenHaken, and Walter L Hughes. Physiological effects of hyperthermia: response of capillary blood flow and structure to local tumor heating. *Radiology*, 137(3):805–809, 1980.

[66] Heiko Enderling, Alexander RA Anderson, Mark AJ Chaplain, Alastair J Munro, and Jayant S Vaidya. Mathematical modelling of radiotherapy strategies for early breast cancer. *Journal of Theoretical Biology*, 241(1):158–171, 2006. doi: 10.1016/j.jtbi.2005.11.015.

[67] Heiko Enderling, Derek Park, Lynn Hlatky, and Philip Hahnfeldt. The importance of spatial distribution of stemness and proliferation state in determining tumor radioresponse. *Mathematical Modelling of Natural Phenomena*, 4(3):117–133, 2009. doi: 10.1051/mmnp/20094305.

[68] Heiko Enderling, Mark AJ Chaplain, and Philip Hahnfeldt. Quantitative modeling of tumor dynamics and radiotherapy. *Acta Biotheoretica*, 58(4):341–353, 2010. doi: 10.1007/s10441-010-9111-z.

[69] Hans Engler. Relations between travelling wave solutions of quasilinear parabolic equations. *Proceedings of the American Mathematical Society*, 93(2):297–302, 1985.

[70] Christian Engwer, Christian Stinner, and Christina Surulescu. On a structured multiscale model for acid-mediated tumor invasion: the effects of adhesion and proliferation. *Mathematical Models and Methods in Applied Sciences*, 27(07):1355–1390, 2017.

[71] David Eriksson and Torgny Stigbrand. Radiation-induced cell death mechanisms. *Tumor Biology*, 31:363–372, 2010.

[72] Magdy A Ezzat, Noorah S AlSowayan, Zeid IA Al-Muhiameed, and Shereen M Ezzat. Fractional modelling of Pennes' bioheat transfer equation. *Heat and Mass Transfer*, 50(7):907–914, 2014.

[73] Rae Helen Farnsworth, Martin Lackmann, Marc G Achen, and Steven A Stacker. Vascular remodeling in cancer. *Oncogene*, 33(27):3496–3505, 2014.

[74] Antonio Fasano, Miguel A Herrero, and Marianito R Rodrigo. Slow and fast invasion waves in a model of acid-mediated tumour growth. *Mathematical Biosciences*, 220(1): 45–56, 2009.

[75] Ana Faustino-Rocha, Paula A Oliveira, Jacinta Pinho-Oliveira, Catarina Teixeira-Guedes, Ruben Soares-Maia, Rui Gil Da Costa, Bruno Colaco, Maria Joao Pires, Jorge Colaco, Rita Ferreira, and Mário Ginja. Estimation of rat mammary tumor volume using caliper and ultrasonography measurements. *Lab Animal*, 42(6):217–224, 2013. doi: 10.1038/laban.254.

[76] Paul C Fife. *Mathematical Aspects of Reacting and Diffusing Systems*, volume 28. Springer Science & Business Media, 2013.

[77] Ronald Aylmer Fisher. The wave of advance of advantageous genes. *Annals of Eugenics*, 7(4):355–369, 1937.

[78] Martine Franckena, Daryoush Fatehi, Maarten de Bruijne, Richard AM Canters, Yvette van Norden, Jan Willem Mens, Gerard C van Rhoon, and Jacoba van der Zee. Hyperthermia dose-effect relationship in 420 patients with cervical cancer treated with combined radiotherapy and hyperthermia. *European Journal of Cancer*, 45(11): 1969–1978, 2009.

[79] Linnea C Franssen, Tommaso Lorenzi, Andrew EF Burgess, and Mark AJ Chaplain. A mathematical framework for modelling the metastatic spread of cancer. *Bulletin of Mathematical Biology*, 81:1965–2010, 2019.

[80] Hermann B Frieboes, Fang Jin, Yao-Li Chuang, Steven M Wise, John S Lowengrub, and Vittorio Cristini. Three-dimensional multispecies nonlinear tumor growth—II: tumor invasion and angiogenesis. *Journal of Theoretical Biology*, 264(4):1254–1278, 2010.

[81] SC Gad and T Pham. Encyclopedia of toxicology. *Reference Module in Biomedical Sciences*, pages 1106–1108, 2014.

[82] Thierry Gallay and Corrado Mascia. Propagation fronts in a simplified model of tumor growth with degenerate cross-dependent self-diffusivity. *Nonlinear Analysis: Real World Applications*, 63:103387, 2022.

[83] Robert A Gatenby and Edward T Gawlinski. A reaction-diffusion model of cancer invasion. *Cancer Research*, 56(24):5745–5753, 1996.

[84] Alf Gerisch and Mark AJ Chaplain. Mathematical modelling of cancer cell invasion of tissue: local and non-local models and the effect of adhesion. *Journal of Theoretical Biology*, 250(4):684–704, 2008.

[85] Eugene W Gerner and Michael J Schneider. Induced thermal resistance in HeLa cells. *Nature*, 256(5517):500–502, 1975.

[86] Robert J Gillies, Paul A Schomack, Timothy W Secomb, and Natarajan Raghunand. Causes and effects of heterogeneous perfusion in tumors. *Neoplasia*, 1(3):197–207, 1999. doi: 10.1038/sj.neo.7900037.

[87] Robert J Gillies, Ian Robey, and Robert A Gatenby. Causes and consequences of increased glucose metabolism of cancers. *Journal of Nuclear Medicine*, 49(Suppl 2): 24S–42S, 2008.

[88] Dudley T Goodhead. Saturable repair models of radiation action in mammalian cells. *Radiation Research*, 104(2s):S58–S67, 1985. doi: 10.2307/3583513.

[89] Kaitlin Graham and Evan Unger. Overcoming tumor hypoxia as a barrier to radiotherapy, chemotherapy and immunotherapy in cancer treatment. *International Journal of Nanomedicine*, pages 6049–6058, 2018.

[90] Mark Gray, Arran K Turnbull, Carol Ward, James Meehan, Carlos Martínez-Pérez, Maria Bonello, Lisa Y Pang, Simon P Langdon, Ian H Kunkler, Alan Murray, and David Argyle. Development and characterisation of acquired radioresistant breast cancer cell lines. *Radiation Oncology*, 14(1):1–19, 2019.

[91] Harvey P Greenspan. Models for the growth of a solid tumor by diffusion. *Studies in Applied Mathematics*, 51(4):317–340, 1972. doi: 10.1002/sapm1972514317.

[92] Sebastian P Haen, Philippe L Pereira, Helmut R Salih, Hans-Georg Rammensee, and Cécile Gouttefangeas. More than just tumor destruction: immunomodulation by thermal ablation of cancer. *Clinical and Developmental Immunology*, 2011, 2011.

[93] Erich Dieter Hager. Intracavitary hyperthennic perfusion. In *Hyperthermia in Cancer Treatment: A Primer*, pages 218–226. Springer, 2006.

[94] Reihaneh Haghniaz, Rinku D Umrani, and Kishore M Paknikar. Temperature-dependent and time-dependent effects of hyperthermia mediated by dextran-coated La0. 7Sr0. 3MnO3: in vitro studies. *International Journal of Nanomedicine*, pages 1609–1623, 2015.

[95] Philip Hahnfeldt, Dipak Panigrahy, Judah Folkman, and Lynn Hlatky. Tumor development under angiogenic signaling: a dynamical theory of tumor growth, treatment response, and postvascular dormancy. *Cancer Research*, 59(19):4770–4775, 1999.

[96] Sara Hamis, Mohammad Kohandel, Ludwig J Dubois, Ala Yaromina, Philippe Lambin, and Gibin G Powathil. Combining hypoxia-activated prodrugs and radiotherapy in silico: Impact of treatment scheduling and the intra-tumoural oxygen landscape. *PLOS Computational Biology*, 16(8):e1008041, 2020.

[97] Douglas Hanahan and Robert A Weinberg. The hallmarks of cancer. *Cell*, 100(1): 57–70, 2000.

[98] Douglas Hanahan and Robert A Weinberg. Hallmarks of cancer: the next generation. *Cell*, 144(5):646–674, 2011.

[99] Leonid Hanin and Marco Zaider. A mechanistic description of radiation-induced damage to normal tissue and its healing kinetics. *Physics in Medicine & Biology*, 58 (4):825, 2013.

[100] Leonid Hanin and Marco Zaider. Optimal schedules of fractionated radiation therapy by way of the greedy principle: biologically-based adaptive boosting. *Physics in Medicine & Biology*, 59(15):4085, 2014.

[101] Gary Hannon, Felista L Tansi, Ingrid Hilger, and Adriele Prina-Mello. The effects of localized heat on the hallmarks of cancer. *Advanced Therapeutics*, page 2000267, 2021.

[102] Yoko Harima, Kenji Nagata, Keizo Harima, Valentina V Ostapenko, Yoshimasa Tanaka, and Satoshi Sawada. A randomized clinical trial of radiation therapy versus thermoradiotherapy in stage IIIB cervical carcinoma. *International Journal of Hyperthermia*, 25(5):338–343, 2009.

[103] Gabriel Helmlinger, Paolo A Netti, Hera C Lichtenbeld, Robert J Melder, and Rakesh K Jain. Solid stress inhibits the growth of multicellular tumor spheroids. *Nature Biotechnology*, 15(8):778–783, 1997.

[104] Patries M Herst and Michael V Berridge. Cell surface oxygen consumption: a major contributor to cellular oxygen consumption in glycolytic cancer cell lines. *Biochimica et Biophysica Acta (BBA)-Bioenergetics*, 1767(2):170–177, 2007.

[105] Thomas Hillen, Kevin Painter, Christian Schmeiser, et al. Global existence for chemotaxis with finite sampling radius. *Discrete and Continuous Dynamical Systems Series B*, 7(1):125, 2007.

[106] Franziska Hirschhaeuser, Heike Menne, Claudia Dittfeld, Jonathan West, Wolfgang Mueller-Klieser, and Leoni A Kunz-Schughart. Multicellular tumor spheroids: an underestimated tool is catching up again. *Journal of Biotechnology*, 148(1):3–15, 2010.

[107] Andrew B Holder, Marianito R Rodrigo, and Miguel A Herrero. A model for acid-mediated tumour growth with nonlinear acid production term. *Applied Mathematics and Computation*, 227:176–198, 2014.

[108] Michael R Horsman and Jens Overgaard. Hot topic: Can mild hyperthermia improve tumour oxygenation? *International Journal of Hyperthermia*, 13(2):141–147, 1997.

[109] Michael R Horsman and Jens Overgaard. Hyperthermia: a potent enhancer of radiotherapy. *Clinical Oncology*, 19(6):418–426, 2007.

[110] Bao-Tian Huang, Jia-Yang Lu, Pei-Xian Lin, Jian-Zhou Chen, De-Rui Li, and Chuang-Zhen Chen. Radiobiological modeling analysis of the optimal fraction scheme in patients with peripheral non-small cell lung cancer undergoing stereotactic body radiotherapy. *Scientific Reports*, 5(1):1–9, 2015.

[111] Huang-Wen Huang and Tzyy-Leng Horng. Bioheat transfer and thermal heating for tumor treatment. In *Heat Transfer and Fluid Flow in Biological Processes*, pages 1–42. Elsevier, 2015.

[112] Matthew E Hubbard and Helen M Byrne. Multiphase modelling of vascular tumour growth in two spatial dimensions. *Journal of Theoretical Biology*, 316:70–89, 2013.

[113] Kazuro Iwata, Abdus Shakil, Won-Joo Hur, Carol M Makepeace, Robert J Griffin, and Chang W Song. Tumour pO2 can be increased markedly by mild hyperthermia. *The British Journal of Cancer. Supplement*, 27:S217, 1996.

[114] Sahar Jafari Nivlouei, Madjid Soltani, João Carvalho, Rui Travasso, Mohammad Reza Salimpour, and Ebrahim Shirani. Multiscale modeling of tumor growth and angiogenesis: Evaluation of tumor-targeted therapy. *PLoS Computational Biology*, 17(6): e1009081, 2021.

[115] Junhwan Jeon, Vito Quaranta, and Peter T Cummings. An off-lattice hybrid discrete-continuum model of tumor growth and invasion. *Biophysical Journal*, 98(1):37–47, 2010.

[116] Jeho Jeong, Jung Hun Oh, Jan-Jakob Sonke, Jose Belderbos, Jeffrey D Bradley, Andrew N Fontanella, Shyam S Rao, and Joseph O Deasy. Modeling the cellular response

of lung cancer to radiation therapy for a broad range of fractionation schedules. *Clinical Cancer Research*, 23(18):5469–5479, 2017. doi: 10.1158/1078-0432.CCR-16-3277.

[117] Sheetal Jha, Pramod Kumar Sharma, and Rishabha Malviya. Hyperthermia: role and risk factor for cancer treatment. *Achievements in the Life Sciences*, 10(2):161–167, 2016.

[118] Bénédicte F Jordan and Pierre Sonveaux. Targeting tumor perfusion and oxygenation to improve the outcome of anticancer therapy. *Frontiers in Pharmacology*, 3:94, 2012.

[119] Horst Jung. A generalized concept for cell killing by heat. *Radiation Research*, 106 (1):56–72, 1986.

[120] Friedrich Kallinowski, G Tyler, Wolfgang Mueller-Klieser, and Peter W Vaupel. Growth-related changes of oxygen consumption rates of tumor cells grown in vitro and in vivo. *Journal of Cellular Physiology*, 138(1):183–191, 1989.

[121] Toshiharu Kamura, Ole S Nielsen, Jens Overgaard, and Anders H Andersen. Development of thermotolerance during fractionated hyperthermia in a solid tumor in vivo. *Cancer Research*, 42(5):1744–1748, 1982.

[122] Marta Kapałczyńska, Tomasz Kolenda, Weronika Przybyła, Maria Zajaczkowska, Anna Teresiak, Violetta Filas, Matthew Ibbs, Renata Bliźniak, Łukasz Łuczewski, and Katarzyna Lamperska. 2D and 3D cell cultures–a comparison of different types of cancer cell cultures. *Archives of Medical Science*, 14(4):910–919, 2018.

[123] Kohkichi Kawasaki, Atushi Mochizuki, Mitsugu Matsushita, Takayoshi Umeda, and Nanako Shigesada. Modeling spatio-temporal patterns generated bybacillus subtilis. *Journal of Theoretical Biology*, 188(2):177–185, 1997.

[124] Debra K Kelleher and Peter W Vaupel. No sustained improvement in tumor oxygenation after localized mild hyperthermia. In *Oxygen Transport to Tissue XXXI*, pages 393–398. Springer, 2010.

[125] Debra K Kelleher, Tina Engel, and Peter W Vaupel. Changes in microregional perfusion, oxygenation, ATP and lactate distribution in subcutaneous rat tumours upon water-filtered IR-A hyperthermia. *International Journal of Hyperthermia*, 11(2):241–255, 1995.

[126] Igor K Khvostunov and Hooshang Nikjoo. Computer modelling of radiation-induced bystander effect. *Journal of Radiological Protection*, 22(3A):A33, 2002.

[127] Andrey Kolmogorov, Ivan Petrovsky, and Nikolai Piskunov. Etude de l'équation de diffusion avec croissance de la quantité de matière et son application à un problème biologique. *Bulletin de l'Université d'état à Moscou. Série International. Section A, Mathématiques et Mécanique.*, 1:1–25, 1937.

[128] Maria Konopacka, Jacek Rogoliński, Aleksander Sochanik, and Krzysztof Ślosarek. Can high dose rates used in cancer radiotherapy change therapeutic effectiveness? *Contemporary Oncology/Współczesna Onkologia*, 20(6):449–452, 2016. doi: 10.5114/wo.2016.65603.

[129] James A Koziol, Theresa J Falls, and Jan E Schnitzer. Different ODE models of tumor growth can deliver similar results. *BMC Cancer*, 20(1):1–10, 2020. doi: 10.1186/s12885-020-6703-0.

[130] Dinesh Kumar and Kavindra N Rai. A study on thermal damage during hyperthermia treatment based on DPL model for multilayer tissues using finite element legendre wavelet galerkin approach. *Journal of Thermal Biology*, 62:170–180, 2016.

[131] Leoni A Kunz-Schughart, Marina Kreutz, and Ruth Knuechel. Multicellular spheroids: a three-dimensional in vitro culture system to study tumour biology. *International Journal of Experimental Pathology*, 79(1):1–23, 1998.

[132] Maxim Kuznetsov and Andrey Kolobov. Optimization of antitumor radiotherapy fractionation via mathematical modeling with account of 4 R's of radiobiology. *Journal of Theoretical Biology*, 558:111371, 2023.

[133] Urszula Ledzewicz and Heinz Schättler. Multi-input optimal control problems for combined tumor anti-angiogenic and radiotherapy treatments. *Journal of Optimization Theory and Applications*, 153:195–224, 2012.

[134] Sun-Young Lee, Gyula Peter Szigeti, and Attila Marcell Szasz. Oncological hyperthermia: The correct dosing in clinical applications. *International Journal of Oncology*, 54(2):627–643, 2019.

[135] Lorenzo Leoncini, Maria Teresa Del Vecchio, Tiziana Megha, Paolo Barbini, Piero Galieni, Stefano Pileri, Elena Sabattini, Filippo Gherlinzoni, Piero Tosi, Rainer Kraft, et al. Correlations between apoptotic and proliferative indices in malignant non-hodgkin's lymphomas. *The American Journal of Pathology*, 142(3):755, 1993.

[136] James R Lepock, Kwan-Hon Cheng, Hisham Al-qysi, Ida Sim, Cameron J Koch, and Jack Kruuv. Hyperthermia-induced inhibition of respiration and mitochondrial

protein denaturation in chl cells. *International Journal of Hyperthermia*, 3(2):123–132, 1987.

[137] Romain Levayer, Carole Dupont, and Eduardo Moreno. Tissue crowding induces caspase-dependent competition for space. *Current Biology*, 26(5):670–677, 2016.

[138] Thomas D Lewin, Philip K Maini, Eduardo G Moros, Heiko Enderling, and Helen M Byrne. The evolution of tumour composition during fractionated radiotherapy: implications for outcome. *Bulletin of Mathematical Biology*, 80(5):1207–1235, 2018. doi: 10.1007/s11538-018-0391-9.

[139] Thomas D Lewin, Helen M Byrne, Philip K Maini, Jimmy J Caudell, Eduardo G Moros, and Heiko Enderling. The importance of dead material within a tumour on the dynamics in response to radiotherapy. *Physics in Medicine & Biology*, 65(1): 015007, 2020.

[140] Thomas D Lewin, Philip K Maini, Eduardo G Moros, Heiko Enderling, and Helen M Byrne. A three phase model to investigate the effects of dead material on the growth of avascular tumours. *Mathematical Modelling of Natural Phenomena*, 15:22, 2020. doi: 10.1051/mmnp/2019039.

[141] GC Li, Nahid F Mivechi, and G Weitzel. Heat shock proteins, thermotolerance, and their relevance to clinical hyperthermia. *International Journal of Hyperthermia*, 11 (4):459–488, 1995.

[142] William W Li, Vincent W Li, Michelle Hutnik, Albert S Chiou, et al. Tumor angiogenesis as a target for dietary cancer prevention. *Journal of Oncology*, 2012, 2012.

[143] Mark P Little, Johnny AN Filipe, Kevin M Prise, Melvyn Folkard, and Oleg V Belyakov. A model for radiation-induced bystander effects, with allowance for spatial position and the effects of cell turnover. *Journal of Theoretical Biology*, 232(3): 329–338, 2005.

[144] Junyan Liu, David A Hormuth, Tessa Davis, Jianchen Yang, Matthew T McKenna, Angela M Jarrett, Heiko Enderling, Amy Brock, and Thomas E Yankeelov. A time-resolved experimental–mathematical model for predicting the response of glioma cells to single-dose radiation therapy. *Integrative Biology*, 2021. doi: 10.1093/intbio/zyab010.

[145] Ruirui Liu, Kathryn A Higley, Maciej H Swat, Mark AJ Chaplain, Gibin G Powathil, and James A Glazier. Development of a coupled simulation toolkit for computational

radiation biology based on Geant4 and CompuCell3D. *Physics in Medicine & Biology*, 66(4):045026, 2021.

[146] Shuqing Liu, Susan M Edgerton, Dan H Moore, and Ann D Thor. Measures of cell turnover (proliferation and apoptosis) and their association with survival in breast cancer. *Clinical Cancer Research*, 7(6):1716–1723, 2001.

[147] Kumar Mahesh, Kavindra N Rai, and Rajeev. A study of fractional order dual-phase-lag bioheat transfer model. *Journal of Thermal Biology*, 93:102661, 2020.

[148] Patrick Maier, Linda Hartmann, Frederik Wenz, and Carsten Herskind. Cellular pathways in response to ionizing radiation and their targetability for tumor radiosensitization. *International Journal of Molecular Sciences*, 17(1):102, 2016.

[149] Luisa Malaguti and Cristina Marcelli. Sharp profiles in degenerate and doubly degenerate Fisher-KPP equations. *Journal of Differential Equations*, 195(2):471–496, 2003.

[150] Mahmoud BA Mansour. Traveling wave solutions of a nonlinear reaction–diffusion–chemotaxis model for bacterial pattern formation. *Applied Mathematical Modelling*, 32(2):240–247, 2008.

[151] Ben P Marchant, John Norbury, and Jonathan A Sherratt. Travelling wave solutions to a haptotaxis-dominated model of malignant invasion. *Nonlinearity*, 14(6):1653, 2001.

[152] Filipa G Marques, Esmeralda Poli, José Rino, Marta Teixeira Pinto, Isabel Diegues, Filomena Pina, and Susana Constantino Rosa Santos. Low doses of ionizing radiation enhance the angiogenic potential of adipocyte conditioned medium. *Radiation Research*, 192(5):517–526, 2019.

[153] Filipa G Marques, Lara Carvalho, Joana S Sousa, José Rino, Isabel Diegues, Esmeralda Poli, Filomena Pina, Leonor Saúde, and Susana Constantino Rosa Santos. Low doses of ionizing radiation enhance angiogenesis and consequently accelerate post-embryonic development but not regeneration in zebrafish. *Scientific Reports*, 10(1): 3137, 2020.

[154] Natasha K Martin, Eamonn A Gaffney, Robert A Gatenby, and Philip K Maini. Tumour–stromal interactions in acid-mediated invasion: a mathematical model. *Journal of Theoretical Biology*, 267(3):461–470, 2010.

[155] Andriy Marusyk, Vanessa Almendro, and Kornelia Polyak. Intra-tumour heterogeneity: a looking glass for cancer? *Nature Reviews Cancer*, 12(5):323–334, 2012.

[156] Andriy Marusyk, Michalina Janiszewska, and Kornelia Polyak. Intratumor heterogeneity: the rosetta stone of therapy resistance. *Cancer Cell*, 37(4):471–484, 2020.

[157] Corrado Mascia, Pierfrancesco Moschetta, and Chiara Simeoni. Numerical investigation of some reductions for the gatenby-gawlinski model. *arXiv preprint arXiv:2103.02657*, 2021.

[158] Jessica B McGillen, Eamonn A Gaffney, Natasha K Martin, and Philip K Maini. A general reaction–diffusion model of acidity in cancer invasion. *Journal of Mathematical Biology*, 68(5):1199–1224, 2014.

[159] Stephanie R McKeown. Defining normoxia, physoxia and hypoxia in tumours—implications for treatment response. *The British Journal of Radiology*, 87 (1035):20130676, 2014. doi: 10.1259/bjr.20130676.

[160] Stephen J McMahon. The linear quadratic model: usage, interpretation and challenges. *Physics in Medicine & Biology*, 64(1):01TR01, 2018. doi: 10.1088/1361-6560/aaf26a.

[161] Stephen J McMahon and Kevin M Prise. Mechanistic modelling of radiation responses. *Cancers*, 11(2):205, 2019.

[162] Stephen J McMahon, Karl T Butterworth, Colman Trainor, Conor K McGarry, Joe M O'Sullivan, Giuseppe Schettino, Alan R Hounsell, and Kevin M Prise. A kinetic-based model of radiation-induced intercellular signalling. *PloS One*, 8(1):e54526, 2013.

[163] Cameron Meaney, Gibin G Powathil, Ala Yaromina, Ludwig J Dubois, Philippe Lambin, and Mohammad Kohandel. Role of hypoxia-activated prodrugs in combination with radiation therapy: An in silico approach. *Mathematical Biosciences and Engineering*, 16(6):6257–6273, 2019.

[164] John Metzcar, Yafei Wang, Randy Heiland, and Paul Macklin. A review of cell-based computational modeling in cancer biology. *JCO Clinical Cancer Informatics*, 2:1–13, 2019.

[165] John L Meyer. The clinical efficacy of localized hyperthermia. *Cancer Research*, 44 (10_Supplement):4745s–4751s, 1984.

[166] Fabien Montel, Morgan Delarue, Jens Elgeti, Danijela Vignjevic, Giovanni Cappello, and Jacques Prost. Isotropic stress reduces cell proliferation in tumor spheroids. *New Journal of Physics*, 14(5):055008, 2012.

[167] Fabien Montel, Morgan Delarue, Jens Elgeti, Danijela Vignjevic, Giovanni Cappello, Jacques Prost, and Jean-Francois Joanny. Stress clamp experiments on multicellular tumor spheroids. *Biophysical Journal*, 102(3):220a, 2012.

[168] Eui Jung Moon, Pierre Sonveaux, Paolo E Porporato, Pierre Danhier, Bernard Gallez, Ines Batinic-Haberle, Yu-Chih Nien, Thies Schroeder, and Mark W Dewhirst. NADPH oxidase-mediated reactive oxygen species production activates hypoxia-inducible factor-1 (HIF-1) via the ERK pathway after hyperthermia treatment. *Proceedings of the National Academy of Sciences*, 107(47):20477–20482, 2010.

[169] Pierfrancesco Moschetta and Chiara Simeoni. Numerical investigation of the Gatenby-Gawlinski model for acid-mediated tumour invasion. *Rendiconti di Matematica e delle sue Applicazioni*, 40(3-4):257–287, 2019.

[170] Wolfgang Mueller-Klieser and Peter W Vaupel. Effect of hyperthermia on tumor blood flow. *Biorheology*, 21(4):529–538, 1984.

[171] Bert Müller, Sabrina Lang, Marco Dominietto, Markus Rudin, Georg Schulz, Hans Deyhle, Marco Germann, Franz Pfeiffer, Christian David, and Timm Weitkamp. High-resolution tomographic imaging of microvessels. In *Developments in X-Ray Tomography VI*, volume 7078, page 70780B. International Society for Optics and Photonics, 2008. doi: 10.1117/12.794157.

[172] Hope Murphy, Hana Jaafari, and Hana M Dobrovolny. Differences in predictions of ODE models of tumor growth: a cautionary example. *BMC Cancer*, 16(1):1–10, 2016. doi: 10.1186/s12885-016-2164-x.

[173] Ryan J Murphy, Alexander P Browning, Gency Gunasingh, Nikolas K Haass, and Matthew J Simpson. Designing and interpreting 4D tumour spheroid experiments. *Communications Biology*, 5(1):91, 2022.

[174] James D Murray. *Mathematical Biology*. Interdisciplinary Applied Mathematics. Springer New York, NY, 2002.

[175] Barbara Muz, Pilar de la Puente, Feda Azab, and Abdel Kareem Azab. The role of hypoxia in cancer progression, angiogenesis, metastasis, and resistance to therapy. *Hypoxia*, 3:83, 2015.

[176] Sara Neira, Araceli Gago-Arias, Jacobo Guiu-Souto, and Juan Pardo-Montero. A kinetic model of continuous radiation damage to populations of cells: comparison to the LQ model and application to molecular radiotherapy. *Physics in Medicine & Biology*, 65(24):245015, 2020. doi: 10.1088/1361-6560/aba21d.

[177] Donald F Newgreen, Graeme J Pettet, and Kerry A Landman. Chemotactic cellular migration: smooth and discontinuous travelling wave solutions. *SIAM Journal on Applied Mathematics*, 63(5):1666–1681, 2003.

[178] Hooshang Nikjoo and Igor K Khvostunov. Biophysical model of the radiation-induced bystander effect. *International Journal of Radiation Biology*, 79(1), 2003.

[179] Arlene L Oei, Lianne EM Vriend, Johannes Crezee, Nicolaas AP Franken, and Przemek M Krawczyk. Effects of hyperthermia on DNA repair pathways: one treatment to inhibit them all. *Radiation Oncology*, 10(1):165, 2015.

[180] Hitoshi Okada and Tak W Mak. Pathways of apoptotic and non-apoptotic death in tumour cells. *Nature Reviews Cancer*, 4(8):592–603, 2004.

[181] David P O'Neill, Tingying Peng, Philipp Stiegler, Ursula Mayrhauser, Sonja Koestenbauer, Karlheinz Tscheliessnigg, and Stephen J Payne. A three-state mathematical model of hyperthermic cell death. *Annals of Biomedical Engineering*, 39(1):570–579, 2011.

[182] Esteban Ortiz-Prado, Jeff F Dunn, Jorge Vasconez, Diana Castillo, and Ginés Viscor. Partial pressure of oxygen in the human body: a general review. *American Journal of Blood Research*, 9(1):1, 2019.

[183] Jens Overgaard. The design of clinical trials in hyperthermic oncology. In *Physics and Technology of Hyperthermia*, pages 598–620. Springer, 1987.

[184] Jens Overgaard, Ole Steen Nielsen, and Jacob Christian Lindegaard. Biological basis for rational design of clinical treatment with combined hyperthermia and radiation. In *Physics and Technology of Hyperthermia*, pages 54–79. Springer, 1987.

[185] Jens Overgaard, Soren M Bentzen, Dionisio G Gonzalez, Maarten CCM Hulshof, G Arcangeli, Olav Dahl, and Olav Mella. Randomised trial of hyperthermia as adjuvant to radiotherapy for recurrent or metastatic malignant melanoma. *The Lancet*, 345(8949):540–543, 1995.

[186] Jasmina Panovska, Helen M Byrne, and Philip K Maini. Mathematical modelling of vascular tumour growth and implications for therapy. In *Mathematical Modeling of Biological Systems, Volume I*, pages 205–216. Springer, 2007. doi: 10.1007/978-0-8176-4558-8_18.

[187] Jan C Peeken, Peter W Vaupel, and Stephanie E Combs. Integrating hyperthermia into modern radiation oncology: what evidence is necessary? *Frontiers in Oncology*, 7:132, 2017.

[188] Harry H Pennes. Analysis of tissue and arterial blood temperatures in the resting human forearm. *Journal of Applied Physiology*, 1(2):93–122, 1948.

[189] Abraham Peper, Cornelis A Grimbergen, Jos AE Spaan, Jan EM Souren, and Roeland Van Wijk. A mathematical model of the hsp70 regulation in the cell. *International Journal of Hyperthermia*, 14(1):97–124, 1998.

[190] Benoît Perthame. Parabolic equations in biology. In *Parabolic Equations in Biology*, pages 1–21. Springer, 2015.

[191] Abbey J Perumpanani, Jonathan A Sherratt, John Norbury, and Helen M Byrne. Biological inferences from a mathematical model for malignant invasion. *Invasion Metastasis*, 16:209–221, 1996.

[192] Abbey J Perumpanani, David L Simmons, Andrew JH Gearing, Karen M Miller, George Ward, John Norbury, Markus Schneemann, and Jonathan A Sherratt. Extracellular matrix-mediated chemotaxis can impede cell migration. *Proceedings of the Royal Society of London. Series B: Biological Sciences*, 265(1413):2347–2352, 1998.

[193] Abbey J Perumpanani, Jonathan A Sherratt, John Norbury, and Helen M Byrne. A two parameter family of travelling waves with a singular barrier arising from the modelling of extracellular matrix mediated cellular invasion. *Physica D: Nonlinear Phenomena*, 126(3-4):145–159, 1999.

[194] Abbey J Perumpanani, Ben P Marchant, and John Norbury. Traveling shock waves arising in a model of malignant invasion. *SIAM Journal on Applied Mathematics*, 60 (2):463–476, 2000.

[195] Ion Petre, Andrzej Mizera, Claire L Hyder, Annika Meinander, Andrey Mikhailov, Richard I Morimoto, Lea Sistonen, John E Eriksson, and Ralph-Johan Back. A simple mass-action model for the eukaryotic heat shock response and its mathematical validation. *Natural Computing*, 10:595–612, 2011.

[196] Vincent A Potiron, Rym Abderrahmani, Karen Clément-Colmou, Séverine Marionneau-Lambot, Thibauld Oullier, François Paris, and Stéphane Supiot. Improved functionality of the vasculature during conventionally fractionated radiation therapy of prostate cancer. *PloS One*, 8(12):e84076, 2013.

[197] Gibin G Powathil, Mohammad Kohandel, Michael Milosevic, and Siv Sivaloganathan. Modeling the spatial distribution of chronic tumor hypoxia: implications for experimental and clinical studies. *Computational and Mathematical Methods in Medicine*, 2012, 2012. doi: 10.1155/2012/410602.

[198] Gibin G Powathil, Douglas JA Adamson, and Mark AJ Chaplain. Towards predicting the response of a solid tumour to chemotherapy and radiotherapy treatments: clinical insights from a computational model. *PLoS Computational Biology*, 9(7):e1003120, 2013.

[199] Gibin G Powathil, Alastair J Munro, Mark AJ Chaplain, and Maciej Swat. Bystander effects and their implications for clinical radiation therapy: Insights from multiscale in silico experiments. *Journal of theoretical biology*, 401:1–14, 2016.

[200] Kevin M Prise and Joe M O'sullivan. Radiation-induced bystander signalling in cancer therapy. *Nature Reviews Cancer*, 9(5):351–360, 2009.

[201] Kevin M Prise, Giuseppe Schettino, Melvyn Folkard, and Kathryn D Held. New insights on cell death from radiation exposure. *The Lancet Oncology*, 6(7):520–528, 2005.

[202] Sotiris Prokopiou, Eduardo G Moros, Jan Poleszczuk, Jimmy Caudell, Javier F Torres-Roca, Kujtim Latifi, Jae K Lee, Robert Myerson, Louis B Harrison, and Heiko Enderling. A proliferation saturation index to predict radiation response and personalize radiotherapy fractionation. *Radiation Oncology*, 10(1):1–8, 2015.

[203] Ignacio Ramis-Conde, Dirk Drasdo, Alexander RA Anderson, and Mark AJ Chaplain. Modeling the influence of the E-cadherin-β-catenin pathway in cancer cell invasion: a multiscale approach. *Biophysical Journal*, 95(1):155–165, 2008.

[204] Katarzyna A Rejniak and Alexander RA Anderson. Hybrid models of tumor growth. *Wiley Interdisciplinary Reviews: Systems Biology and Medicine*, 3(1):115–125, 2011.

[205] Theodore R Rieger, Richard I Morimoto, and Vassily Hatzimanikatis. Mathematical modeling of the eukaryotic heat-shock response: dynamics of the hsp70 promoter. *Biophysical Journal*, 88(3):1646–1658, 2005.

[206] Mark Robertson-Tessi, Robert J Gillies, Robert A Gatenby, and Alexander RA Anderson. Impact of metabolic heterogeneity on tumor growth, invasion, and treatment outcomes. *Cancer Research*, 75(8):1567–1579, 2015.

[207] Russell Rockne, Ellsworth C Alvord, Jason K Rockhill, and Kristin R Swanson. A mathematical model for brain tumor response to radiation therapy. *Journal of Mathematical Biology*, 58(4):561–578, 2009. doi: 10.1007/s00285-008-0219-6.

[208] Robert B Roemer and Thomas C Cetas. Applications of bioheat transfer simulations in hyperthermia. *Cancer Research*, 44(10 Supplement):4788s–4798s, 1984.

[209] Tiina Roose, S Jonathan Chapman, and Philip K Maini. Mathematical models of avascular tumor growth. *SIAM Review*, 49(2):179–208, 2007. doi: 10.1137/S0036144504446291.

[210] Thomas P Ryan and Christopher L Brace. Interstitial microwave treatment for cancer: historical basis and current techniques in antenna design and performance. *International Journal of Hyperthermia*, 33(1):3–14, 2017.

[211] Mikołaj Rybiński, Zuzanna Szymańska, Sławomir Lasota, and Anna Gambin. Modelling the efficacy of hyperthermia treatment. *Journal of The Royal Society Interface*, 10(88):20130527, 2013.

[212] Fatemeh Saberian, Archis Ghate, and Minsun Kim. Optimal fractionation in radiotherapy with multiple normal tissues. *Mathematical Medicine and Biology: a Journal of the IMA*, 33(2):211–252, 2016.

[213] Faustino Sánchez-Garduño and Philip K Maini. Existence and uniqueness of a sharp travelling wave in degenerate non-linear diffusion Fisher-KPP equations. *Journal of Mathematical Biology*, 33(2):163–192, 1994.

[214] Faustino Sánchez-Garduño and Philip K Maini. Travelling wave phenomena in non-linear diffusion degenerate Nagumo equations. *Journal of Mathematical Biology*, 35: 713–728, 1997.

[215] Faustino Sánchez-Garduño, Philip K Maini, and Makis E Kappos. A shooting argument approach to a sharp-type solution for nonlinear degenerate Fisher-KPP equations. *IMA Journal of Applied Mathematics*, 57(3):211–221, 1996.

[216] Razvan A Satnoianu, Philip K Maini, Faustino Sánchez-Garduno, and Judith P Armitage. Travelling waves in a nonlinear degenerate diffusion model for bacterial pattern formation. *Discrete and Continuous Dynamical Systems - Series B.*, 1(3): 339–362, 2001.

[217] Gernot Schaller and Michael Meyer-Hermann. Continuum versus discrete model: a comparison for multicellular tumour spheroids. *Philosophical Transactions of the Royal Society A: Mathematical, Physical and Engineering Sciences*, 364(1843):1443–1464, 2006. doi: 10.1098/rsta.2006.1780.

[218] Jeremy D Scheff, Jonathan D Stallings, Jaques Reifman, and Vineet Rakesh. Mathematical modeling of the heat-shock response in HeLa cells. *Biophysical Journal*, 109 (2):182–193, 2015.

[219] Stephan Scheidegger, Hans U Fuchs, Kathrin Zaugg, Stephan Bodis, and Rudolf M Füchslin. Using state variables to model the response of tumour cells to radiation and heat: a novel multi-hit-repair approach. *Computational and Mathematical Methods in Medicine*, 2013, 2013.

[220] Nikolaos Sfakianakis, Anotida Madzvamuse, and Mark AJ Chaplain. A hybrid multiscale model for cancer invasion of the extracellular matrix. *Multiscale Modeling & Simulation*, 18(2):824–850, 2020.

[221] Abdus Shakil, James L Osborn, and Chang W Song. Changes in oxygenation status and blood flow in a rat tumor model by mild temperature hyperthermia. *International Journal of Radiation Oncology* Biology* Physics*, 43(4):859–865, 1999.

[222] Lawrence F Shampine and Mark W Reichelt. The Matlab ODE suite. *SIAM Journal on Scientific Computing*, 18(1):1–22, 1997.

[223] Jonathan A Sherratt, Stephen A Gourley, Nicola J Armstrong, and Kevin J Painter. Boundedness of solutions of a non-local reaction–diffusion model for adhesion in cell aggregation and cancer invasion. *European Journal of Applied Mathematics*, 20(1): 123–144, 2009.

[224] Joseph J Skitzki, Elizabeth A Repasky, and Sharon S Evans. Hyperthermia as an immunotherapy strategy for cancer. *Current Opinion in Investigational Drugs (London, England: 2000)*, 10(6):550, 2009.

[225] Kieran Smallbone, David J Gavaghan, Robert A Gatenby, and Philip K Maini. The role of acidity in solid tumour growth and invasion. *Journal of Theoretical Biology*, 235(4):476–484, 2005.

[226] Chang W Song. Effect of local hyperthermia on blood flow and microenvironment: a review. *Cancer Research*, 44(10_Supplement):4721s–4730s, 1984.

[227] Chang W Song, Man-Sik Kang, Juong G Rhee, and Seymour H Levitt. Vascular damage and delayed cell death in tumours after hyperthermia. *British Journal of Cancer*, 41(2):309, 1980.

[228] Chang W Song, Heonjoo Park, and Robert J Griffin. Improvement of tumor oxygenation by mild hyperthermia. *Radiation Research*, 155(4):515–528, 2001.

[229] Gordon G Steel, Judith M Deacon, Gillian M Duchesne, Alan Horwich, Lloyd R Kelland, and John H Peacock. The dose-rate effect in human tumour cells. *Radiotherapy and Oncology*, 9(4):299–310, 1987. doi: 10.1016/s0167-8140(87)80151-2.

[230] William G Stetler-Stevenson, Sadie Aznavoorian, and Lance A Liotta. Tumor cell interactions with the extracellular matrix during invasion and metastasis. *Annual Review of Cell Biology*, 9(1):541–573, 1993.

[231] Theresa Stocks, Thomas Hillen, Jiafen Gong, and Martin Burger. A stochastic model for the normal tissue complication probability (NTCP) and applications. *Mathematical Medicine and Biology: a Journal of the IMA*, 34(4):469–492, 2017.

[232] Bernadette J Stolz, Jakob Kaeppler, Bostjan Markelc, Franziska Braun, Florian Lipsmeier, Ruth J Muschel, Helen M Byrne, and Heather A Harrington. Multiscale topology characterizes dynamic tumor vascular networks. *Science Advances*, 8(23): eabm2456, 2022.

[233] Maximilian AR Strobl, Andrew L Krause, Mehdi Damaghi, Robert Gillies, Alexander RA Anderson, and Philip K Maini. Mix and match: Phenotypic coexistence as a key facilitator of cancer invasion. *Bulletin of Mathematical Biology*, 82(1):1–26, 2020.

[234] Xiaorong Sun, Ligang Xing, Clifton C Ling, and Gloria C Li. The effect of mild temperature hyperthermia on tumour hypoxia and blood perfusion: relevance for radiotherapy, vascular targeting and imaging. *International Journal of Hyperthermia*, 26(3):224–231, 2010.

[235] Hyuna Sung, Jacques Ferlay, Rebecca L Siegel, Mathieu Laversanne, Isabelle Soerjomataram, Ahmedin Jemal, and Freddie Bray. Global cancer statistics 2020: GLOBOCAN estimates of incidence and mortality worldwide for 36 cancers in 185 countries. *CA: a Cancer Journal for Clinicians*, 71(3):209–249, 2021.

[236] Zuzanna Szymańska and Maciej Zylicz. Mathematical modeling of heat shock protein synthesis in response to temperature change. *Journal of Theoretical Biology*, 259(3): 562–569, 2009.

[237] Zuzanna Szymańska, Jakub Urbański, and Anna Marciniak-Czochra. Mathematical modelling of the influence of heat shock proteins on cancer invasion of tissue. *Journal of Mathematical Biology*, 58:819–844, 2009.

[238] Xueyan Tao, Yuanwei Qi, and Shulin Zhou. Mathematical analysis of a tumor invasion model—global existence and stability. *Nonlinear Analysis: Real World Applications*, 61:103297, 2021.

[239] Cornelius A Tobias. The repair-misrepair model in radiobiology: comparison to other models. *Radiation Research*, 104(2s):S77–S95, 1985. doi: 10.2307/3576635.

[240] Andrea Tosin and Luigi Preziosi. Multiphase modeling of tumor growth with matrix remodeling and fibrosis. *Mathematical and Computer Modelling*, 52(7-8):969–976, 2010.

[241] Murat Tunç, Ünal Çamdali, Cem Parmaksizoğlu, and Sermet Çikrikçi. The bio-heat transfer equation and its applications in hyperthermia treatments. *Engineering Computations*, 2006.

[242] Ingela Turesson, Jörgen Carlsson, Anders Brahme, Bengt Glimelius, Björn Zackrisson, Bo Stenerlöw, and Swedish Cancer Society Investigation Group. Biological response to radiation therapy. *Acta Oncologica*, 42(2):92–106, 2003.

[243] Stephen Turner and Jonathan A Sherratt. Intercellular adhesion and cancer invasion: a discrete simulation using the extended Potts model. *Journal of Theoretical Biology*, 216(1):85–100, 2002.

[244] Da Yu Tzou and D y Tzouc. Macro- to micro-scale heat transfer: Past, present and future, 1996.

[245] Jacoba van der Zee, Dionisio González, Gerard C van Rhoon, Jan DP van Dijk, Wim LJ van Putten, and Augustinus AM Hart. Comparison of radiotherapy alone with radiotherapy plus hyperthermia in locally advanced pelvic tumours: a prospective, randomised, multicentre trial. *The Lancet*, 355(9210):1119–1125, 2000.

[246] Caspar M Van Leeuwen, Arlene L Oei, Johannes Crezee, Arjan Bel, Nicolaas AP Franken, Lukas JA Stalpers, and Petra H Kok. The alfa and beta of tumours: a review of parameters of the linear-quadratic model, derived from clinical radiotherapy studies. *Radiation Oncology*, 13(1):1–11, 2018.

[247] Jesús Vaquero, Mercedes Zurita, Concepción Aguayo, and Santiago Coca. Relationship between apoptosis and proliferation in secondary tumors of the brain. *Neuropathology*, 24(4):302–305, 2004.

[248] Peter W Vaupel and Debra K Kelleher. Pathophysiological and vascular characteristics of tumours and their importance for hyperthermia: heterogeneity is the key issue. *International Journal of Hyperthermia*, 26(3):211–223, 2010.

[249] Peter W Vaupel, Helmut Piazena, Markus Notter, Andreas R Thomsen, Anca-L Grosu, Felix Scholkmann, Alan Graham Pockley, and Gabriele Multhoff. From localized mild hyperthermia to improved tumor oxygenation: Physiological mechanisms critically involved in oncologic thermo-radio-immunotherapy. *Cancers*, 15(5):1394, 2023.

[250] Bhanu Prasad Venkatesulu, Lakshmi Shree Mahadevan, Maureen L Aliru, Xi Yang, Monica Himaani Bodd, Pankaj K Singh, Syed Wamique Yusuf, Jun-ichi Abe, and Sunil Krishnan. Radiation-induced endothelial vascular injury: a review of possible mechanisms. *JACC: Basic to Translational Science*, 3(4):563–572, 2018. doi: 10.1016/j.jacbts.2018.01.014.

[251] Pierre Vernotte. Les paradoxes de la théorie continue de l'équation de la chaleur. *Comptes Rendus de l'Académie des Sciences de Paris*, 246:3154–3155, 1958.

[252] Chiara Villa, Mark A Chaplain, and Tommaso Lorenzi. Modeling the emergence of phenotypic heterogeneity in vascularized tumors. *SIAM Journal on Applied Mathematics*, 81(2):434–453, 2021.

[253] Chiara Villa, Mark AJ Chaplain, and Tommaso Lorenzi. Evolutionary dynamics in vascularised tumours under chemotherapy: Mathematical modelling, asymptotic analysis and numerical simulations. *Vietnam Journal of Mathematics*, 49:143–167, 2021.

[254] Aĭzik Isaakovich Volpert, Vitaly A Volpert, and Vladimir A Volpert. *Traveling wave solutions of parabolic systems*, volume 140. American Mathematical Society, 1994.

[255] Zeljko Vujaskovic, Jean M Poulson, Amanda A Gaskin, Donald E Thrall, Rodney L Page, Hal C Charles, James R MacFall, David M Brizel, Robert E Meyer, Deborah M Prescott, Thaddeus V Samulski, and Mark W Dewhirst. Temperature-dependent changes in physiologic parameters of spontaneous canine soft tissue sarcomas after combined radiotherapy and hyperthermia treatment. *International Journal of Radiation Oncology* Biology* Physics*, 46(1):179–185, 2000.

[256] Brett A Wagner, Sujatha Venkataraman, and Garry R Buettner. The rate of oxygen utilization by cells. *Free Radical Biology and Medicine*, 51(3):700–712, 2011. doi: 10.1016/j.freeradbiomed.2011.05.024.

[257] Zhihui Wang, Joseph D Butner, Romica Kerketta, Vittorio Cristini, and Thomas S Deisboeck. Simulating cancer growth with multiscale agent-based modeling. In *Seminars in Cancer Biology*, volume 30, pages 70–78. Elsevier, 2015.

[258] Otto Warburg, Franz Wind, and Erwin Negelein. The metabolism of tumors in the body. *The Journal of General Physiology*, 8(6):519, 1927.

[259] Yoichi Watanabe, Erik L Dahlman, Kevin Z Leder, and Susanta K Hui. A mathematical model of tumor growth and its response to single irradiation. *Theoretical Biology and Medical Modelling*, 13(1):1–20, 2016. doi: 10.1186/s12976-016-0032-7.

[260] Zena Werb. ECM and cell surface proteolysis: regulating cellular ecology. *Cell*, 91 (4):439–442, 1997.

[261] Catharine M West and Gillian C Barnett. Genetics and genomics of radiotherapy toxicity: towards prediction. *Genome Medicine*, 3(8):1–15, 2011.

[262] Mathias S Weyland, Pauline Thumser-Henner, Katarzyna J Nytko, Carla Rohrer Bley, Simone Ulzega, Alke Petri-Fink, Marco Lattuada, Rudolf M Füchslin, and Stephan Scheidegger. Holistic view on cell survival and DNA damage: how model-based data analysis supports exploration of dynamics in biological systems. *Computational and Mathematical Methods in Medicine*, 2020, 2020.

[263] Neil T Wright. Comparison of models of post-hyperthermia cell survival. *Journal of Biomechanical Engineering*, 135(5):051001, 2013.

[264] Wenjuan Wu, Chen Bi, Kelly M Credille, Jason R Manro, Victoria L Peek, Gregory P Donoho, Lei Yan, John A Wijsman, S Betty Yan, and Richard A Walgren. Inhibition of tumor growth and metastasis in non–small cell lung cancer by LY2801653, an inhibitor of several oncokinases, including MET. *Clinical Cancer Research*, 19(20): 5699–5710, 2013. doi: 10.1158/1078-0432.CCR-13-1758.

[265] Peter Wust, Bert Hildebrandt, Geetha Sreenivasa, Beate Rau, Johanna Gellermann, Hanno Riess, Roland Felix, and Peter M Schlag. Hyperthermia in combined treatment of cancer. *The Lancet Oncology*, 3(8):487–497, 2002.

[266] Ozlem Yersal and Sabri Barutca. Biological subtypes of breast cancer: Prognostic and therapeutic implications. *World Journal of Clinical Oncology*, 5(3):412, 2014.

[267] Mohammad U Zahid, Abdallah SR Mohamed, Jimmy J Caudell, Louis B Harrison, Clifton D Fuller, Eduardo G Moros, and Heiko Enderling. Dynamics-adapted radiotherapy dose (DARD) for head and neck cancer radiotherapy dose personalization. *Journal of Personalized Medicine*, 11(11):1124, 2021. doi: 10.3390/jpm11111124.

[268] Lifei Zhu, Michael B Altman, Andrei Laszlo, William Straube, Imran Zoberi, Dennis E Hallahan, and Hong Chen. Ultrasound hyperthermia technology for radiosensitization. *Ultrasound in Medicine & Biology*, 45(5):1025–1043, 2019.